**ADVERTIMENT**. La consulta d’aquesta tesi queda condicionada a l’acceptació de les següents condicions d'ús: La difusió d’aquesta tesi per mitjà del servei TDX (www.tesisenxarxa.net) ha estat autoritzada pels titulars dels drets de propietat intel·lectual únicament per a usos privats emmarcats en activitats d’investigació i docència. No s’autoritza la seva reproducció amb finalitats de lucre ni la seva difusió i posada a disposició des d’un lloc aliè al servei TDX. No s’autoritza la presentació del seu contingut en una finestra o marc aliè a TDX (framing). Aquesta reserva de drets afecta tant al resum de presentació de la tesi com als seus continguts. En la utilització o cita de parts de la tesi és obligat indicar el nom de la persona autora.

**ADVERTENCIA**. La consulta de esta tesis queda condicionada a la aceptación de las siguientes condiciones de uso: La difusión de esta tesis por medio del servicio TDR (www.tesisenred.net) ha sido autorizada por los titulares de los derechos de propiedad intelectual únicamente para usos privados enmarcados en actividades de investigación y docencia. No se autoriza su reproducción con finalidades de lucro ni su difusión y puesta a disposición desde un sitio ajeno al servicio TDR. No se autoriza la presentación de su contenido en una ventana o marco ajeno a TDR (framing). Esta reserva de derechos afecta tanto al resumen de presentación de la tesis como a sus contenidos. En la utilización o cita de partes de la tesis es obligado indicar el nombre de la persona autora.

**WARNING**. On having consulted this thesis you’re accepting the following use conditions: Spreading this thesis by the TDX (www.tesisenxarxa.net) service has been authorized by the titular of the intellectual property rights only for private uses placed in investigation and teaching activities. Reproduction with lucrative aims is not authorized neither its spreading and availability from a site foreign to the TDX service. Introducing its content in a window or frame foreign to the TDX service is not authorized (framing). This rights affect to the presentation summary of the thesis as well as to its contents. In the using or citation of parts of the thesis it’s obliged to indicate the name of the author

# Design and characterization of magnetic systems in race – track microtrons

Juan Pablo Rigla Pérez
PhD THESIS

Instituto de Técnicas Energéticas
Universidad Politécnica de Cataluña
2013

“Nuestras virtudes y nuestros defectos son inseparables, como la fuerza y la materia. Cuando se separan, el hombre no existe”.

Nikola Tesla (1856 – 1943)

# Contents.

## List of Figures.

**List of Tables.**

# Agradecimientos

En primer lugar me gustaría agradecer a mi familia, a mi madre y a mi hermano, todo su apoyo durante estos años, ya que sin ellos no podría haber realizado esta tesis y por darme ánimos en los momentos mas difíciles de estos años. Sin ellos mo podría haber llevado a cabo este trabajo. También me gustaría darle las gracias a mi padre, aunque no ha podido ver culminar este trabajo el haberme inculcado el amor al trabajo y que con el esfuerzo uno puede conseguir lo que desee.

Me gustaría dar las gracias a mi mejor amigo "Gordi" por haberme hecho pasar momentos muy divertidos durante estos años y por demostrarme todo su cariño así como su fidelidad tanto en los buenos como en los malos momentos. Gracias por haber sido un gran amigo. Nunca te olvidaré.

Me gustaría dar las gracias a mi director de tesis el Dr.Youri Koubychine por haberme iniciado en el campo de los aceleradores de partículas y por inducirme el amor a este campo científico. Le doy las gracias por haber confiado en mí desde el principio y por demostrarme que con el esfuerzo se pueden conseguir los frutos deseados. Por último me gustaría agradecerle la paciencia que ha demostrado tener conmigo en determinados momentos durante el desarrollo de esta tesis.

Me gustaría dar las gracias al resto de los miembros del proyecto microtron de la UPC (Universidad Politécnica de Cataluña), Alexandre Sánchez, Xavier González y en especial al Dr.Vasily Shvedunov por sus consejos y comentarios durante el desarrollo de esta tesis y el haberme tratado con un miembro mas de su equipo durante mi estancia en el SINP (Skobeltsyn Institute of Nuclear Physics).

Me gustaría dar las gracias a todos los miembros del INTE en especial a Vicente Blasco, otro Navarresino, al que considero un gran amigo y al que me gustaría darle las gracias por su humanidad y por sus magníficos consejos durante mis años en el INTE. También me gustaría dar las gracias a Mª Amor Duch por haberme ayudado con sus consejos en momentos de animo mas bajos y tensos durante el desarrollo de esta tesis y por último a Juan Antonio Romero por su ayuda informática, sin su ayuda no podría haber terminado esta tesis.

Me gustaría dar las gracias al Dr. Miquel Ferrer del Departamento de Resistència de Materials i Estructures a l'Enginyeria de la Universidad Politécnica de Cataluña y a Enrique Ruiz de Villa Valdés de Elytt Energy por los consejos y la ayuda que me han dado sobre el código de simulación ANSYS de vital importancia para el desarrollo de esta tesis.

Me gustaría agradecer los momentos tan divertidos que hemos pasado en estos años a mis compañeros de la antigua sala de becarios: Marina, Elisabet, Cristina, Victor, Vitaly, Raimon,… y al resto de los becarios: Marta y Roger.

Me gustaría dar las gracias al Dr. Guillermo Benlloch Petit por haber sido un gran amigo durante momentos muy difíciles de mi vida en estos años y por haber encontrado siempre un momento por quedar y hablar conmigo.

Me gustaría dar las gracias a Luís Fernando Vidal “Koldo” por haber sido un gran amigo durante mi estancia en Valencia y posteriormente en Barcelona y por sus magníficos consejos durante todos estos años.

A mi familia francesa por haberme acogido en momentos muy dificiles y por demostrarme su cariño durante todos estos años.

Por último me gustaría dar las gracias a los miembros del Colegio Mayor Universitario Monterols con Jordi Pujol Soler a la cabeza por el ambiente familiar con el que me han tratado durante los seis años que he convivido con ellos. Muchas gracias.

Juan Pablo Rigla Pérez.

# Abstract

This thesis is devoted to the design and optimization of magnetic system for electron race – track microtrons (RTMs), to the study of their magnetic characteristics and analysis of some effects of the particle beam dynamics in them. Design calculations of magnetic systems of a 12 MeV RTM for medical applications, which is currently under construction at the Technical University of Catalonia (Universitat Poltècnica de Catalunya, UPC), and optimization studies of an extraction dipole of a 55 MeV RTM for the detection of explosives currently, which in the stage of tests at the Skobletsyn Institute of Nuclear Physics of the Moscow State University are carried out. The design and optimization were performed by means of 2D and 3D simulations using different codes (POISSON, FEMM, ANSYS).

Also a technique for the calculation of the phase slip effect, important for RTMs with low energy injection, is developed and applied to the analysis of beam dynamics in the UPC 12 MeV RTM. Finally a detailed study of the beam focusing in RTM end magnets with additional dipole is performed.

**Keyword: Microton, magnetic system design, end magnet, extraction magnet, focusing magnet, permanent magnet, magnetic measurements, magnetic screens, stray magnetic field, fringe field, phase – slip and optical beam.**

# Chapter 1

# Introduction

## 1.1. – Race-track microtrons as accelerators with beam recirculation.

In the last four-five decades there has been a growing demand in particle accelerators which can provide electron beams in the energy range from 10 MeV to 100 MeV with high energy resolution, high duty factor and relatively high intensity. The main sectors interested in such machines are industry (non-destructive radiography of materials, sterilization, etc.), medicine (radiotherapy and isotope production for PET), security systems (cargo inspection) and nuclear physics research (in this case beam energies up to few GeV are desirable). Low power consumption and low capital cost of the construction of the accelerators are other important factors to be taken into account. Among the variety of small and medium size electron accelerators *race-track microtrons* [1, 2] turned out to be most optimal machines for certain applications as it will be described in more detail further in this section. Also, as it will be explained shortly this type of accelerators combine the principles of operation and certain advantages of classical (circular) microtrons and linear accelerators (linacs). Studies of some aspects of operation of RTMs and design simulations of their magnetic systems will be the subjects of the present thesis.

The concept of circular microtron was proposed by W. Veksler from the Lebedev Physical Institute (Moscow) and dates back to 1944 [3]. The idea of the machine was to accelerate electrons to relativistic energies by their multiple passages through an accelerating cavity and arrange their recirculation by means of a uniform magnetic field. This design was first coined as “electron cyclotron”. Later, since these accelerators use a microwave or radiofrequency (RF) cavity, its name was changed to “microtron”.

The principle of operation of this circular microtron (also called classical microtron) can be seen in from Fig. 1. Its main components are an electron source (electron gun) and a microwave (or radiofrequency, RF) cavity (1), magnet (2), a circulating beam (3) and an extraction channel (4). The electrons are emitted by the cathode of the gun and are accelerated by a high frequency electromagnetic field excited inside the RF cavity. All the trajectories pass inside a constant uniform magnetic field whose vector is orthogonal to the orbit plane. The function of the field is to bend the beam trajectory and in this way provide its recirculation through the RF cavity. When the electrons reach the maximum energy they exit the vacuum chamber of the microtron and are directed towards the beam output window. The first microtron was built at the Physics Division of the National Research Council of Canada [4], it began its operation in 1947 producing a 4.6 MeV electron beam.

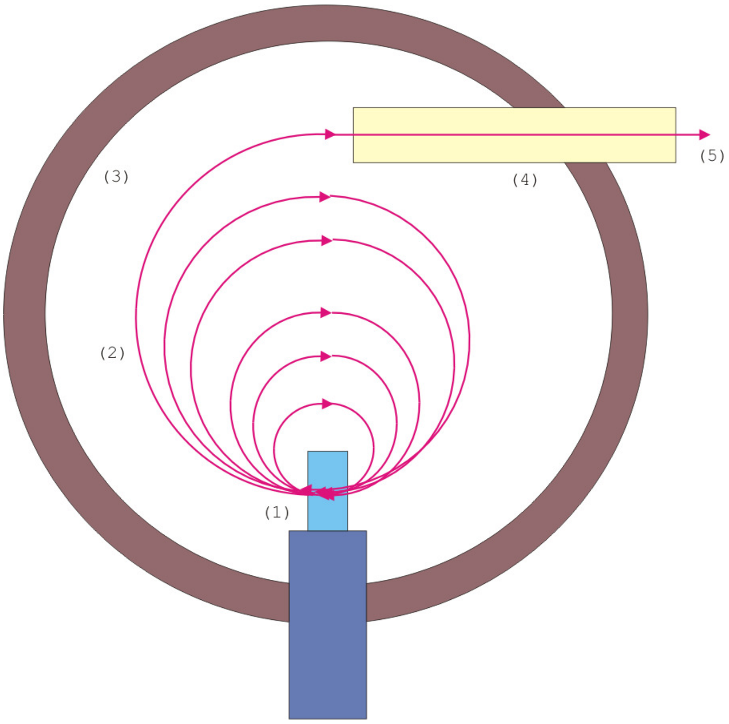

Figure 1: Scheme of the circular Microtron.

The main disadvantage of the circular microtron is that the accelerating structure consists of a single resonant cavity and therefore the energy gain per turn is limited to 0.5 – 1 MeV. As a consequence, due to an existing relation between the energy gain and bending magnetic field (see below) the latter is only 0.1-0.2 T (for a typical frequency of the RF accelerating electromagnetic is 3 GHz). Then, for the electron beam to reach a high energy the magnet must be large enough and this becomes a practical limitation of the machine. Moreover, the circular microtron design does not allow to place focusing magnets. Typically the beam energies obtained in accelerators of this type are from 5 MeV to 25 MeV with an average beam current of 20-30 μA. The highest energy obtained in circular microtrons is 35.0 MeV [5].

With the aim to overcome these limitations and to add more flexibility in the control of the synchronicity condition, J.S. Schwinger proposed in 1945 the concept of RTM [1]. The idea was to modify the design of the circular microtron by splitting its magnet in two halves, pulling them apart and use the opened drift space for placing an accelerating structure with few cavities thus allowing for the acceleration of several units of the relativistic factor $\gamma$ per pass. Results of first studies of the RTM beam dynamics and reviews on the RTM systems and operation can be found in Refs. [6, 7].

A general layout of the RTM and the principle of its operation are illustrated in Fig. 2. Electrons are injected from an electron gun or some other accelerator (1). To ensure the correct injection of the electrons into the machine, dedicated bending magnets (2) may be used. The beam recirculation is provided by two 180º bending magnets (3), usually called end magnets. At each turn the electrons pass through the accelerating structure (5) thus increasing their energy. Also focusing magnets providing stable beam optics and/or correction magnets for correcting magnetic errors of the end magnets can be installed on the individual or common (4) sections of the RTM orbits.

Once the electrons have reached the required energy, the beam is deviated by a extraction dipole magnet (6) and it is directed towards the RTM beam output.

The general advantages of RTMs with respect to the circular microtron are the following:

1. The electron injection is more flexible and can be optimized,
2. It is possible to place a few RF cavities in the space between the end magnets thus allowing to increase the beam energy gain per orbit,
3. It is possible to place focusing magnets and other systems (phase shifter, beam position monitor, etc.) in the space between magnets to improve the beam stability and beam control.

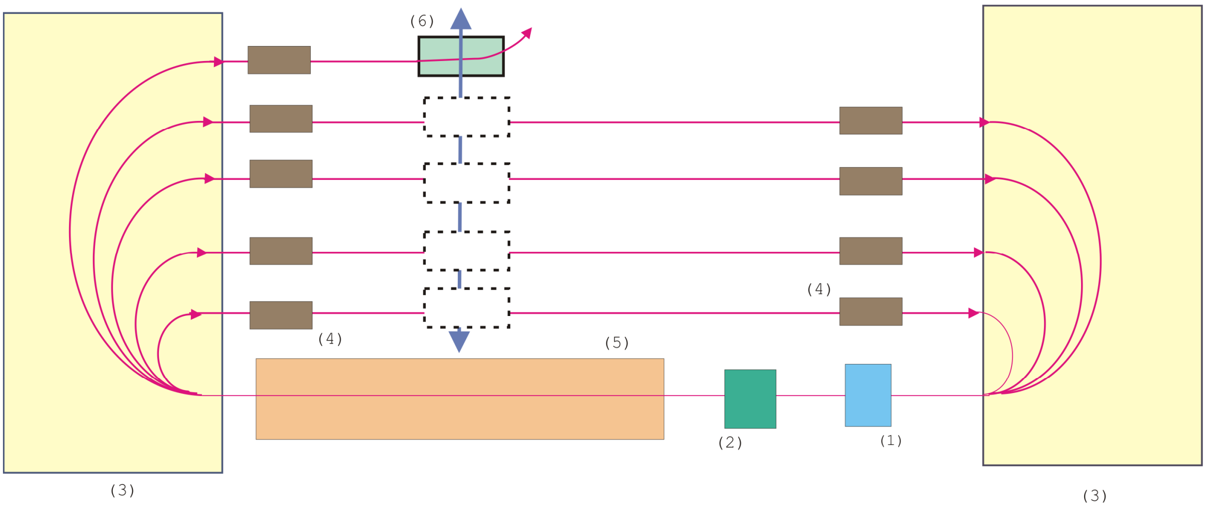

Figure 2: Scheme of a race - track Microtron.

As in the case of all circular accelerators, the general principle of operation of RTMs is based on two relations [1]. The first one is the equilibrium condition following from the Lorentz force formula:

$$\frac{p_n}{R_n} = |e| B_0 \tag{1}$$

It establishes a relation between the magnetic field induction $B_0$ in the end magnets, the particle momentum $p_n$ at the $n$-th orbit and the radius $R_n$ of the trajectory inside the end magnet also at the $n$-th orbit. Here $e$ is the elementary electric charge.

The second relation is the synchronicity condition or condition of resonance acceleration:

$$T_n = \mu_n T_{RF} \tag{2}$$

where the harmonic numbers $\mu_n$ are positive integers. Eq. (2) states that the time of particle revolution at the $n$-th orbit is an integer multiple of the period $T_{RF} = 1/f_{RF}$ of the accelerating RF electromagnetic wave. A specific feature of RTMs is that the harmonic number $\mu_n$ varies with $n$ remaining to be a positive integer. This distinguishes RTMs from other types of circular accelerators, for example synchrotrons or cyclotrons, in which case the harmonic number is constant. Parameters of an RTM must be chosen in such a way that the increase of the harmonic number from orbit to orbit is a constant integer number, i.e.

$$\Delta T = T_{n+1} - T_n = \nu T_{RF} \tag{3}$$

The positive integer $\nu$ determines the mode of operation of the machine.

As we will see in Chapter 2 resonance conditions (2) and (3) are fulfilled for a so called reference (or synchronous) particle whose dynamics determines the design parameters of a given accelerator. It can be easily seen that the basic RTM relations, Eqs.(1) – (3), imply that the energy gain $\Delta E_s$ of the reference particle at each passage through the accelerating structure satisfies

$$\Delta E_s = \frac{\nu c \lambda |e|}{2\pi} B_0, \tag{4}$$

where $\lambda = cT_{RF}$ is the wavelength of the accelerating RF field. Eq.(4) is often referred to as the main RTM relation, it also holds in the case of circular microtrons [1].

The RTM can be considered as a linac with beam recirculation and therefore has several advantages with respect to common linear accelerators:

1. – To accelerate an electron beam to a given energy the accelerating structure of an RTM with *N* beam recirculations is in general *N* times shorter than that of a linear accelerator. Therefore the length and weight of the accelerating structure are roughly N times smaller in the case of RTM. Though RTMs include two end magnets in general the dimensions of the accelerating module turns out to be considerably smaller then in the case of a linac of the same beam energy. Alternatively the accelerating field gradient may be reduced below 10-15 MeV/m thus avoiding the appearance of a dark current.

2. – Due to the previous property the beam acceleration in RTMs requires less RF power. This reduces the pulse power of the RF source and pulse generator (modulator) and also their cost, size and weight.

3. - The RTM principle of operation allows to change easily the output beam energy with a fixed step in a wide range by simply extracting the beam from the corresponding orbit.

4.- RTM end magnets act as a precise spectrometer, i.e. only particles with energy close to the reference one follow the correct orbit and continue their circulation inside the machine. Because of this a highly monoenergetic output beam is generated without any special beam control. Typically the energy spread of the RTM beam at the last orbit is only ~50-100 keV and does not have low energy tail.

RTMs have certain limitations, the main of them are the following:

1. The fringe field of the end magnets produces a defocusing of the beam. Imperfections of the magnetic field are a source of additional errors.

2. The weight of the ends magnets which grows with energy as ~ $E^3$, this is a serious technical limitation on the maximal beam energy.
3. In case of a low energy injection the problem of linac bypass by the beam at the first orbit exists and this requires more complicated design of the magnets or of the accelerating structure.
4. Slip of the phase and impossibility to fulfil the synchronicity condition at the first orbit in case of low energy injection reduce the effectiveness of acceleration and capture of the beam.
5. For certain regimes of operation beam instabilities may develop.

In the present thesis, solutions to some these problems are proposed and analyzed.

The RTMs turn out to be the most efficient machine for applications with relatively low pulse beam current (about 10-20 mA) and medium or high energies (between 10 MeV and 100 MeV). Such applications include electron injectors in synchrotrons [8] and free-electron lasers [9], radiotherapy [10], isotope production [11], explosives detection [12] and the nuclear physics research [13] (see Table 1). Currently new applications of RTMs are emerging such as a compact muon source [14] or X-ray source based on the Compton backscattering [15].

Table 1: Main applications of RTMs.

| **Application** | **Range of energies (MeV)** | **Average beam current** |
|---|---|---|
| Injector | 4 - 100 | ~ 50 μA – 100 mA |
| Intraoperative radiation Therapy | 6 MeV – 12 MeV | ~1 μA |
| External radiation therapy | 4 MeV – 50 MeV | ~100 μA |
| Cargo inspection, defectoscopy | 2.5 MeV – 10 MeV | ~10-100 μA |
| Elemental analysis | 15-40 MeV | ~10 μA |
| Explosive detection | 30-70 MeV | ~10-100 μA |
| Isotopes production (PET, $I^{123}$, etc) | 15-30 MeV | ~100 μA |

As examples of two RTMs in operation we can refer to the electron accelerators of the Electron Beam Laboratory at the Skobeltsyn Institute of Nuclear Physics (SINP) of the Moscow State University, Russia [16]. One of them is the machine generating an electron beam with output energies between 30 MeV and 70 MeV commissioned in 2002 [17]. The particles are injected from a 50 keV electron gun and are accelerated by an accelerating structure with the energy gain 4.8 MeV per pass. The maximal energy is achieved in 14 beam recirculations. Initially the RTM was used as a mobile light source for experiments with a Carbon/Nitrogen chamber at the SINP. Now it is mainly used as a part of a pulsed source of photons and neutrons for nuclear experiments [18]. A general view of the 70 MeV RTM is given in Fig. 3, its parameters are listed in Table 2.

The other SINP RTM commissioned in 1998 [19] produces an electron beam with the output energy between 5 and 35 MeV (see main parameters in Table 2). This machine has a high energy injection from a 5 MeV pre-accelerator formed by a photocathode, α-magnet and an accelerating structure. Once the beam is injected and accelerated by the main acceleration structure with the energy gain 2.43 MeV per pass, the maximal number of beam orbits is 14. This RTM is capable of generating a bright electron beam with short bunches (a few ps), high charge per bunch (~150 pC) and low emittance (~ 5 mm mrad of normalized emittance).

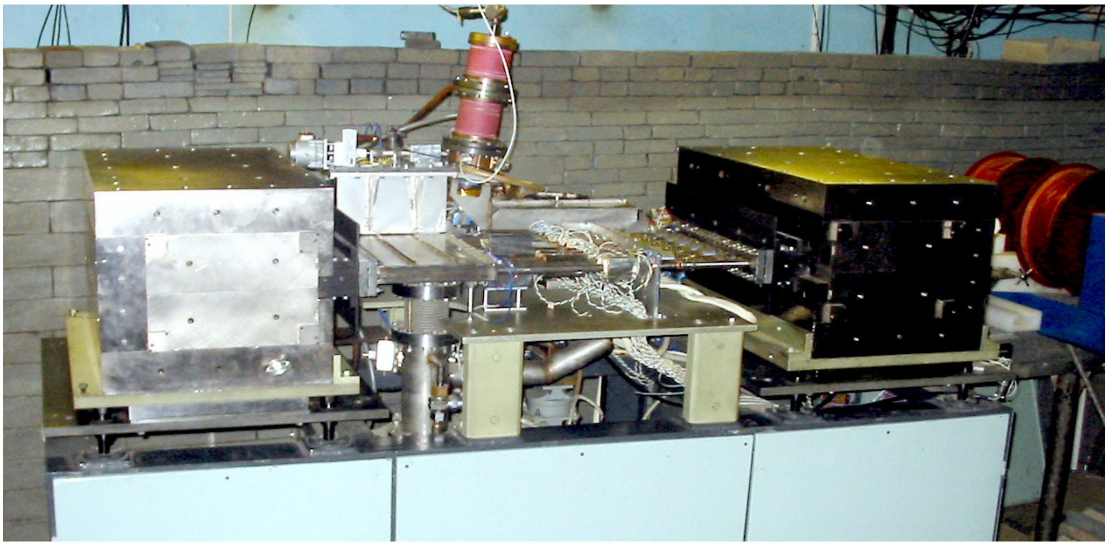

Figure 3: General view of the 70 MeV RTM of the SINP, Moscow State University.

Table 2: Main characteristics of the RTMs of the SINP, Moscow State University.

| **Parameter** | **70 MeV RTM** | **35 MeV RTM** |
|---|---|---|
| Injection energy | 48 – 50 keV | 4.85 MeV |
| Energy gain per turn | 4.8 MeV | 2.43 MeV |
| Output energy | 14.8 – 68.3 MeV | 4.85 – 34.20 MeV |
| Number of orbits | 14 | 14 |
| RF frequency | 2856 MHz | 2856 MHz |
| End magnet field | 0.963 T | 0.486 T |
| End magnet working region | 50x250x20 $mm^3$ | 50x250x20 $mm^3$ |

For technical resasons it is not possible to provide beam focusing for the whole range of energies in high energy RTMs. To overcome this problem and obtain beams with energies higher than 100 MeV it was proposed to connect a few RTMs in a cascade. A remarkable example of a cascade of RTMs is the MAMI (Mainzer Microtron) facility at the Johannes Gutenberg Universität in Mainz (Germany) (see, for example, [20]). The MAMI A and MAMI B sections consist of a linac injector and three RTMs which produce a continuous wave (CW) electron beam with the maximal energy 855 MeV for nuclear physics experimental lines (see Fig. 4 and table 3). In 1999 as a response to the need in higher energies for nuclear physics experiments it was decided to increase the maximal energy of the electron beam to 1.5 GeV. Since the weight of the end magnets of a standard RTM design would then exceed 2400 tons making its construction not feasible it was proposed to choose a double-sided microtron design that was developed by K.H. Kaiser in 1981 [21]. This machine known, as Harmonic Double - Sided Microtron (HDSM), was commissioned in 2006 [22]. It consists of two long accelerating structures and two pairs of 90° bending magnets (see Fig. 5).

A part of the present thesis is devoted to the design and optimizations of a compact RTM which is under construction at the Technical University of Catalonia (Universitat Politècnica de Catalunya, UPC) and a 55 MeV RTM recently commissioned at the SINP. Detailed descriptions of these machines are given in Sect. 1.3 and Sect. 1.4, respectively.

Table 3: Main parameters of the MAMI facility.

| | Accelerator | Extraction Energy (MeV) | Turn | Energy gain per turn (MeV) | Year of commissioning |
|---|---|---|---|---|---|
| **MAMI A** | Van. Graaff | 3 | - | - | 1979 - 1988 |
| | Linac | 3.97 | - | - | 1988 |
| | RTM 1 | 3.97 – 14.86 | 18 | 0.6 | 1979 |
| | RTM 2 | 14.86 – 180 | 51 | 3.24 | 1983 |
| **MAMI B** | RTM 3 | 180 – 855 | 90 | 15 | 1990 |
| **MAMI C** | HDSM | 855 - 1508 | 43 | 41.1 | 2006 |

Figure 4: General view of the MAMI A and MAMI B.

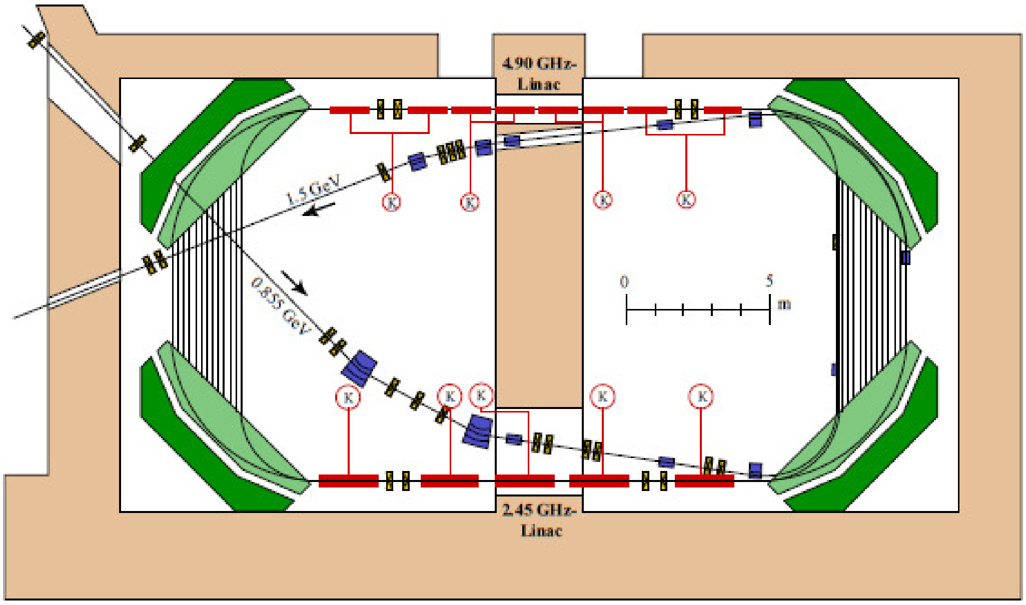

Figure 5: Scheme of the Harmonic Double - Sided Microtron of the MAMI facility.

We would like to add that due to the advantages of the race-track geometry, a considerable number of electron accelerators with beam recirculation have been commissioned in the recent years. The largest of them built so far is the Thomas Jefferson National Accelerator Facility, known as CEBAF (Continuous Electron Beam Accelerator Facility) [23] commissioned in 1994. Its characteristic feature is that each orbit has its own magnetic system in the bending arcs (see Fig. 6). Note that this accelerator is an isochronous recirculating machine, whereas RTMs and HDSM discussed above are non-isochronous ones. In the CEBAF facility the beam acceleration is produced in superconducting RF cavities, this allows to achieve an accelerating field gradient up to 15 MV/m. At present the accelerator produces an electron beam with energy of 6 GeV, its upgrade to 12 GeV output energy is currently going on. Just for completeness let us mention that there are a few other race-track type recirculators built earlier, namely the recyclotron in Darmstadt (commissioned 1990) and electron beam recirculator at Stanford (1972).

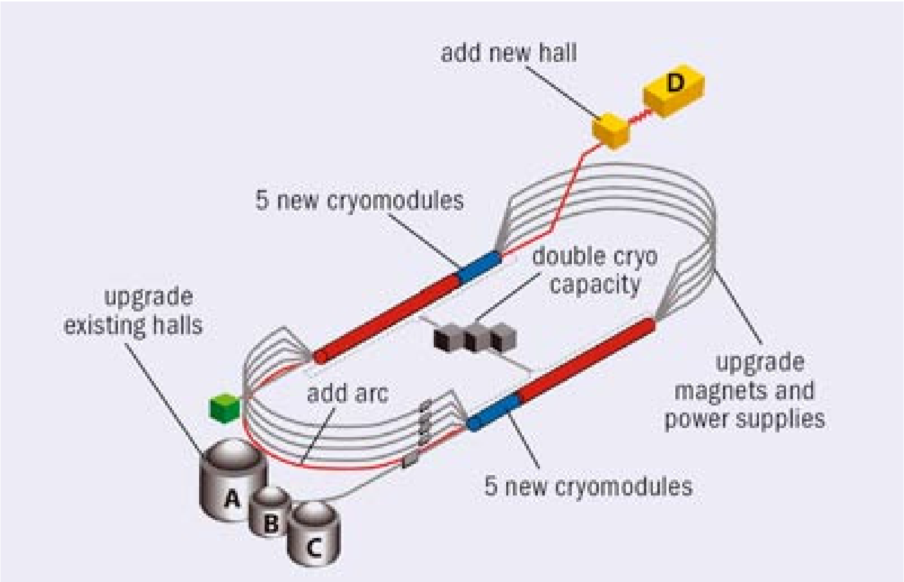

Figure 6: Scheme of the CEBAF facility.

## 1.2. – State of the art.

Since the first proposal of the RTM a wide and detailed study of beam dynamics in this type of accelerators has been carried out [1]. Many aspects of beam motion in RTMs are the same as in case of other circular accelerators [24]. However there are some specific features which are of particular importance in case of RTMs.

One of them is the fringe field in the end magnets that produces a strong defocusing in the vertical plane. A solution was proposed by H. Babic and M. Sedlacek in 1967 [25] and consisted in adding an additional dipole of inverse magnetic field polarity at the entrance to the end magnet. In what follows we will referred to it as inverse pole.

Another specific feature of RTM beam dynamics is related to cases of low energy injection. Indeed, frequently in order to have a simple machine the initial beam is emitted from an electron gun with the voltage between the anode and cathode about 20-50 kV. Since the magnetic field in the end magnets and the energy gain per turn are related through Eq.(4) the radius of the electron trajectory in the end magnet may not be large enough to surpass the accelerating structure after the first turn and the beam may hit the linac wall. To avoid the beam loss a few solutions have been proposed and implemented. One of them is to make a channel in the accelerating structure to allow the beam path [26]. Another one, proposed by P. Alvisson and M. Ericsson in 1976 [1] and for the first time used in the RTM design of the Wisconsin University, consisted in the reflection of the beam back into the accelerating structure and its second acceleration in the direction inverse with respect to the injected trajectory. To arrange the beam reflection they proposed to place a pair of dipoles with opposite polarities at the entrance to the end magnet that create a parallel displacement of the beam and adjust their magnetic fields accordingly (see Ref. [1]). In an alternative RTM magnet design described in Ref. [27] only one dipole with inverse field is added. It was shown that in this way both the problem of fringe field defocusing can be solved and the reflection of the beam trajectory back into the linac can be achieved. Beam dynamics properties of this design are the object of the analysis in Sect. 5 of the present thesis. It turns out that the approach of Ref. [28] works for the RTM operating at the RF wavelength $\lambda$=10 cm, but is not applicable for shorter wavelengths, as in the case of the UPC 12 MeV RTM. We will see that for this compact accelerator with low energy injection another end magnet design should be used. Such new design is described and studied in detail in Sect. 4.

Another effect relevant in case of low energy injection schemes is a phase slip in the longitudinal beam dynamics. Since the electrons are not sufficiently relativistic at the first or a few first orbits the conditions of synchronicity (2) and (3) are not fulfilled at these orbits. The phase slip effect leads to a low efficiency of beam acceleration, additional beam losses and even to a beam instability. In Ref.[28] a first detailed analytic study and numerical simulations of this effect were given. In this paper only the case of a simple magnet without the fringe field and additional poles was considered. The phase slip for more general magnetic field distributions is the object of analysis in Sect. 5 of the present thesis.

A large part of the thesis is devoted to the design simulations and optimization of magnetic systems with permanent magnets, like end magnet, focusing quadrupole and extraction dipoles. There exists a large experience and extensive literature on the magnetic and beam dynamic properties of RTM magnets, their technical characteristics, design considerations, etc. As a common practice magnets used in particular accelerators are electromagnets. However, in the recent 15-20 years an increasing use of systems with Rare-Earth Permanent Magnet (REPM) materials with a strong residual magnetization as a source of the magnetic field has taken place [29]. Permanent magnets have certain advantages over electromagnets, namely they (a) do not require power supply and cooling system, (b) allow to achieve a quite strong magnetic field with a required field profile in the median plane; (c) allow building compact systems, (d) are resistant to a radiation damage, and (e) can be used in a high vacuum environment provided their design is adapted to this (Ni coating if necessary, fixing without gluing, etc.). The major disadvantage of magnetic systems with permanent magnets is that the field level cannot be varied in a simple way during the machine operation. Therefore their machining and magnetization must be highly precise and require a considerable previous experience.

Important developments of methods and techniques of the calculation in accelerator magnetic systems with permanent magnets and their design were carried out at the Lawrence Berkeley Laboratory and SLAC (Stanford Linear Accelerator Centre) by K. Halbach in 70s and 80s [30, 31, 32]. An important step forward was a novel design of the magnet of a compact cyclotron known as "Cyclotrino" proposed by A. Young [33]. Namely, an REPM material was used as a source of the magnetic field and it was of the so called "box type" which consisted of two steel poles whose surfaces were in contact with REPM blocks except the one facing the particle trajectories. Later similar magnets were used in a number of machines, for example in the SINP 70 MeV RTM [17] and 12 MeV UPC RTM (see Sect. 1.3).

Among alternative designs of RTM magnetic systems with permanent magnets we would like to mention a QSM (Quasi - Sheet Multipole) type structures [34]. It has certain advantages in comparison with the Halbach one, in particular it requires 30% less magnetic material to generate the magnetic field of the same strength and two-thirds less steel, thus allowing to obtain more compact and lighter systems. The main disadvantages of the QSM design are that it uses triangular REPM blocks, which are technologically are more complicated, and hence more expensive, than rectangular blocks, it is more difficult to get a required field homogeneity in the region of beam trajectories and the magnetic field is normally limited to ~ 1T. The QSM technology was used in the end magnet of the 35 MeV RTM of the SINP [34,35].

Initially permanent magnets were used in focusing quadrupoles [36]. Recently there are more and more example of bending dipoles using REPM material as a field source [16, 8], including designs of a whole storage ring lattice built out of permanent magnet dipoles [37, 38]. Accelerator systems in which permanent magnets are widely used are insertion devices of synchrotron radiation sources, both wigglers and undulators [39]. The field is usually produced by REPM sintered material such as $Nd_2Fe_{14}B$ and $SaCo_5$ which have a high residual magnetization up to 1.1 – 1.4 T. We would like to add that first designs of magnets for such systems were proposed and developed also by K. Halbach [30,31,32]. Much experience and technical data on permanent magnets have been obtained from the design, machining and magnetization of magnetic blocks for insertion devices. In particular the successful development of in-vacuum undulators showed that it is possible to have the magnets in a high-vacuum environment and this influenced the design of the main module of the UPC 12 MeV RTM (see Sect. 1.3). One of the current tendencies in this field is the search and use of new permanent magnets with better properties, like for example $Pr_2Fe_{14}B$ [40] which allows to maintain high magnetization up to 1.7T.

The development of compact RTMs for industrial and medical applications requires new design solutions which include, in particular, small size end magnet systems with a few additional dipoles and with a rather strong (up to ~1 T) magnetic field between the main poles, as well as extraction dipoles and focusing quadrupoles, all of which can be used in a high vacuum environment. Design simulations and definition of technical parameters of such systems is one of the goals of the present thesis.

### 1.3. – 12 MeV RTM project of the Universitat Politècnica de Catalunya.

An important part of the thesis is devoted to theoretical studies and design simulations of the magnets for a compact 12 MeV RTM [41,42]. The construction and commissioning of this electron accelerator is a project carried out at Universitat Politècnica de Catalunya (UPC) in a close collaboration with specialists from the SINP and CIEMAT (Madrid). The project is coordinated from Institut de Tècniques Energètiques (INTE) of the UPC.

The main features of the 12 MeV RTM design were proposed in Ref.[43] with the idea that this accelerator would be used as a source of an electron beam for a mobile complex for the Intraoperative Radiation Therapy (IORT). The IORT is a radiotherapy technique consisting in the delivery of a single and high dose (up to 20-40 Gy) during a surgical operation directly to a cancer tumor or a tumor bed after the tumor removal [44]. Clear advantages of the IORT technique is a good local control and a minimization of healthy tissue damage. The development of the IORT and its implementation have experienced a fast development with appearance of mobile irradiation complexes based on linear accelerators, like Mobetron [45] or Liac [43], which can be used directly in an operation room. The challenging goal of the UPC project is to build an IORT complex with an RTM as an electron beam source taking advantage of RTMs with respect to linacs explained above.

The architecture of the UPC 12 MeV RTM is shown in Fig. 7. The central component is the accelerating module whose 3D model is given in Fig. 8. It is housed by a vacuum chamber coupled to an ion pump through a pumping tube which can also play the role of a supporting arm of a future IORT complex. The accelerating structure is fed by a 1 MW power magnetron through a system of waveguides. The magnetron and the electron gun are powered by 3 μs high voltage pulses from a modulator. The main parameters of the RTM are given in Table 4.

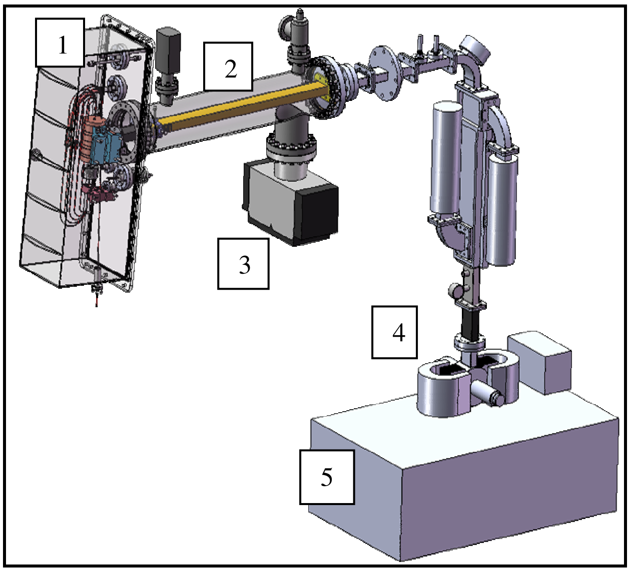

Figure 7: Main components of the UPC 12 MeV RTM: (1) vacuum chamber, (2) pumping out tube, (3) ion pump, (4) RF power source (magnetron), (5) modulator.

Table 4: UPC 12 MeV RTM parameters.

| | |
|---|---|
| **Beam energies** | 6, 8 , 10 and 12 MeV |
| **Energy gain per turn** | 2 MeV |
| **Operating wavelength** | 5.25 cm |
| **Maximum beam current** | 2.5 µA |
| **Length pulse** | 3.0 µs |
| **Repetition Rate** | 1 – 250 Hz |
| **End magnet field** | 0.8 T |
| **Injection kinetic energy** | 25.0 keV |
| **Pulsed RF power** | <750 kW |
| **Delivered dose rate** | 10 – 30 Gy/min |
| **Accelerator head dimensions** | 578x200x123 mm |
| **Accelerator head weight** | <80kg |

The beam makes up to six recirculations inside the accelerator head (see Fig. 8). The electrons are emitted from an on-axis electron gun, accelerated in a standing wave accelerating structure with four cells, bended by two end magnets with additional dipoles and focused by a quadrupole magnet. The extraction of the electrons from one of the last four orbits is achieved by deflecting the beam towards the output channel by one of the four extraction dipoles hold by a frame which is moved vertically by a step motor (not seen in Fig.8). All these elements are fixed on a rigid platform placed in the vacuum of about $10^{-7}$ mbar created inside the vacuum chamber.

The design of the UPC 12 MeV RTM includes some technical solutions which are novel or not common for this class of particle accelerators and which allow to get a competitive IORT dedicated machine. The most essential of them are the following:

1. – C-band accelerating structure [47, 48, 49].
2. – Compact on-axis electron gun with an off-axis cathode [50].
3. – Compact in-vacuum end magnet system with additional dipoles using REPM as the source of the magnetic field [51].

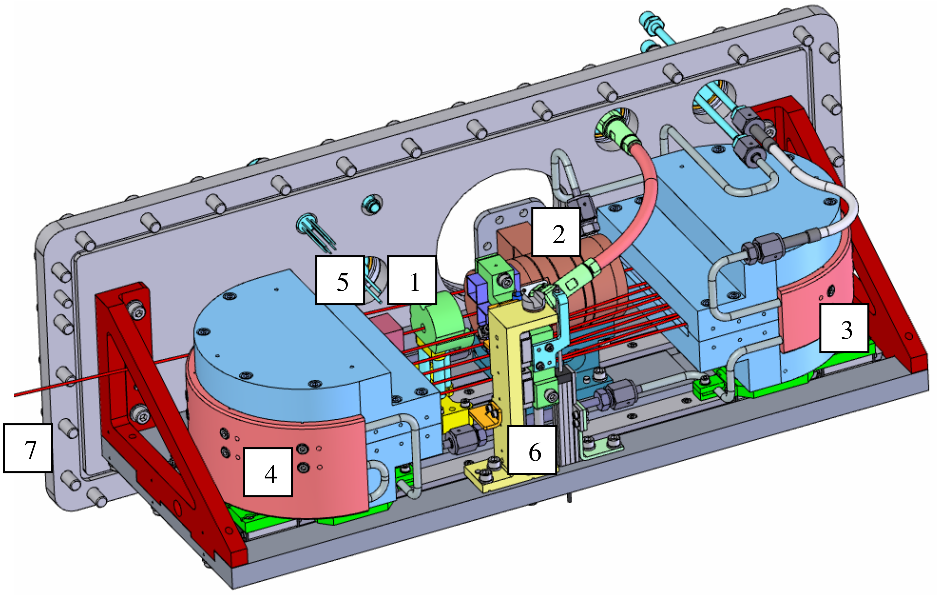

Figure 8: 3D view of the RTM accelerating module: (1) electron gun, (2) accelerating structure (linac), (3) and (4) end magnet, (5) quadrupole magnet, (6) frame with extraction magnets, (7) output beam.

The magnetic systems of the UPC 12 MeV RTM include two end magnets, four extraction magnets and one focusing quadrupole magnet. They will be a subject of a detailed study in this thesis.

At the present time the UPC 12 MeV RTM is at the stage of system assembling and tests [48]. Also numerical simulations of generated radiation and analysis of safety issues [52], mounting of a test bench, etc. are going on. Fig.9 shows a session of vacuum tests of the vacuum chamber connected to the turbomolecular and ion pumps, whereas Fig.10 shows the supporting platform with the linac, electron gun, beam extraction mechanism and cooling tubes already mounted.

Figure 9: Vacuum chamber and pumping tube assembly connected to the turbomolecular (right) and ion pumps during one of the vacuum test sessions.

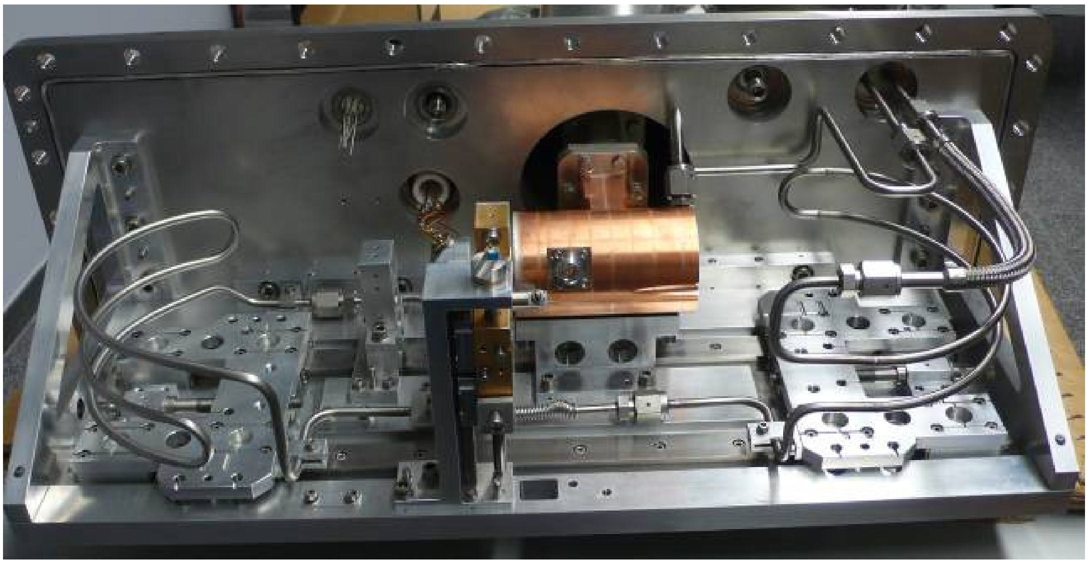

Figure 10: Supporting platform with linac, electron gun, beam extraction mechanism and cooling tubes installed.

## 1.4. – 55 MeV RTM of the Skobeltsyn Institute of Nuclear Physics.

Another electron accelerator related to the present thesis is the 55 MeV RTM constructed and commissioned at the SINP (Moscow State University) in collaboration with the Lebedev Institute of Physics of the Russian Academy of Science (Moscow) [53]. The main parameters of this machine are given in Table 5, its general view is shown in Fig. 11. Electrons are emitted by a 50 keV electron gun (6) and are accelerated by linac (7). The beam trajectories are bent by two electromagnets, (1) and (2), corrected by steering magnets (4) at each orbit and controlled by beam current monitors (3). Extraction magnet (5) is a hybrid magnet in which the main field is produced by REPM blocks and which also includes excitation coils used to adjust the field level. An improvement of the extraction magnet design of this RTM and optimization of its parameters is the subject of the study in Sect. 4.4 of this thesis.

Table 5: Parameters of the SINP 55 MeV RTM.

| Parameter | Value |
|---|---|
| **Output energy** | 55 MeV |
| **Output pulse current** | 10 mA |
| **Pulse repetition rate** | 5-50 Hz |
| **Maximal number of orbits** | 11 |
| **Energy gain per turn** | 5MeV |
| **Pulse duration** | 5 µs |
| **End magnet field** | 1.0 T |
| **Maximum pulse RF power** | 2.5 MW |
| **Operating frequency** | 2856 MHz |

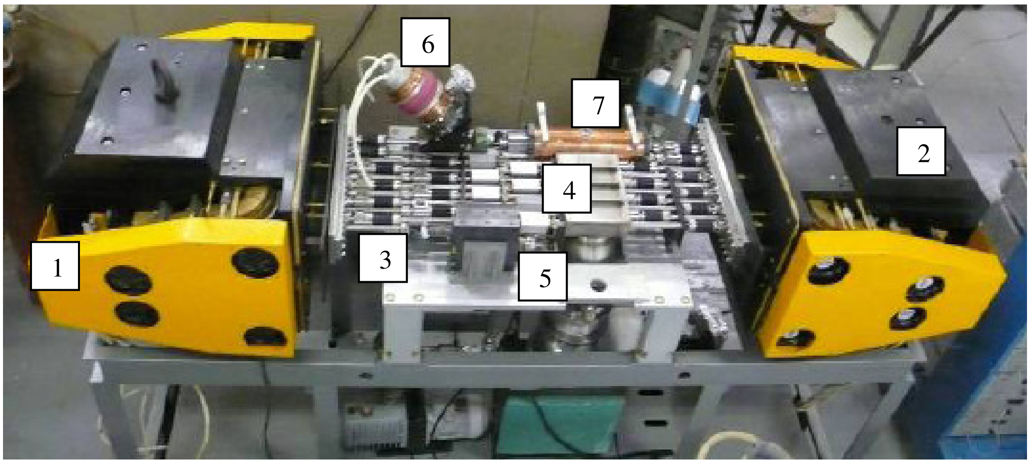

Figure 11: 55 MeV RTM general view.

The envisaged application of the SINP 55 MeV RTM is the detection of explosives using the photonuclear method [54].

## 1.5. - Objectives and structure of the thesis.

The general objectives of the present thesis are the design and characterization of magnetic systems of RTMs and the study of beam dynamics effects in such systems. As concrete aims the following issues are addressed:

- Carry out the design simulations and definition of technical parameters of the magnetic systems of the UPC 12 MeV RTM.
- Perform optimization studies of magnetic shielding screens of the extraction magnet of the 55 MeV RTM of the SINP (Moscow State University) with the aim to reduce the stray field.
- Develop a general formalism for the description of the beam phase dynamics in the case of arbitrary magnetic systems and low energy beams and apply it for the calculation of the phase-slip effect in RTMs with low energy beam injection.
- Carry out an analytical study of the transverse beam dynamics in end magnets with an inverse pole for RTMs with low energy injection.

The thesis includes five chapters and three appendixes.

**Chapter 1** contains an introduction to the subject and principles of operation of RTMs. It also includes a summary of the state of the art and a short description of the two projects related to the thesis.

In **Chapter 2** an introduction into RTM magnets and their functions is given and the main properties of transverse and longitudinal beam dynamics in this type of accelerators are summarized.

The **Chapter 3** is devoted to properties of systems with permanent magnets. The main parameters characterizing permanent magnets, their types, measurement techniques and methods of field tuning are briefly described there.

The **Chapter 4** contains main results of the thesis on the design of magnetic systems of the UPC 12 MeV RTM and the extraction magnet of the SINP 55 MeV

RTM. Design considerations, numerical simulations, parameters optimization and experimental measurements (in the case of the 55 MeV RTM) are discussed in detail.

In **Chapter 5** results of the study of the beam motion in magnetic system are presented. Firstly, the dynamics for non-relativistic beams is considered, more specifically numerical and analytic calculations of the phase slip effect are carried out. Secondly, properties of end magnets with inverse field dipole are studied and implications for RTM magnet design are discussed.

In **Chapter 6** results obtained in the thesis are summarized and some concluding remarks are given. It also includes a list publications in which the results of the thesis are reported.

In **Appendix 1** a description of main features of the codes used in this thesis is given.

# Chapter 2

# Particle dynamics in RTM magnets

## 2.1. – RTM magnetic systems.

The most important aspects of the beam dynamics in RTMs are particle acceleration in the accelerating structure and beam bending, steering and focusing in magnetic fields created inside various magnetic systems. As it was already stated in Introduction design simulations of certain types of magnetic systems and calculations of some effects of beam dynamics in such systems are the object of the study in the present thesis.

A variety of magnetic devices are used in RTMs. The magnetic field in the region of particle trajectories is created either by an electric current in current coils surrounding magnet poles or by blocks of permanent magnet material. In the present thesis the study is focused on design solutions with permanent magnets. Below we give a short description of main types of magnets used in RTMs.

1.– End magnets are dipole magnets which provide the beam recirculation in the RTM by bending the beam trajectory by the angle 180º. In Figs. 3, 8 and 12 the end magnets of the 70 MeV RTM of SINP, 12 MeV RTM of the UPC and 55 MeV RTM, respectively, are clearly seen. The vertical component of a homogeneous magnetic field is created in the space between two parallel poles where beam trajectories pass (see Fig. 12). The poles, current coils or permanent magnetic material blocks are usually surrounded by a steel yoke, as it can be seen in Fig.13, which provides the magnetic field flux circulation. In the standard design the machine has two identical end magnets with characteristics as close to each other as possible. As it will be explained in the following chapters for the optimal operation of an RTM they must satisfy very tight requirements on the field homogeneity in the region of beam trajectories, long term field stability, high precision in the equality of the fields in both end magnets, etc.

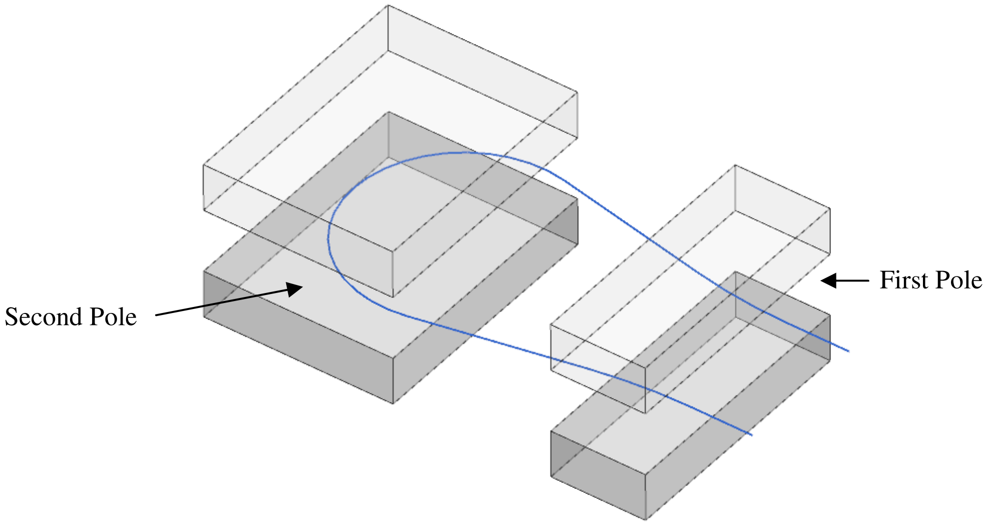

Figure 12: Schematic view of an RTM end magnet and an electron trajectory.

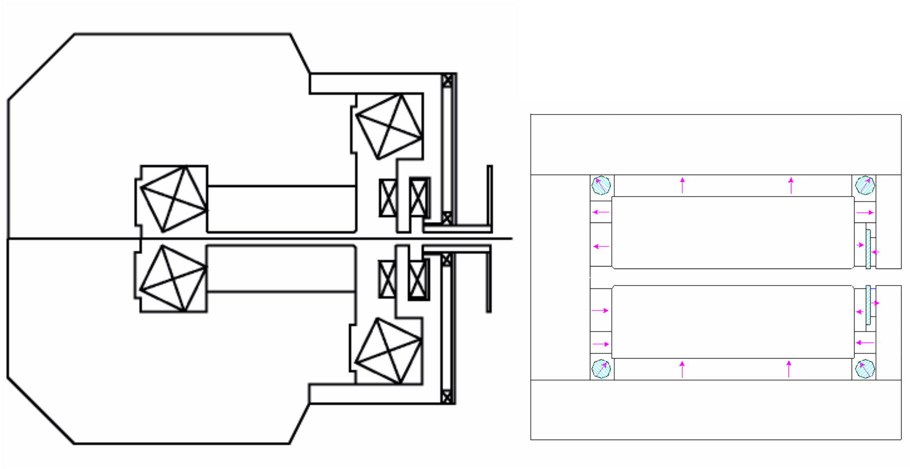

(a) (b)

Figure 13: Cross sections of typical RTM end electromagnet (a) and end magnet with permanent magnetic material as a field source (b).

It turns out that the fringe field, i.e. the magnetic field existing at the edge of the magnet (see Sect. 2.2.2 for more details), produces strong defocusing of the particle trajectories. In order to achieve the stability of the beam transverse motion some measures must be taken. As it was already mentioned in Sect. 1.2 a possible solution is to add a pair of poles which create a magnetic field of inverse polarity with respect to the main magnet and in this way reduce the defocusing effect or even get a net vertical beam focusing by the magnetic system [25]. For example, a box-type bending magnet with high field generated by Rare-Earth Permanent Magnet (REPM) material and fringe field shape optimized for specific beam properties is used in the SINP 70 MeV RTM [55].

We would like to mention that in the case of electromagnets the magnetic field in the region of particle trajectories can be adjusted by varying the current in the coils. In the case of systems with permanent magnets the field level adjustment is a more complicated task. Possible solutions are displacement of special tuners or rotation of special blocks of magnetic material. These techniques will be described in more detail in Ch. 3, the design of a tuning mechanism for the UPC 12 MeV RTM will be considered in Ch. 4.

2. – Beam extraction magnet. Once the electrons have reached the required energy they are directed towards a beam output channel. This beam deflection is produced by a dipole type magnet [1].

Depending on the RTM application mainly two beam extraction schemes are used. In the case of the fixed output energy the extraction magnet is placed at the last orbit at which the electrons have the maximal energy (see Fig.14a), this scheme is used for example in the 55 MeV RTM (see Fig.11). As it was mentioned in Ch. 1 one of the advantages of RTMs with respect to some other types of particle accelerator is the possibility of producing the electron beam with different energies by simply extracting it from different orbits. In this case the machine is equipped with a set of extraction magnets. One of them deflects the electrons of the required energy by a properly calculated angle and directs them towards the end magnet so that the particles follow a pre-established path and enter the output channel as it is shown in Fig.14b. The extraction mechanism of this type used in the UPC 12 MeV RTM is shown in Fig.8. Its design is considered in Ch. 4 of the present thesis.

The simplest design of an extraction magnet is a dipole electromagnet. It allows to adjust the field level and therefore the beam deflection angle by varying the electric current in the coils. However the dimensions of the system reduce considerably if a permanent magnet material is used as a source of the magnetic field. In many machines, for example in the SINP 70 MeV RTM, in addition to such main field source correcting coils are used. Such magnets are referred to as hybrid magnets.

To extract a high energy beam quite strong magnetic fields must be used. This may create strong parasitic or stray fields outside the magnet which can influence neighboring orbits. This undesired effect can be reduced to an acceptable level by surrounding the extraction magnet by special magnetic screens of optimal dimensions and geometry. Optimization of the screen design for the extraction magnet of the 55 MeV RTM is the subject of Sect. 4.4 of the thesis.

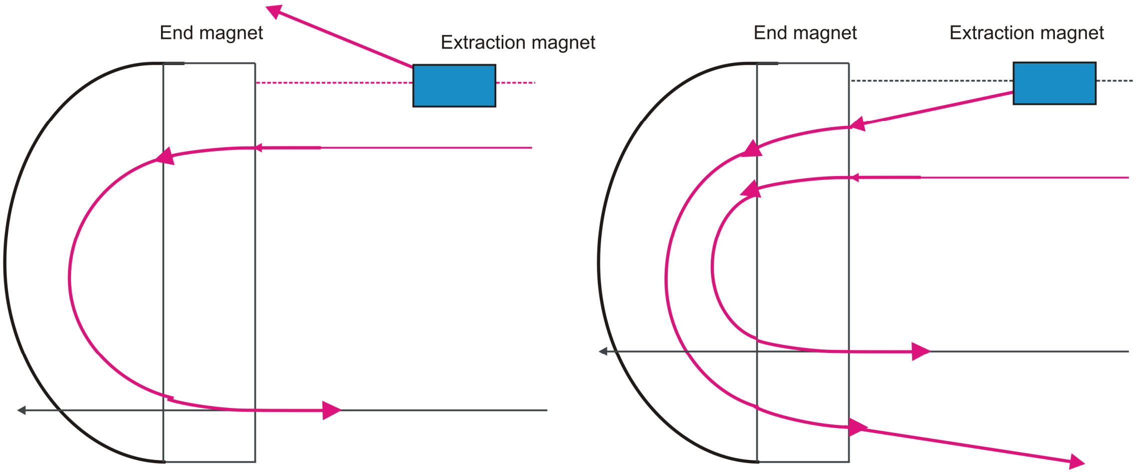

(a) (b)

Figure 14: RTM beam extraction schemes, (a) with fixed output energy, and (b) with variable output energy.

3. - Focusing systems. To provide the beam stability in the transverse plane magnetic focusing lenses are used. Typically they are quadrupoles, either electromagnets or devices with permanent magnets as the field source. In the latter case typical examples are the Halbach design [30] or QSM quadrupole [34]. In Sect. 4.3 the design simulations of a focusing quadrupole for the UPC 12 MeV are described.

Systems of another type used for beam focusing at low energies are solenoid lenses. In this case the magnetic field is generated by a rotationally symmetric coil and it has only longitudinal component in the inner part of the coil and radial components at the entrance and exit of the solenoid. Such configuration of the field creates a radial focusing force acting on off-axis particles [24]. Solenoid lenses are installed, for example, in the injection line of the SINP 70 MeV RTM [56].

4. - Steering magnets. They are used for steering purposes to compensate field non-uniformities in the end magnets, parasitic fields and possible magnet misalignments [57]. Usually they are simple window frame magnets (see Fig.15) which create quite moderate field of order 0.01 – 0.05 T. Depending on the plane in which they displace

the beam the steering magnets are classified as vertical, horizontal and combined horizontal-vertical, correctors. These magnets can be placed on a common orbit or on each of the returns paths.

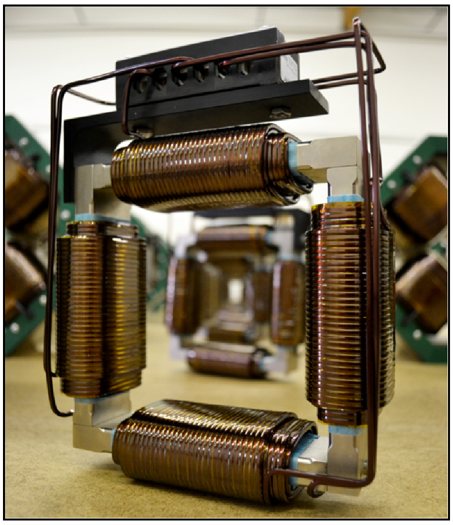

Figure 15: Horizontal – vertical corrector of window frame type.

5. - Injection magnets. In certain designs the electron gun is placed off-axis and the emitted particles are directed towards the accelerating structure (or one of the end magnets) following a curvilinear trajectory. This is achieved by using a few bending magnets, usually of dipole type [58]. The number of such magnets and the bending angles very much depend on the concrete injection scheme. In the case of high energy beam injection lines they are also equipped with focusing quadrupoles or solenoids.

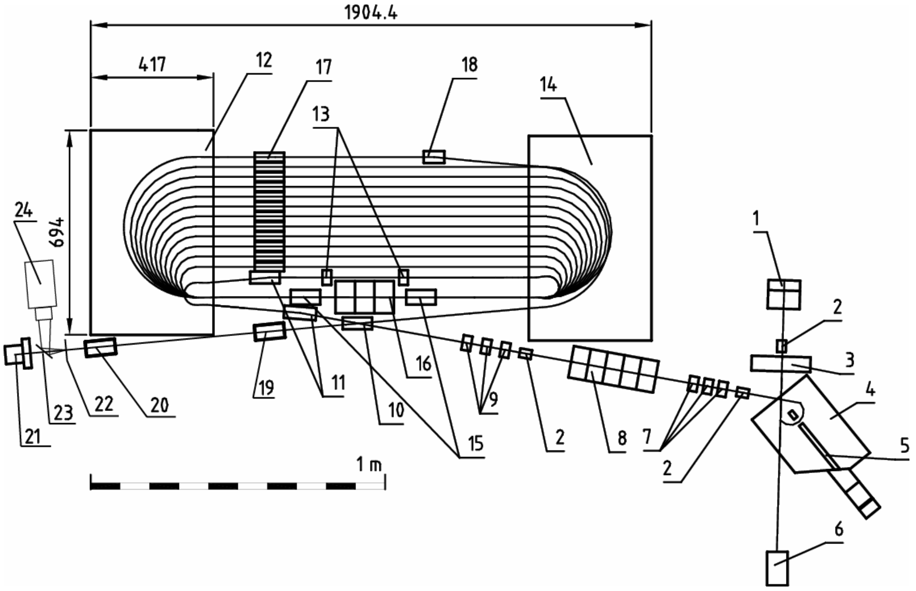

Figure 16: Magnetic systems of the SINP 35 MeV RTM: (1) photocathode gun; (2,17) steering coils; (3) solenoid lens; (4) $\alpha$-magnet; (5) collimating slit; (6) laser, (7,9,13,15) quadrupoles; (8) injector accelerating structure; (10,11) injection dipole magnets; (12) end magnets M1 and (14) M2; (16) main accelerating structure; (18) extraction magnet and (21) Faraday cup.

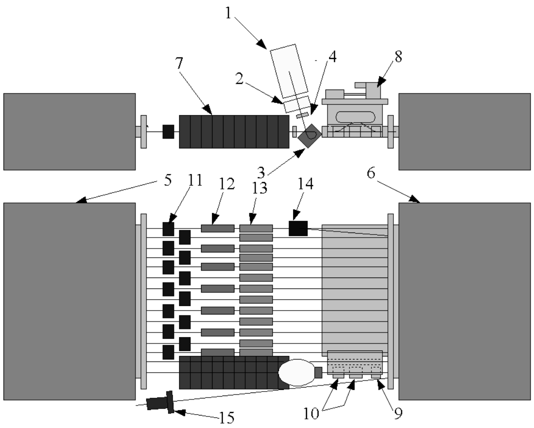

Figure 17: Magnetic systems of the SINP 70 MeV RTM: 1 RF gun, (2) pre-buncher; (3) α-magnet; (4) focusing lens; (5,6) end magnet; (7) accelerating structure; (8) beam phase-shifter; (9) quadrupole lens; (10) RE dipoles; (11) current monitors; (12) RE quadrupole triplets**;** (13) steering coils; (14) extraction magnet**; (15)** Faraday cup and (16) quadrupole.

Another magnetic system used in the beam particle injection of RTMs is an α-magnet [59]. The first α-magnet was designed by H.A.Enge in 1963 [60,61]. They are also known as "mirrors" because the beam enters and exits them at the same point [61] following an α-like path. This magnet is essentially a half quadrupole sliced vertically with the deflection angle equal to 270°+2α, where α is angle with which the beam enters and exits the magnet. In the special case α=40.7° an achromatic deflection takes place, i.e. the exit point and entrance points coincide irrespective of the particle energy (see Fig.18b). Apart from being used for off-axis injection into the accelerating structure the α-magnets are suitable for efficient bunch compression, this is because the particle path length in them is energy dependent. They are also used for reducing the energy spread of the beam.

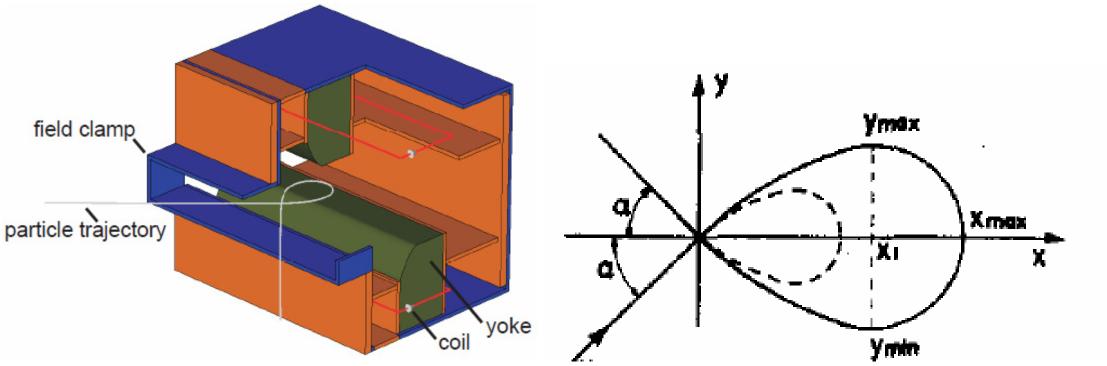

(a) (b)

Figure 18: (a) An α-magnet, (b) beam path in the case of entrance angle α=40.7°.

6. – Phase shifter is used to increase the path length of electrons and in this way adjust the particle phase at the entrance to the accelerating structure. It is required that such magnetic system (a) does not introduce spatial or angular dispersion of the beam, (b) has a minimal longitudinal dispersion such that it compresses bunches. As an example let us mention a phase shifter with a mechanism to adjust the deviation angle and for the longitudinal delay for a few periods used in the SINP 70 MeV RTM [62] (see Fig.19). Its function is to adjust the path length of the first 5 MeV orbit and in this way compensate ~ 30º delay in the phase caused by one of the end magnets.

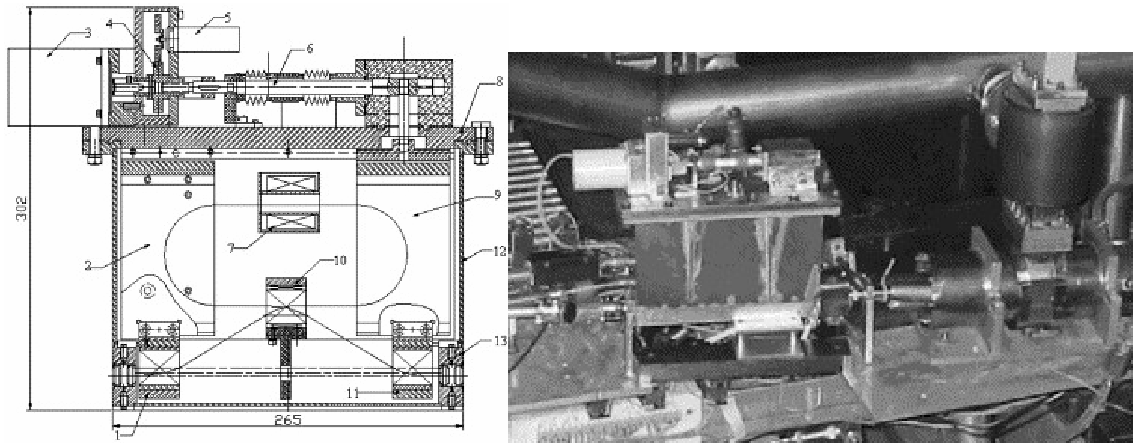

(a) (b)

Figure 19: Scheme (a) and general view (b) of the phase shifter of the SINP 70 MeV RTM. The following elements are shown: (1, 10, 11) 30º dipole magnets; (2, 9) 180º dipoles; (3) step motor (4) reducer; (5) multi-turn-around resistor; (6) vacuum lead; (7) fast current monitor; (8) flange; (12) magnetically soft walled vacuum chamber and (13) indium seals.

## 2.2. – Magnetic field description.

### 2.2.1. – Multipole expansion.

One of the first steps in the design of a particle accelerator is to define a reference trajectory which must be followed by a particle with nominal energy. This particle is usually referred to as ideal or reference particle. The design of the accelerator must be such that particles of a real beam move in a vicinity of the reference trajectory and their oscillations around it are stable, i.e. with bounded amplitude.

For guiding particles inside an accelerator, namely bending and focusing their trajectories, usually magnetic devices with appropriate distribution of a slow varying or static magnetic field are used. The forces acting on charged particles are Lorentz forces related to the magnetic field induction $\vec{B}$ by the following relation:

$$\vec{F} = q\,\vec{v} \times \vec{B},$$

where $v$ is the particle velocity and $q$ is its charge. The particles move through a region in the vicinity of the central axis of the magnetic systems inside a vacuum chamber which is free of currents and charges, as well as of material. Therefore, the magnetic field encountered by the beam particles is determined by the Maxwell equations

$$div\vec{B} = 0 \tag{5}$$

$$rot\vec{B} = 0 \tag{6}$$

From Eq.(5) it follows that a vector potential $\vec{A}$ exists such that the magnetic field induction can be written as

$$\vec{B} = rot\vec{A} \tag{6a}$$

Eq.(6) tells that inside the vacuum chamber the vector $\vec{B}$ is of gradient type and therefore can be written in terms of some scalar potential $\Phi$ as

$$\vec{B} = -grad\Phi \tag{6b}$$

In what follows we will use either relation (6a) or (6b) depending on which is more appropriate for a concrete calculation.

The reference trajectory is described by equations in a reference frame related to the machine. We will refer to it as laboratory reference frame and denote the coordinates in it by (X,Y,Z). As evolution parameter it is more convenient to use the arc length $s$ along the reference trajectory instead of the time variable. The magnetic field distribution in RTM end magnets also has a simpler form in this frame. However, for the description of particle beam oscillations around the reference trajectory the natural reference frame is an orthogonal, right-handed coordinate system $(x,y,z)$ that follows the reference particle along its trajectory. The origin of this frame, shown in Fig. 20, is at the location of the reference particle and the coordinate vector $z$ is tangential to the reference trajectory. The coordinate vector $x$ is chosen to lie in the reference trajectory plane, which is usually the horizontal plane, pointing towards the exterior of the machine. The coordinate vector $y$ is then vertical.

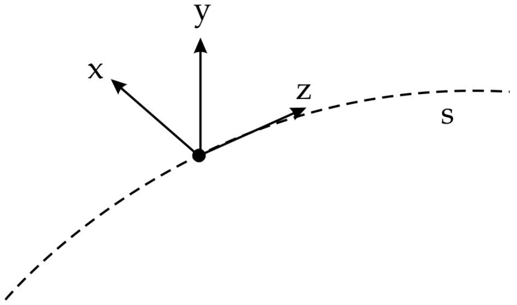

Figure 20: Moving reference frame related to the reference particle.

First we consider the case when the length of a magnet seen by the particle is much larger than the transverse dimensions of its mechanical aperture. Then inside the magnet effects of magnetic field variation in the longitudinal direction, i.e. along the reference trajectory, including those at the ends of the magnet, are rather small and can be neglected. This is the so called hard edge model. In this approximation the magnetic field is described by transverse coordinates $x$ and $y$ and the problem of finding the components $B_x, B_y$ from Maxwell equations (5), (6) becomes two-dimensional.

We can define a complex potential by

$$\Gamma(z) = A_s(x,y) + i\Phi(x,y) \tag{7}$$

where $A_s(x,y)$ is the magnetic vector potential along the path described by the particle and $\Phi(x,y)$ is the scalar potential. This complex potential is an analytic function and can be expanded in a power series in $z = x + iy$

$$\Gamma(z) = \sum_{n=1}^{\infty} \kappa_n z^n \tag{8}$$

where $\kappa_n = \lambda_n + i\mu_n$ and $\kappa_n$, $\mu_n$ are real constants. Then Eq.(7) can be written as,

$$\Gamma(z) = A_s(x,y) + i\Phi(x,y) = \sum_{n=1}^{\infty} (\lambda_n + i\mu_n)(x+iy)^n$$

(9)

If now we substitute the following definitions

$$\lambda_n = -B_{main}\frac{b_n}{n}, \qquad \mu_n = -B_{main}\frac{a_n}{n} \tag{10}$$

in Eq.(9) and separate the real and imaginary parts of the complex potential $\Gamma(z)$ we can express the magnetic vector and scalar potentials in terms of the arbitrary real coeficients $B_{main}$, $a_n$ and $b_n$,

$$A_s(x,y) = \mathrm{Re}\sum_{n=1}^{\infty} \kappa_n z^n = -B_{main}\left[b_1 x - a_1 y + \frac{b_2}{2}\left(x^2 - y^2\right) - a_2 xy + ....\right] \tag{11}$$

$$\Phi(x,y) = \mathrm{Im}\sum_{n=1}^{\infty} \kappa_n z^n = -B_{main}\left[a_1 x + b_1 y + \frac{a_2}{2}\left(x^2 - y^2\right) + b_2 xy + ....\right]. \tag{12}$$

Using Eqs.(6a) and (6b) it can be easily seen that,

$$B_x(x,y) = -\frac{\partial\Phi}{\partial x} = \frac{\partial A_s}{\partial y}, \qquad B_y(x,y) = -\frac{\partial\Phi}{\partial y} = -\frac{\partial A_s}{\partial x}. \tag{13}$$

Equations (13) are known as Cauchy-Riemann conditions of the complex function $\Gamma(z)$. To get the cartesian components of the magnetic field we have to calculate the gradient of $-\Phi(x,y)$ in the cartesian coordinates,

$$B_x(x,y) = -\frac{\partial\Phi}{\partial x} = B_{main}\left[a_1 + b_2 y + a_2 x - ....\right] \tag{14}$$

$$B_y(x,y) = -\frac{\partial\Phi}{\partial y} = B_{main}\left[b_1 - a_2 y + b_2 x + ...\right] \tag{15}$$

Now we take into account that for magnets with normal orientation the magnetic field distribution has midplane (or median plane) symmetry:

$$B_x(x,y) = -B_x(x,-y) \qquad B_y(x,y) = B_y(x,-y) \tag{15a}$$

From the first relation it follows that in the plane of reference trajectory, provided it coincides with the median plane of the magnet, $B_x(x,0) = 0$. The midplane symmetry implies that a part of the coefficients in expansions (14), (15) become zero and the most general solution is

$$B_x(x,y) = B_{main}\left[b_2 y + \ldots\right] \tag{16}$$

$$B_y(x,y) = B_{main}\left[b_1 + b_2 x + \ldots\right] \tag{17}$$

In real accelerators and beam transport systems most of magnetic devices reproduce only one multipole, in some cases combine two of them.

### Dipole magnet.

The field distribution of this magnet corresponds to the term with $n = 1$ in Eqs. (16), (17) and in the case of the right magnet (normal dipole) is given by

$$B_x = 0, B_y = B_0 \tag{18}$$

where $B_0 = B_{main} b_1$. Such magnets are used for bending the particle trajectories in the horizontal plane. An equipotential surface of constant scalar potential $\Phi$ coincides with a ferromagnetic pole surface and is given by $y = const$. Lines of the magnetic field of a dipole magnet are shown in Fig.21a.

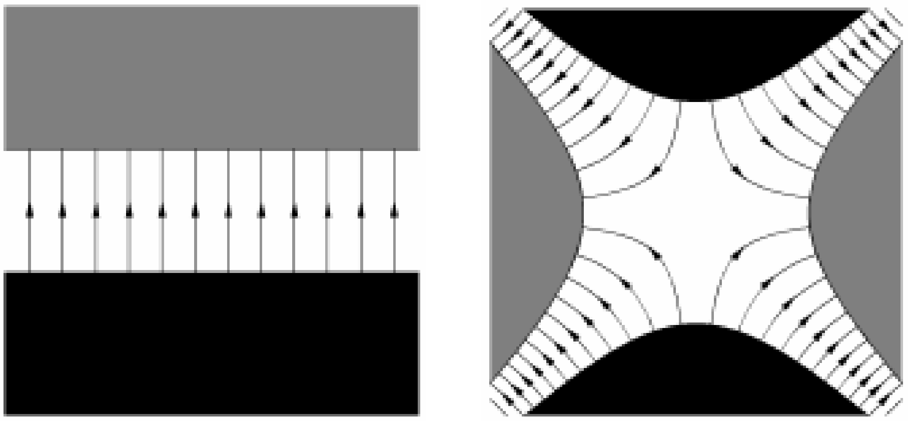

(a) (b)

Figure 21: Lines of magnetic field of a dipole (a) and quadrupole (b) magnets.

### Quadrupole magnet.

The magnetic field of a quadrupole magnet corresponds to the $n = 2$ terms in expansions (16)-(17). The field is linear in terms of particle deviation from the reference orbit and for a normal quadrupole is equal to

$$B_y(x,y) = -\frac{p}{e} kx = gx \tag{19}$$

$$B_x(x,y) = -\frac{p}{e} ky = gy \tag{20}$$

Here $k$ is the focusing strength, it is equal to $k = -\frac{e}{p}\frac{\partial B_y}{\partial x} = -\frac{e}{p} g$ and $g$ is the field gradient, where $g = B_{main} b_2$. Lines of the magnetic field are shown in Fig. 21b. Due to the linear property (19), (20) quadrupole magnets can be used as beam focusing devices. For a given value of the gradient $g$ such magnet acts as focusing lens in one plane (horizontal or vertical) and as defocusing lens in the orthogonal one. The focal distance is related to the focusing strength $k$ and its length $l_Q$ by

$$\frac{1}{f} = kl_Q \tag{21}$$

The equipotential surfaces are described by a relation $xy = const$, therefore the shape of the iron poles of a quadrupole magnet are given by the branches of a hyperbola (see Fig. 21b).

### 2.2.2. - Fringe field.

In the previous section the description of magnets and the magnetic field were done in the framework of the hard edge model. In a real magnet the field grows smoothly from zero beginning at some distance from the entrance to the magnet to a certain value in its center. The magnetic field existing at the edge of the magnet is called fringe field. An example the magnetic field distribution with a fringe field created by two parallel poles is shown in Fig. 22. The extent of the dipole fringe field is approximately the gap height, i.e. the distance between the magnet poles.

As it was mentioned in Sect. 2.1 the fringe field of the RTM end magnets produces strong defocusing which must be taken into account in the design of the machine.

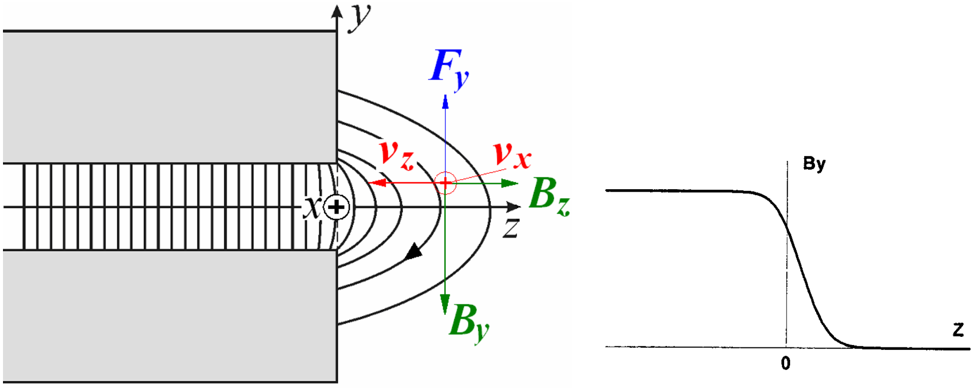

(a) (b)

Figure 22: (a) Lines of the magnetic field induction at the entrance of the end magnet, (b) distribution of the vertical component $B_y$ of this field in the median (trajectory) plane, Z=0 corresponds to the pole face.

Due to the fringe field the interval in which a magnet affects a particle trajectory is longer than the physical length of the magnet in the longitudinal direction. To characterize this property the notion of effective length $L_{eff}$ is introduced [64], [65]. It is defined by the formula

$$L_{eff} = \frac{\int_{\infty}^{-\infty} B_y(0,0,s)}{B_0} ds \ , \tag{22}$$

where the integration is performed along the particle trajectory and $B_0$ is the value of the field in the magnet center. In practice of course the integral is calculated with finite limits, only in the interval where the magnetic field is different from zero. In beam dynamics calculations it is often convenient to substitute a dipole magnet with fringe field by an equivalent hard edge magnet with its effective field boundary situated at $Z_1 = Z_0 - EFB$ with EFB defined as

$$EFB = \int_{Z_B}^{Z_2} \frac{B_y(0,0,Z)}{B_0} dZ - (Z_B - Z_0)\,. \tag{23}$$

Here $B_0$ is the magnetic filed value in the uniform magnetic field region, $Z_0$ is the position of the end face of the pole of the magnet, $Z_B$ is the point where the constant magnetic field region begins and $Z_2$ is the point where non-zero fringe field begins (see Fig. 23). Note that the definition above is written in the laboratory reference frame.

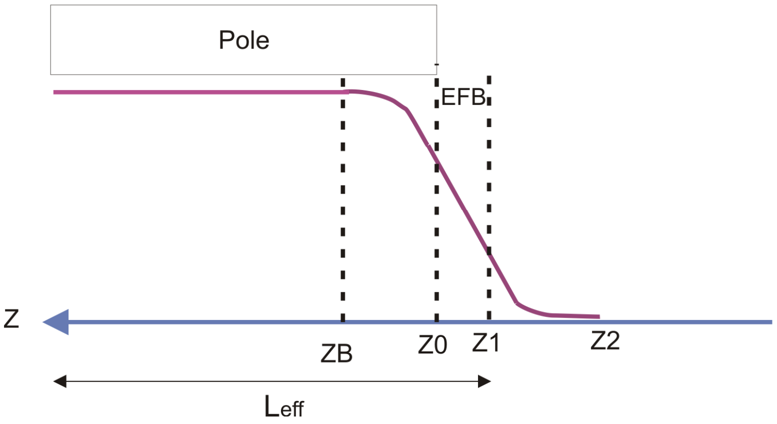

Figure 23: Vertical component $B_y$ in the median plane of a dipole magnet.

Let us consider an RTM end magnet, i.e. a dipole magnet with the bending angle 180º, and introduce a laboratory reference frame as it is shown in Fig.24. Suppose that the magnet dimension in the $X$ -direction is large in comparison with the gap between the poles so that the dependence of the magnetic field on $X$ can be neglected. Let us denote by $B(Z)$ the vertical field component distribution $B_y(0,0,Z)$ in the median plane $Y = 0$. Examples of this function are shown in the plots in Fig. 22b and Fig. 23. Then for small deviations from the median plane one can find a general solution for the scalar potential $\Phi(Y,Z)$ as a series in powers of $Y$ [20]. One obtains

$$\Phi(Y,Z) = -B(Z)Y + \frac{1}{6} Y^3 B''(Z) + \ldots \tag{24}$$

Using representation (6b) one gets the corresponding expansions for the components of the magnetic field:

$$B_Y(Y,Z) = -\frac{\partial \phi}{\partial Y} = B(Z) - \frac{Y^2}{2}\frac{d^2 B(Z)}{dZ^2} + \ldots \tag{25}$$

$$B_Z(Y,Z) = -\frac{\partial \phi}{\partial Z} = Y\frac{dB(Z)}{dZ} - \frac{Y^3}{6}\frac{d^3 B(Z)}{dZ^3} + \ldots \tag{26}$$

Note that in this approximation the magnetic field in the gap between the poles is described in terms of only one function $B(Z)$ and its derivatives.

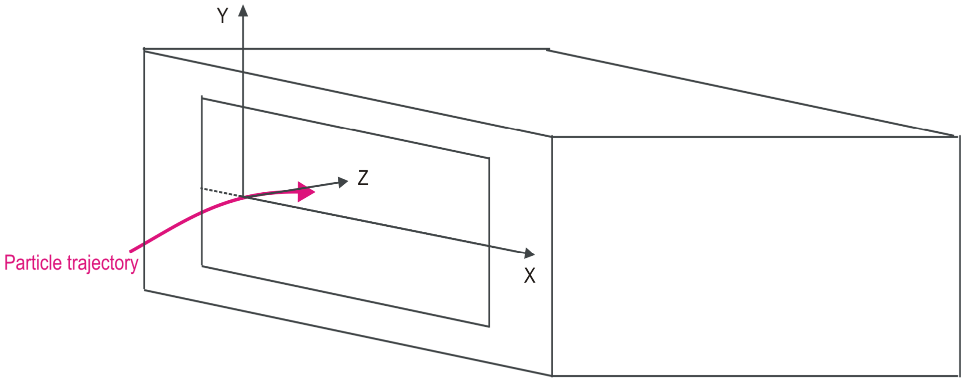

Figure 24: An RTM end magnet and definition of the laboratory reference frame (X,Y,Z).

### 2.2.3. – Magnetic systems for beam recirculation.

As it was already mentioned in the previous sections simple 180º dipole magnets used as end magnets in RTMs do not always provide an optimal beam dynamics. One of the problems is a strong vertical defocusing effect due to the fringe field. In fact, as it is shown in Sect. 2.3.1 the focal length of an end magnet is of the order of the radius of the orbit in the homogeneous field region of this magnet. As a result for low energies the focal length turn out to be too short and this leads to an unstable beam oscillations. For a stable vertical beam motion the focal length must be not less than the distance between the end magnets. A solution proposed by H.Babic and M.Sedlacek in 1967 [25] consisted in placing a short additional dipole with inverse field polarity next to the 180º dipole magnet. Such magnetic systems were coined as 2-pole magnets, and we will use this term in the present thesis. The magnetic field profile and trajectories for a simple (1-pole) end magnet and 2-pole magnetic system with inverse pole are shown in Fig. 25. The field at the inverse pole partially compensates the effect of the fringe field of the main pole thus reducing the vertical defocusing of the 2-pole end magnet. However, the distance $\Delta$ between the entering and exiting trajectories becomes smaller in this case (compare trajectories (1) and (2) in Fig.25(a).

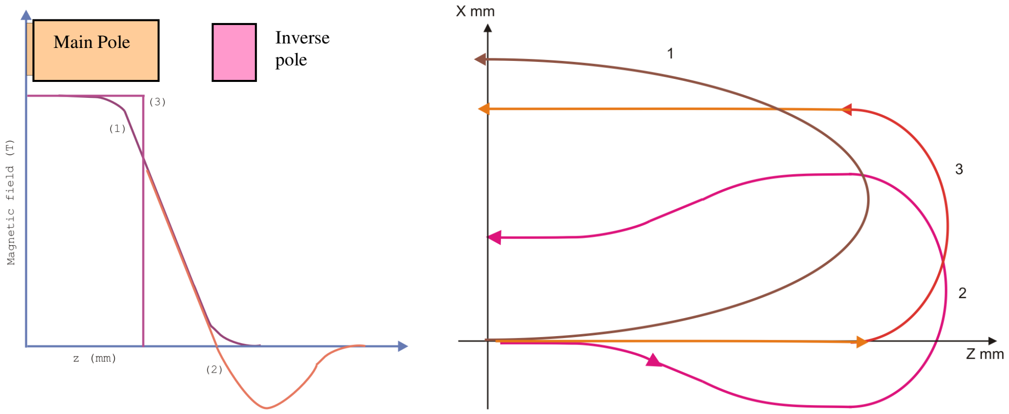

(a) (b)

Figure 25: (a) Magnetic field profile for three types of magnets: (1) 1-pole end magnet with fringe field, (2) 2-pole magnetic system with inverse pole, (3) 1-pole end magnet in the hard-edge approximation. (b) Trajectories in the X-Z plane for these magnets.

The second problem that may appear in some RTMs, especially in those with low energy beam injection, is the accelerating structure by-pass. It may turn out that after first acceleration the energy of the electrons is not sufficiently large and after the 180º turn in the end magnet they would not by-pass the accelerating structure and would hit its wall. Simple estimates show that the distance Δ between the beam trajectories entering and exiting the end magnet must be larger than at least $0.37\lambda$, where $\lambda$ is the wavelength of the accelerating electromagnetic field [66]. In 1976 R. Alvinsson and M. Ericsson proposed to accelerate particles twice before they pass through the drift space between the end magnets [25,26]. The idea is to place two additional short dipoles that displace the beam as it is shown in Fig.26. Here m3 deviates the incident beam whereas m4 directs it towards the M2 end magnet. After a 180º turn in M2 the particle trajectories are bent by the same dipoles and return to the accelerating structure axis. The particles pass through it in the inverse direction and at this second acceleration acquire enough energy to by-pass the RF cavities after 180º bent in M1. Of course, the magnetic field in the additional dipoles and their location must be carefully calculated for the precise beam reflection back to the main axis and its efficient acceleration on the second pass through the accelerating structure. To compensate the displacement caused by the m3 and m4 dipoles on the higher orbit trajectories identical dipoles m5 and m6 are placed between M1 end magnet and the accelerating structure. Such magnetic system was used for example in the RTM of the NIST-LANL (National Institute of Standards and Technology - Los Alamos National Laboratory), Los Alamos [67]. We would like to note that though this design solves the problem of the linac by-pass it necessarily increases the distance between the end magnets.

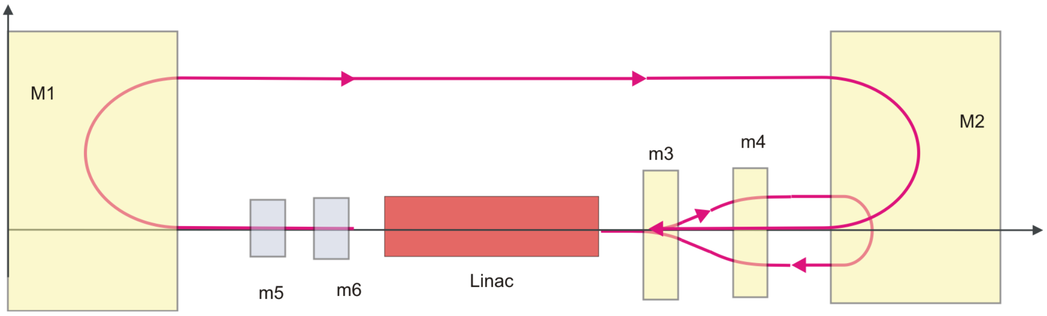

Figure 26: Alvinsson-Ericsson magnetic system design.

In the RTM magnet design described in Ref. [68] only one dipole with inverse field is added. It was shown that in this way both the problem of the fringe field defocusing can be solved and the reflection of the beam trajectory back into the linac can be achieved.

In some RTMs other solutions of linac by-pass were applied. As an example we would like to mention the design proposed by P.Axet in 1975 for accelerators with low energy injection and superconducting accelerating structure used in MUSL-1 and MUSL-2 facilities at University of Illinois [69]. In these machines the beam is accelerated to 78 MeV in 6 turns, therefore high energy gain per turn is required. This can be achieved using a superconducting accelerating structure. However the structure must be housed inside a cryostat to maintain it in the superconducting state, therefore the accelerating module turns out to be of large volume. For the injected beam to by-pass it a special transport line was designed as it is shown in Fig.27.

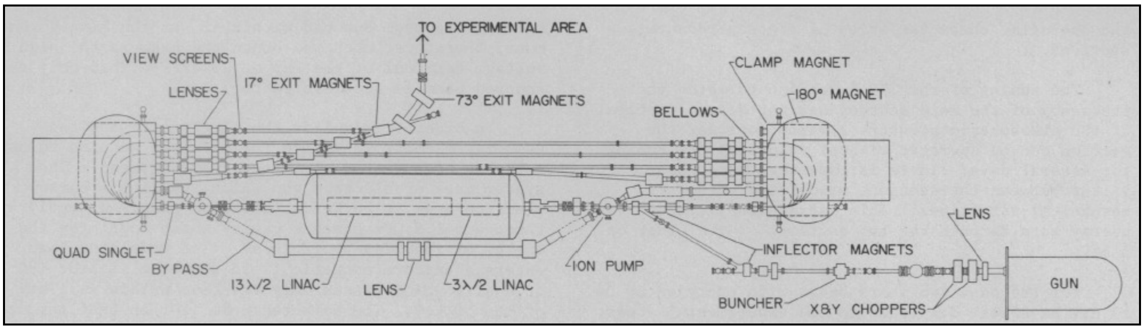

Figure 27: Scheme of the MUSL-1 RTM.

## 2.3. – Transverse beam dynamics.

### 2.3.1. – Linear beam transport formalism.

For certain beam optics the transverse and longitudinal motion of particles in the beam are decoupled and can be studied separately. In this section we give a short review of the formalism used for the description of the transverse motion [1], [24], basics of the longitudinal dynamics are considered in Sect. 2.4.

As it was already mentioned in Sect. 2.2.1 it is natural to describe the transverse deviations of an arbitrary particle with respect to the reference trajectory in the mobile reference frame $(x, y, z)$ attached to the reference particle introduced there (see Fig. 20). In the linear approximation the equations of motion for on-momentum particles are

$$x''(s) + K_x x(s) = 0 \qquad (27a)$$

$$y''(s) + K_y y(s) = 0 \qquad (27b)$$

Here the prime denotes the derivative with respect to the path length $s$ and $K_x(s)$, $K_x(s)$ are functions determined by the distribution of dipole and quadrupole magnets along the reference trajectory.

In the case of the hard edge model for the magnets

$$K_x = \frac{1}{\rho_0^2} - k \qquad\qquad K_y = k$$

where $k$ is the focusing strength and $\rho_0$ is bending radius for the particle trajectory in the dipole magnetic field. It is convenient to describe the beam motion determined by equations (27a), (27b) in terms of transformation matrices [24]. In this formalism the state of a particle is described by a vector

$$X(s) = \begin{bmatrix} x \\ x' \\ y \\ y' \end{bmatrix} \qquad (28)$$

The trajectory slopes $x'$ and $y'$ are related to the transverse components of the particle momentum as

$$x' = \frac{p_x}{p_0} \qquad y' = \frac{p_y}{p_0} \tag{29}$$

where $p_0$ is the total momentum of the particle. Consider a particle characterized by the initial state vector $X_0 = X(s_0)$ at some point $s = s_0$. Then its transport along the reference trajectory till $s = s_1$ is described by

$$X(s_1) = MX_0 \tag{30}$$

where $M$ is a 4x4 matrix corresponding to the accelerator sections along this path, like bending and quadrupole magnets or drift spaces, and $X(s_1)$ is the final state vector. For the calculation of the beam transport it is sufficient to know the individual transport matrix of each element of the accelerator transport line. Then the transformation matrix for the whole path from $s = s_0$ to $s = s_1$ is just equal to the product of them. In what follows we describe the matrices of the main elements which are encountered in RTMs.

### a. – Drift space.

For a section without magnetic field the transport matrix is equal to

$$M_{DS} = \begin{bmatrix} 1 & l & 0 & 0 \\ 0 & 1 & 0 & 0 \\ 0 & 0 & 1 & l \\ 0 & 0 & 0 & 1 \end{bmatrix} \tag{31}$$

### b. – Quadrupole magnet.

The transfer matrix of a quadrupole magnet is the following

$$M_q = \begin{bmatrix} \cos(kl_Q) & \dfrac{\sin(kl_Q)}{k} & 0 & 0 \\ -k\sin(kl_Q) & \cos(kl_Q) & 0 & 0 \\ 0 & 0 & \cos k(kl_Q) & \dfrac{\sinh(kl_Q)}{k} \\ 0 & 0 & k\sinh(kl_Q) & \cosh(kl_Q) \end{bmatrix} \tag{32}$$

where $l_Q$ is the effective length of the quadrupole and $k$ is the quadrupole strength related to the field gradient by Eqs.(192), (20). Very often the focal length of the quadrupole magnet is much larger than its length, i.e. $|l_Q/f| << 1$. In this case the so called thin length approximation is valid. It is obtained by taking the limit $l_Q \to 0$ in matrix (25) while keeping the inverse focal length $f^{-1}$ to be finite. One obtains

$$M_q = \begin{bmatrix} 1 & 0 & 0 & 0 \\ -\dfrac{1}{f} & 1 & 0 & 0 \\ 0 & 0 & 1 & 0 \\ 0 & 0 & \dfrac{1}{f} & 1 \end{bmatrix} \tag{33}$$

The quantity $1/f$ is called focusing power. For $f > 0$ the quadruple magnet in Eq.(33) is focusing in the horizontal plane and defocusing in the vertical one.

c. - **Dipole magnet.**

First we consider a pure dipole magnet in the hard edge approximation whose pole faces at the entrance and exit are orthogonal to the particle beam. Such magnet is called sector magnet. Its transport matrix is equal to

$$M_{dip,\sec t} = \begin{bmatrix} \cos\theta & \rho_0 \sin\theta & 0 & 0 \\ -\dfrac{\sin\theta}{\rho_0} & \cos\theta & 0 & 0 \\ 0 & 0 & 1 & \rho_0\theta \\ 0 & 0 & 0 & 1 \end{bmatrix} \tag{34}$$

where $\rho_0$ is the radius of the reference trajectory inside the magnet and $\theta$ is the bending angle. The arc length $l = \rho_0\theta$. Note that in the vertical plane this magnet is simply a drift space of length $l$.

For the studies carried out in the present thesis the transport matrix for a more general case is needed. So, in what follows we consider the following generalizations:

(a) The fringe fields at the entrance and exit of the dipole magnet are included. We assume, however, that the fringe field extent is short in comparison with the bending radius $\rho_0$. This takes place if $2G/\rho_0 >> 1$, where $2G$ is the gap height.

(b) We allow the reference trajectory to enter and exit the magnet at arbitrary angles $\alpha_{in}, \alpha_{out}$ with the pole face, respectively. Such magnets with arbitrary pole face rotation are often referred to as wedge magnets.

The transport matrix in this case is given by

$$M_{wedge} = \begin{bmatrix} 1 & 0 & 0 & 0 \\ \dfrac{\tan(\alpha_{out})}{\rho_0} & 1 & 0 & 0 \\ 0 & 0 & 1 & 0 \\ 0 & 0 & -\dfrac{\tan(\alpha_{out} - \psi_{out})}{\rho_0} & 1 \end{bmatrix} M_{dip,sect} \begin{bmatrix} 1 & 0 & 0 & 0 \\ \dfrac{\tan(\alpha_{in})}{\rho_0} & 1 & 0 & 0 \\ 0 & 0 & 1 & 0 \\ 0 & 0 & -\dfrac{\tan(\alpha_{in} - \psi_{in})}{\rho_0} & 1 \end{bmatrix} \tag{35}$$

The sign of the angles $\alpha_{in}, \alpha_{out}$ are determined according to the rule: the angle is positive if the outward normal to the face of the magnet lies outside the trajectory in the straight section (see Fig. 28) [24] (see also [61]). The correction terms $\psi_{in}, \psi_{out}$ describing an additional vertical focusing produced by the fringe field are equal to [61]

$$\psi_a = \frac{G}{\rho_0}\left[\frac{1+\sin^2\alpha_a}{\cos\alpha_a}\right]K_{1,a}, \tag{36}$$

where $\alpha_a = \alpha_{in}, \alpha_{out}, G$ is the half of the gap between the poles. The factor $K_{1,a}$ depends on the fringe field profile $B(Z)$ of the magnet and is calculated in terms of the following integrals

$$K_{1,a} = \frac{1}{G}\left[\int_{-\infty}^{\infty}\frac{B(Z)}{B_0}dZ - \int_{-\infty}^{\infty}\left(\frac{B(Z)}{B_0}\right)^2 dZ\right]. \tag{37}$$

Here the integration is done over the fringe field interval and $B_0$ is the magnetic field in the uniform field region. For a single pole end magnet the corrections $\psi_{in}, \psi_{out}$ are positive, therefore they describe additional defocusing.

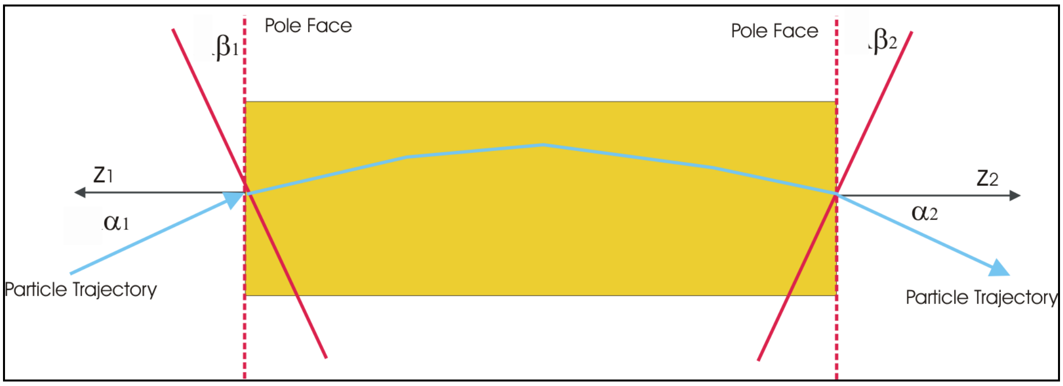

Figure 28: Definition of the entrance and exit angles.

Let us consider now two particular cases which are of interest for us.

### c.1 - Rectangular dipole magnet.

In practice dipole magnets usually have parallel end faces. If such magnet, called rectangular magnet, is placed symmetrically with respect to the entering and exiting beams then $\beta_1, \beta_2 = -\theta/2$ (see Fig.28), where θ is the bending angle. As it follows from Eq. (35) the 2x2 transport matrix in the $x$-plane is equal to

$$M_{dip,rect,x} = \begin{bmatrix} 1 & 0 \\ \frac{1}{\rho_0}\tan(\beta_2) & 1 \end{bmatrix}\begin{bmatrix} \cos(\theta) & R\sin(\theta) \\ -\frac{\sin(\theta)}{\rho_0} & \cos(\theta) \end{bmatrix}\begin{bmatrix} 1 & 0 \\ \frac{1}{\rho_0}\tan(\beta_1) & 1 \end{bmatrix} = \begin{bmatrix} 1 & \rho_0\sin(\theta) \\ 0 & 1 \end{bmatrix} \tag{38}$$

As can be seen from the above result a rectangular magnet in the orbit plane is equivalent to a drift space of length $\rho_0 \sin\theta$ and does not focus the beam.

Provided the corrections $\psi_{in}, \psi_{out}$ are neglected the transport matrix of this magnet in the non-deflecting plane is given by the following formula:

$$M_{dip,rect,y} = \begin{bmatrix} 1 & 0 \\ \frac{1}{f_y} & 1 \end{bmatrix} \begin{bmatrix} 1 & \rho_0\theta \\ 0 & 1 \end{bmatrix} \begin{bmatrix} 1 & 0 \\ \frac{1}{f_y} & 1 \end{bmatrix} = \begin{bmatrix} 1 - \frac{l}{f_y} & l \\ -\frac{2}{f_y} + \frac{l}{f_y^2} & 1 - \frac{l}{f_y} \end{bmatrix} \tag{39}$$

where $\frac{1}{f_y} = \frac{\tan(\beta)}{\rho_0}$ and $l = \rho_0\theta$.

**c.2. – RTM end magnet.**

Another type of dipole magnet important for us is an RTM end magnet with bending angle $\theta = 180°$ . Suppose that the beam enters and exits with the same angle $\alpha_{in}, \alpha_{out} = -\eta$ . Using Eq.(35) we obtain that the 2x2 transport matrices are equal to

$$\begin{aligned} M_{EM,x} &= \begin{bmatrix} 1 & 0 \\ -\frac{\tan(\eta)}{\rho_0} & 1 \end{bmatrix} \begin{bmatrix} \cos\theta & R\sin\theta \\ -\frac{\sin\theta}{\rho_0} & \cos\theta \end{bmatrix} \begin{bmatrix} 1 & 0 \\ -\frac{\tan(\eta)}{\rho_0} & 1 \end{bmatrix} = \\ &= \begin{bmatrix} \cos(\theta) - \sin(\theta)\tan(\eta) & \rho_0 \sin\theta \\ \sin(\theta)\frac{\tan^2(\eta)}{\rho_0} - 2\cos(\theta)\frac{\tan(\eta)}{\rho_0} & \cos(\theta) - \sin(\theta)\tan(\eta) \end{bmatrix} \end{aligned} \tag{40}$$

$$M_{EM,y} = \begin{bmatrix} 1 & 0 \\ \frac{1}{f_y} & 1 \end{bmatrix} \begin{bmatrix} 1 & \rho_0\theta \\ 0 & 1 \end{bmatrix} \begin{bmatrix} 1 & 0 \\ \frac{1}{f_y} & 1 \end{bmatrix} = \begin{bmatrix} 1 - \frac{l}{f_y} & l \\ -\frac{2}{f_y} + \frac{l}{f_y^2} & 1 - \frac{l}{f_y} \end{bmatrix} \tag{41}$$

where $\theta = \pi - 2\eta$ , $\frac{1}{f_y} = \frac{\tan(\eta + \psi)}{\rho_0}$ and $l = \rho_0\theta$.

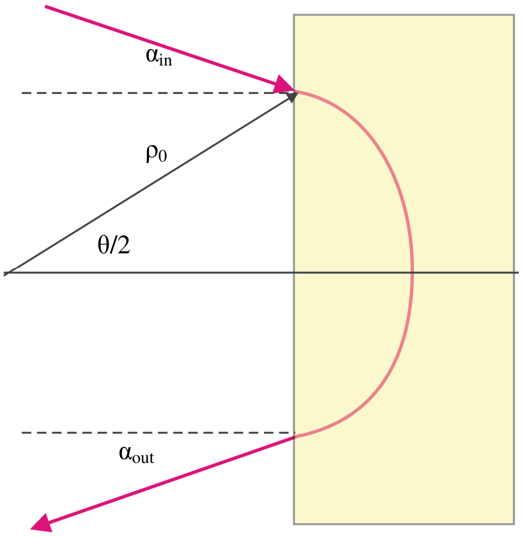

Figure 29: Particle trajectory in an end magnet and definition of entering and exiting angles.

### 2.3.2. – Beam bending in end magnets.

In the following sections we will get more detailed formulas describing the beam motion in RTM end magnets, including magnetic systems of few dipoles. We begin with a study of the bending of a trajectory close to the reference orbit plane. The motion of an electrically charged particle of charge $q$ in a magnetic field $\vec{B}$ is determined by the Lorentz force and is described by the equation

$$\frac{d\vec{p}}{dt} = q\left(\vec{v} \wedge \vec{B}\right), \tag{42}$$

where $p$ is particle momentum and $v$ is its velocity. In the case of an electron $q = -|e|$ and Eq.(42) in the laboratory reference frame is written in components as follows

$$\begin{bmatrix} dp_X/dt \\ dp_Y/dt \\ dp_Z/dt \end{bmatrix} = -|e|\begin{bmatrix} B_Z v_Y - B_Y v_Z \\ B_X v_Z - B_Z v_X \\ v_X B_Y - B_X v_Y \end{bmatrix} \tag{43}$$

where $B_X$ , $B_Y$ and $B_Z$ are the X-, Y- and Z-components of the magnetic field in the fringe field region and $v_X$ , $v_Y$ and $v_Z$ are the components of the particle velocity, respectively. Note that in the case of the reference trajectory the motion takes place in the plane Y=0.

Similar to Sect. 2.2.2 we consider a dipole magnet which is large enough in the X-direction, therefore $B_X = 0$. We also assume that the longitudinal velocity at the entrance, i.e. in the region of the fringe field $v_Z >> v_Y$ . Then Eq. (43) becomes

$$\begin{bmatrix} dp_X/dt \\ dp_Y/dt \\ dp_Z/dt \end{bmatrix} = |e|\begin{bmatrix} B_Y(z) v_Z \\ B_Z v_X \\ -v_X B_Y(z) \end{bmatrix} \tag{44}$$

Let us introduce angle α in the XZ - plane between the vector $\vec{V}$ and the positive direction of the Z – axis, where $\vec{V}$ is the projection of the particle velocity vector to the XZ-plane, its length is $V = \sqrt{v_X^2 + v_Z^2} \approx |\vec{v}|$ (see Fig.30). The angle α is the angle of the reference trajectory bending, it is positive if $\vec{V}$ is in the first quadrant of the ZX – plane. Then the velocity components are equal to

$$v_X = V\sin(\alpha) \tag{45a}$$

$$v_Z = V\cos(\alpha) \tag{45b}$$

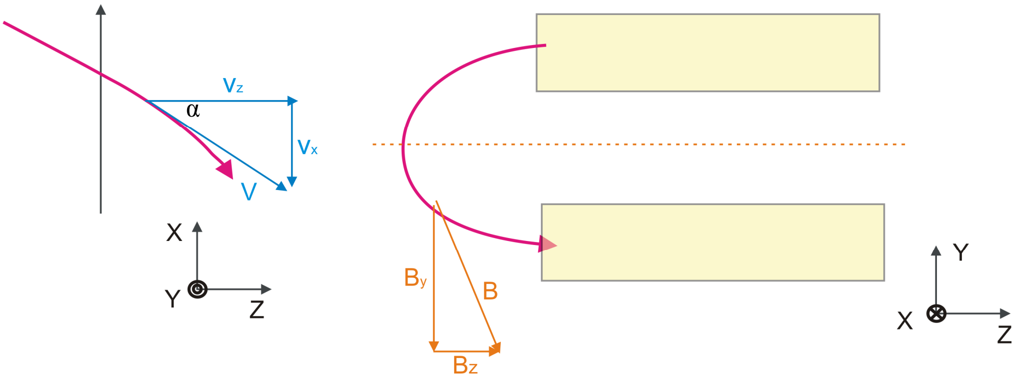

Figure 30: Definition of the coordinate system and angle α.

Using the definition of the relativistic particle momentum $\vec{p} = m\gamma\vec{v}$, the X-component of the equation of motion can be written as

$$\frac{dv_X}{dt} = \frac{|e|}{m\gamma} v_Z B_Y(z) \tag{46}$$

Since $v_Z = dZ/dt$ it follows that

$$\frac{dv_X}{dZ} = \frac{|e|}{m\gamma} B_Y(z) \tag{47}$$

Taking into account Eq.(45a) and integrating Eq.(47) over $Z$ one gets

$$\sin(\alpha(Z)) - \sin(\alpha_0) = \frac{|e|}{m\gamma V} \int_{Z0}^{Z} B_Y(Z)dZ \tag{48}$$

where α$_0$ is the angle of the entrance of the particle trajectory in the fringe field region and $Z_0$ is the point where the non-zero field begins.

Formula (48) for the deflection angle of a particle trajectory in a dipole magnet can be written as

$$\sin(\alpha(Z_{out})) - \sin(\alpha_0) = \frac{|e|}{p} I \tag{49}$$

where as before $p$ is the beam momentum and $I$ is the magnetic field integral along the beam trajectory

$$I = \int_{Zin}^{Zout} B_{dipole} dZ \tag{50}$$

where $Z_{in}$ and $Z_{out}$ are the initial and final points of the region of the dipole magnetic field along Z. In the hard - edge approximation the magnetic field integral is equal to

$$I = d \cdot B_{dipole} \tag{51}$$

where $B_{dipole}$ and $d$ are the magnetic field and length of the magnet, respectively, and the beam deflection in the orbit plane is given by

$$\sin(\alpha_{out}) - \sin(\alpha_0) = \frac{|e|}{p} B_{dipole} d = \frac{d}{R_{dipole}} \tag{52}$$

where $R_{dipole}$ is radius of a particle trajectory inside the magnet.

### 2.3.3.- Orbit displacement.

As it was already explained before the distance between a trajectory at the entrance into an end magnet and at its exit (see Fig.31) is an important parameter which should be controlled in the design of RTMs. We will refer to this distance as beam trajectory displacement in an end magnet system and denote it by $\Delta$. The trajectory displacement must exceed the transverse size of the accelerating structure. As it was mentioned in Sect. 2.2.3 a commonly used estimate for this size is $0.37\lambda$, where $\lambda$ is the wavelength of the accelerating RF field.

In this section we will derive a formula for $\Delta$ for an end magnet system with an arbitrary field distribution in the median plane. For this we will use representation (6a) of $\vec{B}$ in terms of a vector potential $\vec{A}$. With the supposition about RTM end magnets made in the previous sections $\vec{A} = (A_X(Y,Z),0,0)$. Let us denote the potential in the median plane as $A(Z) \equiv A_Z(0,Z))$. Then $B_Y(z) = dA_X(Z)/dZ$. Let us consider first the case of a trajectory entering the magnetic field region with $\alpha_0 = 0$. Then Eq.(48) can be written as

$$\sin(\alpha(Z)) = \frac{|e|}{p} A_X(Z) \tag{53}$$

Let us suppose that $X = X(Z)$ is formula of a trajectory in the median plane in the laboratory reference frame. Then according to the definition of the angle $\alpha(Z)$ we have

$$\tan(\alpha(Z)) = -\frac{dX}{dZ} \tag{54}$$

and using trigonometric relations we get the following formula for the differentials

$$dX = -\frac{\sin(\alpha(Z))}{\sqrt{1-\sin^2(\alpha(Z))}}dZ \tag{55}$$

Integrating both sides of (55) from some initial point, where the magnetic field is still zero, till the point of maximum penetration of the beam inside the end magnet, $Z_{\max}(p)$, and taking into account Eq.(53) we get that the trajectory displacement Δ is given by the formula

$$\Delta = -\frac{2}{B_0R_0}\int_0^{Z_{\max}(p)} \frac{A_X(Z)}{\sqrt{1-\left[\frac{|e|}{p}A_X(Z)\right]^2}}dZ \tag{56}$$

where $B_0$ is the magnetic field value and $R_0$ is the radius of the particle trajectory in the uniform magnetic field region of the main pole. Since the point of maximal penetration is defined by the condition $p_Z = 0$ or $\sin(\alpha(Z_{\max})) = 1$, it is easy to show $eA(Z_{\max}) = p$. This relation can also be written as

$$Z_{\max}(p) = R_0(p) + \Delta l - \frac{I(\Delta l)}{B_0} \tag{57}$$

where $\Delta l$ is a point inside in the uniform magnetic field region and

$$I(\Delta l) = \int_0^{\Delta l} B(Z)dZ \tag{58}$$

These formulas are written under supposition that before entering the magnetic field, i.e. for $Z < 0$, the vector of the particle momentum is $\vec{p} = (0,0,p)$ and $A(Z) = 0$.

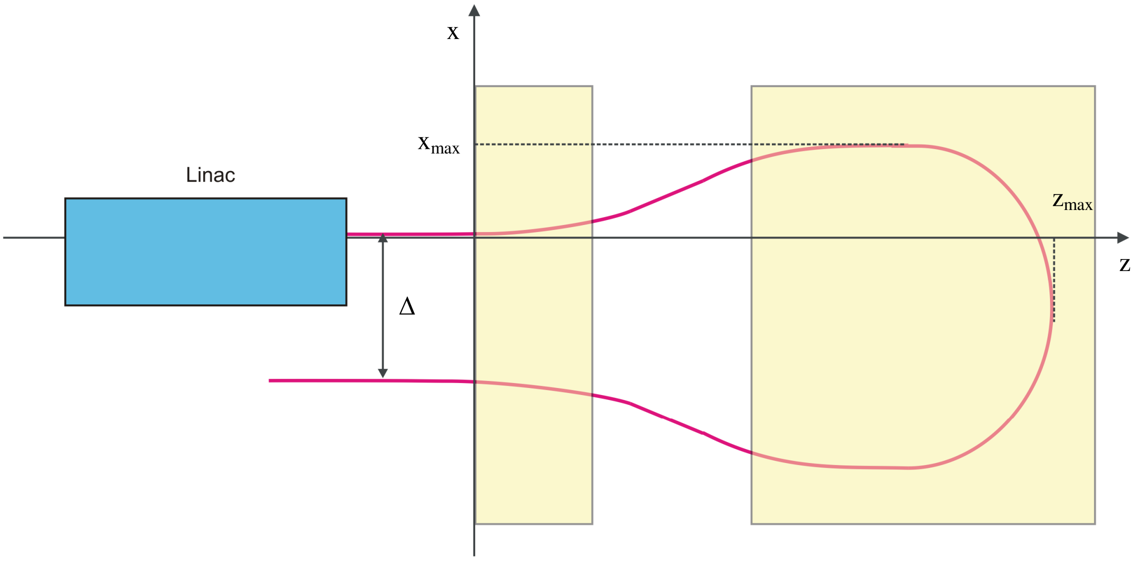

Figure 31: Particle trajectory in a two-pole end magnet

Eq.(50) gives a general formula for the trajectory displacement in an end magnet system with arbitrary magnetic field profile in the median plane. In the rest of this section we will consider simple cases of dipole magnetic systems with one, two and three poles in the hard – edge approximation.

### a. – **Simple dipole end magnet.**

Consider a simple 180º dipole with the magnetic field $B_0$. Then $A(Z) = B_0 Z$ and $Z_{\max}(p) = R_0$. From Eq.(58) it follows immediately that the beam displacement is equal to

$$\Delta = -2R_0 \tag{59}$$

where $R_0$ is the radius of the particle trajectory inside the magnet. Of course, this result also follows from the well known formula of charged particle motion in a static uniform magnetic field.

### b. – **Magnetic system with two poles.**

Consider now a two-pole magnetic system, i.e. a system of two dipoles, with inverse pole described in Sect.2.2.3. In the hard edge approximation the magnetic field in the inverse and main poles is given by

$$B(Z) = \begin{cases} -B_1 & 0 < Z < d \\ 0 & d < Z < Z_B \\ B_0 & Z_B < Z \end{cases} \tag{60}$$

where $B_1$ is the magnetic field of the inverse pole, $B_0$ is the magnetic field of the main pole, $d$ is the width of the inverse pole and $Z_B$ is the position of the entrance face of the main pole. Here we suppose that the fields $B_0$ and $(-B_1)$ are of opposite signs. In Fig.32 the pole sizes and the trajectory of a particle passing through this magnetic system is shown.

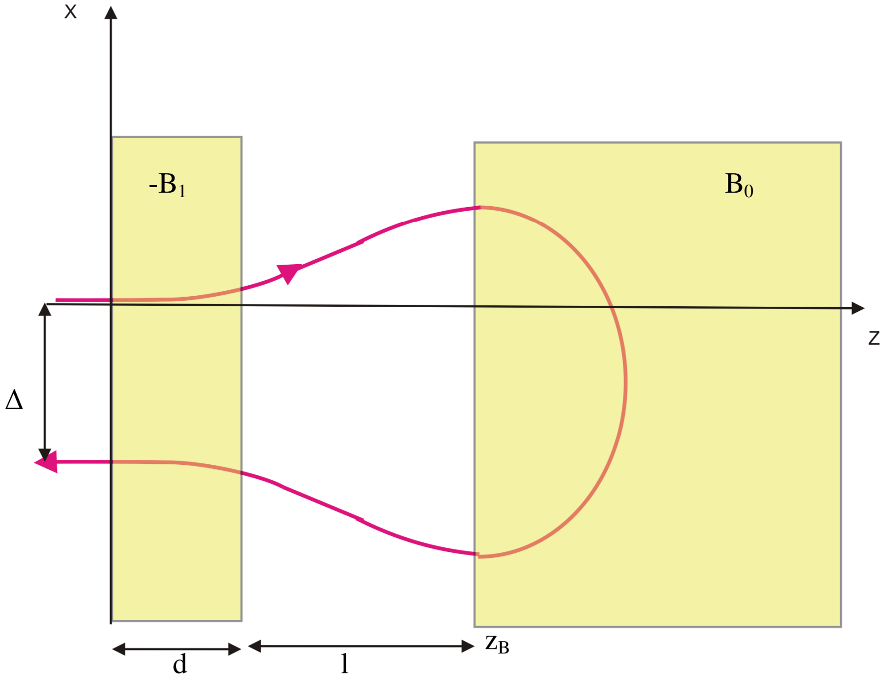

Figure 32: Two-pole end magnet and the trajectory of a particle passing through it.

The X-component of the vector potential of field (60) in the median plane is equal to

$$A(Z) = \begin{cases} -B_1 Z & 0 < Z < d \\ -B_1 d & d < Z < Z_B \\ B_0(z - z_B) - B_1 d & Z_B < Z \end{cases} \tag{61}$$

Using general formula Eq.(56) we obtain the beam displacement in the two-pole end magnet system

$$\Delta = 2\left[ R_1 - \sqrt{R_1^2 - d^2} + \frac{ld}{\sqrt{R_1^2 - d^2}} - \sqrt{R_0^2 - (dk)^2} \right] \tag{62}$$

where $R_1$ and $R_0$ are the radii of the particle trajectory in the field of the inverse and main poles, respectively, $l$ is the distance between two pole faces and $k = |B_1/B_0|$.

### 2.3.4 – Fringe field focusing.

In the previous section it was already stressed that the fringe field of RTM end magnets produces a strong focusing or defocusing in the vertical plane at low energy orbits that must be taken into account in beam tracking and design simulations. In this section we give a derivation of the formula of the focusing power of this field.

Let us consider a particle trajectory with a small initial deviation in the vertical plane from the reference trajectory. We suppose that at an initial point $s = 0$ before entering into a dipole magnet the initial conditions in the reference frame $(x, y, z)$ are:

$$x(0) =, x'(0) = 0, y(0) = y_0, y'(0) = 0 \tag{63}$$

where $y_0$ is small enough so that the linear approximation is valid. Let us also suppose that the initial point at the reference trajectory coincides with the origin of the laboratory reference frame $(X, Y, Z)$. From conditions (63) it follows that for the particle under consideration $v_Y(0, y_0, 0) = 0$.

The particle motion in the vertical plane is described by the $Y$-component of Eq.(44) which can be written as

$$\frac{d}{dZ}\left[v_Z \frac{dY}{dZ}\right] = \frac{|e|}{m\gamma}\frac{v_X}{v_Z} B_Z(Y, Z). \tag{64}$$

Using the definitions in Eqs.(45a) and (45b) one gets

$$\frac{d}{dz}\left[V\cos(\alpha(z))\frac{dY}{dZ}\right] = \frac{|e|}{m\gamma}\tan(\alpha(Z))B_Z(Z) \tag{65}$$

In what follows we suppose that angle $\alpha_0$ at which the trajectory enters the magnetic system is small and that the current angle of the velocity vector in the $XZ$-plane $\alpha(Z)$ is also small, so that approximately $|\cos(\alpha(Z))| \approx |\cos\alpha_0| \approx 1$, and that $|v_Y| << |\vec{v}|$. Substituting Eq.(48) into Eq.(65) the latter becomes

$$\frac{d^2Y}{dZ^2} = \left[\frac{|e|}{p}\right]^2 B_Z(Z)\int_{z0}^{z} B_Y(Z)dZ + \left[\frac{|e|}{p}\right]^2 B_Z(Z)\sin(\alpha_0) \tag{66}$$

To proceed further we use expressions (25) and (26) for the $Y$- and $Z$-components of the magnetic field in terms of $B(Z)$, the distribution $B_Y(0,0,Z)$ in the median plane $Y = 0$, obtained from the representation of the vector $\vec{B}$ in terms of the scalar potential $\Phi$, Eq.(24), in Sect. 2.2.2. Substituting Eqs.(25) and (26) into Eq.(66), leaving only the term independent of $Y$ and the term linear in $Y$ and integrating the obtained equation from $Z_0$ to $Z_f$ one gets

$$\frac{dY}{dZ} = \left[\frac{|e|}{p}\right]^2 \int_{Z_0}^{Z_f} YB'(Z)dZ \int_{Z_0}^{Z} B(Z)dZ + \left[\frac{|e|}{p}\right]\sin(\alpha_0)\int_{Z_0}^{Z_f} YB'(Z) \tag{67}$$

where $Z_f$ is a point at which the resulting focusing power is calculated. Integrating the first term in Eq.(67) by parts and calculating the integral in the second term of the same equation we arrive at the following expression:

$$\frac{1}{Y_0}\frac{dY}{dZ}=\left[\frac{|e|}{p}\right]^2\left[B(Z_f)\int_{Z_0}^{Z_f}B(Z)dZ-\int_{Z_0}^{Z}B^2(Z)dZ\right]+\left[\frac{|e|}{p}\right]\left[B(Z_f)-B(Z_0)\right]\sin(\alpha_0) \qquad (68)$$

Using the definition of the focal length $F$ and of the magnetic power $P=1/F$ of a magnetic system we get that

$$P\equiv\frac{1}{F}=-\frac{1}{y_0}\frac{dY}{ds}=-\frac{1}{y_0}\cos(\alpha_0)\frac{dY}{dZ} \qquad (69)$$

With the suppositions made above from Eq.(68) we obtain the following formula for the focusing power of a magnetic system with field distribution *B(Z)* in the median plane:

$$P=\left[\frac{|e|}{p}\right]\left[B(Z_f)-B(z_0)\right]\sin(\alpha_0)-\left[\left[\frac{|e|}{p}\right]^2\left[B(Z_f)\int_{Z_0}^{Z_f}B(Z)dZ-\int_{z_0}^{z}B^2(Z)dZ\right]\right] \qquad (70)$$

The term proportional to $\sin(\alpha_0)$ is the leading order term and the one proportional to $(|e|/p)^2$ is the first order approximation to it. We would like to note that, as one can easily check, at the exit of the trajectory from an end magnet $\alpha_{fin}\approx\pi$ and $\cos\alpha_{fin}\approx -1$ . Then, in accordance with Eq.(69) the sign of the first order approximation term in Eq.(70) is changed to the opposite.

The formula for the focal length derived here is of course in accordance with Eqs.(35)-(36). For the case $\alpha_0=0$ it was derived in Ref. [20], there also the next-to-leading contribution to the focal power proportional to the off-set $y_0$ was calculated.

## 2.4 – Longitudinal beam dynamics in RTMs.

In this section basic formulas describing the motion of electrons in the longitudinal direction are given.

Let us consider an RTM with the magnetic field induction in the end magnets equal to $B_0$, drift space between the end magnets of the length *l*, and the maximum energy gain provided by the accelerating structure $\Delta E_{\max}$. The longitudinal dynamics variables of an individual electron are its energy *E* and phase $\varphi$ [1].

Let $(\varphi_n, E_n)$ be the variables at the *n*th turn at some arbitrary but fixed point of the orbit. For the sake of convenience we choose this point to be the entrance to the accelerating structure, so that $(\varphi_0, E_0)$ correspond to the particle phase and energy just before its first passage through the accelerating structure. In the designs in which the beam is reversed back to the accelerating structure after the first acceleration, which is the case of the UPC 12 MeV RTM, $E_0$ is then not the energy of injection but the energy before the second passage through the linac.

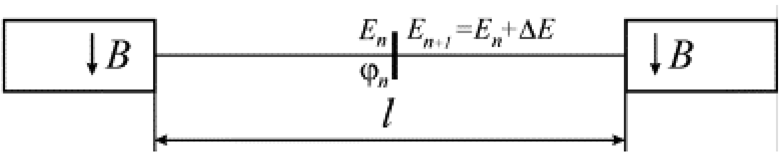

Figure 33: Schematic view of an RTM with the accelerating gap represented by the vertical bar situated in the middle of the drift space between the end magnets.

In this section we will consider the case with the initial energy already large enough so that the electrons are ultra-relativistic and $\beta$=1, as it is usually discussed in the literature [70]. The case of electrons with $\beta$<1, which is important for RTMs with low energy injection, will be studied in Ch. 5.

For the RTM model described above the time of the *n*th revolution of an electron is equal to

$$T_{ns} = \frac{2l}{c} + \frac{2\pi R_n}{c} = \frac{2l}{c} + 2\pi \frac{E_n}{ec^2 B} \ , \tag{71}$$

where $R_n$ is the radius of the trajectory of the particle in the end magnet and $E_n$ is its energy at the *n*th orbit. Then the phase of the particle changes according the relation

$$\varphi_{n+1} = \varphi_n + 2\pi f_{RF} T_n \ , \tag{72}$$

where $f_{RF}$ is the frequency of the accelerating electromagnetic field. The change of the particle energy with turns is described by

$$E_{n+1} = E_n + \Delta E_{mac} \cos(\varphi_n) . \tag{73}$$

Similar to the transverse particle dynamics the notion of reference particle will be important. When discussing longitudinal motion, called also phase motion, it is often referred to as synchronous particle. The dynamics of this particle is characterized by a synchronous phase $\varphi_s$. As it was already mentioned above an RTM is designed in such a way that its parameters satisfy the resonance conditions, given by Eqs. (2), (3), for the synchronous particle. The parameter $\mu \equiv \mu_1$ is equal to the number of RF field periods during the first turn and defines the synchronicity condition at the first orbit, whereas $\nu$ is equal to the increase of the multiplicity factor due to the increase of the synchronous particle period of revolution in one turn. It is clear that as a consequence of Eqs. (2), (3) the period of revolution of the synchronous particle at any orbit is an integer multiple of the RF period, namely

$$T_{ns} = T_{RF} [\mu + \nu (n-1)] . \tag{74}$$

Here and in what follows the subindex *s* indicates characteristics related to the synchronous particle. Relation (74) means that the synchronous particle, i.e. the particle following the synchronous trajectory, passes through the accelerating structure in the same phase of the accelerating field. This is precisely the synchronous phase $\varphi_s$, and at the higher orbits $\varphi_{n,s} = \phi_s (\mathrm{mod}\, 2\pi)$ for all $n \ge 1$. For a correct choice of $\phi_s$ the optimal acceleration of the synchronous particle is achieved. For further calculations we will use relation (4) between the synchronous energy gain per turn

$$\Delta E_{\max}\cos(\varphi_{ns}) = \Delta E_{\max}\cos(\varphi_s) = \Delta E_s$$

and the magnetic field in the end magnets. Using Eq. (64) for $n$=0 one can easily show that for conditions (2), (3) to be fulfilled the following relation between the injection energy of the synchronous particle, its energy gain and the ratio $l/\lambda$ must be valid

$$E_{0,s} = \frac{\Delta E_s}{\nu}\left(\mu - \nu - 2\frac{l}{\lambda}\right) \ . \tag{75}$$

Using relation (4) the system of difference equations (72), (73) describing the evolution of the dynamical variables $(\varphi_n, E_n)$ can be written as follows

$$E_{n+1} = E_n + \Delta E_{mac}\cos(\varphi_n), \tag{76}$$

$$\varphi_{n+1} = \varphi_n + K_0(E_{n+1}), \tag{77}$$

where the function $K_0(E)$ is known as phase advance and is given by the equation

$$K_0(E) = 4\pi\frac{l}{\lambda} + 2\pi\frac{E}{\Delta E_s}. \tag{78}$$

From the previous discussion it is clear that this system has a particular solution describing the synchronous trajectory:

$$E_{ns} = E_{0s} + n\Delta E_s, \tag{79}$$

$$\varphi_{ns} = \varphi_s + 2\pi[\mu n + \nu n(n-1)] \ . \tag{80}$$

One of the tasks of the accelerator design is to assure the stability of oscillations of particle trajectories around the synchronous trajectory (79), (80). The existence and properties of the regime of stable phase motion depends on the synchronous phase $\phi_s$, namely for a certain range of values of $\phi_s$ there exists a region of initial values $(\varphi_0, E_0)$ in the $(\varphi, E)$-phase space, called it longitudinal acceptance, giving rise to stable trajectories. By studying the behaviour of small deviations of an arbitrary phase trajectory $(\varphi_n, E_n)$ from the synchronous one $(\varphi_{ns}, E_{ns})$ in the linear approximation of difference equations (76), (77) it can be shown that the beam phase motion is stable if the synchronous phase fulfils the condition

$$0 < \tan\phi_s < \frac{2}{\pi\nu}. \tag{81}$$

A general phase trajectory includes then a term describing stable oscillations around the synchronous trajectory $(\varphi_{ns}, E_{ns})$. In terms of the phase it is of the form

$$\varphi_n = \varphi_{ns} + C\sin(Qn + \chi_0), \tag{82}$$

where $C$ and $\chi_0$ are integration constants determined by initial conditions and the phase advance per turn $Q$ is given by the relation

$$\cos Q = 1 - \pi\nu \tan\varphi_s . \tag{83}$$

# Chapter 3

# Magnetic systems with permanent magnets

## 3.1. – Introduction.

Since A.M.Clogston and H.Heffner in 1954 proposed a design of a system for particle beam focusing in which the magnetic field was created by permanent magnets (see [71]) these systems have rapidly become widely used in particle accelerators because of clear advantages of permanent magnets:

1. The systems with permanent magnets do not need power supply and cooling,
2. The permanent magnets allow building compact systems,
3. A permanent magnet can be placed inside another magnetic system without essential change of the magnetic field generated by permanent magnet,
4. The magnetic field generated by a permanent magnet is negligible outside the magnetic system,
5. Permanent magnets can be placed in a high vacuum environment.

However, such systems have the following disadvantages:

1. Adjustment of the field level in not simple (as in the case of electromagnets) and requires a special mechanism or technique.
2. The value of the generated magnetic field is quite temperature sensitive,
3. In the case of designs without steel pole small variations in the magnetization of permanent magnet blocks lead to a considerable non-uniformity in the field region,
4. Because of strong magnetic forces between the permanent magnet blocks building and assembling of such systems require special technique, fixings and tools.

In this chapter main properties of permanent magnets are described with a special emphasis on the Rare Earth Permanent Magnet (REPM) materials which are now widely used in many particle accelerators and facilities, in particular in RTMs. Also main methods of field measurements and field tuning in magnetic systems with permanent magnets are outlined.

## 3.2. – Main properties of permanent magnets.

The magnetic materials are classified according to their magnetic properties into three types: diamagnetic, paramagnetic and ferromagnetic [72]. The diamagnetic materials are characterized by the property that applying an external magnetic field the magnetic dipole moments are aligned in the direction opposite to the direction of applied magnetic field. A typical example of the diamagnetic material is cooper. The property of the paramagnetic materials is that on applying an external magnetic field the magnetic dipole moments of the sample are aligned parallel to the direction of applied magnetic field thus defining the magnetization axis, i.e., the paramagnetic magnetic materials are magnetized weakly in the same direction as the applied magnetic field. Examples of the paramagnetic material are aluminum and air. When a ferromagnetic material is placed in an external magnetic field the magnetic dipole moments of the sample are aligned in the direction of the magnetic field. Thus the ferromagnetic materials exhibit the same behavior as the paramagnetic materials but their magnetization is considerably stronger than in the case of the paramagnetic materials. The ferromagnetic materials are classified in two types. If switching off the external magnetic field the magnetic dipole moments return to their initial state such material is known as soft magnetic material, the well known example is the steel. If after switching off the external magnetic field the magnetic dipole moments maintain their direction such material is referred to as hard magnetic material. They are also called permanent magnets (see, for example, [73]), examples of them are ferrites and alnico.

Creation of alnico in the 30s and ferrites in the 50s was a breakthrough in the development of the technology of magnetic systems. They possess a high magnetization value with respect to natural permanent magnets and open numerous field of applications. For example, since the 50s permanent magnets have been used in the construction of magnetic systems, mainly focusing devices.

Discovery of Rare Earth Permanent Magnet (REPM) materials in the 60's was a real revolution in the magnet technology. These are materials based on alloys of transition metals with elements of the third family of the rare – earth group. The REPMs have a higher magnetization value than the alnico and ferrites and a remarkable property of having a practically linear demagnetization curve. There are two large subgroups of REPMs: (1) REPMs based on cobalt alloys, for example $SmCo_5$ and $Sm_2Co_{17,}$ and (2) REPMs based on the iron alloys with Neodymium, for example $Nd_2Fe_{14}B$. The REPM materials are now widely used in focusing and bending magnets of particle accelerators or in insertion devices at synchrotron light sources.

Magnetic properties of a permanent magnet are characterized by the hysteresis curve. The equation describing it relates the applied magnetic field *H*, the material magnetization *M*, defined as the magnetic dipole moment per unit volume, and its magnetic field induction $B_m$ *inside the material*. It is the following

$$B_m(H) = \mu_0\left(H + M(H)\right) \tag{84}$$

where $\mu_0$ is the vacuum magnetic permeability. In general the dependence *M(H)* is highly non-linear. Examples of the behavior of the magnetization as a function of the external magnetic field for soft and hard magnetic materials are given in Fig.34. For a strong enough magnetic fields a total alignment of magnetic moments occurs and the material becomes magnetically saturated, for example for the steel this happens at the applied field ~ 2 T, for permendur at about 2.4 T.

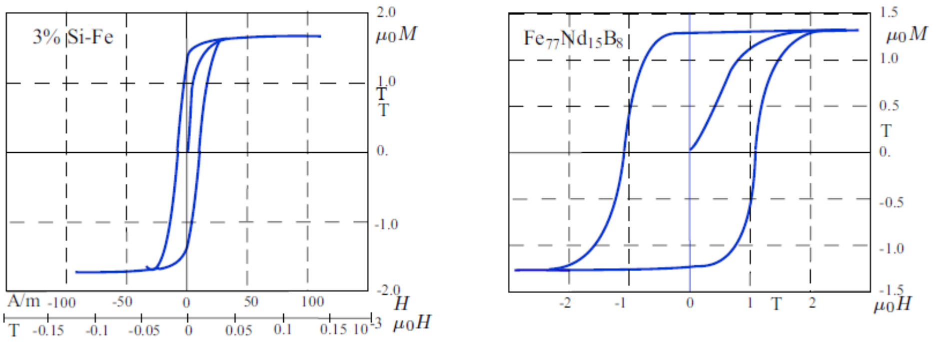

(a) (b)

Figure 34: Magnetization curves *M(H)* for (a) soft material, namely 3% Si-Fe grain oriented laminations, and (b) for NdFeB permanent magnet (hard material) [74].

For a linear isotropic and homogeneus material Eq.(75) can be written as [71],

$$B_m(H) = \mu_0\left(H + \chi_m H\right) = \mu_0\left(1 + \chi_m\right)H = \mu_0\mu_r H \tag{85}$$

where $\mu_r$ is the relativity magnetic permeability and $\chi_m$ is the magnetic susceptibility.

For applications of permanent magnets in accelerator magnetic systems of special importance is the part of the hysteresis curve in the second quadrant also known as demagnetization curve. The value of $B_m$ for $H$=0 is called the residual magnetization and is denoted by $B_r$. The value $H= H_c$ for which the magnetic field induction $B_m$ is zero is called coercive force. Another important characteristic of the permanent magnets is the relative magnetic permeability $\mu_r$. For REPMs the relative magnetic permeability is close to unity, typically it is equal to 1.03 – 1.05, and their demagnetization curve is practically a straight line. In this sense they are close to the ideal permanent magnet. Let $M_{sat}$ be the magnetization saturation and $H_i$ the *intrinsic* coercivity of the material. For the ideal permanent magnet the residual magnetization $B_r=\mu_0 M_{sat}$, the value of the coercive force $H_c=-M_{sat}$ and the demagnetization curve (see Fig.35b) is given by

$$B_m=\mu_0\, \mu_r\, (H_m - H_c), \tag{86}$$

where $B_m$ and $H_m$ are the magnetic field induction and magnetic field (magnetization force) inside the magnetic material, so that $B_r = -\mu_0\mu_r H_c$ (see Fig. 35b) [72].

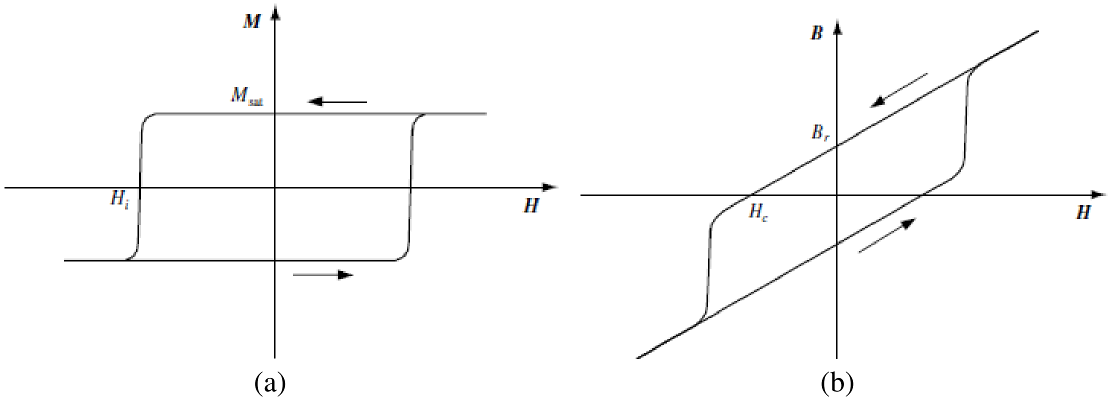

(a) (b)

Figure 35: Examples of variation of the magnetization, *M* (a) and the magnetic field induction (b) as functions of the magnetization force [41].

One factor that influences the hysteresis curves is the temperature. As shown in Fig.36 by increasing the temperature of the permanent magnet the linearity of its demagnetization curve in the second quadrant is lost. For each material there exists a temperature at which the permanent magnet loses its "spontaneous" magnetization. This temperature is known as Curie temperature, $T_c$.

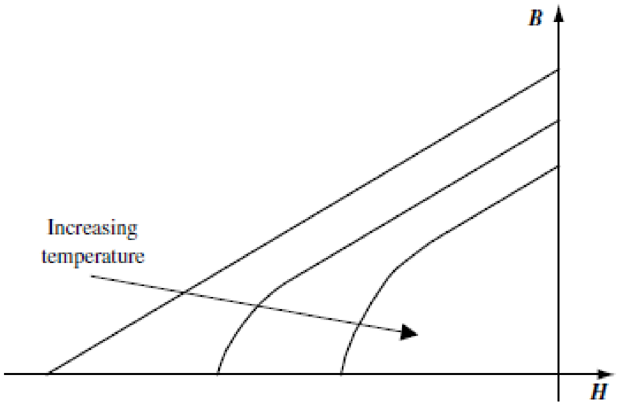

Figure 36: Demagnetization curve for different temperatures [39].

An important characteristic of the permanent magnets is the product $B_m H_m$. For a material with a linear relation between $B_m$ and $H_m$ its magnetic field energy density is given by $B_m H_m / 2$. When plotted in the second quadrant (see Fig.37) $B_m H_m$ achieves a maximum value $(B_m H_m)_{\max}$ for some value of the magnetic field $H_m$. One of the goals of the design of magnetic systems with permanent magnets is to have its working point in the H-B plane to be close to the maximum of $B_m H_m$.

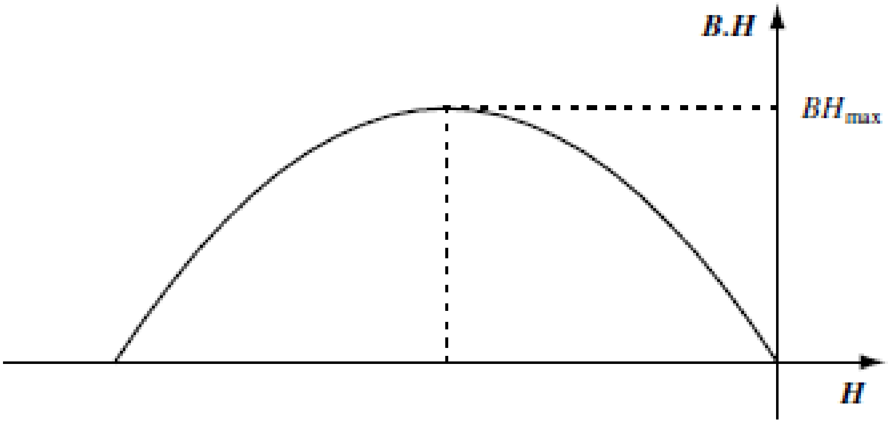

Figure 37: Product $B_m H_m$ as a function of the magnetization force H [39].

The working point, also called operation point, is defined as the point of intersection of the demagnetization curve and a load curve. The latter depends on the geometry and dimensions of the magnetic system. As an example let us consider a C-core permanent magnet shown in Fig.38. It is formed by a yoke with high magnetic permeability (for example steel) and a block of permanent magnet of a height $l_m$ and a cross section area $A_m$. The yoke carries the magnetic flux created by the permanent magnet through the air gap of a height $l_g$ and cross section area $A_g$. For this magnetic circuit the load curve relating the magnetic field induction $B_m$ inside the permanent magnet block and magnetic field $H_m$ is given by the following formula:

$$B_m = \mu_0 P H_m, \tag{87}$$

where $P$ is the permanence coefficient equal to

$$P = -\frac{A_g}{A_m}\frac{l_m}{l_g}. \tag{88}$$

Its derivation will be given in the next Section. Taking into account Eq.(87) for the magnetization curve one easily obtains the working point $(H_m^*, B_m^*)$ (see Fig.39) of this magnet with

$$H_m^* = \frac{B_r}{\left(\frac{B_r}{H_c} + \mu_0 P\right)}, \quad B_m^* = \mu_0 P H_m^*. \tag{89}$$

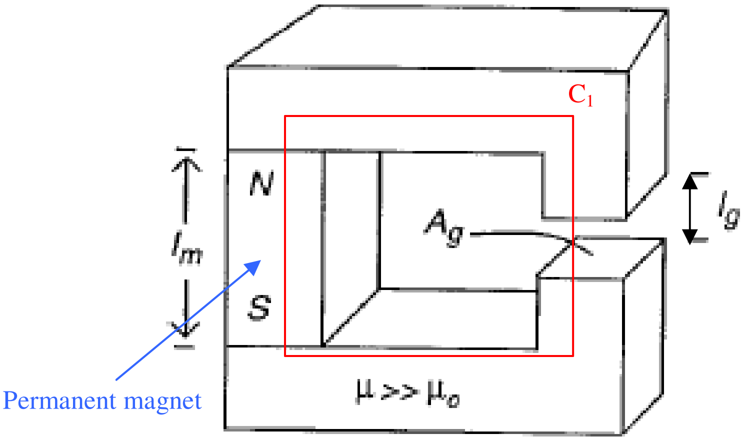

Figure 38: C-core magnet with a block of permanent magnet material.

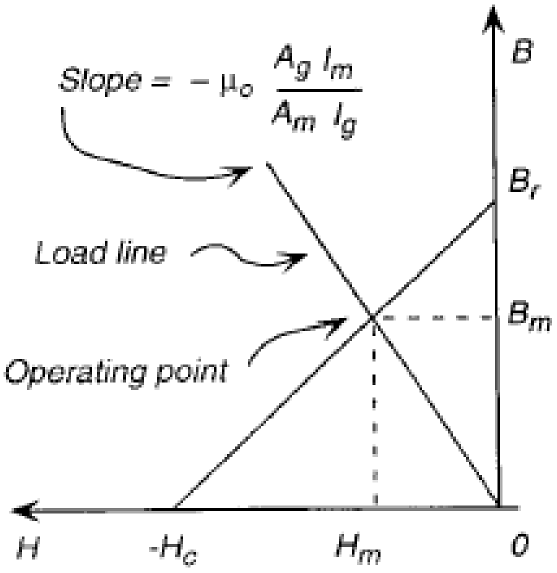

Figure 39: Example of the demagnetization curve and load curve.

The choice of the permanent magnet material depends on its magnetic properties like the residual magnetization, resistance to temperature or the value of the product $(BH)_{max}$, as well as the concrete application. In Table 6 characteristics of main types of easiliy available permanent magnets are given. Here $T_c$ is the Curie temperature. The parameters $\Delta B_r$ and $\Delta H_c$ characterize the relative variation of the residual magnetization $B_r$ and coercive force $H_c$, respectively, due to the change of the temperature of the permanent magnet.

Table 6: Characteristics of some permanent magnet materials.

| Parameter | Units | Ferrite | Alnico | SmCo | NdFeB |
|---|---|---|---|---|---|
| $B_r^{max}$ | T | 0.23 – 0.41 | 0.71 – 0.82 | 0.85 – 1.05 | 1.1 – 1.4 |
| $H_c^{max}$ | kA/m | 147 - 223 | 43.8 – 131.3 | 600 – 800 | 750 - 1000 |
| $(BH)_{max}$ | kJ/m$^3$ | 8.36 – 31.8 | 11.9 - 42.2 | 150 - 200 | 200 -350 |
| Tc | ºC | 250 | 450 – 550 | 250 – 300 | 100 -200 |
| $\Delta B_r$ | %/ºC | -0.2 | -0.02 | -0.004 | -0.12 |
| $\Delta H_c$ | %/ºC | +0.3 | -0.03 | -0.3 | -0.5 |

The permanent magnets used in accelerator magnetic systems are mainly REPM materials. Their clear advantage is that they have a higher value of the magnetic energy density $(BH)_{max}$ than the ferrites and Alnico. At the same time there are considerable differences in characteristics between the groups of the REPM materials. Thus, NdFeB magnets have higher limit of the residual magnetization, higher magnetic field energy density $(BH)_{max}$ and higher mechanical resistence (less fragile), and they are also cheaper than SmCo REPMs. On the other hand SmCo magnets exhibit a higher resistance to the temperature increase and are more resistent to radiation [75] and oxidation than materials from the NdFeB group. Due to the latter property they can be used in the high vacuum environment with special coating, whereas NdFeB materials must be coated with Ni when used in-vacuum. In fact the choice of the permanent magnet material depends on the concrete application. For example, in undulators and wigglers at synhrotron light sources which are exposed to high levels of radiation REPM materials of the SmCo group are used.

## 3.3. – Magnetic systems with permanent magnets.

### 3.3.1. – Simple dipole with permanent magnet.

The magnetic field and induction in magnetic systems with permanent magnets can be calculated using the following two Maxwell equations in the integral form:

$$\oint_C \vec{H}d\vec{l} = 0, \tag{90a}$$

$$\oint_S \vec{B}d\vec{S} = 0 \tag{90b}$$

Here *C* is a closed contour and *S* is a closed surface of interest. The first of the equations is the Ampere law for a contour that does not surround any macroscopic current, which is the case of systems with permanent magnets, whereas the second one essentially means that the magnetic flux is continuous.

Let us consider again the C-core dipole magnet shown in Fig.38 and calculate its load curve and the magnetic field in the gap. In Fig.38 the cross section of this dipole and a contour *C* that will be used for the calculation are shown. Writing Eq.(81a) for this contour one obtains

$$\oint_C \vec{H} d\vec{l} = \int_{gap} \frac{\vec{B}}{\mu_0} d\bar{l} + \int_{PM} \vec{H}_{PM} d\bar{l} + \int_{iron} \frac{\vec{B}}{\mu_{iron}\mu_0} d\bar{l} = 0 \tag{91}$$

Given that $\mu_{iron} >> 1$ Eq.(91) is written as

$$\frac{B_0}{\mu_0} l_g + H_{PM} l_m = 0 \tag{92}$$

where $B_0$ is the magnetic field induction in the gap and, as in the previous chapter, $l_g$ is the gap height and $l_m$ is the thickness of the permanent magnet block. It is also easy to see that for a certain choice of the surface *S* Eq. (90b) gives

$$B_0 A_g = B_m A_m \tag{93}$$

Combining Eqs.(92) and (93) one obtains the following relation between the magnetic field induction and magnetic field (magnetization force) inside the permanent magnet block:

$$B_m = -\mu_0 \frac{A_g l_m}{A_m l_g} H_m \equiv \mu_0 P H_m, \tag{94}$$

which is precisely the load curve, Eq.(90). The working point of the dipole magnet, which is the common point of the load curve and demagnetization curve, is then given by formulas (90). For this value of $B_m$ the magnetic field induction $B_0$ in the gap follows from relation (93) and is equal to

$$B_0^* = \frac{A_m}{A_g} B_m^* = \frac{A_m}{A_g} \frac{B_r}{1 - \frac{\mu_r}{P}} = \frac{A_m}{A_g} \frac{B_r}{1 + \mu_r \frac{A_m}{A_g} \frac{l_g}{l_m}} \tag{95}$$

In particular, for $A_m = A_g$ the magnetic field induction in the gap becomes

$$B_0^* = \frac{B_r}{1 + \mu_r \frac{l_g}{l_m}} \ . \tag{96}$$

As one see, for this geometry the field in the gap can never exceed the residual magnetization $B_r$, from this point of view C-core design is not optimal.

### 3.3.2. – Halbach type magnetic systems with permanent magnets.

A large part of magnetic systems using permanent magnets as a source of the magnetic field are based on ideas and design solutions proposed and developed by K.

Halbach during the 70's [76]. They span a wide range of systems, in particular dipole and quadrupole magnets and undulators. Thus, in Ref.[30] a general approach to the design of arbitrary multipole magnets using REPMs is described.

Here we give a short review of the box-type design of a dipole magnet proposed by K.Halbach in [77] and shown in Fig.40. This magnetic system is formed by two poles separated by a gap. At all their faces, except the ones which face the gap, blocks of permanent magnet material are attached. This assembly is surrounded by a yoke.

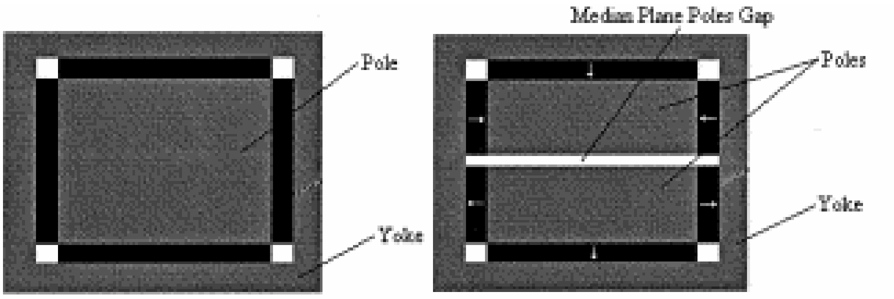

(a) (b)

Figure 40: Box-type dipole magnet: (a) plan (top), (b) elevation (bottom).

End magnets of the box-type design are installed at the SINP 70 MeV RTM [17], this design is also used for the end magnets of the UPC 12 MeV RTM described in Chapter 4.

To determine parameters of a box-type dipole magnet K.Halbach considered a model based on the assumption that the permanent magnets are magnetized homogeneously and these have the relative magnetic permeability close to one and used the electrostatic approximation. In this approach the upper and lower poles have potentials $V_0$ and $-V_0$, respectively, and the potential is zero at the yoke. The geometry of the dipole magnet is described by a number of parameters as shown in Fig.41. The gap height is defined by $h_0$, whereas $D_1$, $D_3$ and $D_0$ are the dimensions that characterize the pole. Parameters $h_1$, $h_2$, $h_3$ and $h_4$ are the sizes of the spaces between the pole and the yoke occupied by the permanent magnet material and $h_6$ and $h_7$ are the yoke dimensions.

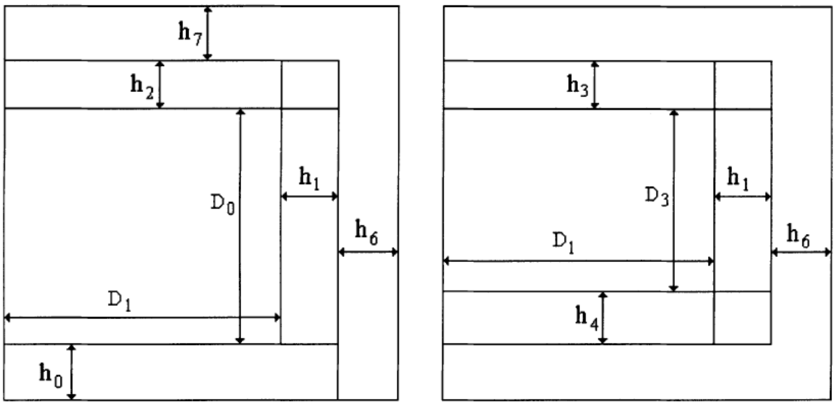

(a) (b)

Figure 41: Parameters defining the geometry of a box-type dipole magnet, (a) vertical cross section (bottom), (b) horizontal cross section (top).

The values of $D_1$ and $D_3$ are given by the following relations:

$$D_{1,3} = R_{0,\max} + \phi h_0 \tag{97}$$

where $R_{0,\max}$ is the radius described by the highest energy particle in the uniform magnetic field region and $\phi$ is a parameter that takes into account the extension of the fringe field. The value of $\phi$ is comprised between 1 - 1.5. The pole height $D_0$ is found from the condition that the total flux (i.e., the sum of the direct and indirect fluxes) through the main pole surface is zero.

To calculate the values $h_1$, $h_2$, $h_3$ and $h_4$ one can use the following relation between the pole potential $V_0$ and $H$ (see Ref. [77])

$$\mu_0 H = \mu_0 \frac{V_0}{h_i} = B_0 \frac{h_0}{h_i} \tag{98}$$

where $B_0$ is the magnetic field induction in the uniform magnetic field region in the gap. To simplify the calculation one assumes that the working point of the permanent magnets is in the middle of the B-H curve. Then

$$\mu_0 H_m^* = \mu_0 \frac{H_c}{2} = \frac{B_r}{2} \tag{99}$$

Substituting Eqs.(90) into Eq.(89) we obtain the following relations that give the values of the sizes $h_i$ (i=1, 2, 3, 4) in terms of the magnetic field induction in the uniform magnetic field region $B_0$, the residual magnetization $B_r$ and the gap height $h_0$:

$$h_i = 2h_0 \frac{B_0}{B_r}. \tag{100}$$

The values of the parameters $h_6$ and $h_7$ determining the yoke thickness depend on the material magnetic saturation. As a material for the yoke the steel is usually used.

### 3.3.3. – Quasi – Sheet Multipole design of magnetic systems with permanent magnets.

Another design of magnetic systems with permanent magnets was proposed in [34] and it was coined as Quasi – Sheet Multipole (QSM) design. QSM magnets are iron-pole-free systems consisting only of permanent magnets, usually REPMs, and a magnetically soft iron yoke. The homogeneously magnetized REPM blocks are arranged around a working region in such a way that a pure multipole field is excited. In this sense QSM magnets are similar to split-pole multipole magnets [77]. Their design is a close analog of “window frame” dipole electromagnets and Panofsky lenses, in particular they have large longitudinal-to-gap dimensions ratio. The type of the multipole field generated depends on the number of the REPM blocks and the residual magnetization direction of each block. In QSM magnets they are placed in such manner that the molecular sheet (surface) currents follow the yoke profile and the leak magnetic flux is very low. Since REPM pieces are difficult to machine in practice QSM magnetic systems are restricted to dipoles [35] and quadrupoles [78] only.

QSM magnets in comparison with the Halbach design have some advantages, for example they require less REPM blocks and in general have a lower magnetic flux leaking. On the other hand, in practice the field in QSM systems is limited to 0.7-0.9 T. This is because their working point on the REPM demagnetization curve is usually chosen near the one with $(BH)_{max}$. In order to get a higher value of the field one has to use a much larger amount of the magnetic material, as a consequence the cost of the system becomes too high.

A formalism that allows of the determination the shape and sizes of the REPM blocks and yoke parts for a given multipole field in the working region was proposed and developed in Ref. [34]. For example, in the case of a quadrupole the magnetic field is generated by triangular REPM blocks as it is shown in Fig.42. Taking into account the symmetry of the magnet only one quater of its cross section is given there. The gradient $G$ is related to the angle $\psi$, the aperture radius $r_0$ and the REPM block residual magnetization $B_r$ by the formula

$$G = \frac{B_r}{2r_0}\sin(2\psi). \tag{101}$$

There are various examples of magnetic systems with REPM material based on the QSM design. One of them are the α-magnets operating in the injection lines of the SINP RTMs [79, 80]. Also, focusing triplets of the SINP 70 MeV RTM consist of QSM quadrupoles [81]. In the present thesis QSM design approach is used for the horizontally focusing quadrupole and extraction dipoles of the UPC 12 MeV RTM (Sections 4.2 and 4.3).

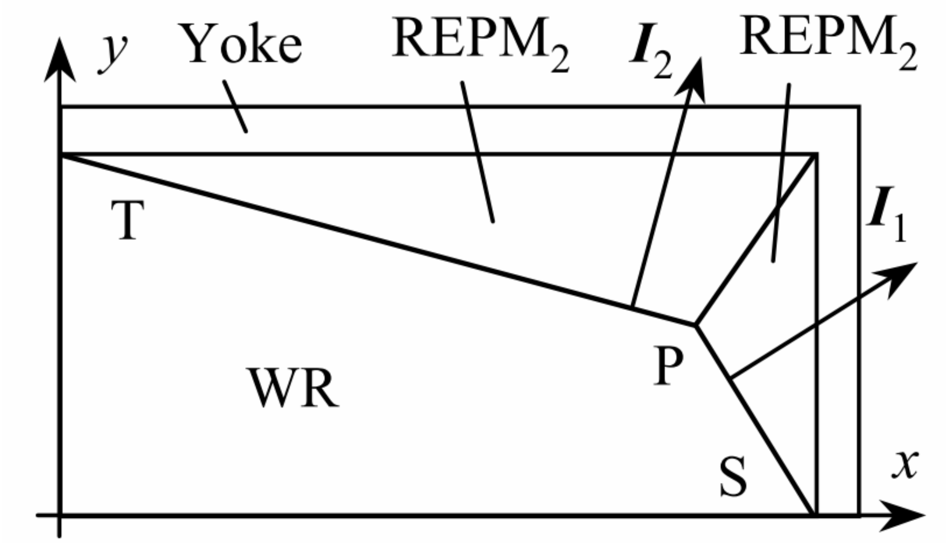

Figure 42: One quater of the cross section of a QSM quadrupole magnet.

### 3.4. - Magnetic field measurements in permanent magnet systems.

There exist a variety of devices that can be used for measurements of magnetic characteristics. The choice of the concrete device depends on the magnetic field range and required precision. Parameters of measuring devices as functions of the field range and precision are shown in the diagram in Fig.43.

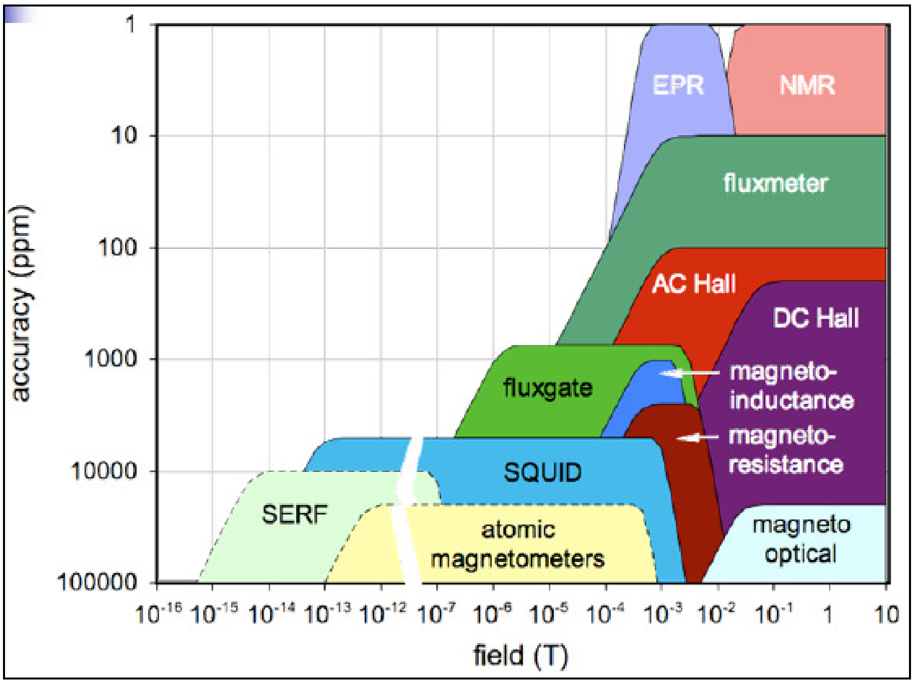

Figure 43: Instruments for magnetic field measurements.

For magnetic field measurements of the systems with permanent magnets typically instruments based on the Hall effect and magnetic induction methods are used. In what follows we discusss the corresponding physical principles and describe the Hall sensor principle.

### a. – **Hall Effect.**

The Hall effect is a galvanomagnetic phenomenon discovered in 1879 by E.H. Hall. It occurs when a metal, especially a semiconductor, through which an external current $I_c$ flows is located inside a magnetic field. Under these conditions a voltage between the ends of semiconductor, called Hall voltage $V_H$ perpendicular to the external current and normal component of the magnetic field $B_z$ appears (see Fig. 44).

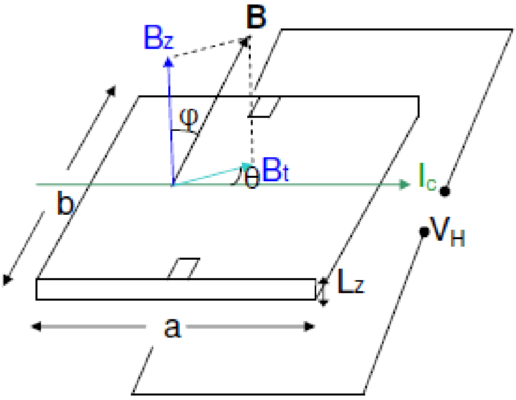

Figure 44: Schematic view of a Hall probe.

A general expression for the Hall voltage is the following [82]:

$$V_H = \frac{R_H}{t} I_c B_z + V_{offset} - P B_t^2 \sin(2\varphi) \qquad (102)$$

The first term is the voltage generated by the magnetic field induction $B_z$, where $R_H$ is known as the Hall coefficient. The second term $V_{offset}$ in Eq.(93) is known as offset voltage, it is equal to a residual voltage between the electrodes which appears in the absence of the magnetic field. This phenomenon depends on the geometry and material inhomogeneities. The third term describes a planar effect, that is a voltage due to the tangential component of the magnetic field $B_t$ which appears in addition to the voltage generated by the normal component. The parameter $P$ is the planar Hall coefficient and $\varphi$ is the angle between the normal component of the magnetic field, $B_z$, and external current, Ic. This effect is due to a difference between the magnetoresistance in the longitudinal and transverse magnetic fields. A way to reduce this effect would be to use highly dopped semiconductors.

A Hall probe measures in fact the voltage generated by the magnetic field of the magnetic system in the semiconductor and not the magnetic field itself. To relate the Hall voltage to the magnetic field the instrument must be previously calibrated with a reference magnetic field. A picture of the Gaussmeter with two Hall probes (transverse and axial) of the SINP accelerator laboratory is shown in Fig. 45.

Figure 45: Caylar GM-H103 Gaussmeter with transverse (1) and axial (2) Hall probes.

Usually magnetic field measurements are performed at a bench that provides the motion of a Hall probe along three axes. A schematic view of such bench is given in Fig. 46. The Hall probe is fixed on platform (1) which moves along the vertical axis (2). The platform support is situated on rails which provide its displacement along two horizontal axes, (3) and (4).

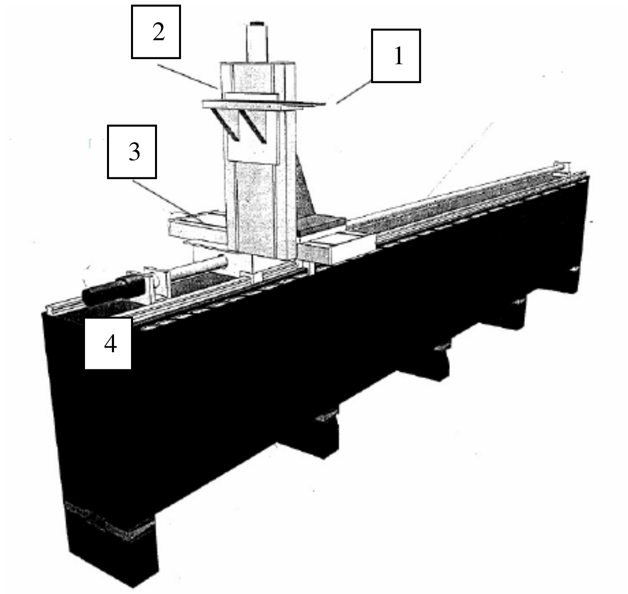

Figure 46: Scheme of a typical magnetic test bench.

The Gaussmeter shown in Fig. 45 and a magnetic measurement table similar to the one in Fig. 46 were used for the characterization of the extraction magnet of the SINP 55MeV RTM, the obtained results are discussed in Sect. 4.4.

## 3.5. – Magnetic field tuning in systems with permanent magnets.

As it was mentioned in Sect. 3.1 one of the disadvantages of magnetic systems with permanent magnets is the difficulty in varying its magnetic field. This may appear to be necessary for a field adjustment or tuning in order to compensate imperfections in the magnet machining or assembling. Obviously such problem does not appear in case of electromagnets for which tuning is easily done by simply varying the current in the coils.

In this section three widely used techniques are described.

### a. – Re-magnetization and demagnetization techniques

This widely used technique essentially consists in applying a strong pulse of magnetic flux generated by an iron free coil powered with a pulse generator at the surface of a permanent magnet with the aim to change its magnetization [35].

The operating principle of this method is the following (see Fig.48). A permanent magnet is placed on an iron platform and is magnetized to a certain value, normally to the saturation value. The coil connected to a pulse generator (PG) is maintained at a certain distance from the permanent magnet surface with the coil plane being oriented perpendicularly to the axis of the magnetic block magnetization. A pulse through the coil produces a local demagnetization of the permanent magnet block. The process of adjustment of the magnetic field is iterative and includes a few successive steps of the re-magnetization and demagnetization until the required magnetic field is achieved.

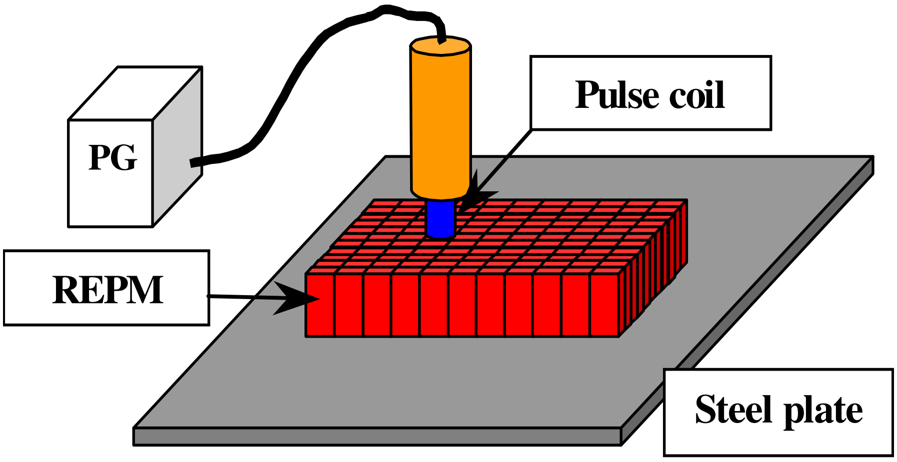

Figure 47 : Permanent magnet re-magnetization technique.

b. - **Tuning with plungers.**

This method consists in moving some pieces of ferromagnetic material thus changing the magnetic field in the gap between the magnet poles. An example of such tuning system is illustrated in Fig.48. There a Halbach box-type end magnet with channels cut symmetrically in the upper and lower parts of the yoke and the REPM surrounding the main pole parts is shown. Two steel plungers move in these channels vertically. To understand the principle of operation of this tuning system let us use the electrostatic approximation outlined in Sect. 3.3.2. When the gap between the plungers and the corresponding poles is maximum, i.e. the upper plunger is in the upper position and the lower one is in the lower position (see Fig. 48a), the potential of the poles are + $V_0$ and ($-V_0$) and the yoke potential is zero.

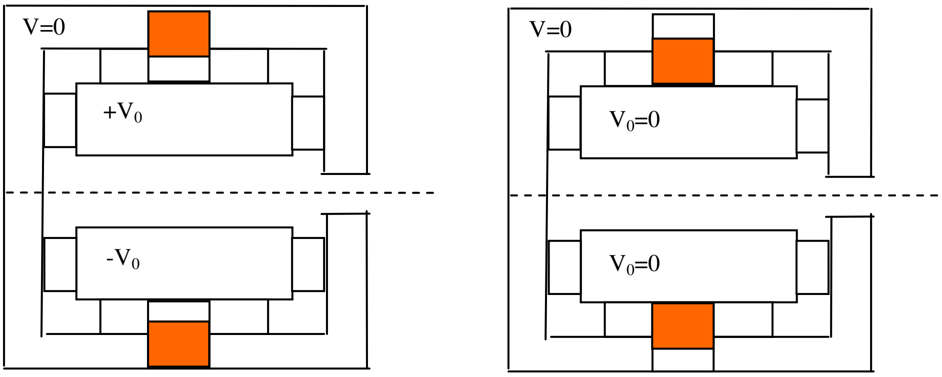

(a) (b)

Figure 48: End magnet with tuning plungers in the two extreme positions: (a) maximal gap and (b) zero gap between the plungers and the poles.

Let us assume now that the material of the plungers has infinite magnetic permeability and consider their another extreme position when they touch the poles (Fig.48b). In this case the pole and yoke potentials are equal to zero and, as a consequence, the value of the field in the median plane of the system is zero. Of course, in reality the material relative permeability is finite, because of this both the pole potentials and the median field have certain non-zero values. Thus, changing the plunger position one varies the potential of each pole and therefore the field in the gap. To maintain the position of the magnet symmetry plane unchanged the plungers have to be displaced symmetrically.

The permanent magnet tuning by means of plungers has been used for adjustment of the magnetic field in steering magnets built for the European Synchrotron Radiation Facility (ESRF) upgrade [83]. This technique is used for the tuning of the end magnets of the UPC 12 MeV RTM as described in Sect. 4.1.3.

c. – **Tuning by means of rotating blocks.**

The third method of field tuning in magnetic systems with permanent magnets is based on moving permanent magnet blocks and thus changing the magnetic circuit. This can be done, for example, by rotating cylindrical blocks of permanent magnet material whose magnetization is perpendicular to the cylinder axis [84], as it is shown in Fig. 50. By rotating the cylinders in one direction or another one increases or decreases the magnetic field in the gap between the poles. This system was used in the end magnet design of the SINP 70 MeV RTM [17].

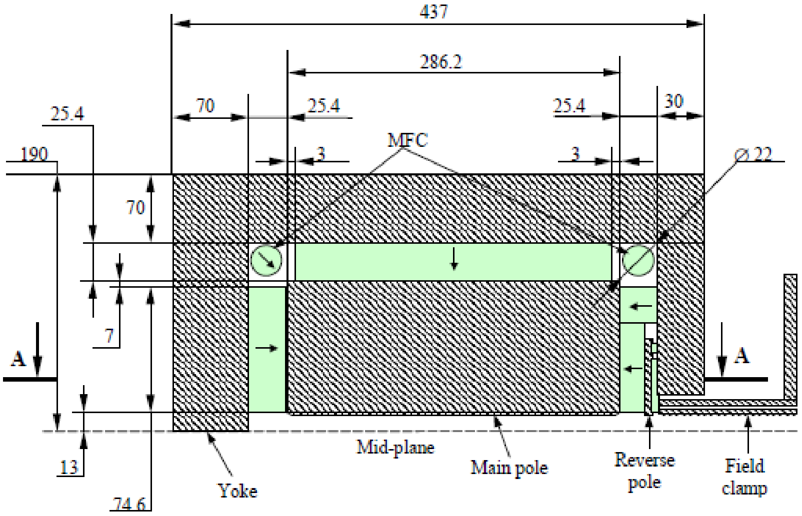

Figure 49: Cross section of the end magnet of the SINP 70 MeV RTM.

# Chapter 4

# Design of magnetic systems for RTM projects

In the first three sections of this chapter design studies and simulations of the magnets of the UPC 12 MeV RTM are given. The last section is devoted the optimization and field measurements of the extraction magnet of the SINP 55 MeV RTM. The magnetic systems considered in this Chapter use REPM material as a source of the magnetic field.

## 4.1. – End magnets of the UPC 12 MeV RTM.

As it has been discussed in Section 2.1 the main function of RTM end magnets is to provide the beam recirculation in the machine. The end magnets of the UPC 12 MeV RTM accelerator have additional functions:

(1) Produce the reflection of the beam trajectory of the first orbit (after the first acceleration) back into the accelerating structure;

(2) Provide the beam trajectory displacements for the second and higher orbits sufficient for by-passing the accelerating structure cavities.

As it was explained above function (1) is due to the fact that in this RTM the kinetic energy of electrons emitted from the electron gun is only 25 keV so that after the first acceleration the beam is not energetic enough to by-pass the accelerating structure. In addition the design of the end magnets must assure that the defocusing effect of the fringe field of their main poles is compensated. The location of the end magnets inside the accelerator head of the UPC 12 MeV RTM is shown in Fig. 8.

First we will discuss the basic design of the end magnets, in the last subsection the mechanism of the magnetic field tuning will be studied.

### 4.1.1. – End magnet specifications and design considerations.

In accordance with the general conceptual design of the UPC 12 MeV RTM and results of beam dynamics simulations with RTMTRACE code [85] the following design specifications of the end magnets have been formulated [66]:

S1. The magnetic field in the uniform field region of the 180º bending dipole must be $B_0$=0.7986 T,
S2. The relative deviation of the magnetic field from its nominal value in the median plane in the center of the dipole must not exceed ±0.05%,
S3. The inhomogeneity of the magnetic field in the *good field region*, defined as the region 15 cm inside the magnet from the pole edge, of the 180º bending dipole must not exceed ± 0.075%,
S4. The full gap height between the poles of the magnet must be optimized with the criterion to minimize both the beam losses and the magnet weight,
S5. The absolute value of the stray magnetic field outside the 180º bending dipole at a distance 2.0 cm from the end magnet face must be less than 1.0 G,

S6. The vertical focusing power $P$ of the end magnet fringe field for all beam orbits must satisfy the condition $|P|<5$ m$^{-1}$,

S7. The end magnet must provide the reflection of the trajectory of electrons with the energy $E_0$= 2 MeV (after the first acceleration) back to the axis of the accelerating structure, i.e. $\Delta_0$=0,

S8. The displacement of the next orbit trajectory $\Delta_1$ with the particle energy $E_1$=4 MeV with respect to the accelerating structure axis must be $\Delta_1 > 2.6$ cm.

Specifications S1-S5 follow from the requirement that the electrons follow the reference trajectory determined from beam dynamics calculations. Fulfillment of condition S6 guarantees that the beam motion is stable in the vertical plane. In fact it means that the focal length $P^{-1}$ of the end magnet fringe field focusing is longer than the distance $L$=20 cm between the end magnets of the RTM (see Fig. 50). Requirement S7 is due to the use of a low energy injection scheme with beam reflection back into the accelerating structure as it was explained previously. Finally, specification S8 is the condition of bypass of the resonant cavities by higher orbit trajectories. According to the accelerating structure design [47] the 4 MeV orbit passes through its body along a specially machined channel. The radius of the cavities is equal to 0.38 λ = 1.98 cm, the radius of the channel is 4 mm. Thus, allowing for a minimal thickness of the wall between the cavity and the channel equal to about 3 mm, the minimal displacement of the 4 MeV orbit turns out to be $\Delta_1$=2.68 cm = 0.51 λ.

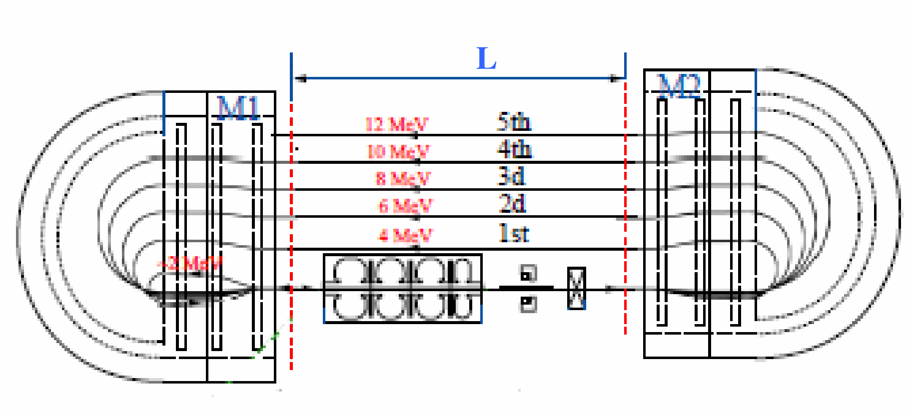

Figure 50: RTM dimensions.

In the design calculations we essentially followed the steps listed below:

(1) Selection of the magnetic system design and its main features (number of poles, material, geometry of the poles, yoke and REPM blocks, etc.).

(2) 2D simulations of the magnetic field distribution in the longitudinal and vertical directions using, for example, the POISSON code [86].

(3) 3D simulations and design optimization using the results of the 2D simulations as the initial configuration. This allows to obtain the magnetic field distribution of the whole magnet taking into account the edge effects, magnetic saturation effects, field non-homogeneities, etc. In the present thesis the ANSYS code [87] was used.

We would like to make a few comments. In principle the RTM end magnet must not depend on the transversal horizontal coordinate so that the magnetic field is essentially two-dimensional, i.e. depends on the longitudinal and vertical coordinates only. However the geometry of the box-type design, that will be implemented, and the use of REPM blocks introduce a non-negligible dependence on the transversal horizontal coordinate that must be taken into account, therefore 3D simulations become necessary. On the other hand, performing the design and its optimization using a 3D code from the beginning would be too time consuming because such procedure would require making numerous iterations that include changes of the 3D geometry. Instead of this, it was decided to use the well known analogy between the magnetostatics and electrostatics to calculate the fringe field distribution with the 2D POISSON code [86]. In this approach one assigns to the poles some relative potential with respect to the yoke and sets the field of the main pole to the design value. This allows to get the magnetic field distribution along the trajectory. These simulations are followed by a calculation of the particle trajectories with the RTMTRACE code. On the basis of the results of the beam dynamics simulations parameters of the magnetic system are adjusted and the 2D simulations of the field are carried out again. This procedure is repeated iteratively until the required beam dynamics is obtained, for example the 2 MeV orbit closure and the optimal end magnet focal power are achieved. Finally, parameters of REPM blocks (dimensions, residual magnetization) generating the corresponding pole potential are calculated using the known approach [66]. This final 2D design is the initial approximation for the subsequent 3D simulations.

As a result of the study a design proposal will be presented with all necessary parameters calculated. Ideally the design and manufacturing of the magnets should be finished by experimental measurements of the magnetic field distributions in X-, Y- and Z-directions and checking whether the design specifications are fulfilled. The magnets of the UPC 12 MeV RTM are currently at the stage of manufacturing, therefore results of their measurements are not available yet.

### 4.1.2. – 2-pole end magnet design.

With the aim to have compact 180º bending magnetic systems that can be placed in vacuum it was decided to use REPM material as a source of the magnetic field. From the discussion in Ch. 2 it is clear that for a simple dipole it is not possible to fulfill requirements S6 and S7 of the list of specifications in the previous section. Therefore, as the first proposal, it was decided to consider a magnetic system of box-type design (see Ch. 3) [77] consisting of two dipoles, a main 180º bending dipole and a narrow dipole of inverse polarity [27]. Such system was successfully implemented at the SINP 70 MeV RTM [27]. For a proper choice of the inverse magnetic field, distance between the dipoles and other parameters it provides beam reflection of the lowest energy orbit and reduces the fringe field vertical defocusing to an acceptable level. For the sake of simplicity here and in the following sections we will refer to the system with two dipoles as to 2-pole system assuming that it includes the main pole and the inverse pole.

From dedicated beam dynamics simulations using the RTMTRACE code it was obtained that the following additional specification must be taken into account [66]:

**S9.** For the inverse dipole the field uniformity in the median plane in the X-direction inside the internal region (region beginning at the distance 15 mm from the pole edges) must be better than 0.5%.

First we will consider a simple hard edge model which will allow us to understand main features of the end magnet, after this results of 2D simulations with the POISSON code will be discussed. We will show that the 2-pole design of the end magnet is not satisfactory and therefore an alternative design will be studied.

### 4.1.2.1. – Simple analytical model of the 2-pole end magnet.

To understand main features of the 2-pole end magnet we consider a simple model shown in Fig. 51 in which the dipoles are approximated by hard edge magnets. It is characterized by the following parameters: the magnetic field value of the main pole $B_0 > 0$, the magnetic field of the inverse pole $B_1<0$, the thickness of the inverse pole $d$ and the distance between the center of the inverse pole and main pole $Z_1$. Let us also introduce the parameter $k=(-B_1)/B_0=R_0(E)/R_1(E)$, where $R_0(E)$ and $R_1(E)$ are the radii of the trajectory of an electron with energy $E$ in the field of the main and inverse poles, respectively.

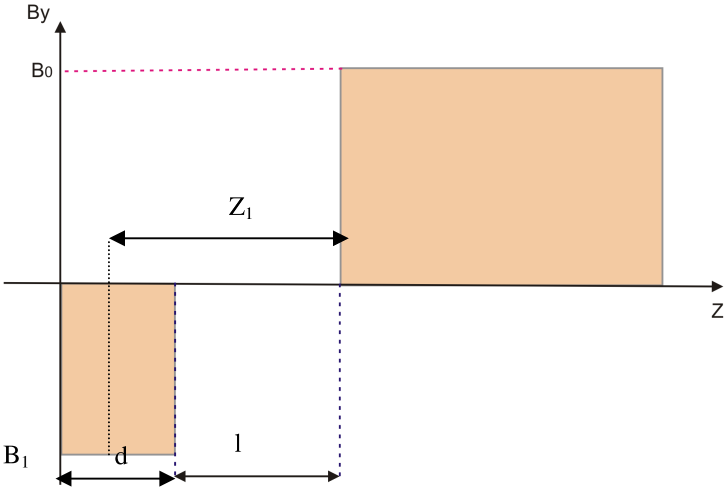

Figure 51: Magnetic field profile of the hard - edge model.

Let us consider first the condition of the reflection of the trajectory of the electrons with the energy $E=E_0$=2.536 MeV. Here we assume that the electrons are emitted from the electron gun with the kinetic energy $K_{inj}$=25 keV and that the energy gain of the reference particle in one passage through the accelerating structure is $\Delta E_s$=2 MeV. Suppose that the inverse pole width $d$ is fixed. For any value of the inverse pole magnetic field $B_1$ from a certain interval (see below) one can adjust the distance $Z_1>d/2$ in such a way that the condition of the trajectory reflection $\Delta_0 \equiv \Delta(E_0) = 0$ is fulfilled. Using Eq.(56) for the trajectory displacement in a 2-pole system and solving the equation $\Delta_0 = 0$ one obtains the relation for $Z_1$ as a function of $k$:

$$Z_1^*(k) = \frac{d}{2} + \frac{R_0^2}{kd}\left[\left(1+\frac{1}{k}\right)\left(1-\left(\frac{kd}{R_0}\right)^2\right) - \frac{1}{k}\sqrt{1-\left(d\frac{k}{R_0}\right)^2}\right] \tag{103}$$

This formula makes sense for $0 < k < k_{\max} = -(R_0(E_0)/d)\sin\alpha^*$, where $\alpha^*$ is given by Eq. (48) in Sect. 2.3.2. For larger values of $k$, i.e. larger values of the magnetic field of the inverse pole $|B_1| = kB_0$ with respect to the main pole field, the trajectory bends too much in the inverse pole and the particles cannot be reflected back with $\Delta_0 = 0$ by the magnetic system. Two examples with *d*=0.568 cm and $R_0 = 1.04$ cm (this corresponds to $B_0 = 0.797$ T) are given in Table 7, these are the cases of interest for the RTM end magnet design.

Table 7: Examples of the values of k and $Z_1$ in the hard edge model.

| $Z_1$, (cm) | 2.0 | 4.25 |
|---|---|---|
| $k=\lvert B_1\rvert/B_0$ | 0.57 | 0.3 |

For the case of reflection of the 2 MeV electron trajectory back into the accelerating structure, i.e. $\Delta_0 = 0$, we calculate the displacement of the orbit with $E=E_1$=4.536 MeV by means of the following formula

$$\Delta_1^* \equiv \Delta(E_1)\Big|_{Z=Z_1^*(k)} \geq 25.0mm \tag{104}$$

where the displacement determined by Eq. (56) is evaluated for the distance between the poles given by Eq.(103). The plots of $Z_1(k)$ and $\Delta_1^*$ as functions of the parameter *k* are shown in Fig.52. They give a qualitative illustration of the behavior of these characteristics. This hard edge model of course does not describe the beam defocusing produced by real end magnets. The more realistic case with the fringe fields taken into account is studied in the next section.

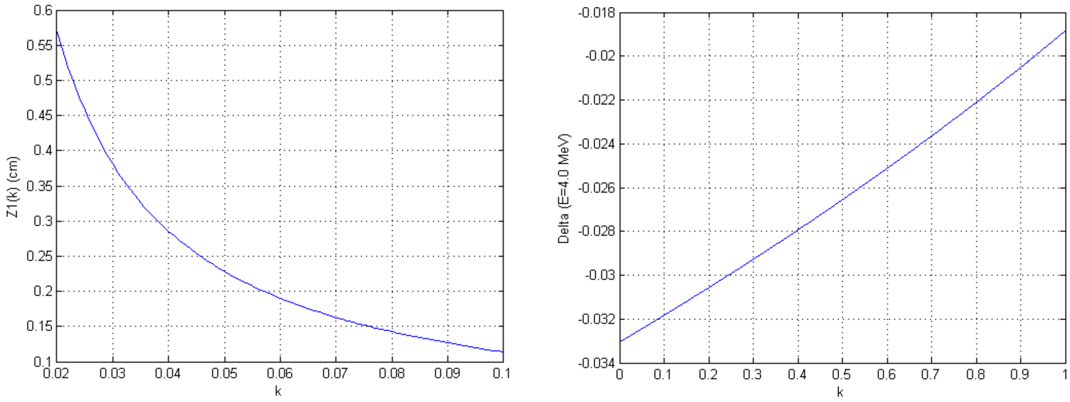

(a) (b)

Figure 52: Plots of the (a) $Z_1(k)$ and (b) $\Delta_1^*$ as functions of *k* for d=0.568 cm and $R_0 = 1.04$ cm.

### 4.1.2.2. – 2D simulations of the 2-pole end magnet.

The initial version of the 2-pole design of the end magnet, shown in Fig. 53, was proposed in [66]. In the version studied here the inverse pole width was decreased to 5 mm, while the height of the gap between the poles was maintained equal to 10 mm. The design study consists in considering a set of configurations with different positions of the inverse pole with respect to the main pole in the longitudinal direction, i.e. with different values of $Z_1$. For each pole position $Z_1$ the ratio of the potentials $V_1/V_0$ is adjusted in a sequence of iterations in order to provide the 2 MeV orbit closure. Here $V_1$ and $V_0$ are the inverse pole and main pole potentials in the electrostatic approximation, respectively. This step is performed by consequent 2D simulations of the magnetic field distribution with the POISSON code and calculations of beam trajectories using the RTMTRACE code. Once the relative potential $V_1$ of the inverse pole and therefore its magnetic field amplitude $B_1$ are fixed we calculate the focusing power of the magnetic system and the distance of the 4 MeV orbit $\Delta_1$ from the common axis. To get the focusing power $P$ we set a test particle in the RTMTRACE input file with the displacement $y_0$=1 mm off the median plane and slope $y_0' = 0$ at the magnet entrance, and calculate the slope $y'$ of its trajectory at the magnet exit. Then $P$ is obtained from the equation $P = -y'/y_0$. The pole potential and the magnetic field in the median plane are related by the following formula

$$V_i = \frac{gB_i}{2\mu_0} \qquad (i=0,1), \tag{105}$$

where $g$ is the gap height, $\mu_0$ in the vacuum magnetic permeability and $B_0$ and $B_1$ are the magnetic fields in the median plane of the main and inverse poles, respectively. A typical 2D geometry used in simulations with the POISSON and the obtained potential distribution are shown in Fig. 55.

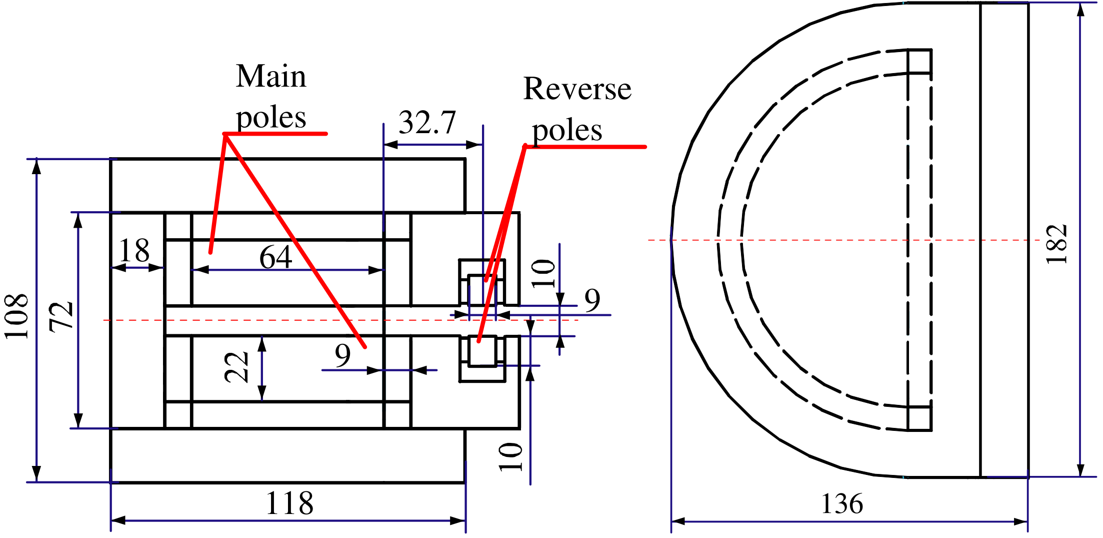

(a) (b)

Figure 53:Initial version of the 2-pole design of the end magnet of the UPC 12 MeV RTM [43].

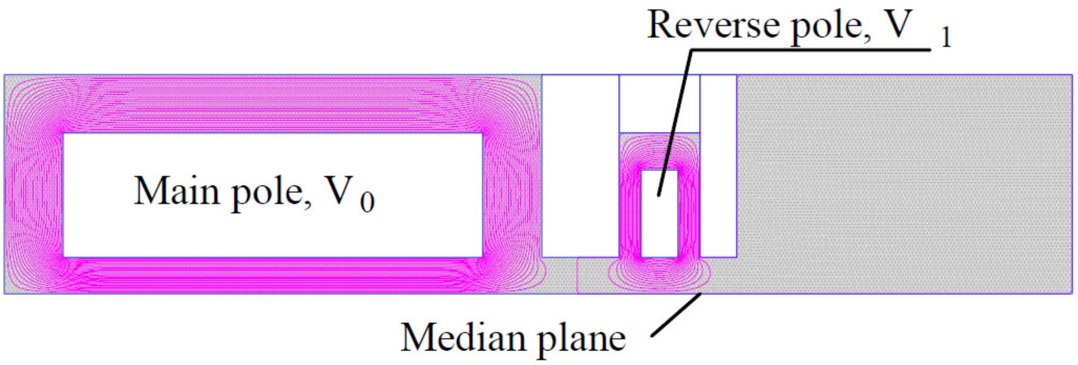

Figure 54: Typical 2D geometry, mesh and potential distribution calculated with the POISSON code.

In total 10 variants of the 2-pole end magnet have been studied. The values of the distance $Z_1$ from the inverse pole center to the main pole edge, the ratio of the electrostatic potentials $V_1/V_0$ in Table 8. As one can see by reducing the distance between the poles we have to increase the inverse pole field in order to produce the 2 MeV orbit closure. The magnetic field profiles in the median plane for these design variants are plotted in Fig. 55, examples of 2 MeV particle trajectories for variants V1 and V10 are shown in Fig.55.

Table 8: Parameters of the 2-pole end magnet design variants.

| | 1 | 2 | 3 | 4 | 5 | 6 | 7 | 8 | 9 | 10 |
|---|---|---|---|---|---|---|---|---|---|---|
| $Z_1$, (cm) | 2.00 | 2.25 | 2.40 | 2.50 | 2.55 | 2.75 | 3.00 | 3.25 | 3.75 | 4.25 |
| $V_1/V_0$ | 0.672 | 0.613 | 0.580 | 0.560 | 0.550 | 0.518 | 0.478 | 0.444 | 0.390 | 0.346 |

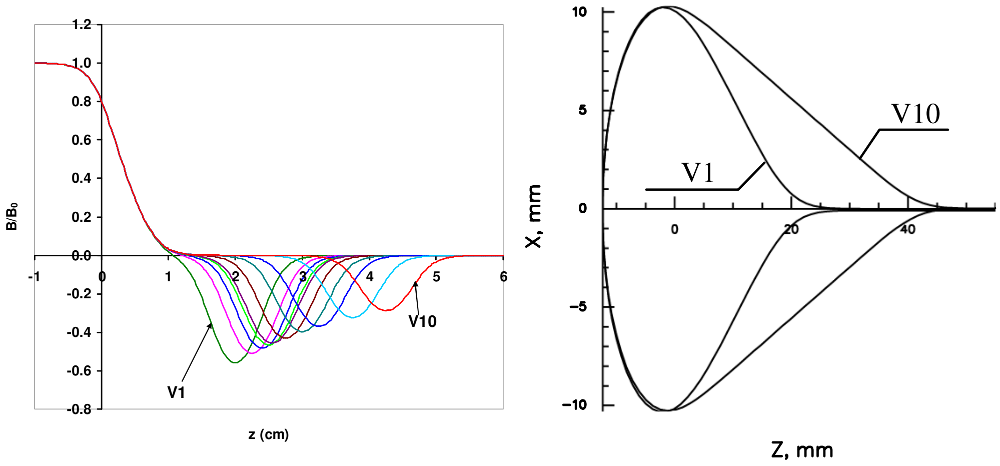

(a) (b)

Figure 55: (a) Magnetic field profile for different positions and field amplitudes of the inverse pole. (b) Trajectories of 2 MeV particles for V1 and V10 design variants.

The plots of the focusing power obtained in these calculations are given in Fig. 56. Analyzing 2 MeV particle trajectories in the end magnet field we conclude that decreasing the distance between the main and inverse poles and simultaneously increasing the inverse pole potential lead to the increase of the focusing power. One can see that for the V3 design the system provides acceptable focusing, i.e. the focal distance is about equal or larger than the distance between the RTM end magnets, at 2 MeV and too strong defocusing for the orbits of 4 MeV, 6 MeV and 8 MeV that would make vertical beam oscillations unstable. Contrary to this for the V10 design with $Z_I$=4.25 cm the focusing power satisfies the requirement $|P|<5$ $m^{-1}$ for trajectories with $E \geq 6$ MeV.

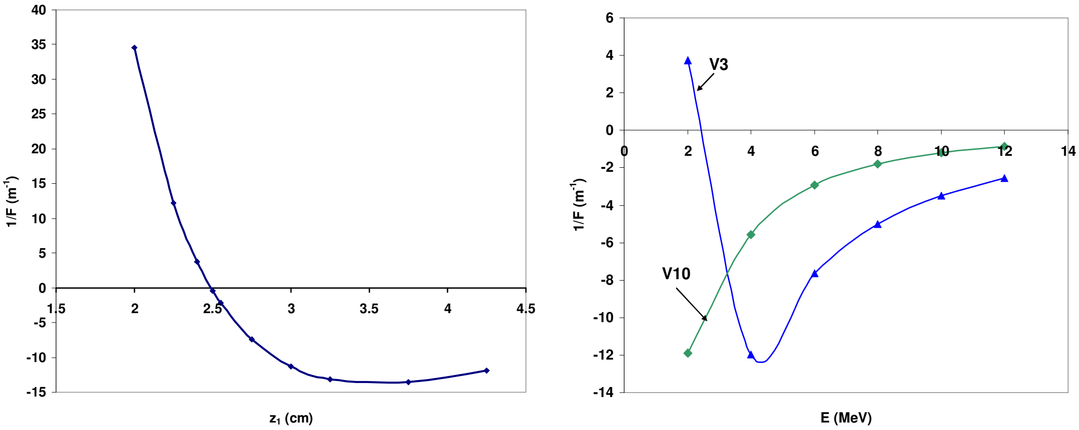

(a) (b)

Figure 56: (a) Focusing power dependence on the inverse pole position for $E_0 = 2$ MeV. (b) Focusing power dependence on the particle energy for V3 and V10 design variants.

Further increase of the distance $Z_l$ between the poles does not give satisfactory solutions. Indeed, as one can see from Fig. 56(a) the dependence of the focusing power on $Z_l$ is quite weak. In addition, the increase of the distance between the poles amounts to the growth of the distance between the two RTM end magnets, which in turn requires lower focusing power |P|. Thus, such modification of the end magnet parameters leads to large RTM dimensions and enters in contradiction with the requirement of compactness of the accelerator head of the UPC 12 MeV RTM. For these reasons it was decided to refuse from the idea to get the 2 MeV orbit closure and satisfactory beam optics for all energies with the same magnetic field profile generated by the inverse and main poles, and therefore abandon the 2-pole end magnet design and look for an alternative solution.

A few remarks are to the point. Firstly, in fact, from the numerical simulations and the considerations given above it is evident that the beam dynamics with stable vertical oscillations can be reached by increasing the distance $Z_1$ between the poles. A detailed analytical study of this issue within a model with linear approximation of the fringe fields is performed in Section 5.2. Secondly, the 2-pole scheme of the end magnet may work for accelerators with longer wavelength $\lambda$ of the accelerating RF wave, as it is the case of the SINP 35 MeV RTM with $\lambda$=10cm. The reason is that, as it was already explained above (see [66]), the radius of the lower energy orbit in the main pole field $R_0 \sim \lambda$ and the focal distance of the end magnet $F \sim R_0$, so that the focusing power turns out to be smaller.

We conclude this section with a plot of the displacement $\Delta_1^*$ of the 4 MeV orbit (see definition in Eq.(95)) as a function of $Z_1$ given in Fig. 57. One can see that $\Delta_1^*$ varies very slowly and for all design variants there is sufficient space in the horizontal transverse direction to install the accelerating structure. This plot is in qualitative agreement with the curves in Figs. 52a and 52b calculated within the hard edge model in the previous section.

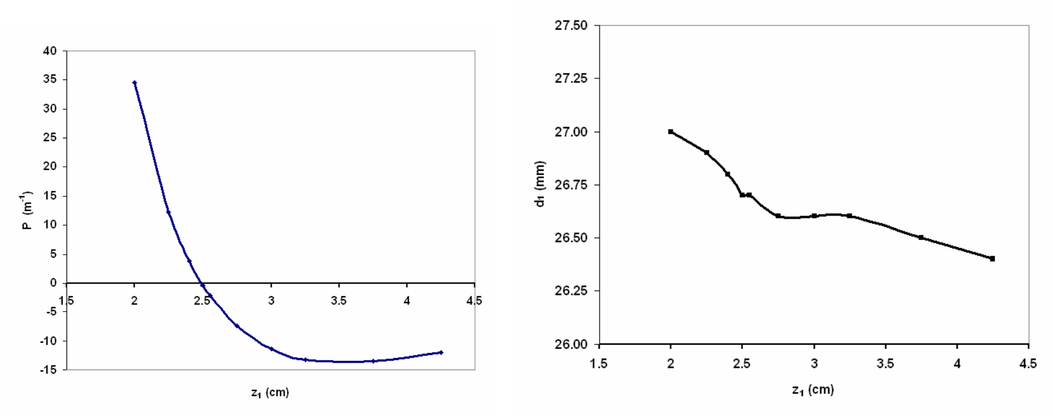

(a) (b)

Figure 57: (a) Focusing power of the 2-pole end magnet for the 2 MeV orbit and (b) the 4 MeV orbit displacement $\Delta_1$ as functions of the distance between the inverse and main poles $Z_1$.

### 4.1.3. – Four-pole design.

A known solution for reflecting the beam in an RTM end magnet after the first acceleration, implemented in several machines, consists in placing two identical dipole magnets with opposite field directions at the entrance to the end magnet [1]. Such scheme is shown in Fig. 26, where m3 and m4 are these additional dipoles whose function is to create the appropriate deviations of the incoming and outcoming particle trajectories so that the beam is reflected back to the axis of the accelerating structure. In this approach the problem of beam reflection is separated from the problem of the vertical beam focusing which can be solved by a specific field profile at the entrance to the main pole, as we will see below. However, this scheme has certain drawbacks. Firstly, though the additional dipoles with parallel pole edges do not produce net focusing in the horizontal plane they give rise to a focusing in the vertical plane with the focusing power dependent on the bending angle and fringe field form. To have a reasonably small focusing power the bending angle must be small enough, about 10º or less, that leads to a distance between the dipoles larger than 10 cm. Secondly, to compensate the beam displacement at the higher orbits caused by m3 and m4 magnets two identical dipoles m5 and m6 must be installed at the entrance to the other RTM end magnet (M1 in Fig. 26). As a result the distance between the end magnets is increased about two times as compared with the initial design proposal [66] that is not acceptable for a compact IORT RTM.

The new design proposal of the UPC 12 MeV RTM end magnets consists in combining the 2-pole system, considered in the previous section, and the two additional dipoles described above. In this way a system of dipole magnets with separated functions is obtained, namely the inverse pole will be responsible for the beam focusing whereas the additional dipoles (similar to m3 and m4 in Fig. 26) will provide the 2 MeV beam reflection. Taking the advantages of the REPM material as a field source all the dipoles will be combined together with the main 180º bending magnet in a single end magnet system thus forming a rather compact device.

From beam dynamics studies it was found that the following specification must be fulfilled:

**S10.** For the additional dipoles the field uniformity in the median plane in the X-direction inside the internal region (region beginning at the distance 15 mm from the pole edges) must be better than 0.5%.

### 4.1.3.1. – 2D simulations.

With the problems of the beam focusing and beam reflection back to the initial trajectory being decoupled, the focusing power of the whole system can be varied in a wide range, from focusing to defocusing, for a given distance $Z_1$ between the main and inverse poles simply by changing the inverse field amplitude.

To begin with we optimized the inverse pole potential for a design variant with minimal $Z_1$=2 cm, which corresponds to V1 in Table 2, in order to have a compact design (Fig.58, upper drawing) and adjusted the field $B_1$ with the aim to have an acceptable focusing properties (we call this variant V11). Then even more compact designs for which the main and inverse poles are not separated by steel wall were considered. We would like to note that in these cases the main pole fringe field affects the magnetic field of the inverse pole and this effect must be taken into account. As before, the study was performed iteratively by combining 2D simulations of the magnetic field profile with the POISSON code and beam dynamics calculations using the RTMTRACE code. The design variant, numbered as V12 and shown in Fig.58 (bottom drawing), was chosen as the basis for further simulations of the full system. It is characterized by the distance between the center of the inverse pole and main pole face, $Z_1 = 1.25$ cm, gap $g$ =12 mm and the distance between the inverse pole face and the yoke equal to 5.0 mm. Mind that the gap was increased in order to reduce fringe field aberrations and particle losses in RTM.

The magnetic field profile and the focusing power as a function of particle energy for V11 and V12 are shown in Fig. 59a and Fig. 59b, respectively. The 2 MeV particle trajectories in the horizontal and vertical planes for V12 are shown in Figs.60 (a) and 60(b), correspondingly.

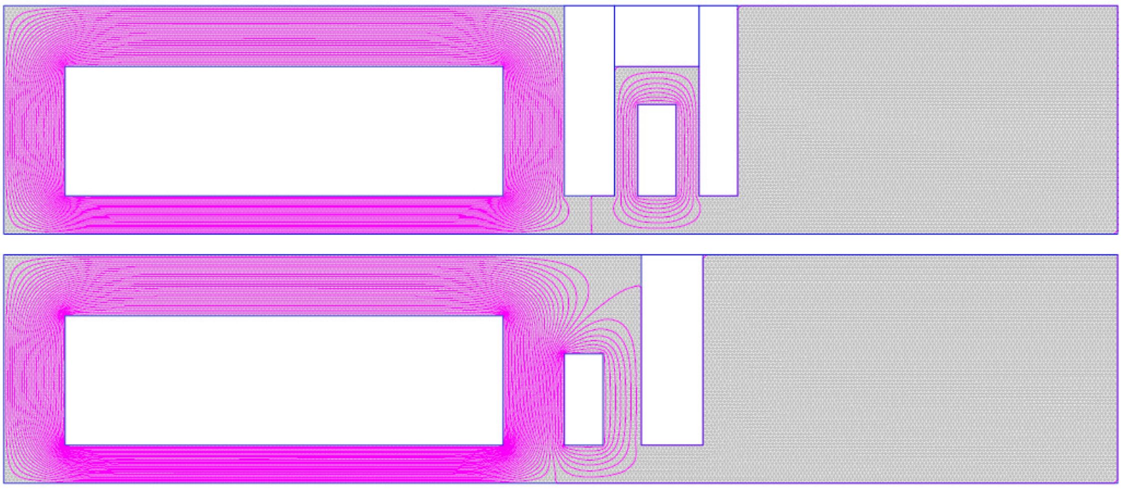

Figure 58: The 2D geometry, mesh and potential distribution for V11 (upper drawing) and V12 (bottom drawing) design variants.

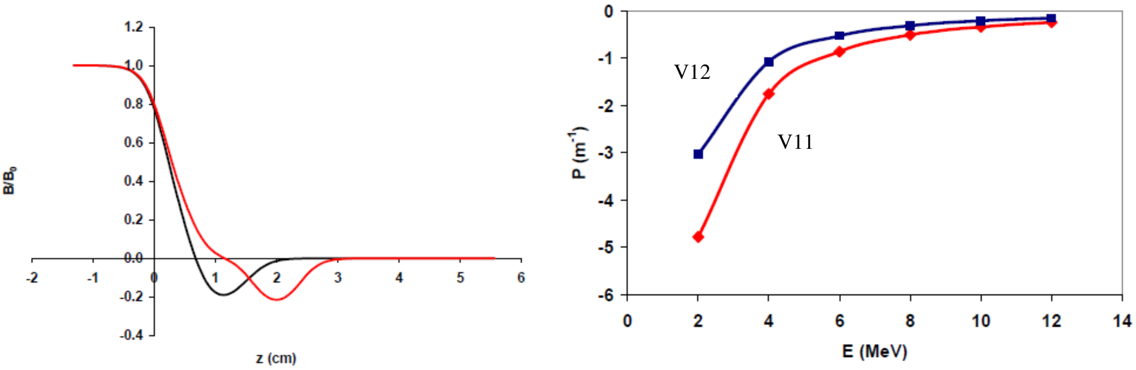

(a) (b)

Figure 59: The magnetic field profile (a) and the focusing power dependence on energy (b) for the V11 and V12 design variants.

As it can be seen from Fig. 60a the distance between the incident and reflected trajectories in the horizontal plane is 18.06 mm. It must be compensated by the two additional dipoles which form part of the 4-pole end magnet. To have a compact design we chose the distance between the dipole field maxima equal to 26 mm. By making a simple estimate one can check that for the dipole effective length 1 cm the bending angle for 2 MeV particles must be about $\theta \sim 20^0$ and the bending radius about $R_{dip} \sim$ 3cm. According to formulas (35)-(37) the dipole fringe field focusing power $P_{dip} = -\tan(\theta - \psi)/R_{dip}$ at the first dipole exit and second dipole entrance and $P_{dip} = \tan\psi / R_{dip}$ at the first dipole entrance and second dipole exit, where $\psi$ is defined by the dipole fringe field profile in the median plane. Thus the vertical plane focusing power strongly depends on the dipole fringe fields and for small $R_{dip}$ can be quite strong. Since after passing through the additional dipoles the beam enters into the inverse pole field at zero angle this focusing can be compensated by the main field defocusing which can be made strong enough by decreasing the inverse field amplitude.

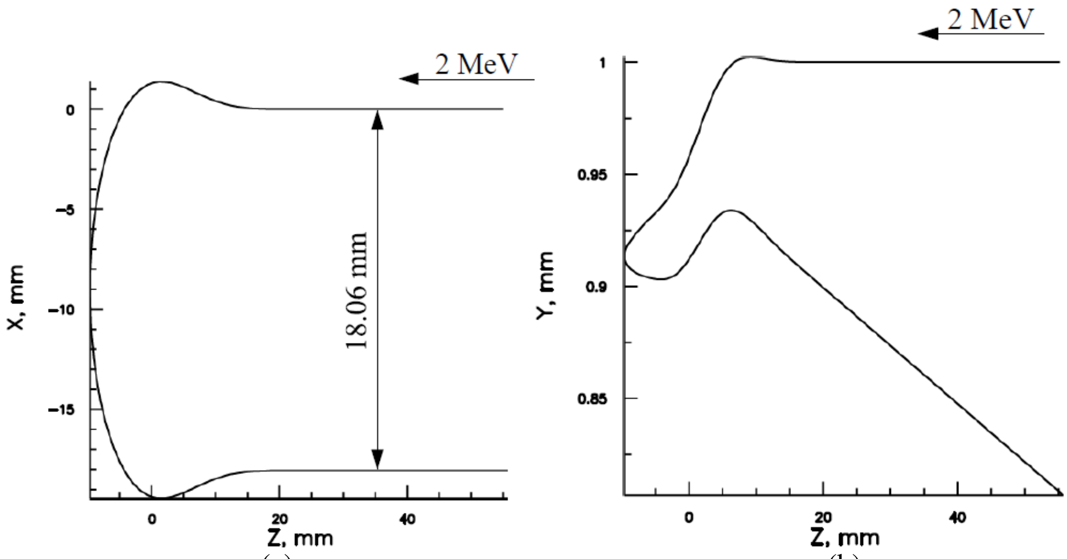

(a) (b)

Figure 60: The 2 MeV particle trajectories in the horizontal (a) and vertical (b) planes for the V12 design variant.

The 2D view of the 4-pole end magnet is shown in Fig.61. As a result of 2D simulations it was found that the optimal values of the pole potentials with respect to the main pole are given by the relations 1:-0.203:0.433:-0.433, the corresponding ratio for the field values in median plane for these poles is

$$B_0 : B_1 : B_2 : B_3 = 1:-0.144:0.330:-0.330 \tag{106}$$

The optimized fringe field profile is plotted in Fig.62. The positions of the centers of the inverse and two additional poles with respect to the main pole face are 12.5mm, 35.5mm and 61.5mm, respectively. Beam dynamics calculations with the RTMTRACE code confirm that for all energies in the range from 2 MeV to 12 MeV the absolute value of the end magnet focusing power does not exceed 5 $m^{-1}$. Also it was checked that the trajectory of 2 MeV electrons in the horizontal plane, shown in Fig.63, is reflected back to the axis of the accelerating structure and that the displacement of the 4 MeV trajectory is equal to $\Delta_1^* = 26.0\,\text{mm}$.

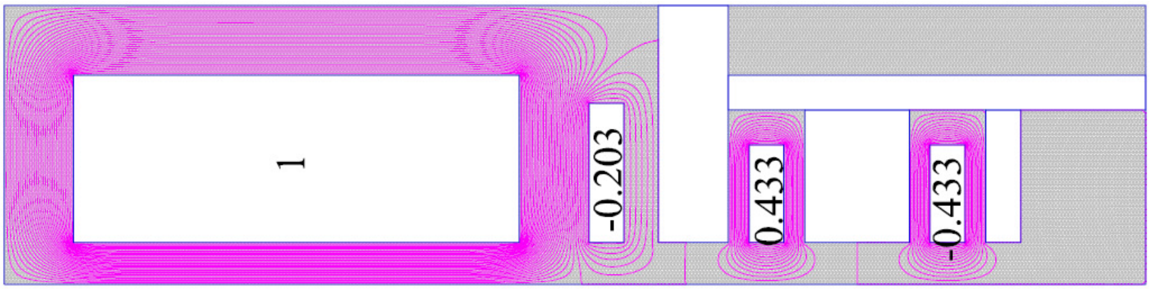

Figure 61: 2D geometry and potential distribution in the 4-pole end magnet. The relative values of the pole potentials with respect to the main pole are indicated.

The magnetic field obtained in the 2D simulations is created by blocks of the REPM material with certain magnetization placed around the poles. Parameters of these REPM blocks, for example the value and direction of the residual magnetization, can be related to the pole potentials using the method described in Refs. [56,78]. The obtained end magnet geometry is the initial approximation for the 3D design simulations.

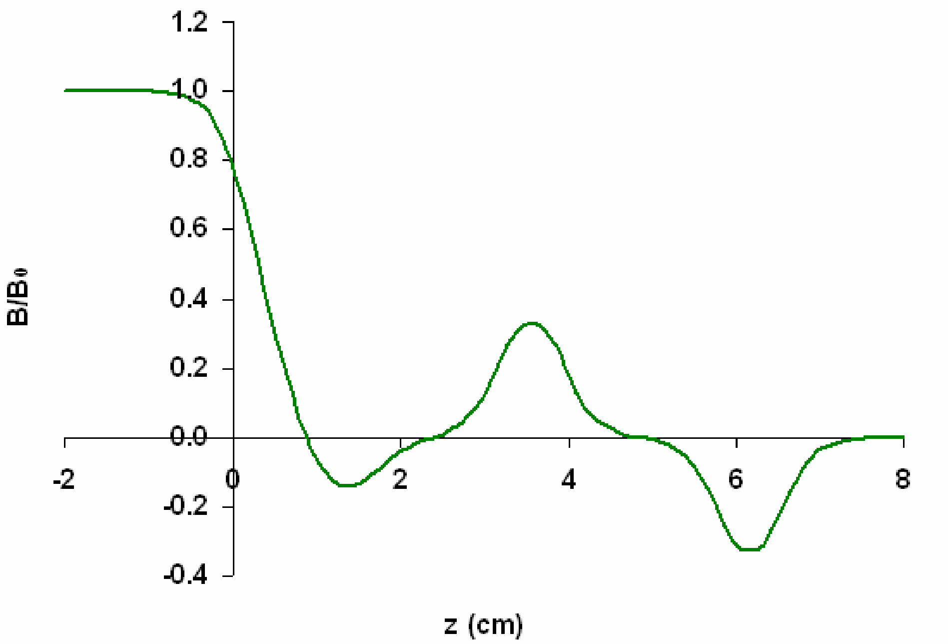

Figure 62: Profile of the magnetic field in median plane for the 4-pole end magnet obtained in 2D simulations.

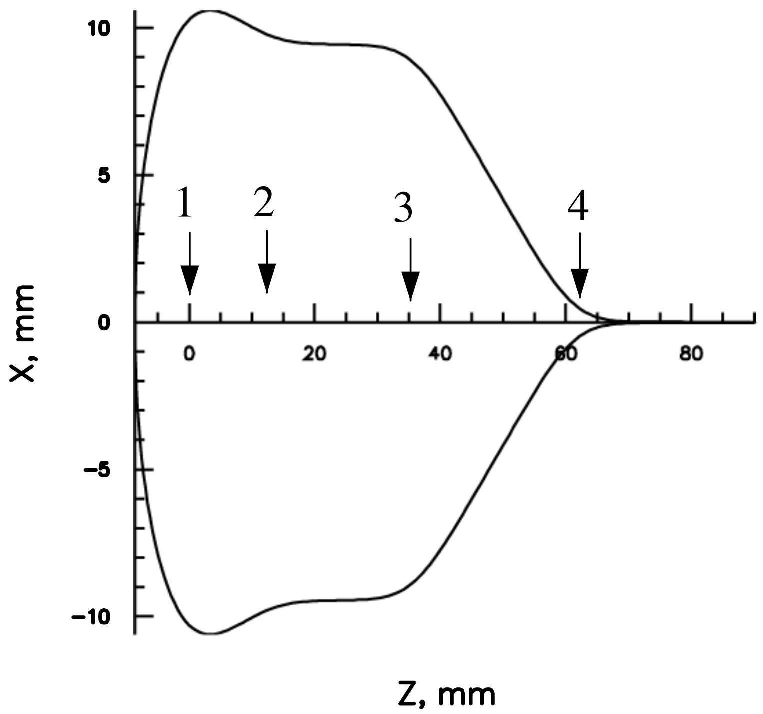

Figure 63: Trajectory of a 2 MeV particle in the median plane of the 4-pole end magnet. The numbers 1, 2, 3 and 4 indicate the position of the main pole face, the centre of the inverse pole and the centres of the two additional poles, respectively.

### 4.1.3.2. – 3D simulations.

The 3D simulations of the end magnet design optimization were performed using the magnetostatic package of the ANSYS code [87]. More details about the structure and capabilities of this code are given in Appendix 2.

An initial 3D model of the end magnet was set on the basis of the results of the 2D simulations and beam dynamics calculations and taking into account the general design considerations. Its dimensions are given in the drawings in Fig.64, the 3D geometry and elements determining the magnetic properties (the poles, REPM blocks and yoke) are shown in Fig.65. Due to the symmetry of the end magnet with respect to horizontal median plane and central vertical plane it is sufficient to describe only one quarter of the system. As a material of the yoke and poles Steel-1010 was considered. To refer to the magnet parts we have introduced the labels of the poles and REPM blocks as shown in Fig.65.

In order to get some intuition about the level of precision, that the ANSYS code provides, before launching the 3D simulations of the end magnets we carried out an exercise with a simple magnetic system.

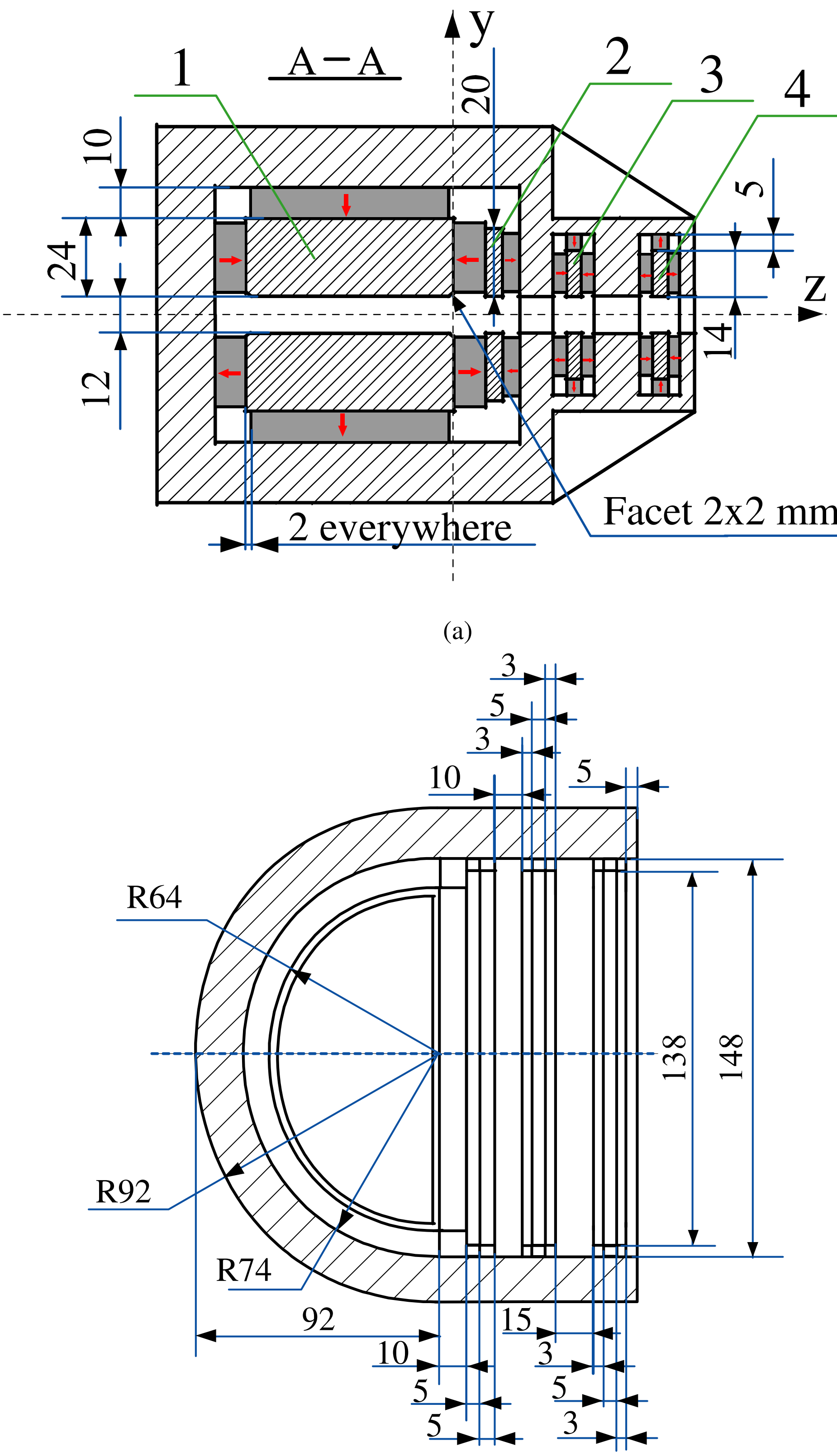

(a)

(b)

Figure 64: Schematic drawings of the 4-pole end magnet in the initial approximation: (a) side view; (b) top view. The elements indicated in the drawing (a) are: (1) main pole, (2) inverse field pole, (3) and (4) additional poles.

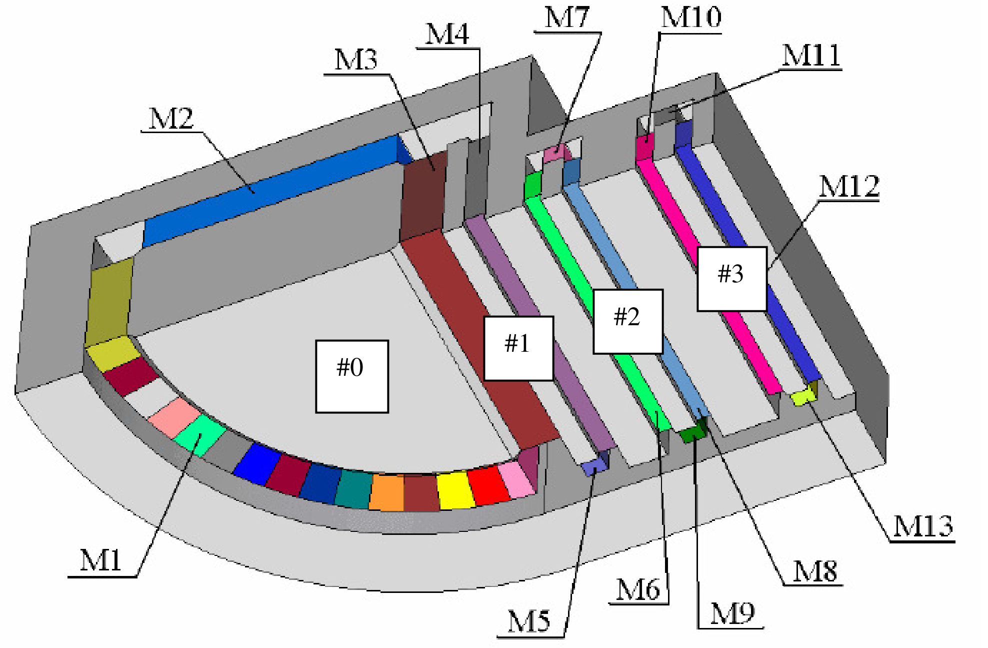

Figure 65: 3D geometry of the 4-pole end magnet geometry. Only one quarter of the magnet is shown. The numbering of the poles and permanent magnet blocks is indicated.

*a. – Comparison of ANSYS computations with analytic calculations for a simple magnet*

For this study we considered a pole-free magnet whose one-quarter part is shown in Fig.65. The magnetic field in the gap is created by two blocks of an REPM material surrounded by a steel yoke. For simplicity the thickness of the permanent magnet material block and the yoke are taken to be the same and equal to $D$. The half-height of the gap of the working aperture $g$=10 mm. The residual magnetization of the REPM material is $B_r = 1$ T, its relative magnetic permeability is $\mu_r = 1$.

The magnetic field of this magnet in the gap can be calculated using formula (84). The results for $B_{0,theor}$ for two values of $D$ are given in Table 9.

The field for the same cases was also computed numerically using the ANSYS code. In these 3D simulations the mesh size was chosen to be equal to 1.0 mm. The value of the magnetic field in the center of the median plane $B_{0,ANSYS}$ and relative error ε defined as

$$\varepsilon = (B_{0,theor} - B_{0,ANSYS}) / B_{0,theor}$$

are presented in Table 8. In the last line the errors of numerical simulations of the magnetic field estimated by the code itself are given. The obtained results give an idea of the precision that can be achieved in the 3D ANSYS simulations.

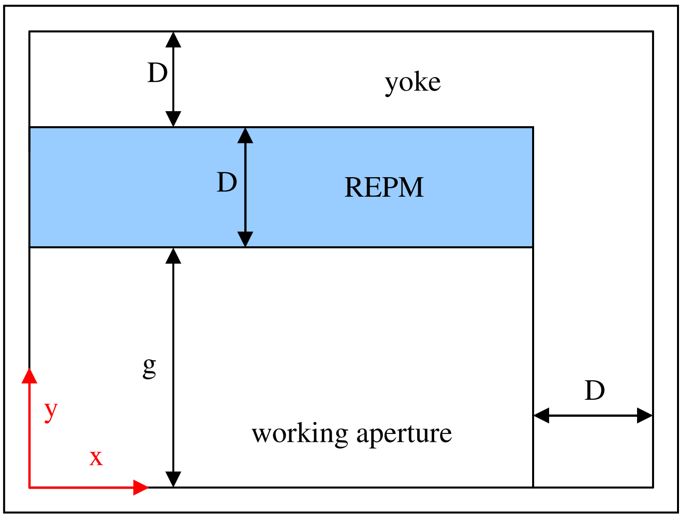

Figure 66: A simple pole-free magnet used for the comparison of ANSYS computations with the analytic formula.

**Table 9Table 9: Results of calculations of the magnetic field in the median plane obtained with the analytic formula and ANSYS code.**

| $D$ (mm) | 5.0 | 10.0 |
|---|---|---|
| $B_{0,theor}$ (T) | 0.333 | 0.5 |
| $B_{0,ANSYS}$ (T) | 0.326 | 0.4997 |
| Relative error ε | 0.021 | 0.0006 |
| ANSYS error estimate (T) | 0.003 | 0.005 |

*b. – 3D geometry and simulation characteristics.*

The design simulations with the ANSYS code followed a certain sequence of steps which are depicted in the diagram of the calculation process in Fig.67.

The initial 3D geometry introduced in the code is shown in Fig.68, the dimensions of the end magnet elements are given in Fig.64. Only a quarter of the full magnet was defined, the full magnet is recovered in the simulations by imposing the symmetry boundary conditions at the horizontal median XY-plane and central vertical YZ-plane. The orientation of the magnetization vector of the REPM blocks is as shown in Fig.64. In the case of the REPM material in the semicircular sector M1 the magnetization vector of each individual block is directed along the radius.

Taking into account the results of the simulations for the example considered above (magnet in Fig.65) as a general rule we have chosen mesh elements of the size equal of 1.0 mm (region 1 in Fig.68). For regions where higher accuracy of calculation is required, for example in the median plane of the end magnet (region 2), a finer mesh of the size 0.5 mm was introduced in the geometry input. A typical mesh over the whole magnet used in our 3D simulations is shown in Fig.68. For such mesh the typical calculation time of each simulation was about 5 hours. All simulations have been performed at a PC with Pentium (R) Dual-core 3.20 GHz processor and 4.0 GB RAM.

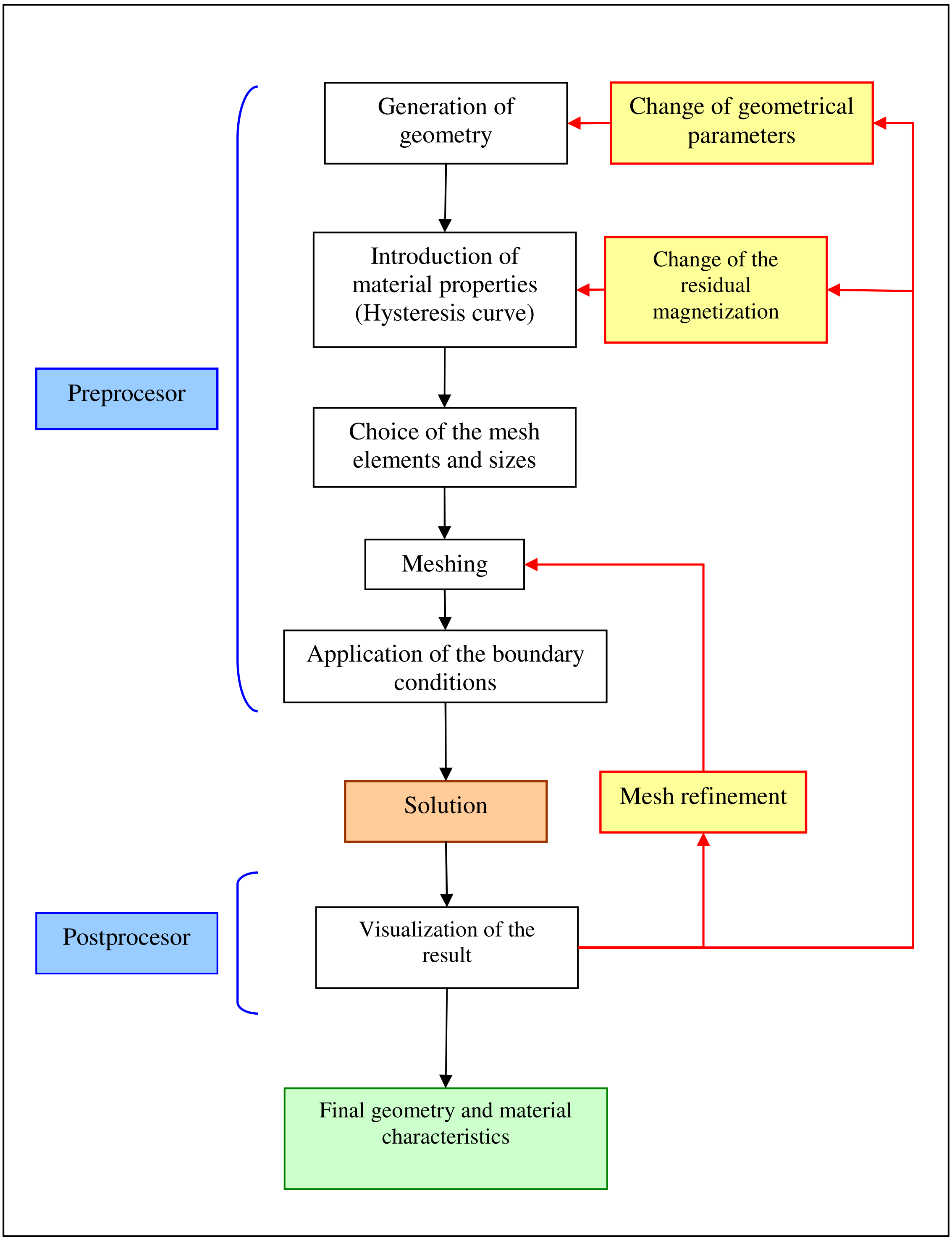

Figure 67: Diagram of the calculation process applied in the 3D simulations of the 4-pole end magnet with the ANSYS code.

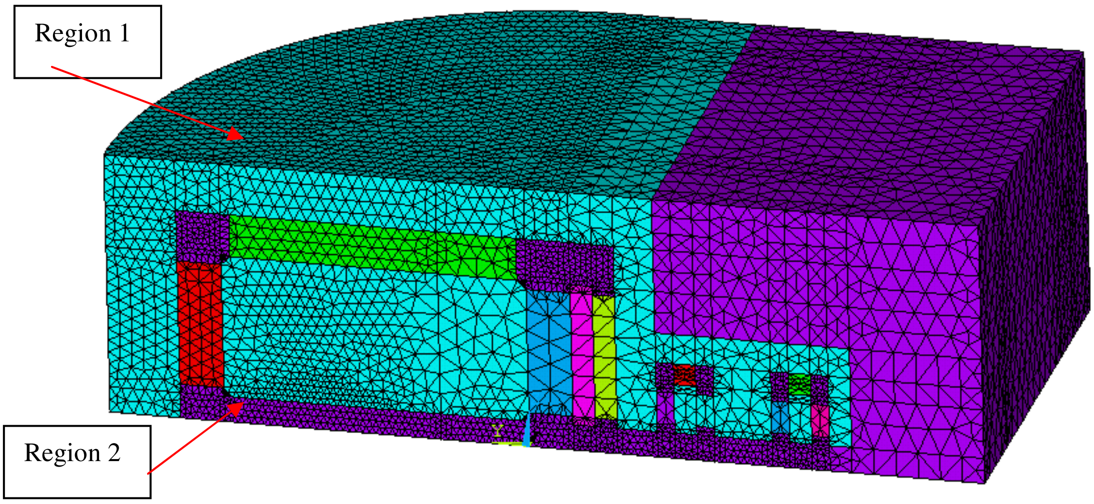

Figure 68: A typical mesh of variable size used in 3D ANSYS simulations.

*c. - Initial results.*

As the first step using the ANSYS we calculated the magnetic field distribution in the end magnet with the dimensions given in Fig.64 and REPM block residual magnetizations deduced from the electrostatic potentials obtained in the 2D simulations. The resulting values of the magnetic fields are

$$B_0:B_1:B_2:B_3 = 0.82264\text{T}:-0.10937\text{T}:0.24995\text{T}:-0.2472\text{T}. \qquad (107)$$

The vertical component $B_y$ of the field profile in the median plane and in the symmetry YZ-plane obtained in these simulations is shown in Fig.69. One can see that it differs considerably from the result of the calculations with the POISSON code, for example for the value of $B_y$ in the constant field region of the main pole the difference is about 3.0%. To obtain the magnetic field distribution prescribed by the 2D simulations we adjusted the dimensions of the poles and the residual magnetization of the REPM blocks.

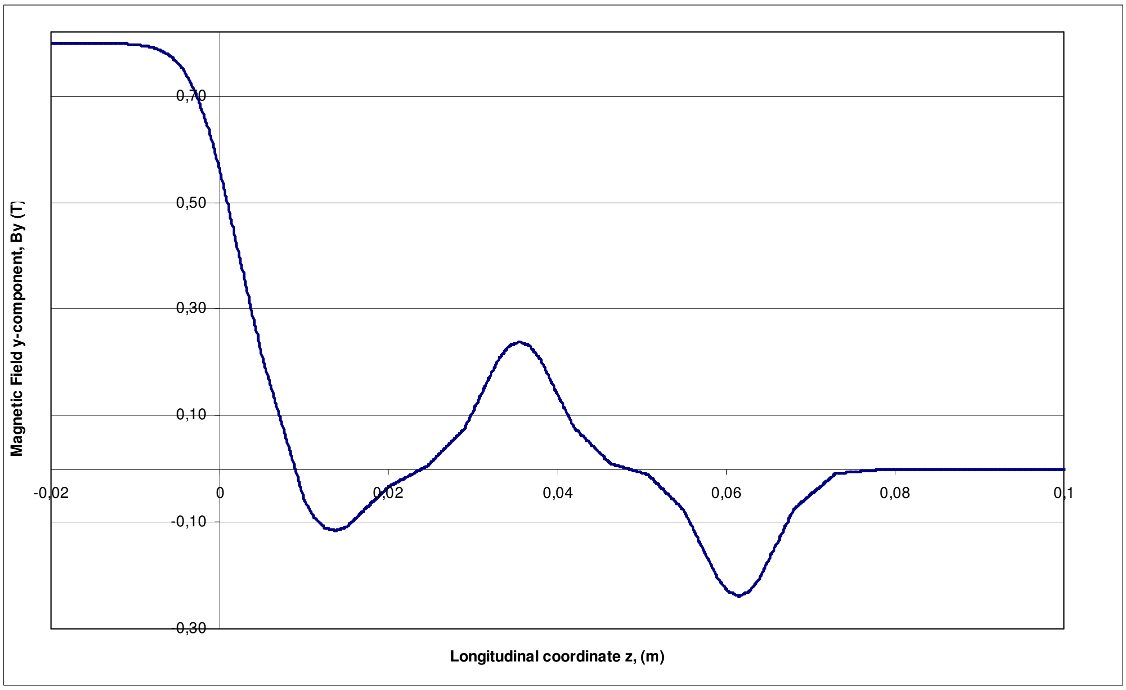

Figure 69: Plot of the vertical component of the magnetic field $B_y$ in the median plane in the centre of the magnet (YZ-plane) as a function of Z obtained in 3D simulations for the initial values of the 4-pole end magnet parameters.

*d. – Optimization of the end magnet geometry*

As a result of 3D simulations of the 4-pole end magnet and subsequent beam dynamics calculations with the obtained magnetic field distribution certain parameters of the initial design were modified with the aim to fulfill specifications S1-S10 listed above.

First of all it was found that for the main pole radius equal to 64 mm (as in Fig. 64) because of the edge effects the field uniformity in the region of the beam orbits is insufficient for the RTM operation without steering coils at the return paths. In particular, the field non-uniformity is a reason of an unacceptable bending angle deviation from $180^0$. For example, a deviation of the bending angle of about 10 mrad ($0.6^0$) would produce a beam displacement in the drift space between the end magnets equal to 2 mm approximately that would lead to a considerable beam current losses (recall that the diameter of the accelerating structure channel is 4 mm). According to performed estimates for the normal RTM operation the beam bending angle in the main pole must be $180^0 \pm 0.1^0$. In order to meet this design requirement it was decided to increase the main pole radius up to 69 mm. To achieve the required field level the height of the main pole was also increased.

After these changes the condition $\Delta_0 = 0$ of the 2 MeV orbit closure became violated. To get the field amplitudes at the additional poles #2 and #3 which provide its fulfillment the thickness of the REPM material blocks adjacent to these poles was increased from 3 mm to 4 mm. As a result the magnetic field profile along the Z-axis near these poles became wider and we were to decrease slightly the field amplitudes as compared with the result of the 2D simulations. The geometry and dimensions of the 4-pole magnet after optimization are shown in Fig. 70.

The final geometry of the 4-pole end magnet is shown in Fig.71.

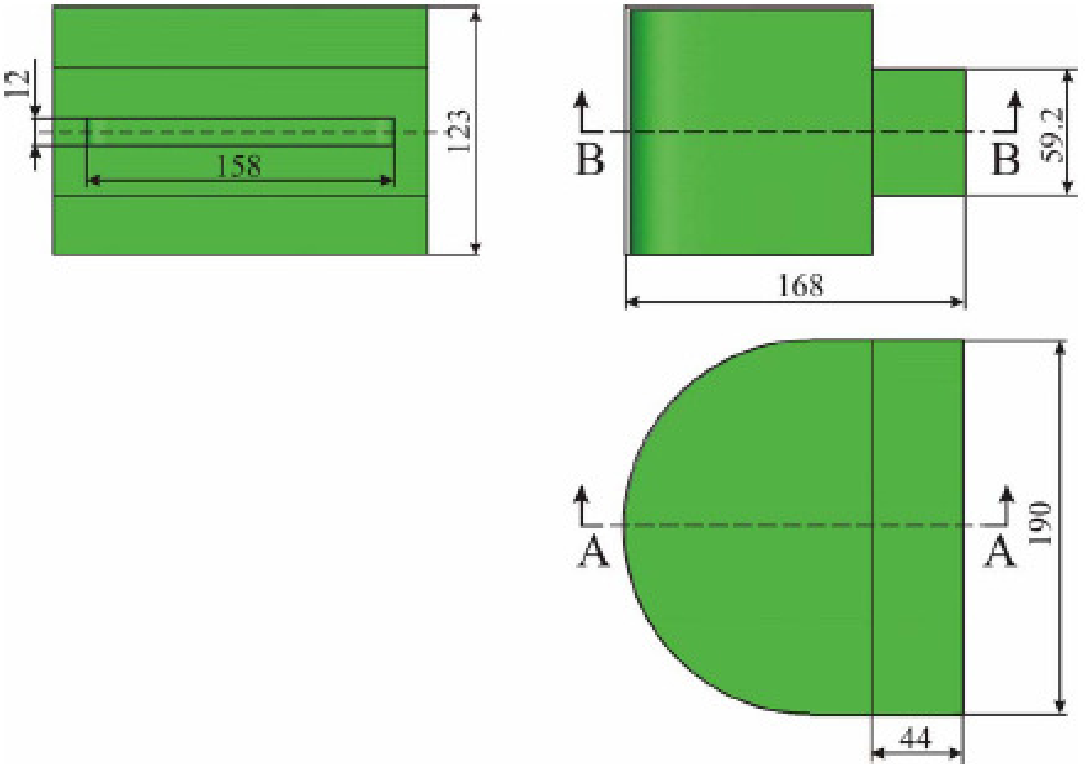

(a)

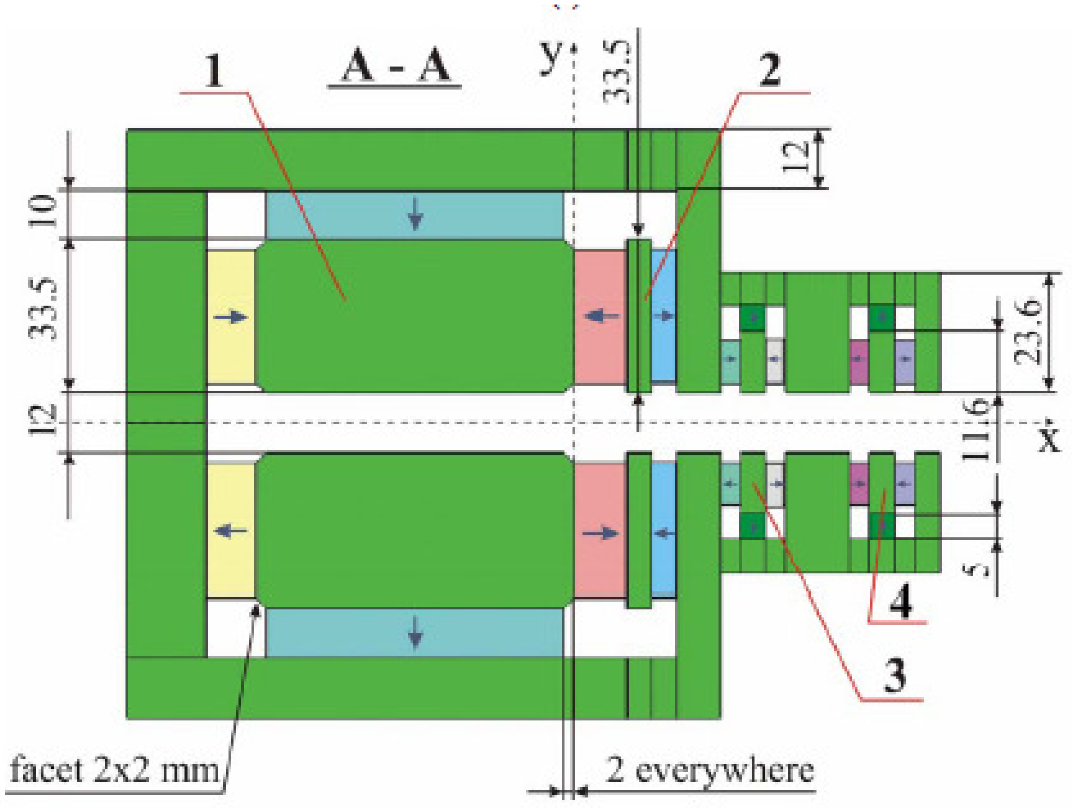

(b)

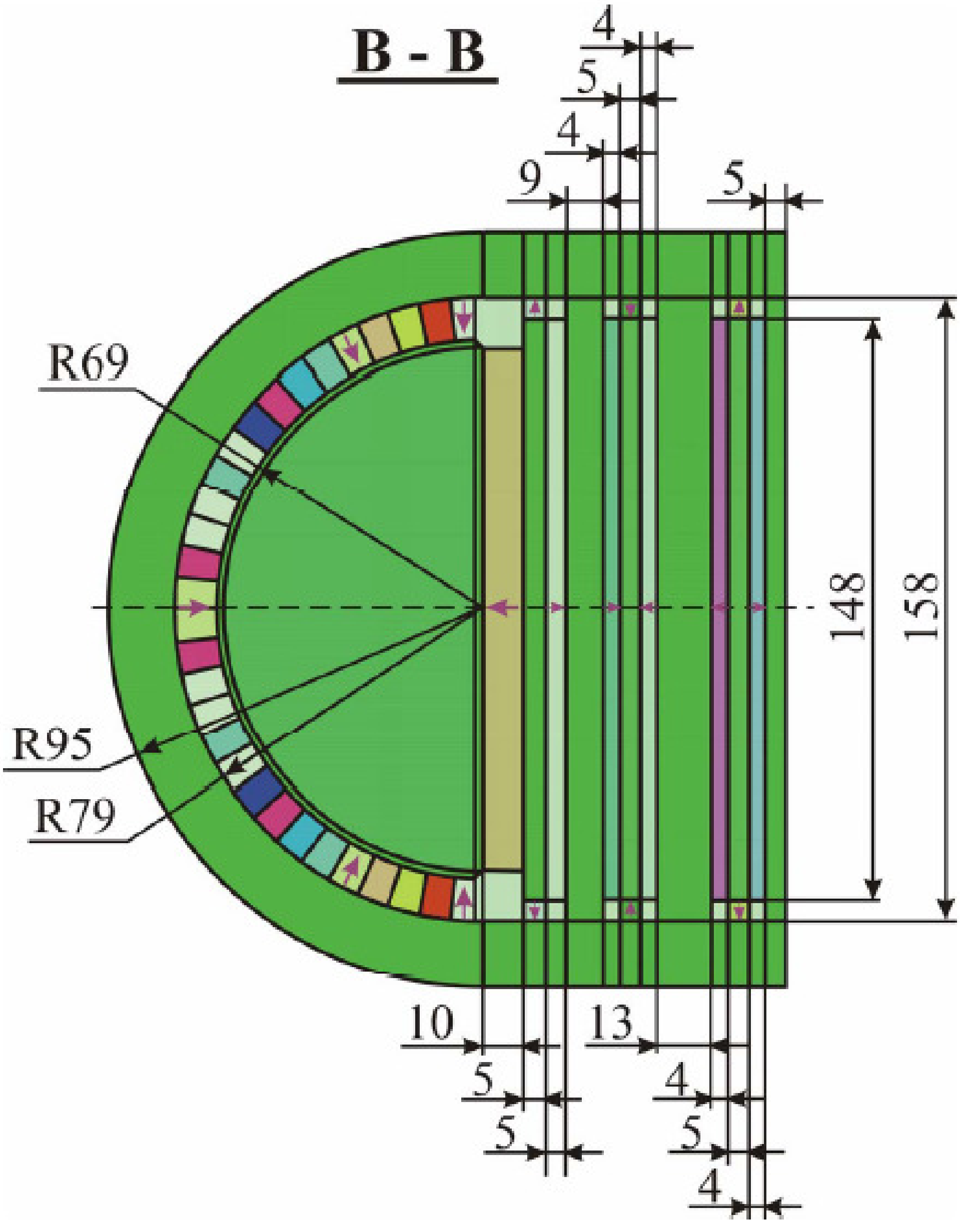

(c)

Figure 70: The geometry and dimensions of the parts of the 4-pole end magnet after optimization: (a) external dimensions; (b) cross section along the vertical central plane; (c) cross section in the median plane. All dimensions are given in mm.

*e) Adjustment of magnetic characteristics.*

Once the modifications of the end magnet geometry were made the magnetic characteristics of the REPM blocks, such as the residual magnetization $B_r$, magnetic permeability $\mu_r$ and the working point, were adjusted in order to reproduce the required magnetic field distribution in the median plane. This was done by iterative 3D simulations following the steps indicated in the diagram in Fig. 67. The final values of $B_r$ and the magnetic permeability $\mu_r$ are listed in Table 10. One can see that the residual magnetization of the REPM magnets M4 and M5 is close to zero. In fact it is easy to generate the required field level in the air gap near pole #2 without magnets M4 and M5. However it was decided to place these magnets in order to have some freedom in the adjustment of the field distribution.

Table 10: Parameters of the blocks of the REPM material obtained in the 3D simulations with the ANSYS code.

| Permanent magnet | Parameters | |
|---|---|---|
| | Permeability | Residual magnetization |
| | $\mu_{||}$ | $B_r$, T |
| M1 | 1.03 | 1.03 |
| M2 | | 1.03 |
| M3 | | 1.03 |
| M4 | | 0.087 |
| M5 | | 0.087 |
| M6 | | 0.9425 |
| M7 | | 0.9425 |
| M8 | | 0.9425 |
| M9 | | 0.9425 |
| M10 | | 0.9346 |
| M11 | | 0.9346 |
| M12 | | 0.9346 |
| M13 | | 0.9346 |

The final magnetic field in the median and vertical symmetry planes obtained in the 3D simulations is described by the $B_{sum}$ distributions shown in Figs.71 and 72, where $B_{sum}$ is the sum of the absolute values of the three components $B_x, B_y, B_z$. The field values for the main pole (pole #0, uniform region), center of the inverse pole (pole #1) and the centers of the additional poles (poles #2 and #3) are the following:

$$B_0:B_1:B_2:B_3= 0.7986\ \text{T} : -0.116\ \text{T} : 0.239\ \text{T}: -0.239\ \text{T} \qquad (108)$$

(compare to the ratio in Eq.(107) for the initial geometry). With respect to the main pole the ratio of the field values is: 1: −0.145:0.299: −0.299 which differs only slightly from the one in Eq.(106) obtained in the 2D simulations.

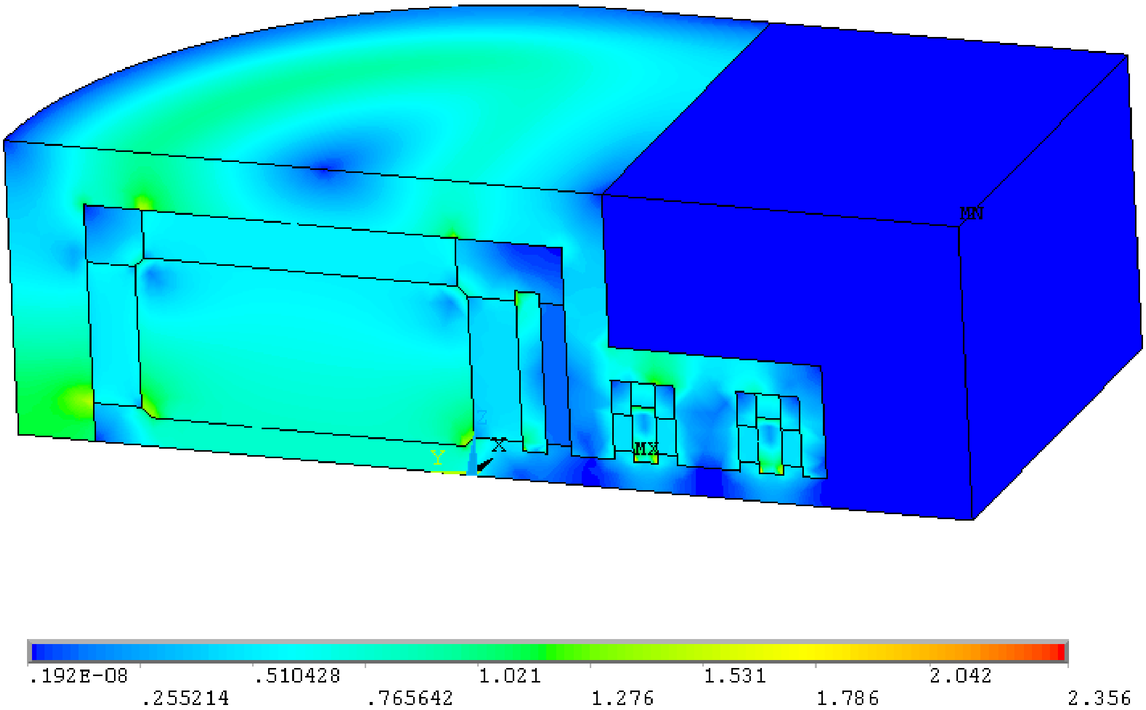

Figure 71: Magnetic field distribution $B_{sum}$ in the vertical symmetry plane of the end magnet.

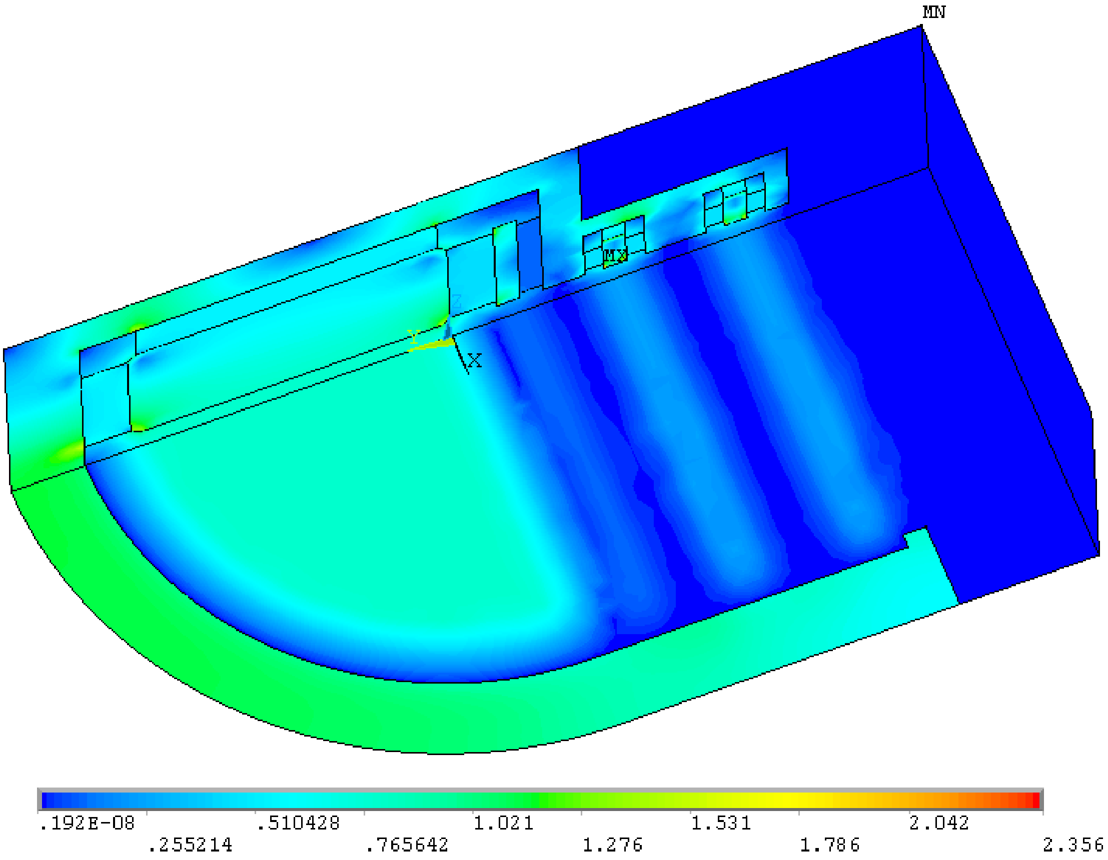

Figure 72: Magnetic field distribution $B_{sum}$ in the median plane of the end magnet.

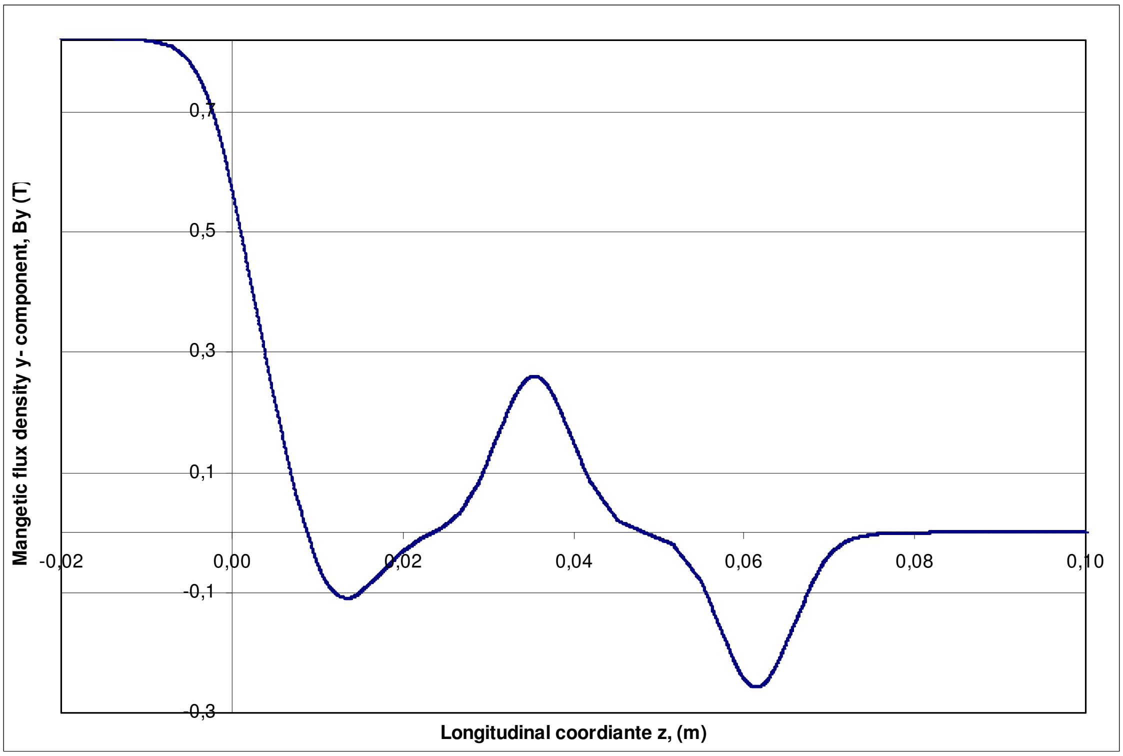

Figure 73: The plot of the vertical component of the magnetic field $B_y$ in the median plane of the 4-pole end magnet after the optimization of the residual magnetizations of the REPM blocks.

*f. Magnetic saturation of the material.*

It was checked in the 3D simulations with the ANSYS code that in the major part of the volume of the yoke and poles, for which the Steel-1010 material was used, the magnetic flux density was not exceeding the level of 1.2 T except a few regions where the magnetic saturation took place and which therefore require a design optimization.

Among these regions are narrow edge strips of the main pole and the yoke adjacent to the semicircular set of REPM blocks M1 (see Fig.74). In this volumes the magnetic field exceeds 1.5 T. In the zone of the tip formed by the semicircular face and the plane face of the pole it is as high as 2.2 T. The increase of the main pole radius up to 69 mm (see subsection *d* above) leads to the decrease of the field below the acceptable level in these regions.

Other regions of saturation are the tips of the poles which are shown inside the pink circles in Fig. 75. This problem is solved by cutting 1.0 mm x 1.0 mm chamfers at the ends of these poles. With this the maximum values of the magnetic field are reduced to an acceptable level, for example; as it is illustrated in Fig. 76, at the additional poles the magnetic field is reduced from 3.0 T to 1.3 T. In any case these regions are situated quite far from the zone of the of beam trajectories and therefore will not influence the beam dynamics.

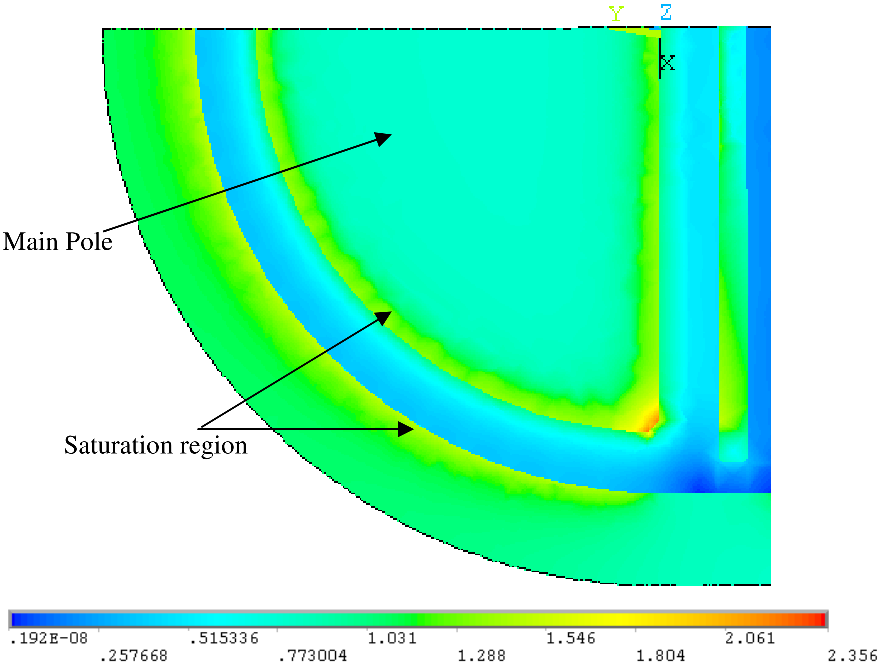

Figure 74: Magnetic field distribution $B_{sum}$ in the plane Y=8 mm parallel to the median plane of the magnet (xz-plane).

Finally, according to the 3D simulation results there is a region in the inverse pole where the magnetic field reaches values around 1.6 T as it can be seen in Fig.77. To avoid the magnetic saturation there it was decided to change the material of pole #2 from low carbon Steel – 1010 to Vanadium – Permendur whose limit of saturation is higher than that of the steel.

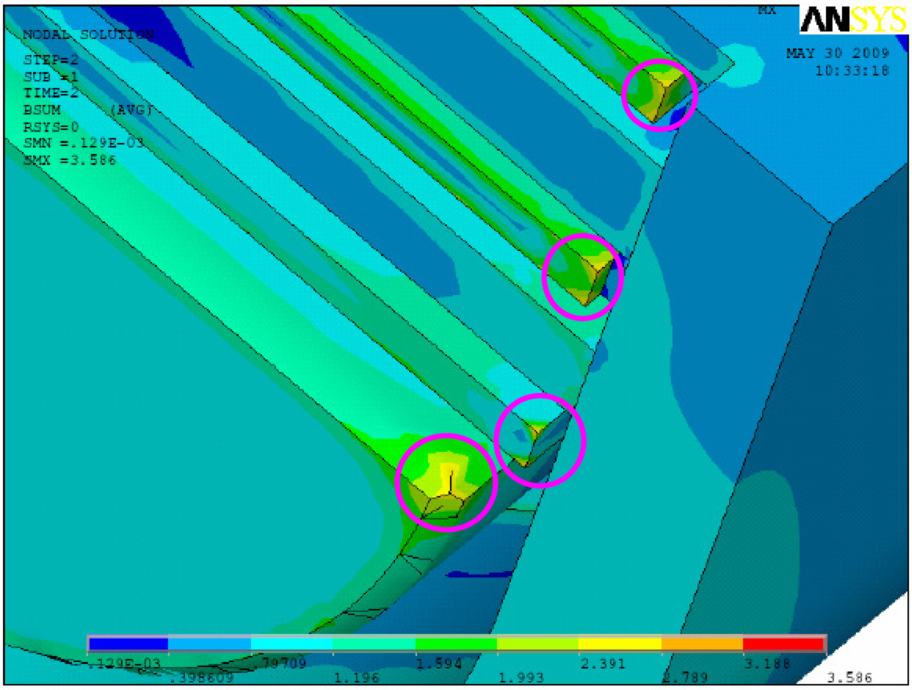

Figure 75: Regions of magnetic saturation at the tips of the poles.

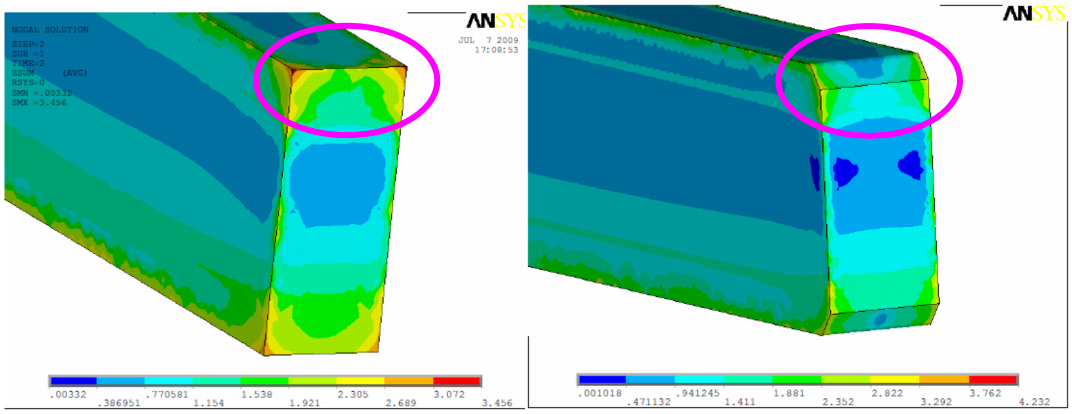

(a) (b)

Figure 76: Distribution of the magnetic flux density at the tip of the additional pole (a) without and (b) with a chamfer.

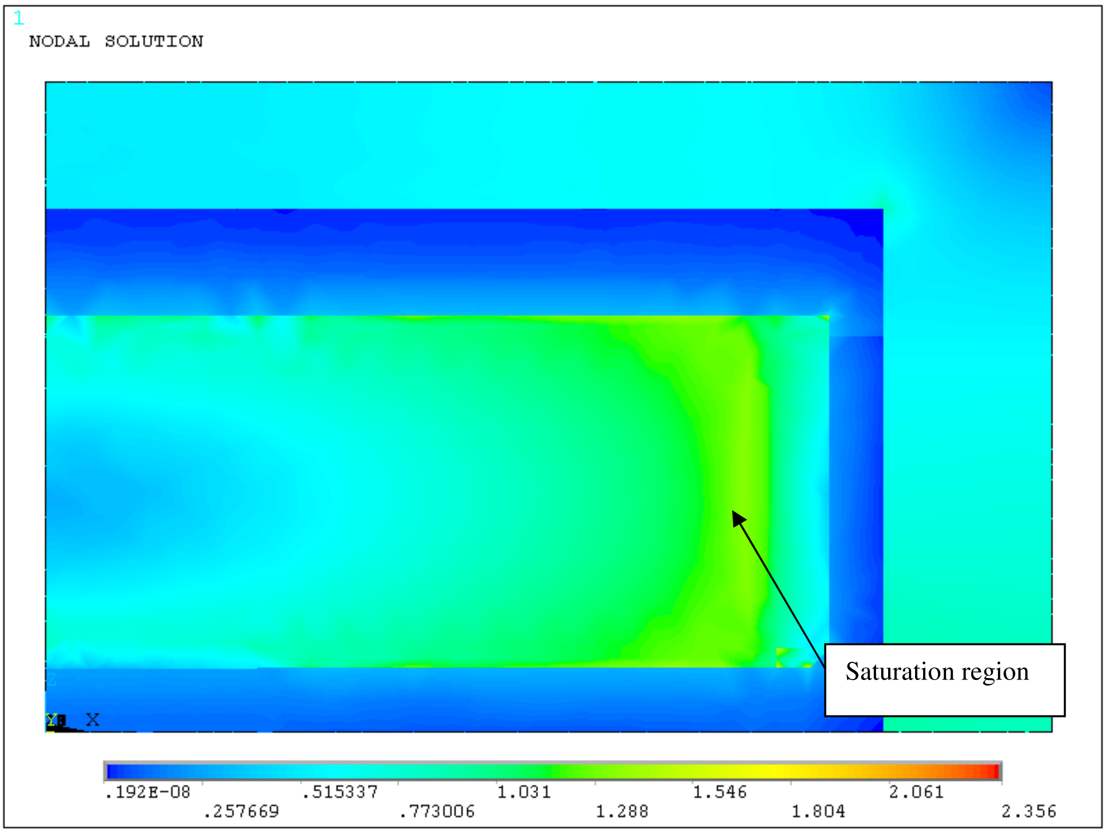

Figure 77: Magnetic field distributions inside de inverse pole and the yoke. The material used in the simulations is low carbon Steel – 1010.

### *g. Field homogeneity and stray fields.*

As it was already stated above the magnetic field distribution in the median plane of the end magnet must satisfy specifications S3, S9 and S10 of the field uniformity in the region of circulation of the particle beam.

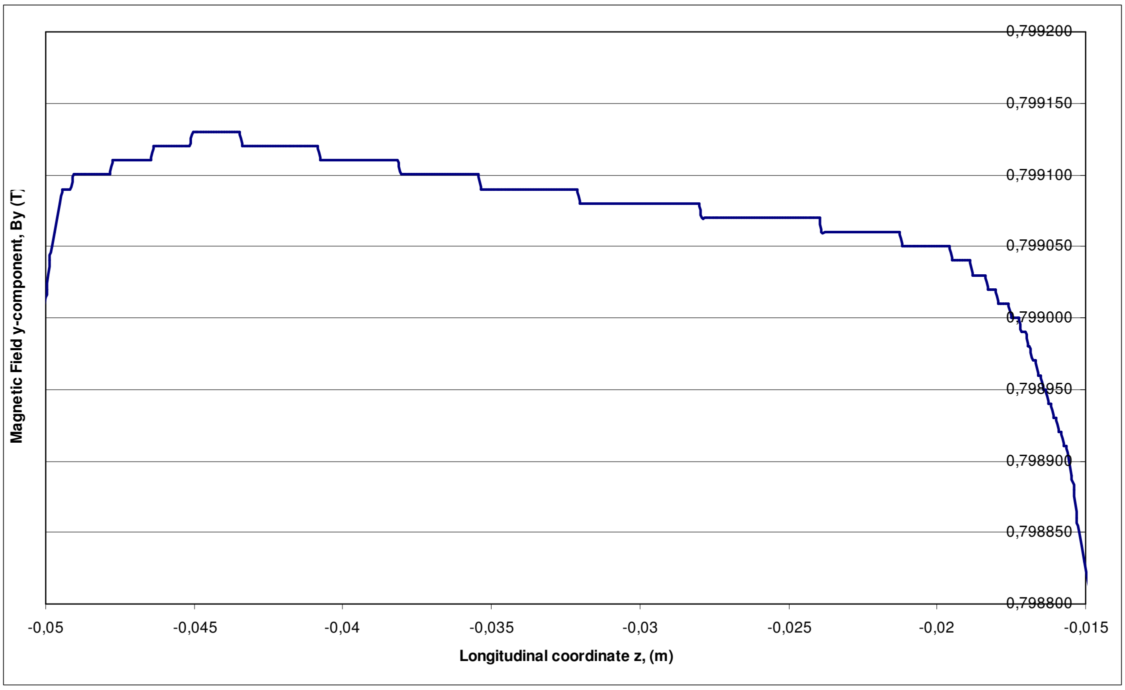

Figure 78: Variation of the vertical component $B_y$ in the median plane and vertical symmetry plane along the Z-axis inside the GFR.

In the case of the main pole this condition must be fulfilled inside the *good field region* (GFR) defined in Sect. 4.1.1. To check this requirement we considered various numerical characteristics calculated from the data obtained in the 3D simulations. Firstly, the vertical field component $B_y$ along the Z-axis in the range $-50.0\,\text{mm} \le Z \le -15.0\,\text{mm}$ for X=0, Y=0 was analyzed (see the plot in Fig. 78). Notice that this interval is situated inside the GFR. As one can see the maximal relative variation of the field is

$$\frac{\Delta B_0}{B_0} = 0.031\% \,. \tag{109}$$

Secondly, we studied the uniformity of $B_y$ in the median plane along the X-axis for different values of Z inside the GFR of the main pole. As an example in Fig. 79 the plot of the field $B_y$ as a function of X for Z=34.5 mm is shown. More examples are given in Table 11. One can see that the relative variation of the field satisfies specification S1.

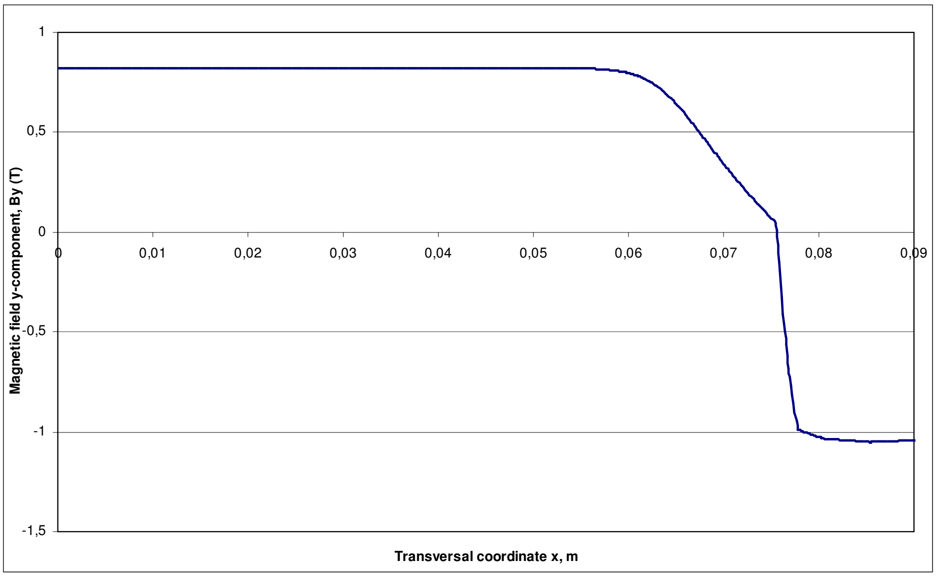

Figure 79: Variation of the vertical component $B_y$ in the median plane along the X-axis for Z=34.5 mm.

Table 11: Uniformity of the $B_y$ component of the magnetic field in the median plane of the main pole inside the GFR.

| **Z (mm)** | **Interval of X (mm)** | **$\Delta B_0/B_0$ (%)** |
|---|---|---|
| 20.0 | 0.0 < X <54.0 | 0.007 |
| 34.5 | 0.0 <X <46.6 | 0.008 |

Finally, in Fig.80 the color contour map of the magnetic field distribution inside the GFR of the main pole is shown. It can be checked that inside this region the field uniformity is better than 0.075%. Thus, from this map and the previous analysis we conclude that specification S3 of the field uniformity is fulfilled.

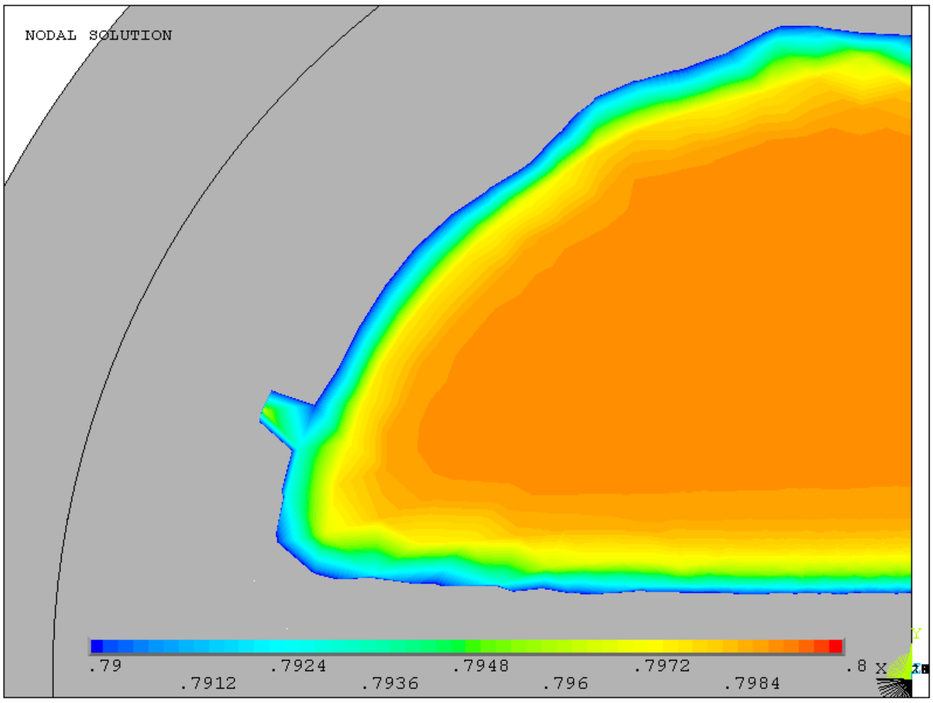

Figure 80: Color contour map of $B_{sum}$ in the median plane inside the GFR of the main pole.

A similar study for the inverse and additional poles was also performed. In this case the field uniformity was analysed for the regions extended in the transverse horizontal direction (X-direction) and separated by at least 15 mm from the both edges of the corresponding poles. The colour contour maps of the field vertical component $B_y$ obtained in the 3D simulations is given in Fig. 81. Estimates of the field uniformity for the inverse and the two additional poles give the following results:

$$\frac{\Delta B_1}{B_1} = 0.042\% , \qquad \frac{\Delta B_1}{B_i} = 0.025\% \quad (i = 2,3) . \tag{110}$$

To summarize, it was checked that for all the poles of the 4-pole end magnet at distances from the edge exceeding the gap height (12 mm) the field uniformity is better than 0.075%.

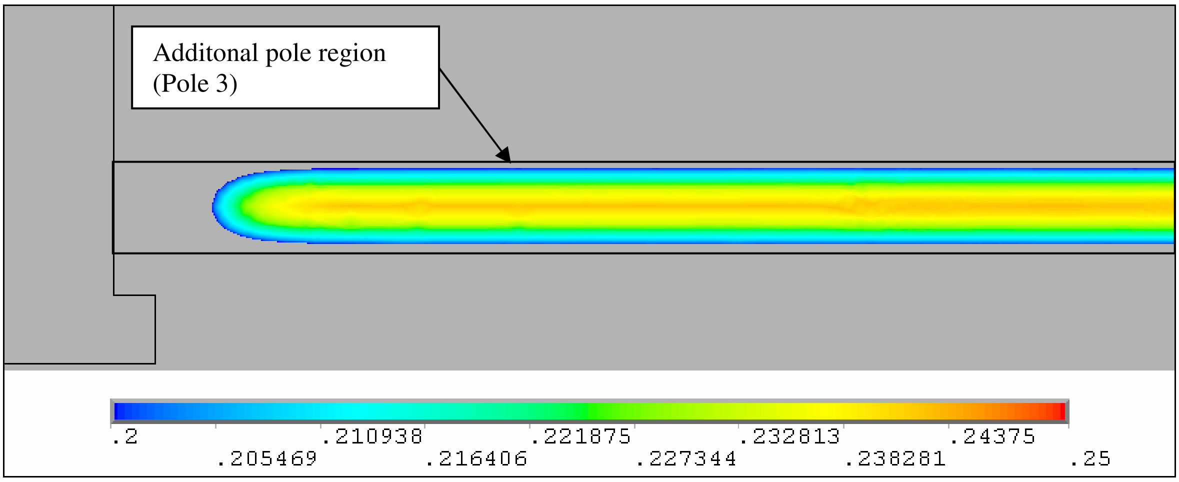

Figure 81: Distribution of the magnetic field vertical component $B_y$ in the median plane along the additional pole #3.

Another characteristic to be controlled in the magnetic system design is the level of the field outside the end magnet close to its entrance. This magnetic field is often referred to as stray field. According to specification S5 its level must not exceed 1G, otherwise its effect on the beam dynamics can lead to a significant deviation of the particle trajectories. The magnetic stray fields appear due to a finite permeability of the yoke material (Steel-1010 in our case) and the material magnetic saturation. From the results of 3D simulations with the ANSYS code we obtained that at the distance of 20.0 mm from the end magnet face the magnetic field is less than $10^{-4}$ T.

*h. Concluding remarks on the 3D design.*

As it was shown in the 2D and 3D simulations of the 4-pole end magnet studied in the previous parts of Sect. 4.1.3 the proposed design satisfies all specifications S1-S5, S9 and S10. The results obtained in these studies, in particular the geometry and dimensions of the parts of the magnet, residual magnetizations of the REPM material blocks and material specifications, form a set of data sufficient for the next step of the development of the UPC 12 MeV RTM end magnets, namely its technical detailed design. The fulfillment of specifications S6-S8 are checked in the following section.

We would like to mention that the results of the 3D simulations obtained with the ANSYS code were checked by independent computations carried out by members of the UPC 12 MeV RTM collaboration using a different code. The results of these parallel simulations were shown to be in a good agreement, the detected differences were within controlled errors of calculations [66]. Partially they were also due to a different definition of the magnetization vectors in the M1 REPM blocks and different choice of the mesh size.

#### 4.1.3.3. - Beam trajectories in the end magnet field.

In order to validate the final version of the design of the 4-pole end magnet described in the previous section we calculated the focusing power and electron trajectories in the magnetic field obtained in the 3D simulations. This study was performed using the RTMTRACE code.

The dependence of the end magnet focusing power *P* on the particle energy is shown in Fig. 82 (see also Table 12). It turns out that an overfocusing of particle trajectories takes place. An example of this effect can be seen in Fig. 83 which shows the trajectory in the vertical plane of a particle with energy *E*=1.9 MeV. Therefore, a positive focusing power corresponds to the case of a particle moving away from the median plane at the magnet exit and hence to defocusing. The opposite case of negative focusing power corresponds to particle focusing. One can see that at *E*=1.9 MeV *P*=+2.7 $m^{-1}$ that corresponds to the focal length about 37 cm. This is much larger than the distance from the edge of magnet M1 (see Fig. 50) to the accelerating structure (~ 3cm) so that the end magnet defocusing of 1.9 MeV particles has little effect on the transverse beam dynamics. At the first orbit (energy equal to 4 MeV) the M2 end magnet is focusing with the focal length about 22 cm. Since the distance between the end magnets is ~20 cm the focusing is appropriate. With the energy increase the end magnet focal length is growing slower than $E^2$. A more detailed beam dynamics study performed in the framework of the UPC 12 MeV RTM design confirms that the end magnet focusing alone provides a stable vertical beam optics in the accelerator.

Another beam dynamics issue that was addressed is the 1.9 MeV orbit closure, trajectory displacements for higher orbits and the choice of the optimal orbit positions inside the end magnet in its median plane. The position of the magnets M1 and M2, (Fig.50) along the X-direction with respect to the accelerating structure axis should be optimized so that all trajectories pass in the region of the high uniformity field. With this purpose in mind a careful beam dynamics study was performed, namely a set of trajectories was calculated using the median plane field distribution obtained in the 3D calculations.

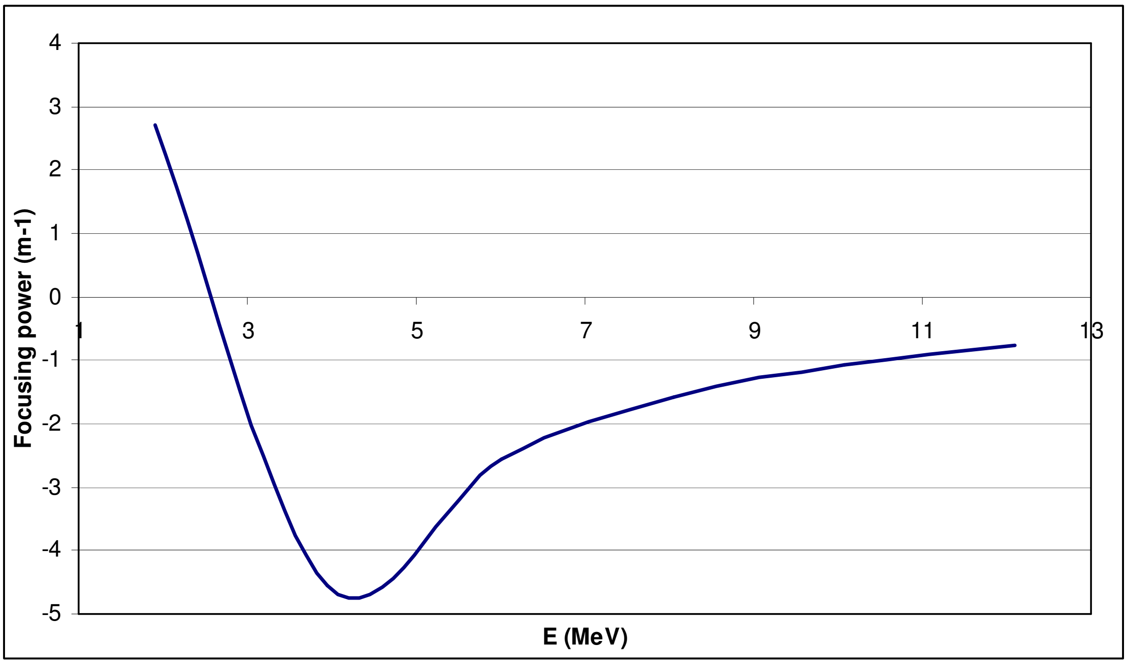

Figure 82: Focusing power of the final design version of the 4-pole end magnet as a function of the beam energy for the magnetic field obtained in the 3D simulations with the ANSYS code.

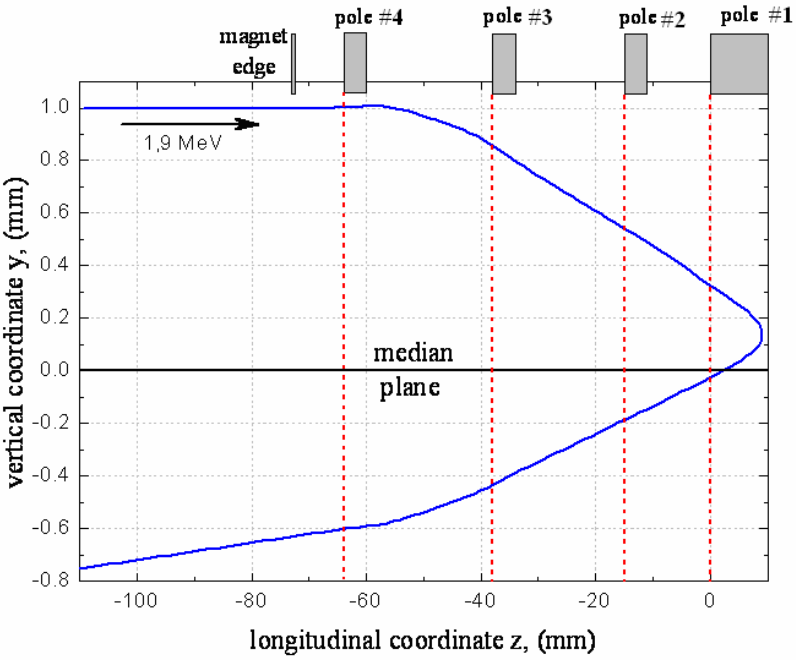

Figure 83: Trajectory of a particle with the energy 1.9 MeV in the vertical plane inside the 4-pole end magnet.

Firstly, the optimal position of the beam trajectory after the first acceleration in the M1 magnet was found. In Fig. 84a set of such 1.9165 MeV trajectories entering into the 4-pole end magnet at different distances from the magnet symmetry plane in the X-direction. Recall that the corresponding main pole edge at $Z = 0$ is situated at X = 69 mm. It was found that the optimal point for the beam entrance is at X>-45 mm. Taking into account that (a) the maximum energy of regular trajectories in M1 is 10 MeV and (b) that the extracted beams must also pass within a sufficiently uniform field as the optimal position of the entrance point of the 1.9165 MeV trajectory X = —38 mm was chosen. In this case the outmost parts of the 10 MeV and 1.9165 MeV trajectories are situated at equal distances from the magnet edges. We would like to stress that the position of the entrance point of the 1.9165 MeV trajectory determines the position of the accelerating structure axis.

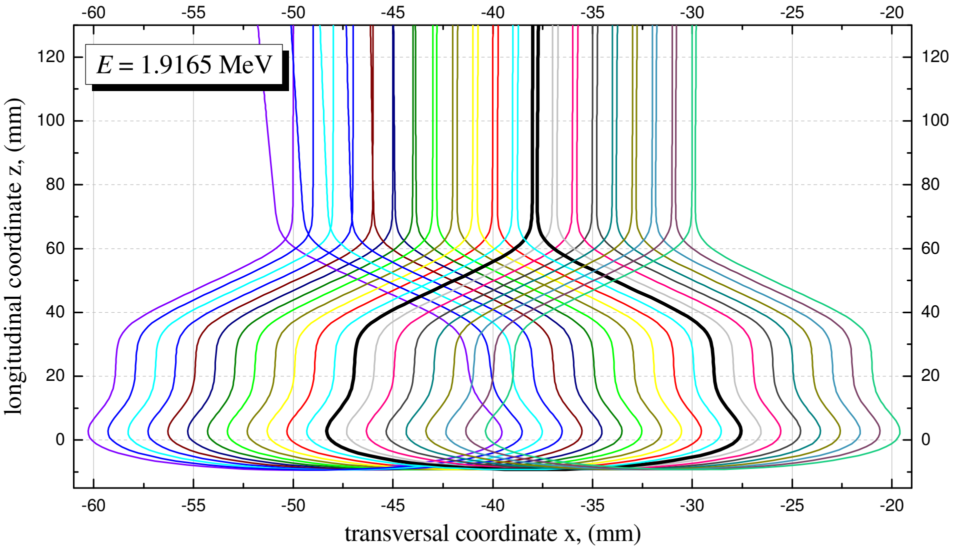

Figure 84: Trajectories of particles with the energy *E*=1.9165 MeV in the median plane inside the M1 end magnet.

The position of the M2 magnet with respect to the accelerating structure axis was optimized with the requirement that the outmost points of the 4 MeV and 12 MeV trajectories were also positioned at equal distances from the magnet edge. The resulting scheme of the particle trajectories in both magnets is shown in Fig. 85. One can see that the accelerating structure axis, which is also the RTM common axis, is shifted with respect to vertical symmetry plane of the M1 magnet by the distance 38 mm and with respect to that of the M2 magnet 48 mm. Beam dynamics calculations give that for this relative positions of the end magnets the maximum deviation of the bending angle from $180^0$ for all orbits does not exceed 1.6 mrad ($0.09^0$).

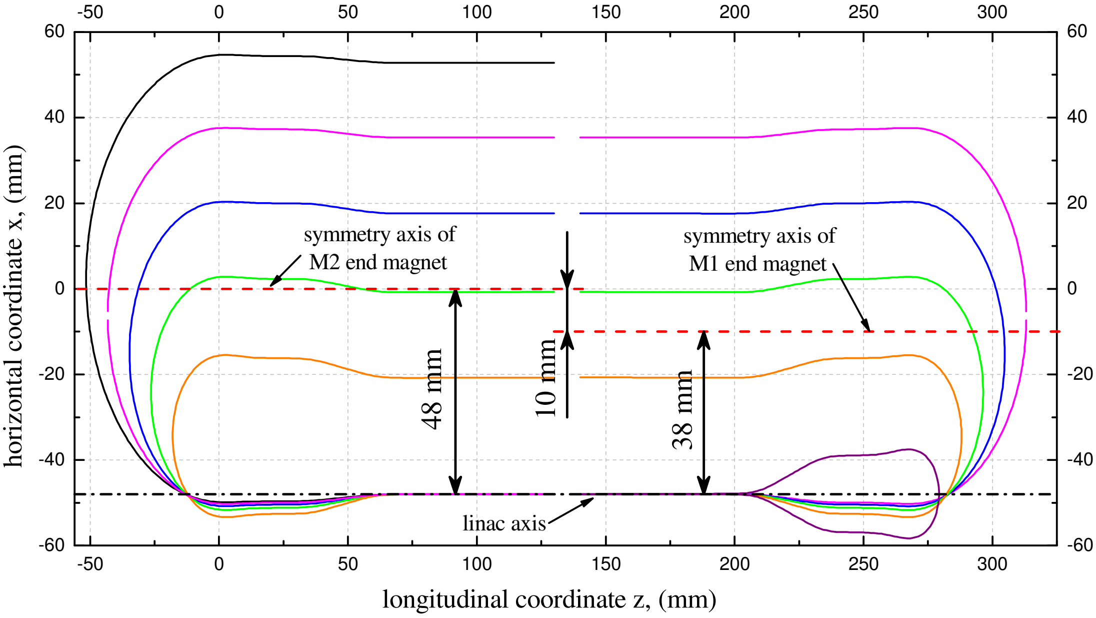

Figure 85: Particle trajectories inside the end magnets M1 and M2.

Finally, orbit displacements with respect to the accelerating structure axis for all orbits of the UPC 12 MeV RTM were calculated. The results are given in Table 12. There also the end magnet focusing power for these orbits is given. One can see that the magnetic field distribution obtained in the 3D simulations provides the 1.9 MeV orbit closure, a displacement of the 4 MeV orbit that allows to bypass the accelerating structure and the acceptable focusing power for all the orbits. Hence, specifications S7-S8 are fulfilled.

Table 12: Beam parameters calculated with the magnetic field obtained in the 3D simulations for the final design version of the 4-pole end magnet.

| Orbit number | Energy (MeV) | $\Delta$ (mm) | P ($m^{-1}$) |
|---|---|---|---|
| 0 | 1.95 | 0.0 | 2.705 |
| 1 | 3.95 | 26.4 | -4.543 |
| 2 | 6.02 | 47.2 | -2.573 |
| 3 | 8.06 | 66.0 | -1.593 |
| 4 | 10.08 | 84.0 | -1.074 |
| 5 | 12.10 | 101.5 | -0.0771 |

### 4.1.4. – End magnet tuning.

In the course of the design of the end magnets of the UPC 12 MeV RTM it was decided to equip them with a mechanism that permits to adjust its magnetic field within certain interval. This field tuning will provide necessary compensation of imperfections that may appear in the magnet machining or assembling.

As a tuning mechanism a system of plungers at the main, inverse and additional poles was chosen. The principle of its operation is described in detail in Sect. 3.5. From estimates of realistic tolerances that can be achieved in the process of the magnetization of the REPM blocks and magnet parts machining and assembling the following specification must be fulfilled:

S11. The 4-pole end magnet described in the previous sections of this chapter with the mechanical tuning elements added must allow to change the field level in the median plane at the main pole (pole #0) by not less than 4 %, at the inverse pole (#1) by not less than 8% and at the additional poles (#2 and #3) by not less than 4%.

In addition the requirements of field uniformity determined by specifications S3, S9 and S10 must be also fulfilled.

In the present thesis results of a study of a first version of the tuning system are described. We would like to note that the final design of the end magnets, which are currently at the stage of manufacturing at a factory, differs in certain aspects from this first one [88], we will comment on these differences at the end of the section. The design of the system of plungers and calculations of its characteristics were carried out by means of 3D simulations of the field distributions using the ANSYS code. The base design of the 4-pole end magnet is the one obtained in Sect. 4.1.3.2, namely given in Fig. 71 and Table 10. First we will study the tuning for each pole separately, after that the influence of the plungers on the field level at the neighboring pole will be analyzed. In order to be able to control the skew fields the half end magnet geometry was used, instead of one quarter geometry, as in the previous sections. For the simulations of the field distributions we used the same mesh as in the 3D simulations in the previous sections, namely a mesh of 1.0 mm size in general and a mesh size of 0.5 mm in the end magnet gap.

#### 4.1.4.1. - Main pole tuning.

The tuning of the field in the main pole region is achieved by moving two cylindrical plungers, one at the upper pole and another at the lower pole, along channels made in the REPM blocks M2 (see Fig. 65) and the corresponding parts of the yoke, as it is shown in Fig. 86. The channel axis is perpendicular to the pole face and is situated on the symmetry axis of the pole. For this first design version the plunger diameter *D* and height *H* were chosen to be the following: *D*=20 mm and *H*=10 mm, equal to the thickness of the M2 REPM block. The plunger material initially used in the 3D simulations is the ARMCO iron.

Let us denote by $h_0$ the gap between the pole face and plunger face looking towards the pole (see Fig. 86). The two extreme plunger positions correspond to $h_{0,min}=0$ and $h_{0,max}=H=10$ mm. In the simulations both plungers, the one of the upper pole and the one of the lower pole, are moved simultaneously so that the magnet symmetry plane always coincides with the median plane. The 3D geometry used in the ANSYS simulations with the plungers in the $h_{0,max}$ position is shown in Fig. 87.

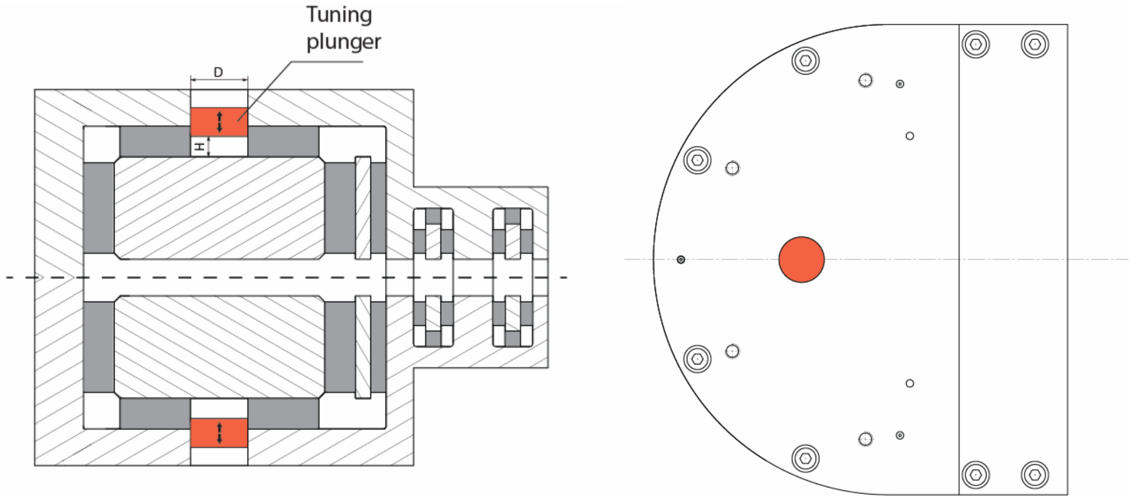

Figure 86: System of tuning of the main pole field.

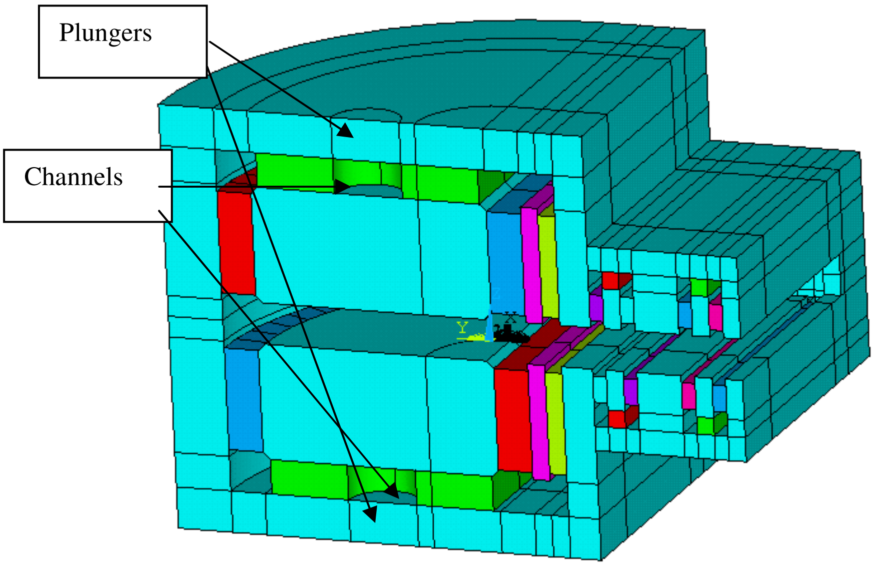

Figure 87: 3D geometry used in the ANSYS simulations of the main dipole of the end magnet. The plungers are in the $h_{0,max}$ position.

The removal of the part of the REPM material corresponding to the channels in the M2 blocks leads to a decrease of the magnetic field in the gap. An estimate of the field reduction can be obtained by calculating the decrease of the magnetic flux Φ as follows:

$$\frac{\Delta\Phi}{\Phi} = \frac{B_{r,M2} S_{channel}}{\sum\limits_{\mathrm{i=1,2,3}} B_{r,Mi} S_{Mi}} \approx 0.02\,, \tag{111}$$

where $B_{r,Mi}$ is the residual magnetization of REPM block *Mi* and $S_{channel} = \pi D^2/4$ is the area of the channel cross section. The summation in (102) goes over all the REPM blocks adjacent to the main pole with $S_{Mi}$ being the area of the block *Mi* touching it. In the 3D simulations with the parts of the M2 corresponding to the plunger channels removed it was obtained that the field in the uniform magnetic field region has reduced by 1.89% that is in a good agreement with estimate (102). This result corresponds to the $h_{0,max}$ position of the plungers.

When the plunger touches the pole (position $h_0 = h_{0,min} = 0$) ideally the potential of the yoke becomes equal to that of the pole and the field in the gap ideally turns out to be zero. However, because of the material saturation in real magnets it remains to be non-zero.

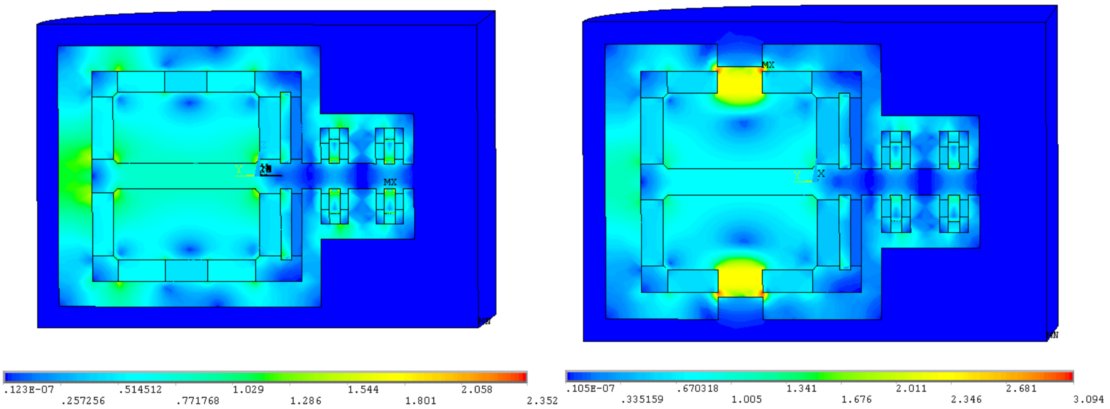

(a) (b)

Figure 88: Distribution of the magnetic flux density $B_{sum}$ in the vertical symmetry plane for the extreme plunger positions: (a) $h_{0,max}$ and (b) $h_{0,min}$.

We performed 3D simulations of the field distribution with the ANSYS code for different positions of the plungers. This study was done after increasing the residual magnetization of the M2 REPM block to $B_{r,M2} = 1.05T$ so that the required field value $B_0$=0.7986 T is achieved for some intermediate position of the plunger. In Fig. 88 the magnetic field distributions obtained for its extreme positions, $h_{0,max}$ and $h_{0,min}$, are shown. One can see that in the latter case (Fig. 88b) there are regions with saturation, especially in zones of contact of the plunger and the yoke where the field reaches values of 3.0 T. The plot of the distribution of the vertical component of the magnetic flux density along the longitudinal axis for the two extreme positions of the plungers is given in Fig. 89. With the plungers moved between these positions the field variation in the uniform field region is 3.25% with respect to the field value in the position $h_{0,max}$.

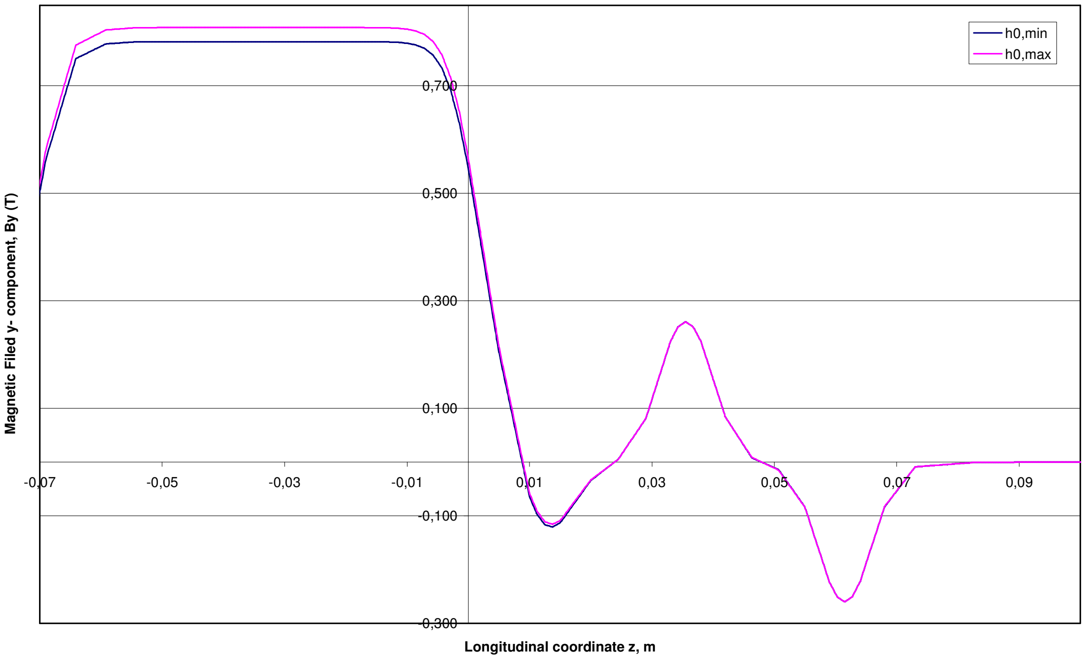

Figure 89: Distribution of the vertical component $B_y$ of the magnetic flux density along the longitudinal axis for the positions $h_{0,max}$ and $h_{0,min}$ of the plungers.

With the aim to reduce the magnetic saturation of the material two changes were introduced into the design. Firstly, the plunger height was increased up to $H$=22 mm so that it became equal to the sum of the thicknesses of the REPM block M2 and of the yoke, so that in the $h_{0,min}$=0 position the plunger fills the whole channel. Secondly, it was decided to change the plunger material from ARMCO iron to Vanadium – Permendur with higher magnetic field saturation value. The magnetic field distributions of the optimized design for the $h_{0,max}$ and $h_{0,min}$ plunger positions are shown in Fig. 91.

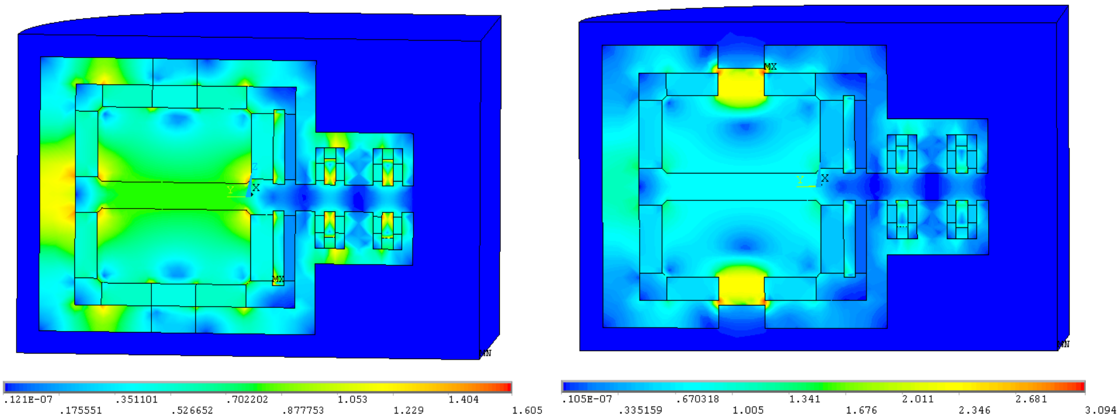

(a) (b)

Figure 90: Distribution of the magnetic flux density $B_{sum}$ in the vertical symmetry plane for the optimized design of the tuning system and two extreme plunger positions: (a) $h_{0,max}$ and (b) $h_{0,min}$.

Comparing the field distributions for the initial (Fig.88) and optimized (Fig.90) designs one can see that the magnetic field value in the uniform magnetic field region are practically the same while the maximum magnetic field values are considerably smaller in the latter case. For example for the $h_{0,max}$ position of the plungers it reduces from 2.35 T to 1.60 T.

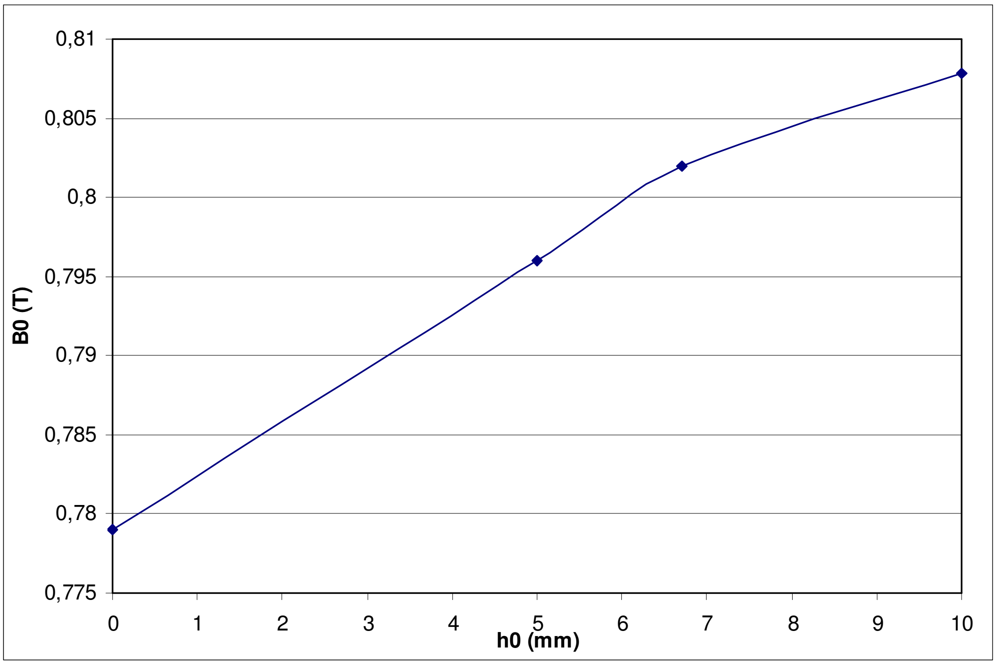

Figure 91: The vertical component $B_0$ of the magnetic flux density in the median plane in the uniform field region of the main pole as a function of the plunger position $h_0$.

The plot of the vertical component $B_0$ of the magnetic flux density in the median plane in the uniform field region of the main pole as a function of the plunger position is shown in Fig.91, the corresponding values are given in Table 13. From these results it follows that while the plungers are moved between the $h_{0,max}$ and $h_{0,min}$ positions the relative field variation is $|\Delta B_0 / B_0| = 0.037$. Note that in this section $\Delta B_0$ denotes the change of $B_0$ at a given point due to a change of the plunger position. We also found that the field at the main pole $B_0$ affects the field at the inverse pole $B_1$. This effect can be seen from the data in Table 13 (last column). Note that the increase of $B_0$ leads to the decrease of the absolute value of $B_1$.

Table 13: The values of the magnetic flux density at the uniform region of the main pole $B_0$ and in the center of the inverse pole $B_1$ for different positions $h_0$ of the main pole plungers.

| $h_0$ (mm) | $B_0$ (T) | $B_1$ (T) |
|---|---|---|
| 10 | 0.8078 | - 0.1166 |
| 6.7 | 0.8020 | - 0.1176 |
| 5.0 | 0.7960 | - 0.1188 |
| 0.0 | 0.7790 | - 0.1210 |

The results of the 3D simulations also allow us to get an estimate of the field uniformity in the *good field region* (GFR) of the main pole. The color map of the distribution of the component $B_y$ of the magnetic flux density in the median plane of the main pole for the middle position of the plungers $h_0$ =5.0 mm is plotted in Fig. 92, the corresponding contour map showing the variation of the magnetic field in this region is given in Fig. 93.

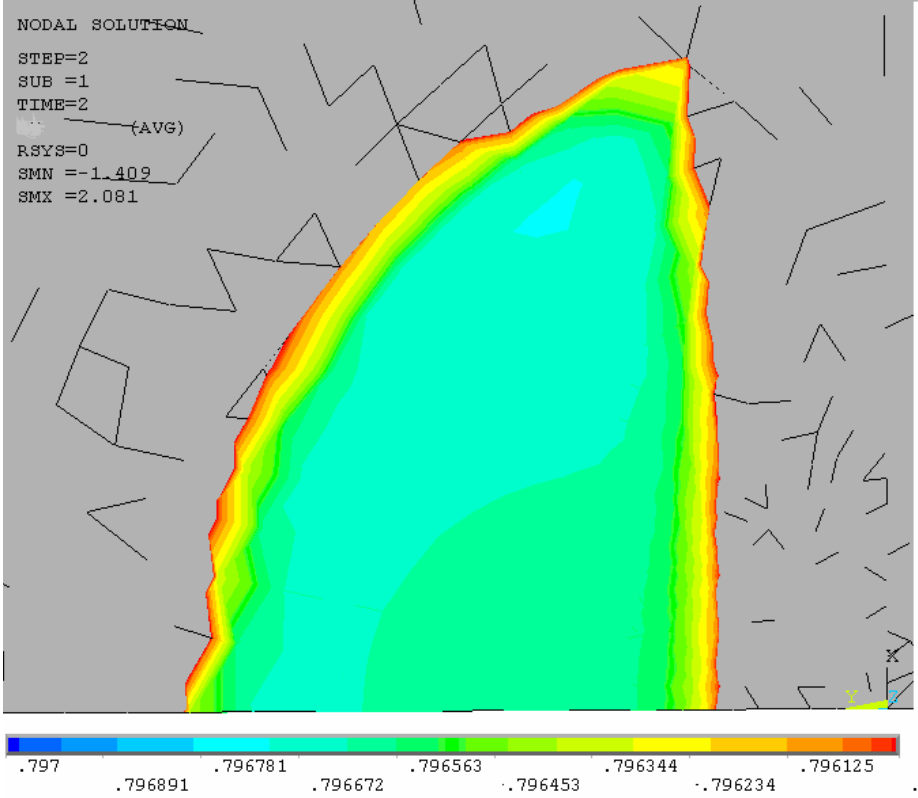

Figure 92: Distribution of the component $B_y$ of the magnetic flux density in the median plane of the main pole for $h_0$ =5.0 mm.

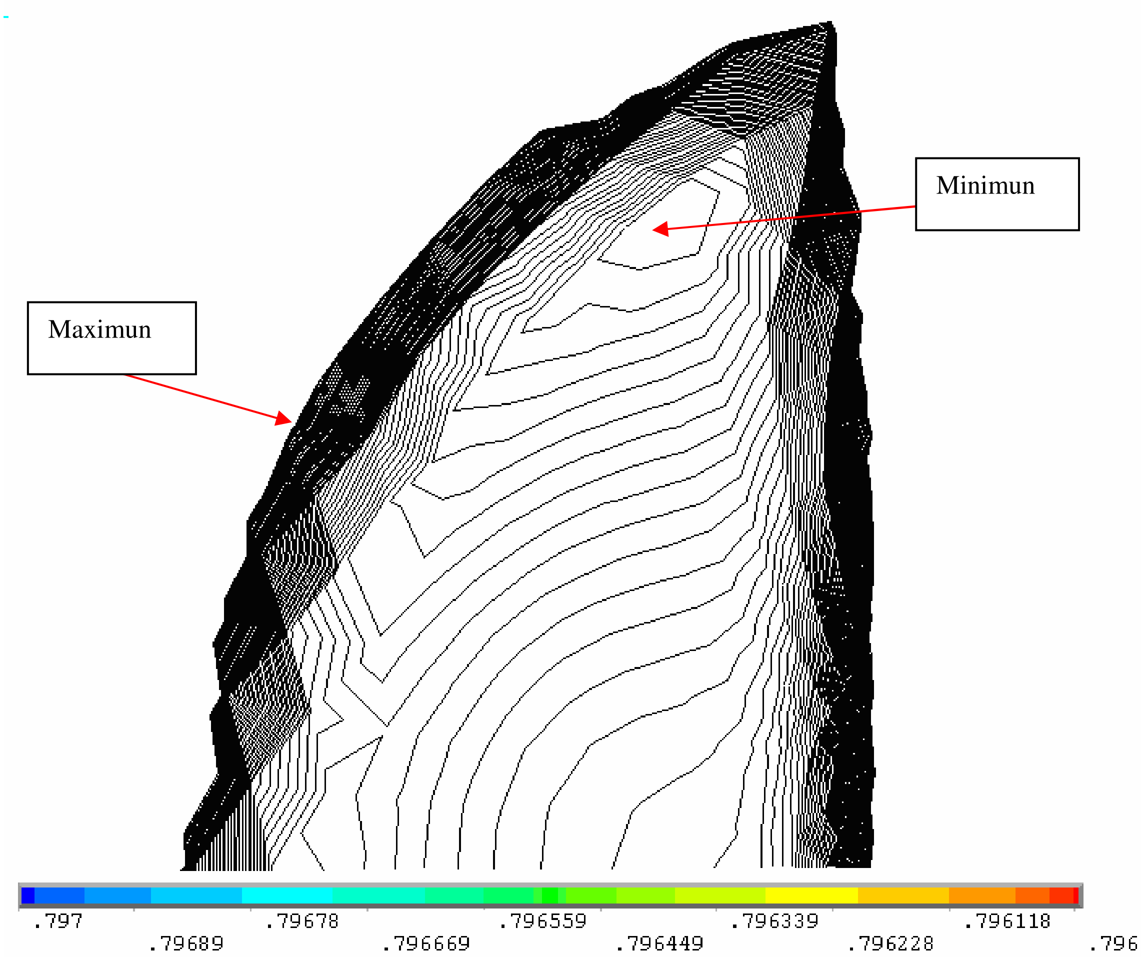

Figure 93: The contour map of the component $B_y$ of the magnetic flux density in the median plane of the main pole for $h_0$ =5.0 mm.

To get a quantitative characterization of the field uniformity we performed an analysis of the results of the 3D simulations. In Table 14 the values of the interval δ between two neighbouring isocurves in Fig. 93, the maximum ($B_{max}$) and minimum ($B_{min}$) value of the field $B_0$ and its relative variation ($|\Delta B_0/B_0|$) in the GFR for three positions of the plungers are given. From these estimates one can see that the field uniformity varies slightly with the change of the plunger position. However, for this design the requirement of field uniformity (specification S3) is not fulfilled and therefore it cannot be considered as satisfactory. At a later stage of the project of the UPC 12 MeV RTM a system of four plungers for each main pole placed in a certain way was considered and was shown to be acceptable. It is this later version which is under manufacturing.

Table 14: Characteristics of the magnetic flux density distribution in the median plane of the main pole for three positions of the plungers.

| $h_0$ (mm) | δ (T) | $B_0$ (T) | $B_{max}$ (T) | $B_{min}$ (T) | $\lvert\Delta B_0/B_0\rvert$ |
|---|---|---|---|---|---|
| 10.0 | $9.4 \times 10^{-6}$ | 0.8072 | 0.807 | 0.808 | 0.15 % |
| 6.7 | $7.8 \times 10^{-6}$ | 0.802 | 0.802 | 0.803 | 0.12 % |
| 5.0 | $7.8 \times 10^{-6}$ | 0.796 | 0.796 | 0.797 | 0.13 % |

### 4.1.4.2. - Inverse pole tuning.

For the tuning of the field in the gap between the poles of the inverse dipole initially it was proposed to use four cylindrical plungers for each pole, in total eight plungers at each end magnet. They move in channels made in the yoke with their axes being parallel to the median plane and orthogonal to the lateral face of the inverse pole (pole #1), as shown in Fig. 94. Because of technical difficulties in drilling channels in the REPM block M4 various alternative solutions were considered. 3D simulations described below are performed with the plunger of the main pole (not shown in Fig. 95) in the position $h_0=h_{0max}$=10 mm.

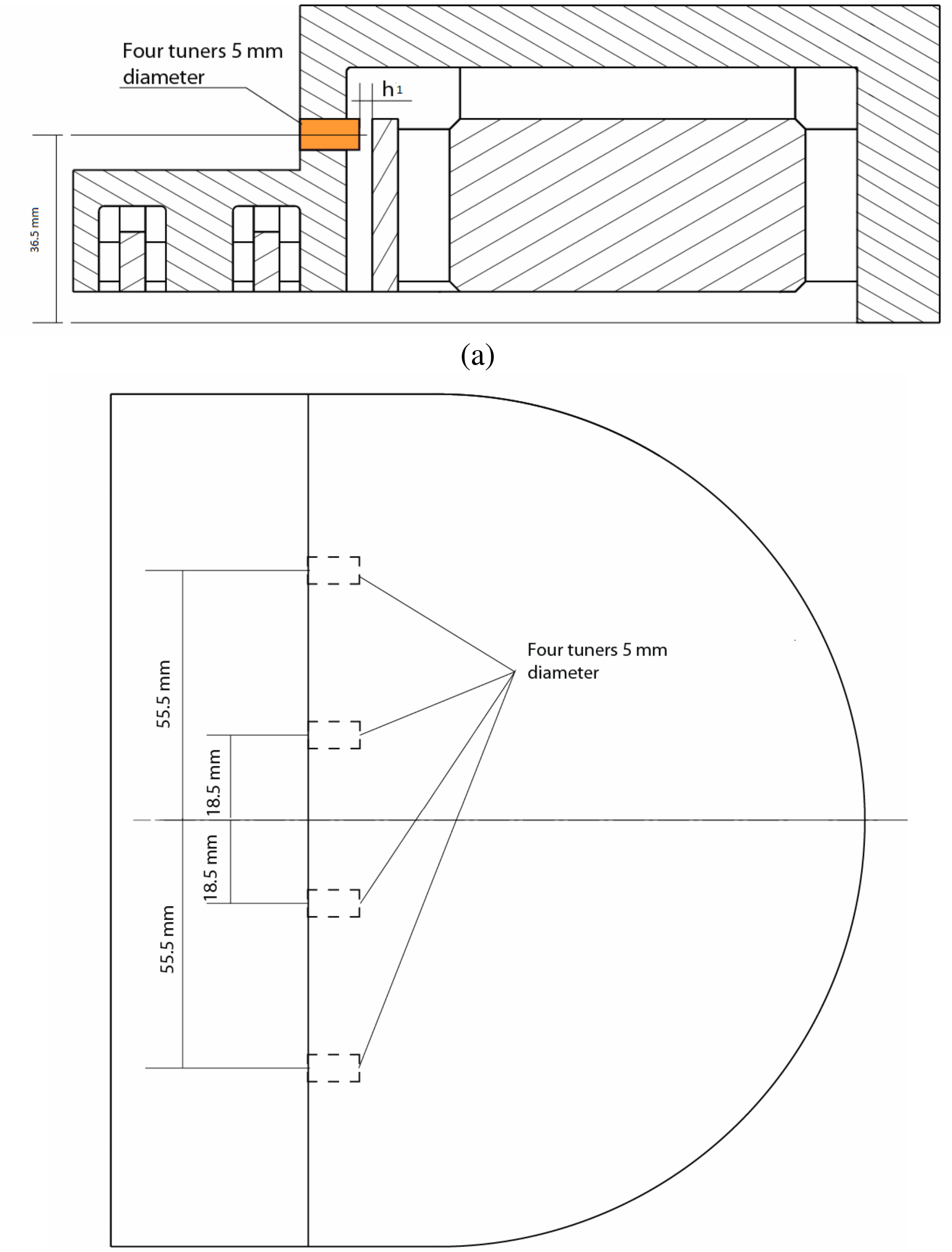

(a)

Figure 94: Scheme of the system of tuning of the inverse pole field. (a) Lateral view, in orange colour one of the plungers is shown. (b) Top view, all four plungers of the upper pole are shown.

First we considered the case with the block M4 completely removed. We obtained that then the value of the $B_y$ field in the median plane at the centre of the inverse pole decreased by almost 15%. With the aim to avoid such large field reduction it was decided to reduce the height of the M4 block to 14.75 mm, i.e. leaving one half of its initial vertical size. We also increased its residual magnetization in order to have the required field value for a middle position of the plungers. The 3D geometry and magnetic field distribution for this new configuration are shown in Fig. 95.

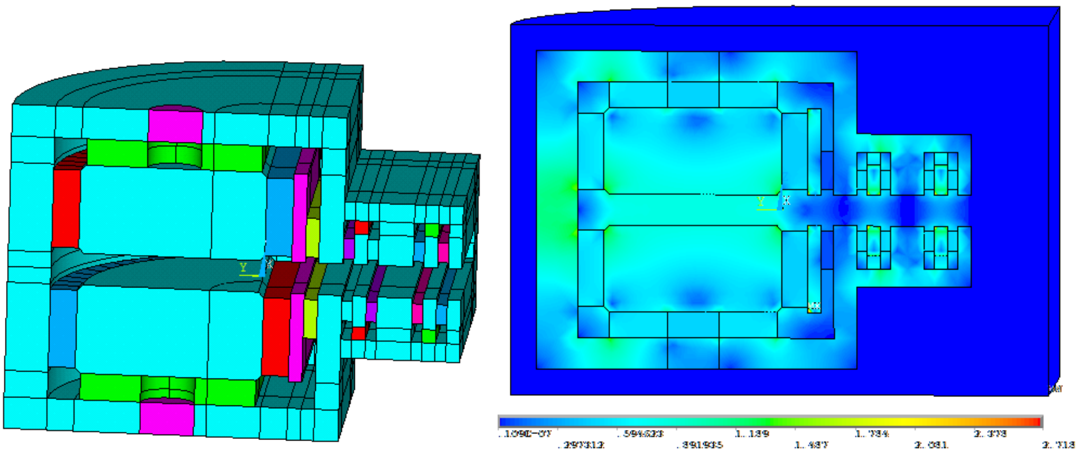

(a) (b)

Figure 95: (a) 3D geometry of the end magnet with the main pole and inverse pole plungers used in simulations with the ANSYS code. (b) Distribution of $B_{sum}$ in the vertical symmetry plane for this end magnet design.

In the study of the characteristics of the inverse pole tuning it was supposed that all inverse pole plungers are identical, their diameter is equal to 5.0 mm and they are moved simultaneously to ensure a close to uniform variation of the magnetic field. As it was mentioned above in this study the main pole plungers are kept in the $h_0=h_{0max}=10$ mm position. Let $h_1$ be the gap between an inverse pole plunger and the pole lateral surface. The gap is varied from its minimal value $h_1 = h_{1\min} = 0$ to the maximal one $h_1 = h_{1max} = 5.0$ mm. The material used for the plungers was Vanadium-Permendur, the same as in the case of the main pole.

From the results of the 3D simulations we obtained that changing the plungers position from $h_{1\max} = 5.0mm$ to $h_1 = 1.0mm$ leads to the reduction of the absolute value of the field in the median plane at the centre of the inverse pole by 5.88% only so that specification S11 is not fulfilled.

To achieve a larger variation of the inverse pole magnetic field it was decided to add two more tuners per each pole situated as it is shown in Fig. 96 (new plungers are shown as red rectangles). For this design the field amplitude decrease while the plungers are moved from $h_{1\max} = 5.0mm$ to $h_1 = 1.0mm$ becomes sufficient and equal to 8.65%. The values of the vertical component $B_1$ of the magnetic flux density in the median plane in the centre of the inverse pole for different positions $h_1$ of the tuners are given in Table 15, the plot of $B_1$ as a function of $h_1$ is shown in Fig. 97.

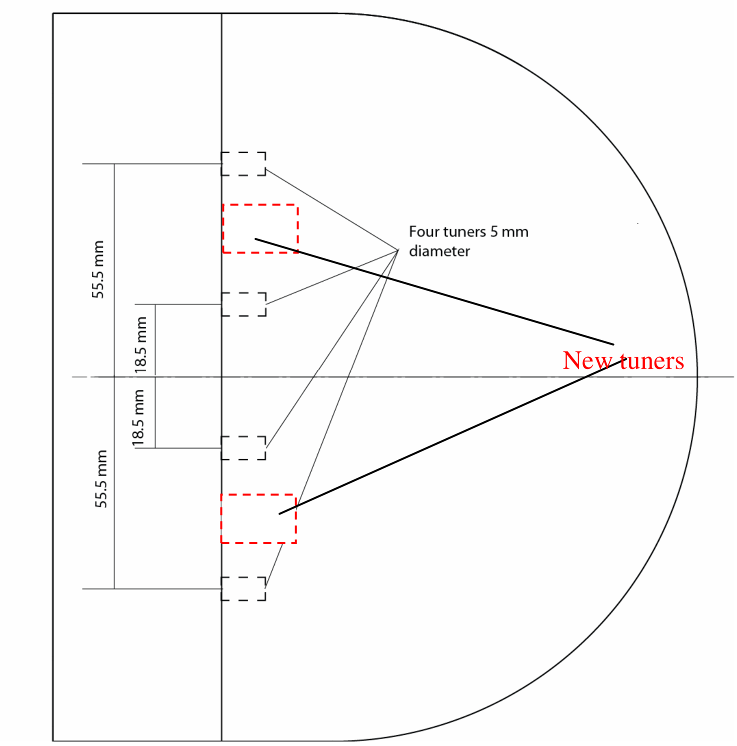

Figure 96: Top schematic view of the optimized system of tuning of the inverse pole field.

Analyzing results of the 3D simulations we found that the variation of the magnetic field at the inverse pole leads to a moderate change of the field in the uniform field region of the main pole. The variation of the magnetic field in the median plane of the inverse pole as a function of the tuners position $h_1$ is shown in fig. 98. The corresponding values are given in the second column of Table 15. The maximum magnetic field variation of the inverse pole is $\left|\Delta B_1 / B_1\right| = 0.086$.

It was also observed that tuning of the inverse pole causes a change of the field of the main pole, namely moving the inverse pole plungers from $h_{1max}$ = 5.0 mm to $h_1$ = 1.0 mm led to a 0.2% increase of $B_0$. In the adjustment of the field of the real end magnet this effect of mutual influence between the poles must be taken into account.

Table 15: The values of the magnetic flux density in the median plane in the uniform region of the main pole $B_0$ and in the center of the inverse pole $B_1$ for different positions $h_1$ of the inverse pole plungers. The main pole plungers are in the $h_0$=$h_{0max}$=10 mm position.

| $h_1$ (mm) | $B_0$ (T) | $B_1$ (T) |
|---|---|---|
| 5.0 | 0.8077 | - 0.11675 |
| 3.0 | 0.8080 | - 0.11496 |
| 1.0 | 0.8093 | - 0.10665 |

We also checked that in the system with 6 plungers (as in Fig. 97) the requirement of field uniformity at the inverse pole (specification S9) is fulfilled.

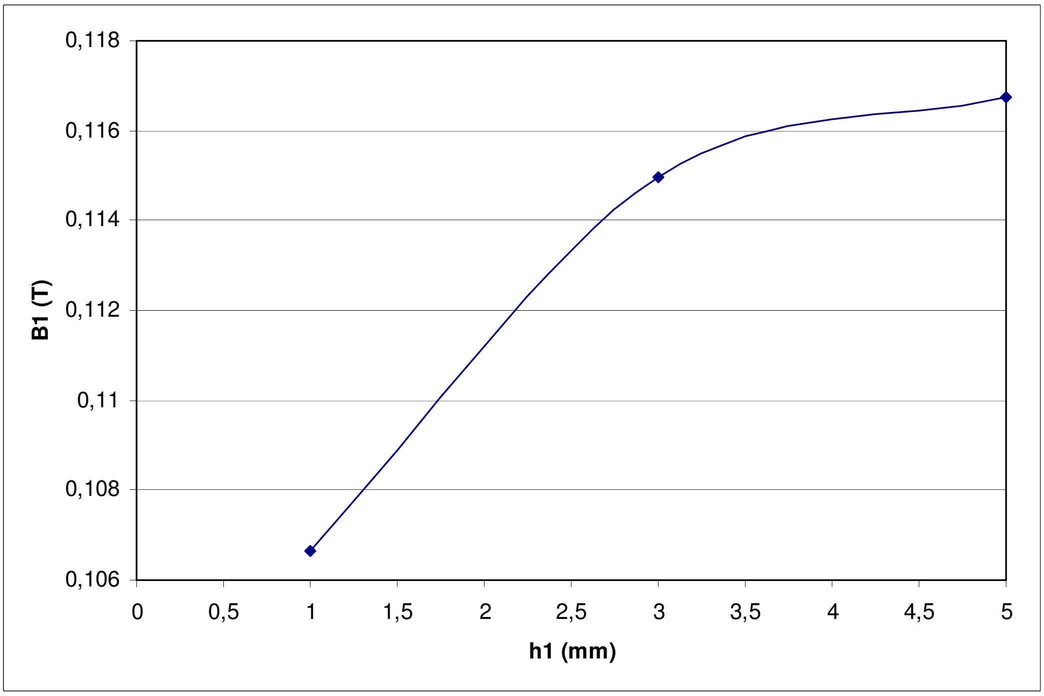

Figure 97: The vertical component $B_1$ of the magnetic flux density in the median plane at the centre of the inverse pole as a function of $h_1$. The main pole plungers are in the $h_0 = h_{0max} = 10$ mm position.

### 4.1.4.3. – Tuning of the additional poles.

The tuning of the magnetic field generated by the additional poles is achieved by moving plungers at poles #2 and poles #3. It was decided to use five cylindrical plungers per pole, that is 10 plungers at each additional dipole, in total 20 plungers at each end magnet. All plungers are identical with the diameter equal to 4.5 mm. They are moved simultaneously in channels made in the permanent magnets M7 and M11 and corresponding parts of the yoke as shown in Fig. 98. For the sake of simplicity of manufacturing of these REPM blocks it was decided to have channels of rectangular cross section with dimensions 5.4 mm x 5.0mm. The axes of the channels and of the plungers are perpendicular to the face of the corresponding pole. The material of the plungers is Vanadium-Permendur.

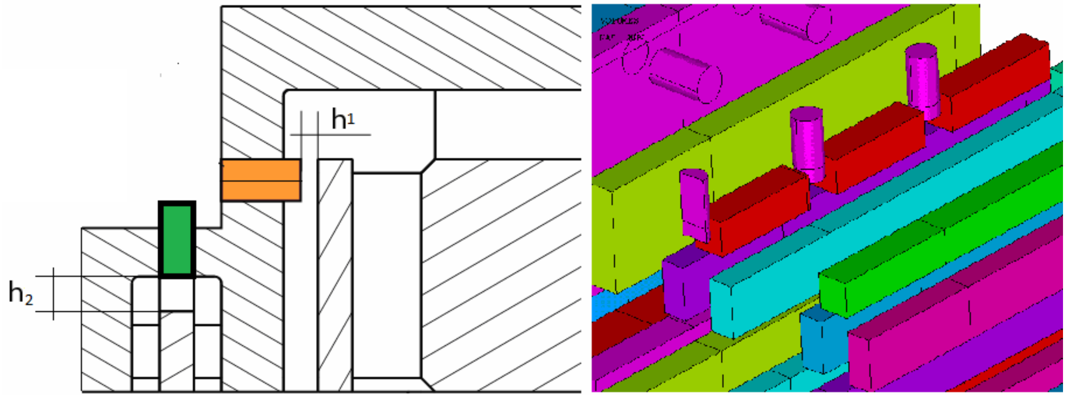

(a) (b)

Figure 98: Tuning system of the additional pole field. (a) Schematic lateral view. A plunger of the additional pole #2 is shown in green, in orange colour one of the plungers of the inverse pole is shown (cf. Fig. 95a). (b) Half of the 3D geometry used in ANSYS simulations. Plungers of the pole #2 are shown.

According to the 3D simulations after removal of the parts of the REPM material of the block M7 corresponding to the channels the magnetic field in the median plane at the centre of the pole #2 decreased by 5.82%. The reduction of the field at pole #3 due to the removal of the corresponding parts of the REPM block M11 is the same. In order to have the required field value in the median plane at the additional poles for the middle position of plungers we increased the residual magnetization of M7 and M11 to 0.9615 T.

Let us denote by $h_2$ and $h_3$ the gaps between the surface of the pole #2 and #3, respectively, and the corresponding plunger (see Fig. 98a). We performed 3D simulations of the magnetic field in the median plane for different positions $h_2=h_3$ of the plungers of the additional poles from $h_{2min}$=1.0 mm to $h_{2max}$=5.0 mm. As an example in Fig. 99 the magnetic flux density distribution in the vertical symmetry plane with the plungers in the position $h_2=h_3$=1.0 mm is shown. We found that for the maximal displacement of the plungers between their extreme positions the field at each pole changes by 4.73%. More detailed data is given in Table 16, the plot of the variation of the vertical component $B_2$ of the magnetic flux density in the median plane at the centre of the additional pole #2 as a function of the position $h_2$ of its plungers is shown in Fig. 101. These calculations were performed for the plungers of the main pole and of the inverse pole in the positions $h_0=h_{0max}$=10 mm and $h_1=h_{1max}$=5 mm, respectively. From these results one can see that the influence of the field of one additional pole to the other is very weak. Indeed, the change of $B_3$ due to the displacement of the plunger of the pole #2 causes only 0.1% variation. We also checked that the influence of the field at the main and inverse poles on the field at the additional poles is negligible.

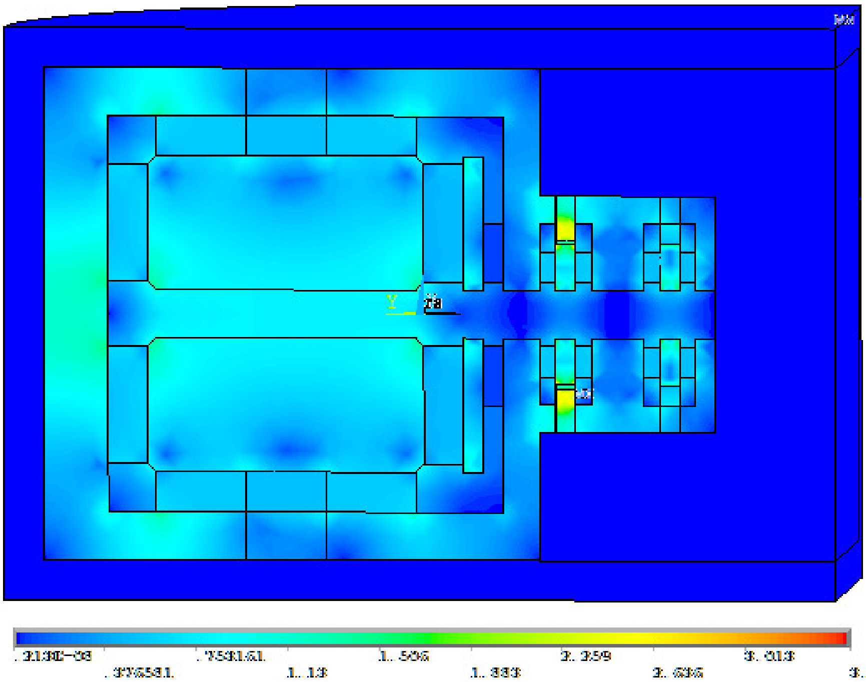

Figure 99: Distribution of the magnetic flux density $B_{sum}$ in the vertical symmetry plane for the plungers of the additional poles in the position $h_2=h_3$=1.0 mm.

Table 16: The values of the magnetic flux density $B_2$ and $B_3$ in the median plane in the center of #2 and #3 additional poles, respectively, for different positions $h_2$ of the plungers of the pole #2. The plungers of the other poles are in the positions $h_0=h_{0max}$=10 mm, $h_1=h_{1max}$=5 mm, $h_3=h_{3max}$=5 mm.

| $h_2$ (mm) | $B_2$ (T) | $B_3$ (T) |
|---|---|---|
| 5.0 | 0.2458 | - 0.2596 |
| 3.0 | 0.2429 | - 0.2599 |
| 1.0 | 0.2342 | - 0.2605 |

The results of the field variation at the pole #3 due to the change of the position of its plungers are similar to those described above. We also checked that the requirement of field uniformity at the additional poles (specification S10) is fulfilled.

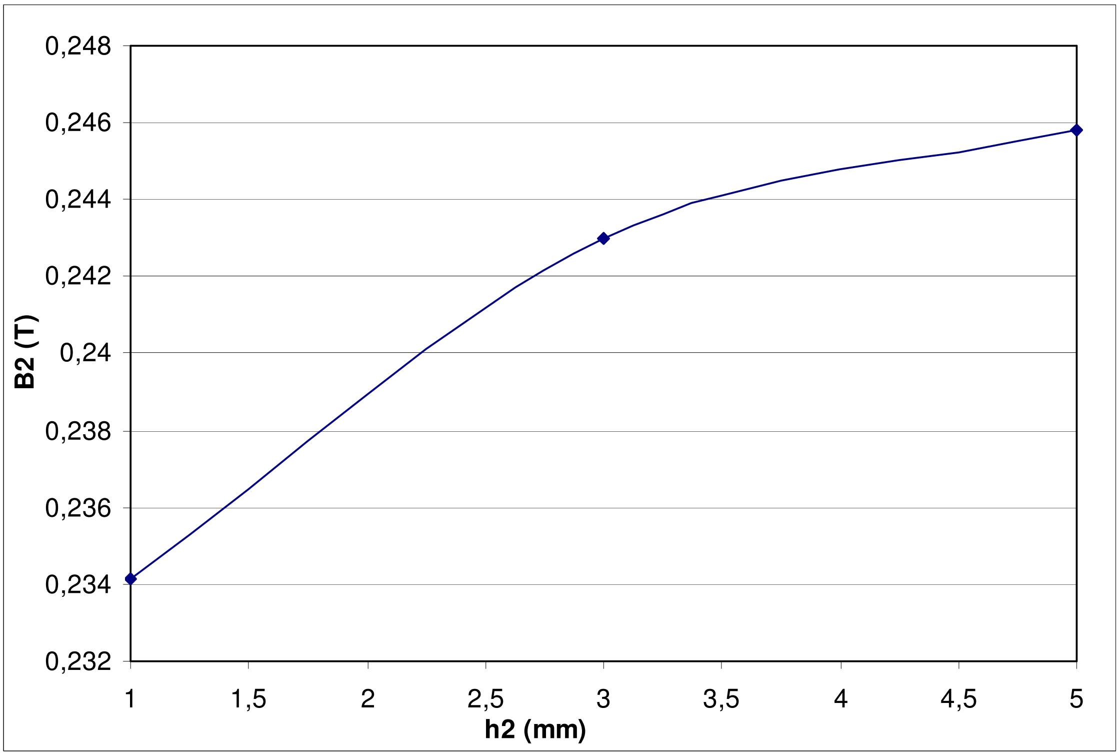

Figure 100: Plot of the vertical component $B_2$ of the magnetic flux density in the median plane at the centre of the additional pole #2 as a function of $h_2$.

### 4.1.4.4. – Summary of the end magnet tuning study.

In the present section preliminary 3D simulations of the tuning of the magnetic field in the median plane of the 4-pole end magnet were carried out. The adjustment is achieved by moving a set of tuners described above. According to the main concept of this design the REPM blocks are magnetized so that the required field profile (see Fig. 69) is obtained for some middle positions of the plungers, for example for $h_0$=5.0 mm, $h_1$=3.0 mm, $h_2=h_3$=3.0 mm. The calculated preliminary values of the residual magnetization $B_{ri}$ for the corresponding REPM blocks were given above, the definite values will be calculated for the final design of the end magnet and plungers at a later stage.

The variation of the magnetic field in the median plane during the tuning was obtained from the 3D simulations of the end magnet for different positions of the plungers. The resulting plots are shown in Figs. 91, 97 and 100. The maximal relative field variations due to the displacements of the plungers over their full ranges are summarized in Table 17.

Table 17: Maximal relative field tuning variations of the magnetic flux density in the median plane at the end magnet poles.

| Pole #*i* | Maximum magnetic field variation $\left\|\Delta B_i / B_i\right\|$ (%) |
|---|---|
| Main pole #0 | 3.25 |
| Inverse pole #1 | 8.65 |
| Additional pole #2 | 4.73 |
| Additional pole #3 | 4.73 |

One can see that in the case of the main pole the relative variation is not enough so that the design requirement of the required field variation (specification S11) is not fulfilled. As we already discussed above, also the field uniformity in the GFR of this pole is not sufficient. Because of this an improved design with four plungers at each pole of the 180º bending dipole was proposed and studied in detail. The rest of the tuning elements are the same as described above. It is this version that was used as the baseline design for the technical drawings and manufacturing of the UPC 12 MeV RTM end magnets [89]. However this later development is beyond the scope of the present thesis.

Another important effect is the mutual influence of the fields at the main and inverse poles. Results of 3D simulations for different plunger positions are given in Tables 13 and 15, the corresponding plots are shown in Figs. 101 and 102.

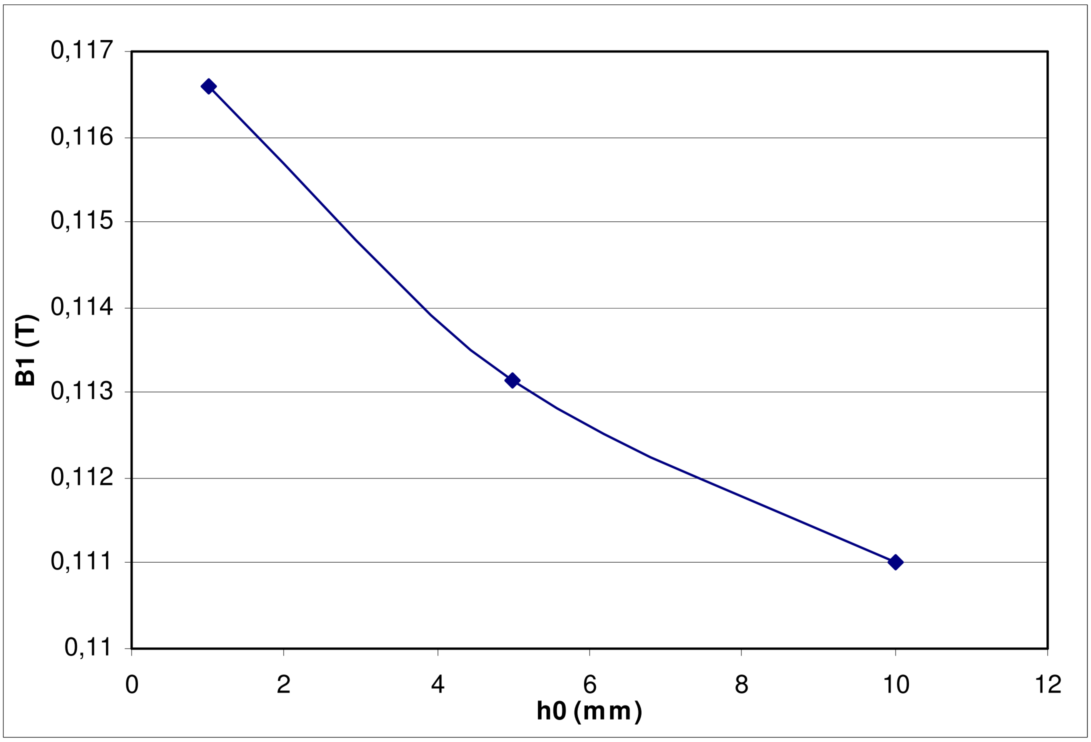

Figure 101: Vertical component $B_1$ of the magnetic flux density in the median plane at the centre of the inverse pole as a function of the position $h_0$ of the main pole plungers.

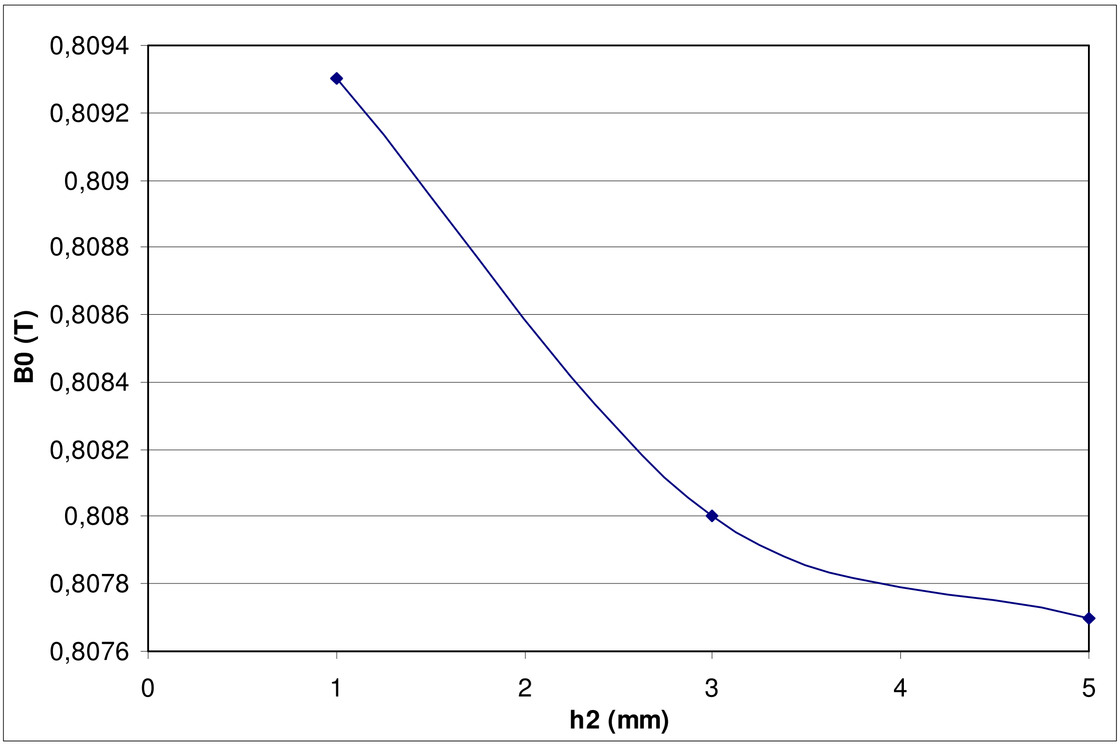

Figure 102: Vertical component $B_0$ of the magnetic flux density in the median plane in the uniform field region of the main pole as a function of the position $h_1$ of the inverse pole plungers.

As a result of the study we suggest the following tuning procedure consisting essentially of three steps.

1. Magnetize the REPM blocks M2, M4, M7 and M11 to the maximum level of the residual magnetization about 1.1 – 1.2 T.
2. After measuring the field in the median plane, whose amplitude hopefully will be above the nominal level, submit the REPM blocks to a demagnetization treatment with the aim to put the end magnet field level within a $(+0.2\%) \div (+2.5\%)$ corridor with respect to the nominal field profile (with the plingers removed).
3. By moving the plungers designed in this section adjust the magnetic field in the median plane to the profile established in Sect. 4.1.3.2 (Fig. 69).

The mutual influence of the fields generated by the main and inverse poles must be taken into account.

### 4.2. – Extraction magnets of the UPC 12 MeV RTM.

One of the advantages of RTMs is that the beam can be easily extracted, in principle, from any of the orbits. As the design solution for the beam extraction system of the UPC 12 MeV RTM the scheme shown in Fig. 14b was chosen. The electrons are deviated by a dipole magnet and are directed towards the exit beam channel. As a source of the magnetic field the REPM material is used.

One possibility is to deflect the trajectories with different energies with a single movable extraction dipole. The magnet is placed at the right trajectory and its magnetic field is adjusted for the beam energy. However it is not simple to change the magnetic field of a permanent magnet dipole, therefore it was decided to use four deflecting magnets of identical design but with different fixed values of the magnetic field [66]. The beam extraction trajectories pass through the end magnet M1 (see Fig. 51). Similar beam extraction system was proposed and described in Ref. [20].

In the present design the beam extraction from the 4 MeV orbit is technically not possible because the deviated trajectory would pass deep inside the accelerating structure body, even traversing the resonant cavities. For this reason it was decided not to exact the 4 MeV beam. We would like to note that electrons with this energy are rather rarely used in the IORT treatments.

### 4.2.1. – Design considerations and analytical estimates.

According to the general requirements of the UPC 12 MeV RTM design the beam extraction system must fulfill the following specifications:

S-EM-1. The system must provide extraction of the electron beam from the 2nd, 3d, 4th and 5th orbits along a common extraction channel.

S-EM-2. The working aperture must be as large as possible, in any case not less than 5 mm x 5 mm. The field uniformity within the working aperture must be better than 1%.

S-EM-3. The stray magnetic field produced by the extraction magnets in the median plane at the location of the neighbor orbits must be less than $10^{-4}$ T.

S-EM-4. The transverse dimensions of the deflecting dipoles must be less than the distance between the orbits, their longitudinal dimension must be minimal possible.

To describe main features of the extraction system design and calculate its characteristics let us consider the scheme shown in Fig.103. The center of the beam deflecting dipole on an *n*th orbit is situated at distance $L_n$ from the effective field boundary (EFB) of the main pole of magnet M1. The electron trajectory is bent by some angle $\alpha$ and follows the exit trajectory. To assure that the beams extracted from any orbit follow the same trajectory after passing the end magnet M1, as it is imposed by specification S-EM-1, the bending angle must be the same for all orbits. In case of the compact pulsed UPC RTM the choice of the extraction angle is a compromise between the beam defocusing by the end magnet fringe field and the RTM dimensions. The larger is the angle $\alpha$, the stronger is the defocusing effect (see Sect.2.2.2), so large angles are not acceptable. On the other hand, as one can see from Fig.103, for small angle $\alpha$ the distance $L_n$ is large and that means a large distance between the end magnets and therefore large dimensions of the RTM accelerating module. As a compromise the deflecting angle was fixed to be $\alpha$=5°.

The ordinary practice in the design of RTM beam extraction systems is to deflect the trajectory with the highest energy ($E_5$=12 MeV in our case) so that it crosses the previous orbit (with $E$=$E_4$=10 MeV) approximately at its entrance into the EFB of the end magnet. Thus, fixing the angle $\alpha$ and the displacement of the 12 MeV trajectory determines in the first approximation the position of the extraction magnet on this orbit with respect to the EFB. Once we have $L_5$ fixed and the condition that all output trajectories follow the same path after exiting the end magnet M1 imposed, the distances $L_n$ ($n$=2,3,4) for other extraction magnets are calculated unambiguously.

The position of the accelerating structure $L_l$ (see Fig.103) with respect to the end magnet M1 is determined by the requirement that the output trajectories bypass it with sufficient clearance. This means that the output beam displacement $R_l$ at the point Z corresponding to the entrance into the accelerating structure (see Fig.103) must be sufficiently large. In fact, in the UPC 12 MeV RTM design in order not to shift the accelerating structure too far from the end magnet M1, thus increasing the RTM size, a recess in its body is made (not shown in Fig.103) which allows the passage of the extracted beams. Thus, in this case $R_l$ is the position of the centre of the recess channel with respect to the central axis of the accelerating structure and is smaller than the radius of its body. Also, for providing a passage to the output beam a hole in the feeding waveguide is drilled and a small recess in the end magnet M2 is cut.

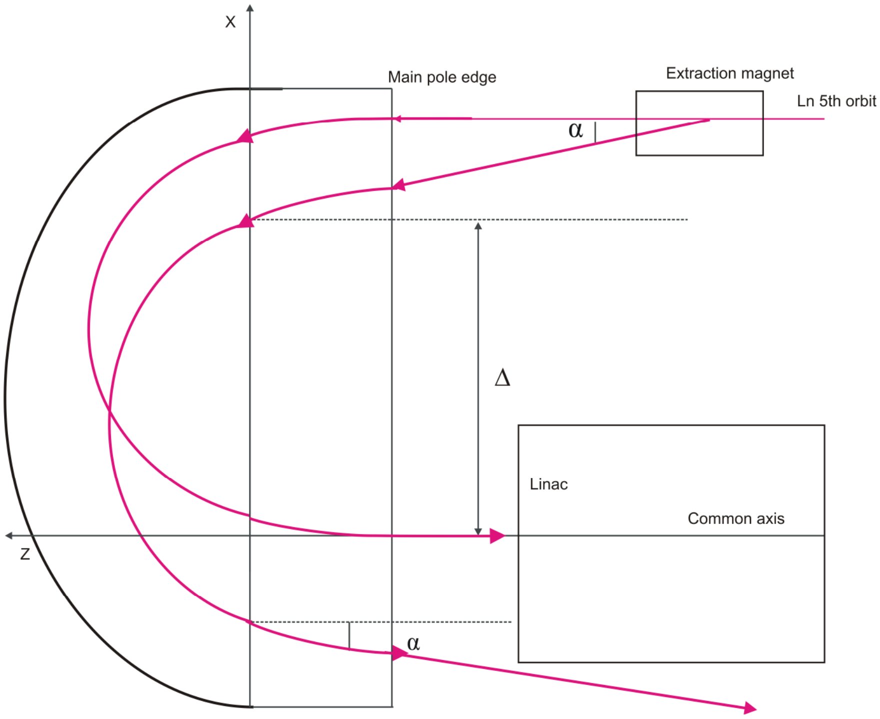

Figure 103: Beam extraction scheme.

Having fixed the angle α the value of the field integral which provides the required deflection of the *n*th orbit with energy $E_n$ ($n$=2,3,4,5) is calculated. The effective length of the corresponding dipole is set following the criteria of having a reasonable magnetic field for a reasonable length. After this simulations of the extraction magnets with 2D and 3D codes are performed with the aim to obtain a design which complies with specifications S-EM-2, S-EM-3 and S-EM-4. An important part of these computations is the minimization of the strayed magnetic field at neighbouring orbits and reducing it below the limit set by S-EM-3.

Let us consider in more detail the procedure of fixing the distances $L_n$ described above within the scheme shown in Fig.103. Here for simplicity reasons it is assumed that the end magnet has just the main pole and its fringe field is ignored. One can easily see that the following main relation is fulfilled

$$(L_n - L_l)\tan\alpha - 2R_n\left(1-\cos(\alpha)\right) = R_l, \qquad (112)$$

where $R_n$ is the radius of the $n$th orbit inside the main pole of the end magnet. The position of the last orbit extraction dipole is fixed by the condition

$$L_5 \tan\alpha = 2(R_5 - R_4)\,. \tag{113}$$

Then the position of the accelerating structure butt-end facing the end magnet M1 is given by Eq.(112) with $n$=5,

$$L_5 \tan\alpha - 2R_5\left(1-\cos(\alpha)\right) = R_l - L_l \tan\alpha\ , \tag{114}$$

and the distances $L_n$ for the rest of the extraction dipoles are calculated from the formula

$$L_n = L_5 + 2(R_n - R_5)\frac{1-\cos\alpha}{\tan\alpha} \qquad (n = 2,3,4)\,. \tag{115}$$

In accordance with Eq. (41) the field integral for the dipole placed at the $n$th orbit calculated for the reference trajectory is given by

$$I_n = \int_{z_1}^{z_2} B_y(0,0,z)dz = \frac{p_n}{|e|}\sin\alpha\,, \tag{116}$$

where the integration is performed within the interval $z_1<z<z_2$ for which the magnet field is non-vanishing. Using Eqs. (113), (115) and (116) we calculated the positions $L_n$ and field integrals $I_n$ of the deflecting dipoles, the results are given in Table 18. Of course, since they were obtained within a simple model introduced here they should be considered as a first approximation. From Eq. (114) using the value of $L_l = 10\,\text{cm}$ one obtains the horizontal displacement of the extracted beam $R_l = 2.61\,\text{cm}$.

Table 18: Positions of the center of the extraction magnets and their field integrals calculated within the simple model.

| Orbit number $n$ | $p_n$ (MeV/c) | $L_n$ (cm) | $I_n$ (T·m) |
|---|---|---|---|
| 2 | 6.511 | 19.072 | $1.90\text{x}10^{-3}$ |
| 3 | 8.556 | 19.1534 | $2.50\text{x}10^{-3}$ |
| 4 | 10.579 | 19.2267 | $3.10\text{x}10^{-3}$ |
| 5 | 12.601 | 19.300 | $3.65\text{x}10^{-3}$ |

More realistic study of the output electron trajectories was performed using the RTMTRACE code. It takes into account the effect of the fringe field of the main pole and the curvilinear shape of the trajectories in the inverse and additional poles of the 4-pole end magnet described in Sect. 4.1, as well as the fact that the distance between the orbits decreases with energy because of weakening of the phase slip effect (see Ch. 5). Under the condition that the trajectories deviated by α=5° from the last four orbits (i.e. $n$=2,3,4,5) follow exactly the same extraction path the extracted beam trajectories were calculated and the positions of the centres of the deviating dipoles were determined. These results and the corresponding field integrals are given in Table 19. In these simulations the accelerating structure was situated at the distance $L_l$=10.5 cm from the main pole edge of the end magnet, then the obtained horizontal displacement of the axis of the output beam channel from the central axis of the accelerating structure $R_l$=2.68 cm.

As one can see by comparing the values of $L_n$ in Tables 17 and 18 the approximation calculated within the model in Fig. 104 differs in 2-3 % from the more exact result obtained in the RTMTRACE simulations. As another illustration of the level of the precision of the model we calculated the extracted beam displacement at the position of the accelerating structure butt-end along Z-axis using Eq.(114) and the value $L_1$=10.5 cm. The result was $R_l$=2.61 cm which is to be compared to $R_l$=2.68 cm obtained in the RTMTRACE simulations.

Table 19: Positions of the centre of the extraction magnets and their field integrals obtained in simulations with the RTMTRACE code.

| Orbit number *n* | $p_n$ (MeV/c) | $R_{n+1}$-$R_n$ (cm) | $L_n$ (cm) | $I_n$ (T·m) |
|---|---|---|---|---|
| 2 | 6.511 | 1.88 | 19.51 | $1.89 \times 10^{-3}$ |
| 3 | 8.556 | 1.8 | 19.61 | $2.49 \times 10^{-3}$ |
| 4 | 10.579 | 1.75 | 19.72 | $3.08 \times 10^{-3}$ |
| 5 | 12.601 | --- | 19.76 | $3.66 \times 10^{-3}$ |

### 4.2.2. – Geometry of the extraction magnets.

Taking into account specification S-EM-4 and the requirement that the extraction dipoles will be placed inside the vacuum chamber it was decided to use an REPM material as the source of the magnetic field. As it was already explained in Ch. 3 this magnetic material allows to obtain quite compact magnetic systems.

For the extraction dipoles it was decided to choose some modification of the QSM design with rectangular yoke [32] described in Sect. 3.3.3. Schematic drawings of the extraction magnet cross sections in the vertical X=0 plane and the transversal symmetry plane Z=0 are shown in Figs.104 and 105, respectively. The dipole aperture is surrounded by prismatic REPM blocks attached to a steel yoke. In order to shield the neighbouring orbits from the strayed fields generated by the dipole its yoke is surrounded by a steel magnetic screen. An aluminium spacer is placed between the yoke and the screen. All four extraction magnets have the same geometry and dimensions. In order to achieve the same bending angle α=5° for all orbits the REPM blocks are magnetized to the values of $B_r$ which provide the required field integrals given in Table 19.

Because of the severe limitation on the extraction magnet outer size in the transverse direction and the necessity to have large physical aperture a thin flat yoke is a preferable and almost the only design solution. By its geometry it corresponds to the QSM dipole with rectangular working zone. In the genuine version of such magnet the magnetization vectors of the lateral triangular permanent magnets would be orthogonal to their inner surfaces facing the working aperture (see [32]). However, in order to simplify the manufacturing of these REPM blocks the direction of the magnetization was decided to be horizontal (see Fig.104). Thus our design of the extraction dipoles is intermediate between the QSM designs with rectangular yoke and rectangular working region. The maximal uniformity of the dipole field will be achieved by the optimization of the geometric parameters of the REPM blocks and the value of their residual magnetization.

As a first step of design simulations the dimensions of the parts of the dipole were fixed and the field distribution in the transverse plane was obtained using the 2D FEMM code [89]. However in the 2D simulations it is assumed that the extraction magnet length is infinite, so to take into account the finite size effects afterwards 3D simulations with the ANSYS code were performed.

Parameters characterizing the extraction magnet geometry are shown in Fig. 106. The thickness *D* of the horizontal REPM blocks can be calculated using Eq. (96). Though that formula was derived for C-type magnets it is also valid for the dipole considered here. In the case of the ideal QSM dipole magnet with rectangular working region a relation between the geometrical parameters can be derived. Namely, as it was shown in Ref.[90], the angles β and θ of the triangular block, given by the formulas $\tan(\beta) = D/l$ and $\tan(\theta) = l/h$, satisfy the relation

$$2\beta = \frac{\pi}{2} + \theta \tag{117}$$

from which it immediately follows that

$$l = D\sqrt{\frac{h}{2D+h}}\ . \tag{118}$$

As it was mentioned above in our design the magnetization vectors of the lateral triangular REPM blocks are horizontal and relations (117) and (118) strictly speaking do not hold and give only an approximation. The corresponding estimates will be done in the next section.

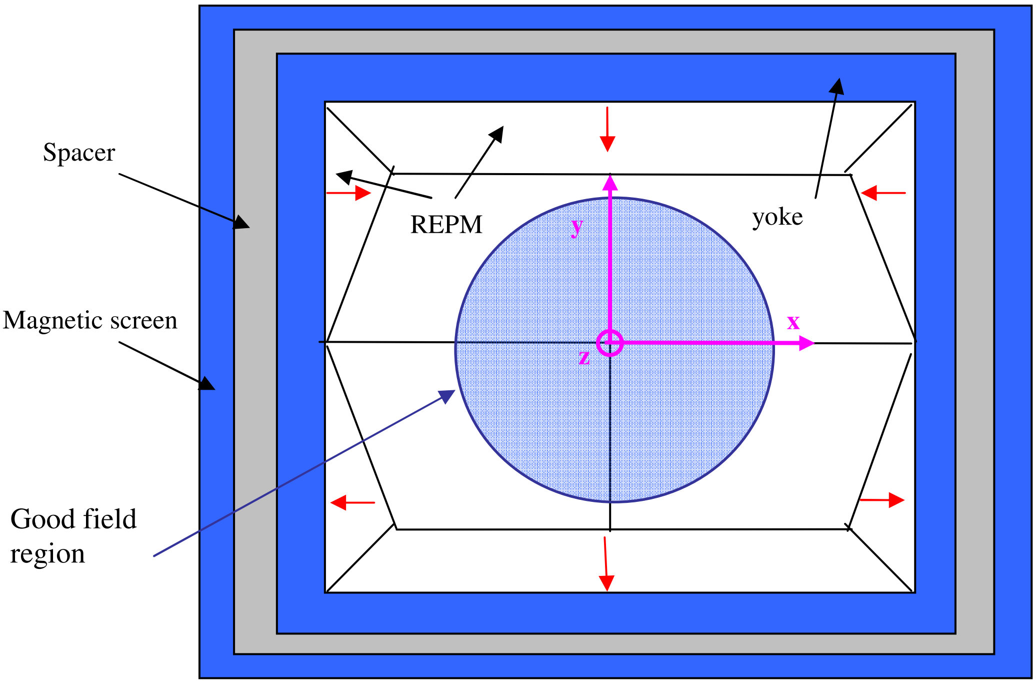

Figure 104: Schematic drawing of the extraction magnet cross section in the transversal symmetry plane Z=0. The red arrows indicate the direction of the magnetization vector of the REPM blocks.

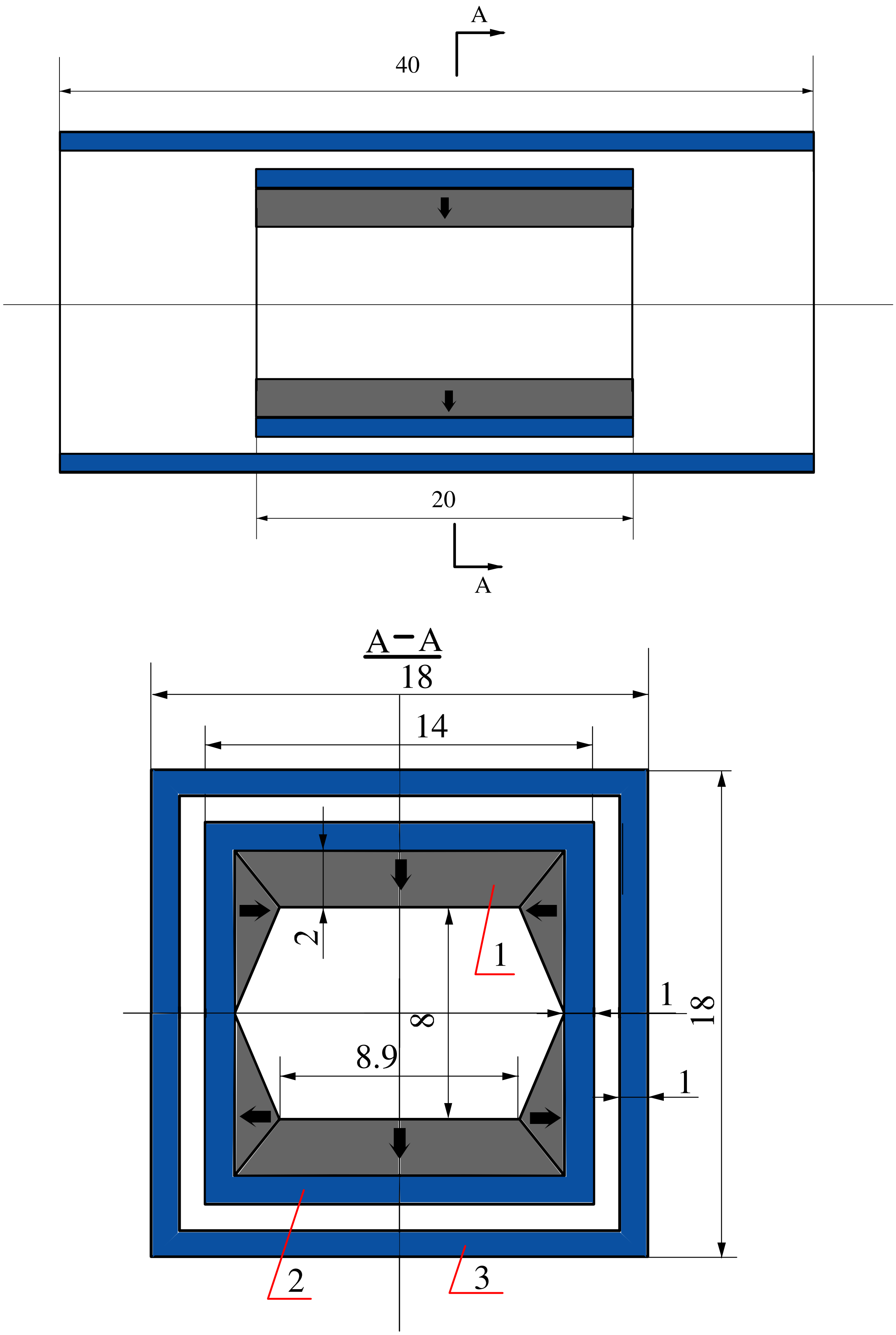

Figure 105:Schematic drawing of the extraction magnet. The numbers in the lower drawings indicate: (1) REPM material; (2) the yoke; (3) the magnetic screen.

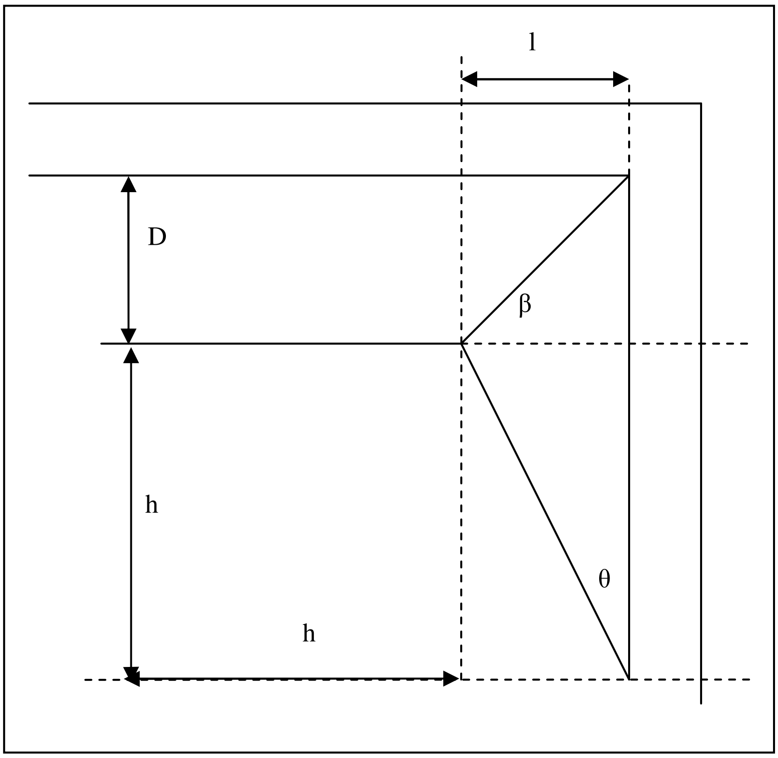

Figure 106: Parameterization of the geometry of the extraction magnet in the transverse cross section. Only the quarter of the cross section in the first quadrant of the YZ-plane is shown.

### 4.2.3. – 2D extraction magnet design.

To fix the parameters characterizing the geometry of the extraction dipoles and obtain the residual magnetization of the REPM blocks we performed 2D design simulations using the FEMM code [89]. Unlike the POISSON, used for the 2D end magnet simulations in the previous sections, the FEMM code is based on the finite element method.

In the simulations the material chosen for the yoke and magnetic screen was the low carbon steel 1010, whereas the material of the spacer was aluminum of the relative magnetic permeability $\mu_r$=1. The relative magnetic permeability of the REPM blocks was taken to be $\mu_r$=1.0.

Due to the space limitations the dimensions of the extraction dipole elements were chosen as follows: the thickness of the trapezium-shape REPM block $D$=2 mm, the vertical half-aperture $h$=4 mm, and the yoke, spacer and screen thicknesses equal to $d_{yoke} = d_{spacer} = d_{screen}$ = 1 mm. The parameters $h_1$ and $l$ determining the horizontal half-aperture and the angle θ of the triangle REPM blocks (see Fig.106) were fixed by the optimization of the magnet geometry under the condition of the maximal uniformity of the vertical component of the magnetic field in the working aperture. The values obtained in the 2D simulations are $h_1$=4.45 mm and $l$=1.55 mm. Then the width of the working aperture in the median plane is equal to 2 $h_1+2l$=12 mm and the dimensions of the yoke box and the whole magnet in the transverse plane are 14 mm x 14 mm and 18 mm x 18 mm, respectively.

The magnetic field distribution $B_{sum}$, sum of the components (x-y-z) of the magnetic field, for the extraction magnet of the 5th (last) orbit with $E_5$=12.611 MeV obtained with the FEMM code is shown in Fig. 107. The plot of the vertical component $B_y$ in the median plane and vertical symmetry plane given in Fig. 108 illustrates the achieved field homogeneity within the working aperture region 5 mm x 5 mm. One can check that the relative field variation across the working aperture calculated as $\pm(B_{\max}-B_{\min})/(B_{\max}+B_{\min})$, where $B_{\max}$ and $B_{\min}$ are the maximal and minimal values in the interval 0<x<5.0mm, gives ±0.55%, so that specification S-EM-2 is fulfilled.

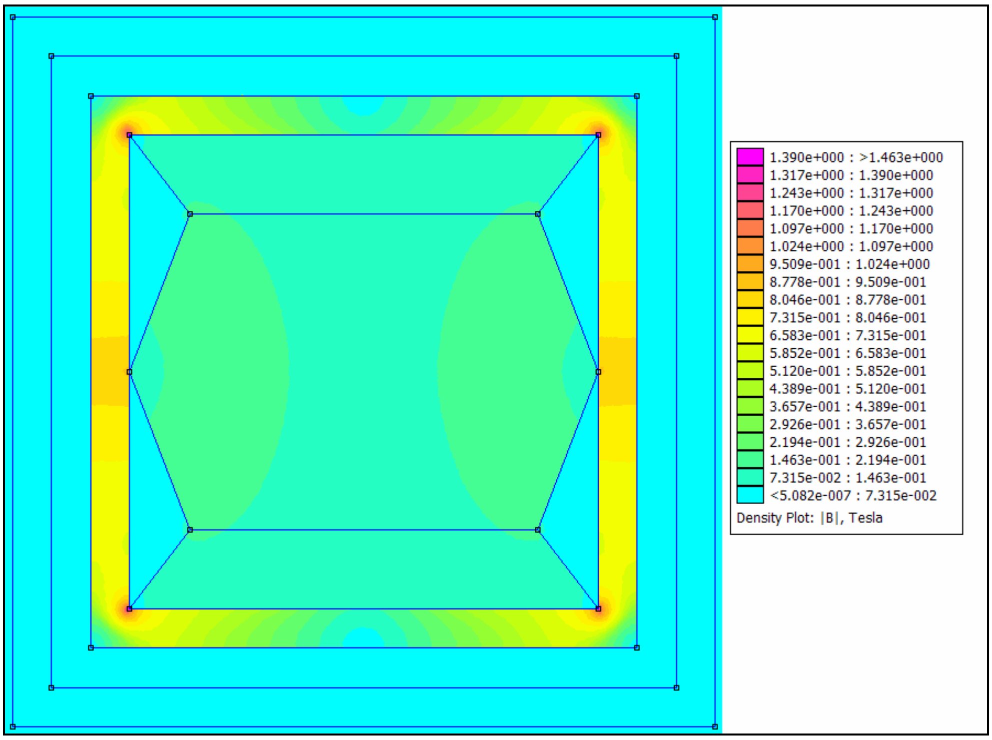

Figure 107: Magnetic field flux density $B_{sum}$ obtained in 2D simulations of the extraction magnet of the 5th orbit using FEMM code.

As it was already mentioned in the previous section the design considered here is not the ideal QSM design with rectangular working region. Hence the optimized magnet dimensions do not fulfil relations (108) and (109). Indeed, in our case the value $2\beta = 104.4^{\circ}$, whereas $\pi/2+\theta = 111.2^{\circ}$. Also, $D\sqrt{h/(2D+h)} = 1.41$ mm, whereas $l = 1.55$ mm. These differences with respect to values obtained from Eqs. (108) and (109) illustrate the level of deviation of our extraction dipole design from the ideal QSM one.

As it was already explained above, all four extraction magnets have exactly the same geometry and dimensions. The same bending angle for different energies is achieved by the appropriate magnetization of the REPM blocks in each magnet. With the FEMM one can calculate the residual magnetization $B_r$ for a given magnetic field in the median plane. To get an estimate of $B_r$ we assume an effective length $L_{eff}$=0.21 mm (this value will be justified in the 3D simulations). In Table 20 the values of the magnetic field and REPM residual magnetization necessary to generate this field for each extraction magnet are given.

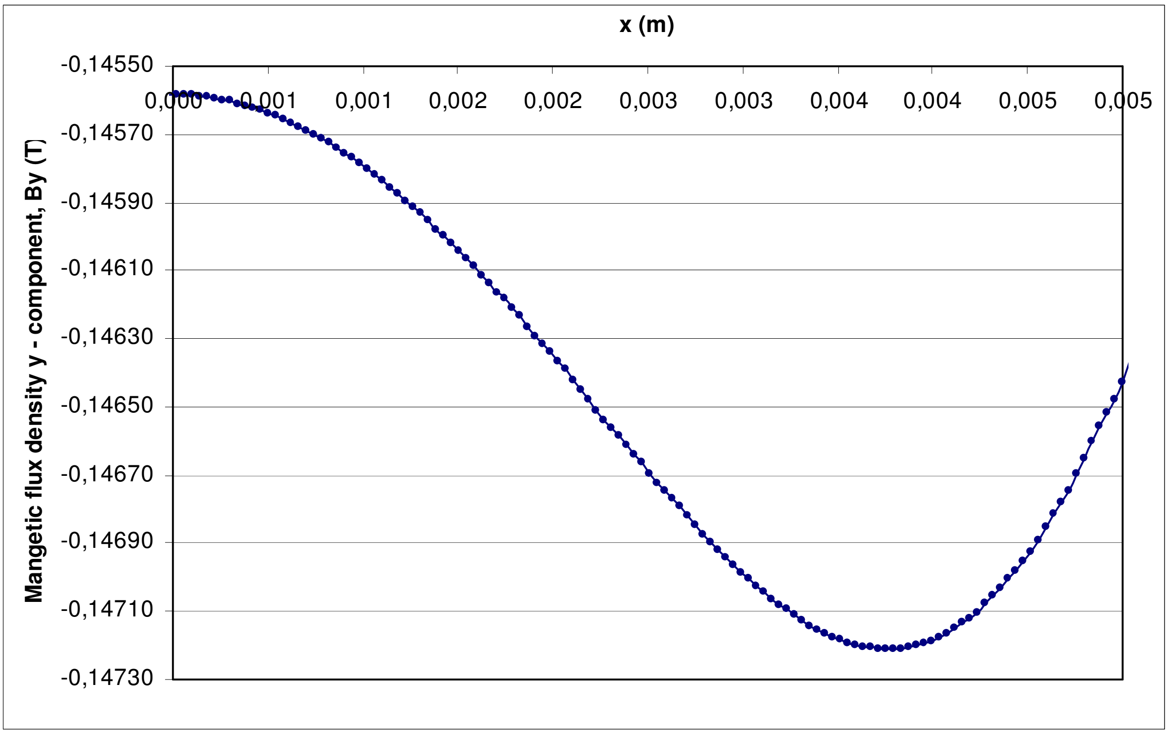

Figure 108: The vertical component $B_y$ of the magnetic flux density in the median plane and vertical symmetry plane of the extraction dipole of the 5th orbit ($E_5$=12.611 MeV) as a function of the horizontal transverse coordinate *X*.

Table 20: The vertical component $B_y$ of the magnetic flux density and the REPM residual magnetization for each extraction magnets calculated with the FEMM code.

| Orbit number *n* | $p_n$ (MeV/c) | $B_{ext,n}$ (T) | $B_{r,n}$ (T) |
|---|---|---|---|
| 2 | 6.511 | 0.0895 | 0.2652 |
| 3 | 8.556 | 0.1178 | 0.3486 |
| 4 | 10.579 | 0.14560 | 0.4308 |
| 5 | 12.601 | 0.17346 | 0.5133 |

As it was already mentioned above the 2D approach does not allow the calculation of the magnetic field integrals $I_n$. For this one has to use a 3D code, in our case it will be ANSYS.

To finish this section we would like to note that the results of 2D simulations given here with the FEMM code are in agreement with results obtained with PANDIRA code in parallell studies performed by members of the UPC 12 MeV RTM project [66].

### 4.2.4 – 3D extraction magnet design.

The dimensions of the extraction dipoles obtained in the 2D simulations and described in the previous section were used to define the 3D geometry (see Fig.109). Due to the magnet symmetry with respect to the median plane and central vertical plane in the simulations of the magnetic field it is sufficient to consider only one quarter of the full magnet imposing appropriate boundary conditions at the symmetry planes. The materials of the parts of the dipoles used in the 3D simulations with ANSYS are the same materials as in the 2D simulations with the FEMM code (see Sect. 4.2.3).

Following the criterion “reasonable magnetic field for a reasonable length” the length of the yoke and REPM blocks in the longitudinal direction (Z-direction) was chosen to be $L_{yoke}$=20 mm (see Fig.105). The length of the screen was optimized in the 3D simulations as it will be explained briefly. The size of mesh elements used in the 3D simulations of the extraction dipoles was chosen to be 0.5mm.

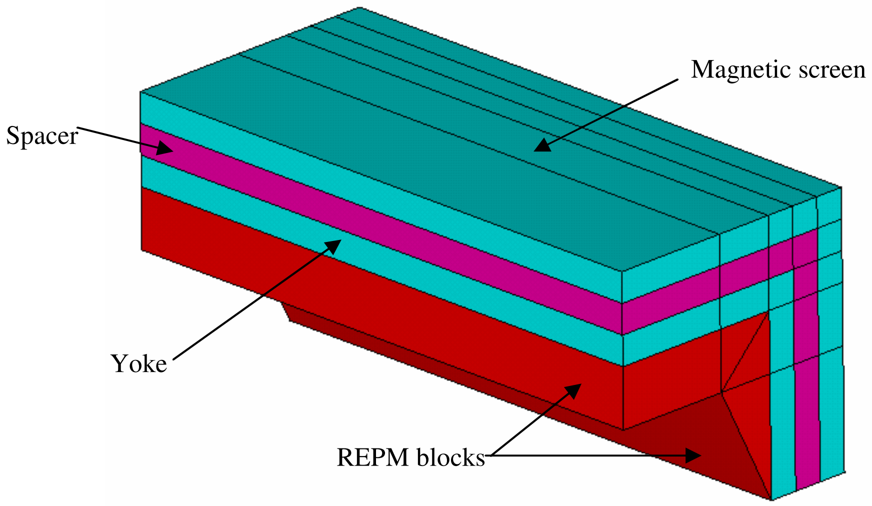

Figure 109: 3D geometry of the extraction dipoles used in simulations with the ANSYS code.

The first step was to fix the length of the magnetic screen $L_{screen}$ with the condition that the stray field at the entrance and exit of the extraction magnet does not exceed the level of $10^{-4}$ T as prescribed by specification S-EM-3. A series of simulations with increasing $L_{screen}$ were performed until the criterion is fulfilled. In each computation the value of the field in certain points was controlled, one of them situated at X=1.2cm, Z=2.3 cm is marked by the red dot in Fig.110. The simulations were began with the minimal screen length $L_{screen}$=20 mm in which case the value of the field at the point indicated above was $B_{sum}$=1.796x$10^{-3}$ T, the corresponding distribution of the stray field in the median plane is shown in Fig.110a. Then simulations were repeated for larger values of $L_{screen}$ until the field in the control points fulfills the requirement. As a result the screen length was fixed at $L_{screen}$=40 mm (see Fig.106) for which the calculated field at the marked point is equal to $B_{sum}$=0.416x$10^{-4}$ T, the corresponding stray field distribution is shown in Fig.111b.

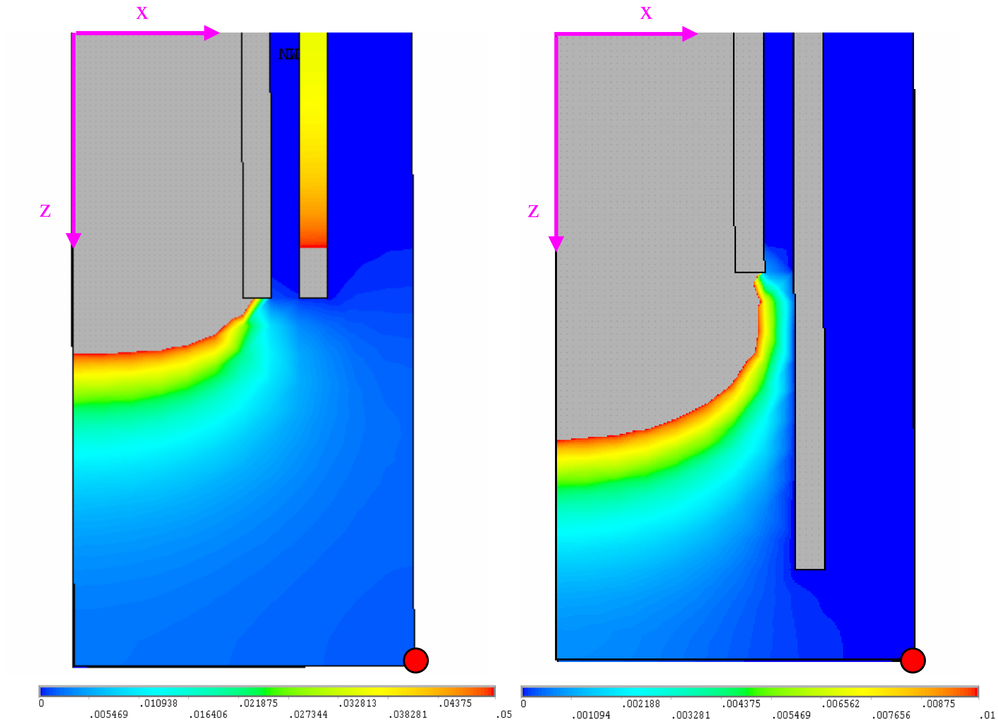

(a) (b)

Figure 110: Stray field distribution in the median plane at the entrance of the extraction magnet of the 5th orbit for two values of the magnetic screen length: (a) $L_{screen}$=20 mm, (b) $L_{screen}$=40 mm. The coordinates of the marked point are X=1.2cm, Z=2.3 cm. In the regions colored with grey color the magnetic field values are outside the scales given below the figures.

After fixing the length of the magnetic screen we calculated the magnetic characteristics of the extraction dipoles for the residual magnetizations of the REPM blocks obtained previously with the FEMM code and listed in Table 20. The results of these 3D simulations are given in Table 21. One can see that the value of the vertical component of the magnetic field $B_{ext,n}$ in the median plane and the central symmetry plane has reduced by 0.3% with respect to the FEMM results, whereas the field integrals $I_n$ obtained by integration along the straight line X=0, Y=0 in the range -30.0mm < Z <30.0mm are about 2.6 % smaller. As it immediately follows from Eq.(107) for these values of $I_n$ the deflection angle would be equal approximately to 4.85 °, well below the required value of α=5 °.

Table 21: Vertical components of the magnetic flux density $B_{ext,n}$ and field integrals of the extraction dipoles obtained in the 2D simulations with FEMM and 3D simulations with ANSYS for the residual magnetization given in Table 20.

| Orbit number $n$ | $p_n$ (MeV/c) | $B_{ext,n\ FEMM}$ (T) | $B_{ext,n\ ANSYS}$ (T) | $I_n$ (Tm) RTMTRACE | $I_n$ (Tm) ANSYS |
|---|---|---|---|---|---|
| 2 | 6.511 | 0.0895 | 0.0894 | 1.89 x$10^{-3}$ | 1.84 x$10^{-3}$ |
| 3 | 8.556 | 0.1178 | 0.1175 | 2.49 x$10^{-3}$ | 2.42 x$10^{-3}$ |
| 4 | 10.579 | 0.1456 | 0.1450 | 3.08 x$10^{-3}$ | 2.99 x$10^{-3}$ |
| 5 | 12.601 | 0.1735 | 0.1730 | 3.66 x$10^{-3}$ | 3.57 x$10^{-3}$ |

As the dimensions of the parts of the extraction magnets were fixed and could not be changed we varied the residual magnetization of the REPM blocks in order to adjust the values of the field integrals $I_n$ to the ones calculated with the RTMTRACE and listed in Table 20. The results obtained in this optimization process for each extraction magnet using the ANSYS code are given in Table 22. The effective lengths of the dipoles were calculated as $L_{eff,n} = I_n / B_{extr,n}$, where $B_{extr,n}$ is the magnetic flux density in the centre of the magnet at the *n*th orbit. As one can see, in order to adjust the field integrals the residual magnetizations and the field at the centre of the dipoles (at the point X=Y=Z=0) were increased. After this the deflection angles became equal to the required value α=5°. The distributions of the vertical components of the magnetic flux density $B_{y,n}$ along the Z-axis in the center of the median plane, i.e. for X=Y=0, are shown in Fig.111. As it can be seen from these plots the functions $B_{y,n}$(0,0,Z) decrease rapidly at the edge of the REPM blocks in the longitudinal direction in a region around to the edge of the REPM blocks (recall that $L_{yoke}$=2 cm). We would like to mention that for the dipoles with higher values of the magnetic field in the center the width of the fringe field region in the Z-direction is larger.

Table 22: Characteristics of the extraction dipoles after the adjustment of the residual magnetizations $B_{r,n}$ of their REPM blocks: vertical component of the magnetic flux density $B_{extr,n}$, field integral $I_n$, effective length $L_{eff,n}$ and deflection angle α.

| Orbit number *n* | $p_n$ (MeV/c) | $B_{r,n}$ (T) | $B_{extr,n.ANSYS}$ (T) | $I_n$ (Tm) | $L_{eff,n}$ (cm) | α (°) |
|---|---|---|---|---|---|---|
| 2 | 6.511 | 0.2727 | 0.0918 | $1.89 \times 10^{-3}$ | 2.06 | 5 |
| 3 | 8.556 | 0.3590 | 0.1208 | $2.49 \times 10^{-3}$ | 2.06 | 5 |
| 4 | 10.579 | 0.4442 | 0.1499 | $3.08 \times 10^{-3}$ | 2.05 | 5 |
| 5 | 12.601 | 0.5280 | 0.1778 | $3.66 \times 10^{-3}$ | 2.06 | 5 |

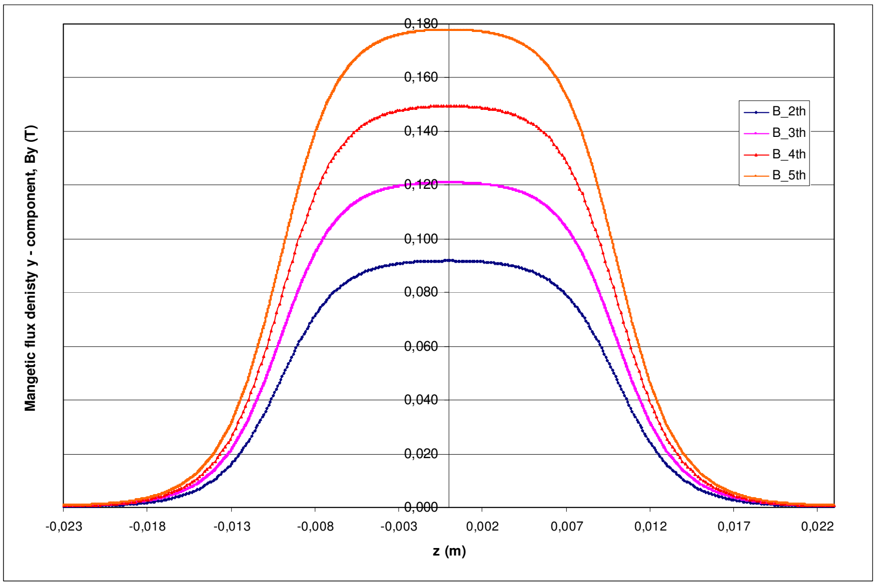

Figure 111: Plots of the vertical components of the magnetic flux densities $B_{y,n}$(0,0,Z) as functions of Z for the four extraction dipoles (*n*=2,3,4,5).

As the next step the uniformity of the magnetic field in the working region of the extraction dipoles was studied using the data obtained in the 3D simulations. For this we analyzed the distributions of the vertical components of the magnetic flux density in the horizontal transverse direction in the median plane and vertical symmetry plane (Z=0). As an example in Fig. 112 the plot of such function for the extraction dipole of the last orbit (5th orbit) is given. The field variation across the working region is approximately

±0.7%. From the results of the study we conclude that the requirement of the field uniformity imposed by specification S-EM-2 is fulfilled.

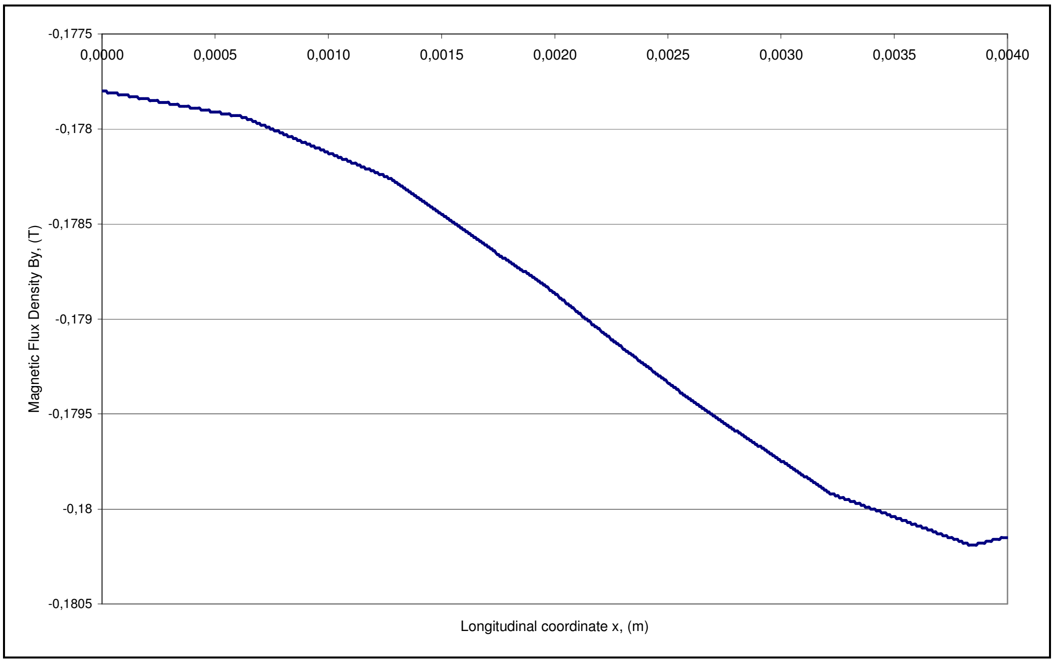

Figure 112: Vertical component of the magnetic flux density $B_y(X,0,0)$ in the median plane and the magnet centre of the extraction dipole of the 5th orbit as a function of the horizontal transverse coordinate X.

Finally we checked that the level of the stray magnetic field around the extraction dipoles is low enough. We chose a set of control points situated at the distance 3 mm from the outer surface of the magnetic screen, as it is shown in Fig. 113, and using the data of the 3D simulations with the ANSYS code obtained the values of the magnetic flux density at these points, the results are given in Table 23. As one can see the values of $B_{sum}$ listed there do not exceed 0.41 G, so we conclude that specification S-EM-3 is fulfilled.

Table 23: Stray magnetic field induction $B_{sum}$ at the points indicated in Fig.114.

| **Point** | **Stray magnetic field induction $B_{sum}$ (T)** |
|---|---|
| 1 | $0.504 \times 10^{-6}$ |
| 2 | $0.312 \times 10^{-4}$ |
| 3 | $0.432 \times 10^{-7}$ |
| 4 | $0.194 \times 10^{-5}$ |
| 5 | $0.409 \times 10^{-4}$ |

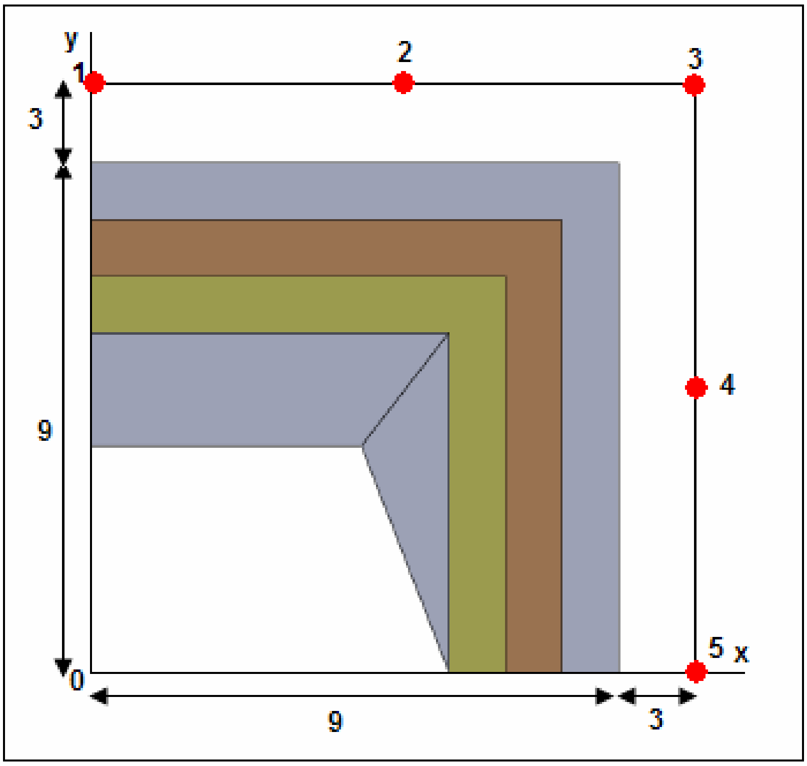

Figure 113: Cross section of the extraction dipole at the magnet centre plane $Z$=0 and the points (marked in red) at which the level of the stray field is evaluated.

### 4.2.5 – Concluding remarks on the extraction system design.

After choosing the most suitable QSM type geometry with rectangular working region for the extraction dipoles of the UPC 12 MeV RTM we performed 2D design simulations using the FEMM code which allowed us to fix some of their dimensions and magnetic characteristics. The design was completed and optimized by carrying out 3D simulations with the ANSYS code. As a result we got a full set of parameters, given in Fig. 106 and in Table 22, necessary for the detailed technical design of the extraction dipoles. With the data obtained in the simulations we confirmed that the proposed design meets specifications S-EM-1 – S-EM-4 and therefore the magnets will provide the correct extraction of the beam from the last four orbits of the RTM.

We would like to mention that in the proposed design of the extraction magnets no adjustment mechanism is foreseen. It is supposed that in order to get the specific residual magnetization of the REPM blocks one of the following approaches will be applied: (a) use the magnetoplast technology to manufacture pieces of the REPM material with the required value of $B_{n,r}$, or (b) use the demagnetization technique to adjust the standard REPM material residual magnetization to the required level. The final choice of the technology will be done at the stage of engineering design.

According to the design of the UPC 12 MeV RTM the four extraction dipoles will be fixed in a frame with some vertical displacement with respect to each other (see Fig. 114 so that the vertical distance between the centre of the dipole of the 2nd orbit (situated to the right in Fig. 114) and the bottom end of dipole of the 5th orbit magnet does not exceed the half height of the end magnet (58 mm, see Sect. 4.1). In the horizontal direction the magnet centres are positioned approximately at the return paths. This assembly of the extraction magnets is moved vertically by means of a stepper motor which is situated outside the vacuum chamber and rotates a frame shaft via a bellow unit. To extract the electrons from a given orbit the corresponding dipole is placed in such a way that its axis coincides with the corresponding orbit path in the RTM median plane. The position of the assembly of the extraction dipoles inside the vacuum chamber is shown in Fig.8.

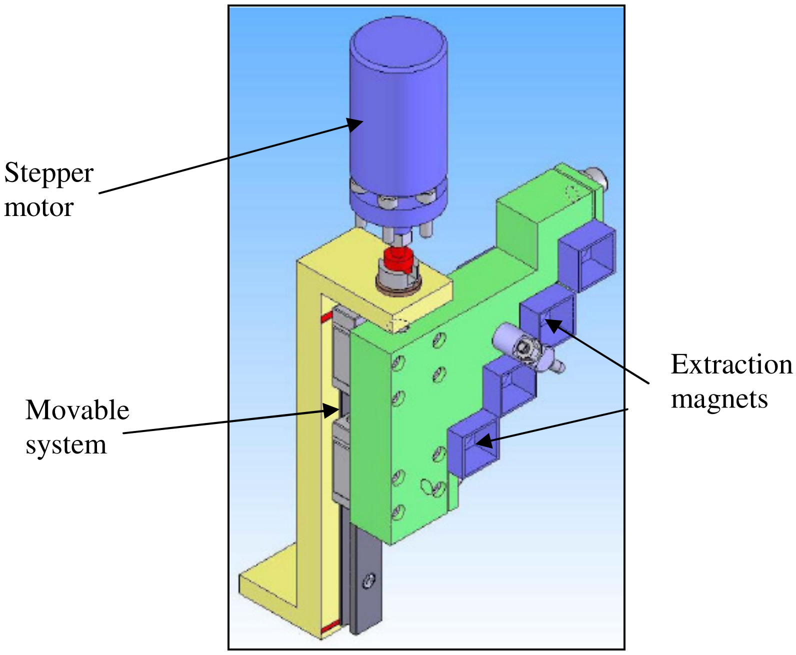

Figure 114: System of extraction magnets of the UPC 12 MeV RTM.

## 4.3. – Focusing magnet of UPC 12 MeV RTM.

According to the design of the UPC 12 MeV RTM the vertical beam focusing is due to the proper adjustment of the main pole fringe field and the field of the inverse pole of the end magnets. This was demonstrated in Sect.4.1. The horizontal beam focusing is provided by a dedicated quadrupole magnet.

Usually in RTMs focusing magnets are installed either on the common axis or on the return paths, and sometimes on both. Installing them at the return paths should be avoided because in this region the beam has dispersion after passing the end magnet and the beam can be displaced off the quadrupole axes and thus can get transverse kick from the magnet.

Studies of beam dynamics of the UPC 12 MeV RTM performed with the RTMTRACE code showed that in order to maintain the beam stability it is sufficient to place one focusing magnet on the common axis between the end magnet and the electron gun as it is shown in Fig. 115 [66]. Its location on the supporting platform can be also seen in Fig. 8 giving the general view of the elements inside the vacuum chamber of the accelerator.

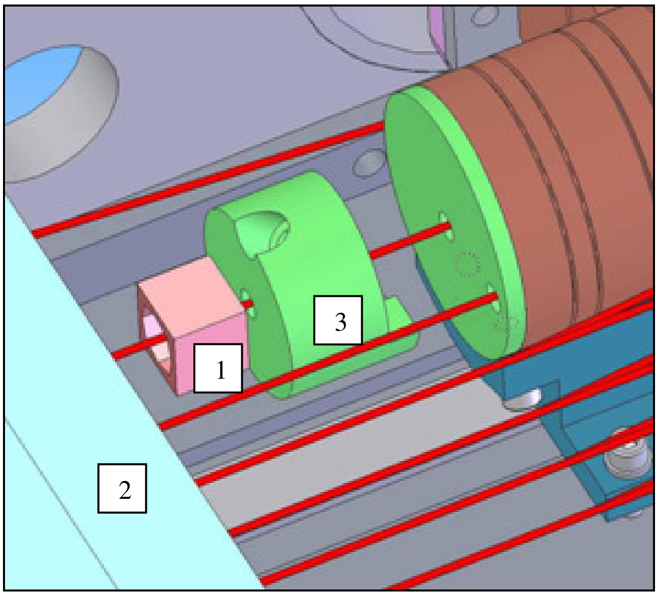

Figure 115: Position of the quadrupole magnet of the UPC 12 MeV RTM. The numbered components are: (1) quadrupole magnet, (2) end magnet, (3) electron gun.

As it was shown in Ch.2 in the case of the ideal quadrupole magnet the vertical and horizontal components of the magnetic field in its transverse plane are given by Eqs.(19), (20). The focusing strength $k$ is related to the field gradient $g$ by the formula $k = -|e|g / p$ and the horizontal focusing power of the magnet is given by

$$\frac{1}{f_x} = kl = -\frac{|e|}{p} gl. \qquad (119)$$

Here $p$ is the particle momentum and $l$ is the quadrupole length.

In the case of a realistic focusing magnet the field changes in the longitudinal direction and the gradient is not constant within the working aperture. A more appropriate description is

$$B_y(x, y, x) = G(x, y, z)x. \qquad (120)$$

The horizontal focusing power of such magnet is determined by the integrated magnetic gradient

$$K = \frac{1}{x} I_y(x) \equiv \frac{1}{x}\int_{z1}^{z2} B_y(x,0,z)dz = \int_{z1}^{z2} G(x,0,z)dz \qquad (x \neq 0) \qquad (121)$$

through the relation

$$\frac{1}{f_x} = -\frac{|e|}{p} K. \qquad (122)$$

The integration in Eq.(121) goes along the interval in *z* for which the field of the magnet is different from zero. Strictly speaking the integrated gradient *K* depends on *x*, we will see that this dependence is quite weak. Formula (121) can also be written as

$$K = G_{2D} L_{eff}\,, \tag{123}$$

where the magnet effective length $L_{eff}$ is defined as

$$L_{eff} = \frac{1}{B_y(x,0,0)} \int_{z1}^{z2} B_y(x,0,z)dz \qquad (x \neq 0) \tag{124}$$

and the effective field gradient $G_{2D}$ in the central (*z*=0) transverse plane is given by

$$G_{2D} = \frac{1}{x} B_y(x,0,0) \qquad (x \neq 0). \tag{125}$$

For the magnet to be a quadrupole type lens the gradient $G_{2D}$ should be approximately constant in a small vicinity of the point *x*=0.

### 4.3.1. – Focusing magnet design considerations and geometry.

According to the beam dynamics study performed with the RTMTRACE code the focusing magnet must meet the following specifications:

S-FM-1. The integrated magnetic gradient *K* on the central axis of the magnet is equal to $K_0 = -2.0 \times 10^{-2}$ T.

S-FM-2. The relative maximal deviation $|\Delta K / K|$ of the value of the integrated magnetic gradient within the interval from *x*=-7.0 mm to *x*=7.0 mm in the horizontal plane *y*=0 must be less than 0.5%.

S-FM-3. The stray magnetic field of the focusing magnet at the location of the return path of the first orbit (4 MeV), i.e. at the distance *x*=2.6 cm from the magnet axis, must be less than $10^{-4}$T.

S-FM-4. The stray magnetic field of the focusing magnet at the position of the electron gun must be less than $10^{-4}$T.

S-FM-5. The transverse size of the focusing magnet in the horizontal plane must be less than 3 cm, the useful working aperture diameter must be larger than 1 cm.

A few comments are in order. Specification S-FM-4 means that the magnetic field produced by the focusing magnet at the position of the electron gun has to be small enough so that it does not affect emitted electrons trajectories and therefore does not generate beam instability. The limit, set by specification S-FM-5, guarantees that the external transverse dimensions of the quadrupole are sufficiently small so that the magnet does not disturb the first orbit trajectory. The working aperture must be as large as possible to avoid losses of electrons in the focusing lens.

Since the focusing magnet is placed inside the vacuum chamber it was decided to use permanent magnets to generate the magnetic field. There are a few designs of quadrupole magnets with REPM material described in the literature: K. Halbach design [91], spilt-pole design [92] and QSM design [93]. The difference between them is in the number of permanent magnet blocks used, their distributions around the working aperture, the working aperture size and the maximum value of the gradient that can be achieved.

For the design of the horizontally focusing quadrupole of the UPC 12 MeV RTM the QSM design was chosen. Its main advantage is that a less permanent magnet blocks are used so that it allows to obtain a rather compact and simple system with a large working aperture. Previously the QSM design was used, for example, in a triplet of quadrupole magnets of the SINP 70 MeV RTM [93].

The chosen QSM-type quadrupole magnet consists of a rectangular yoke with triangular shape REPM blocks with equal magnetizations attached to it as shown in Fig. 116. The working aperture is limited by plane face facets of the permanent magnets. Such QSM quadrupoles are analogs of the Panofsky lens.

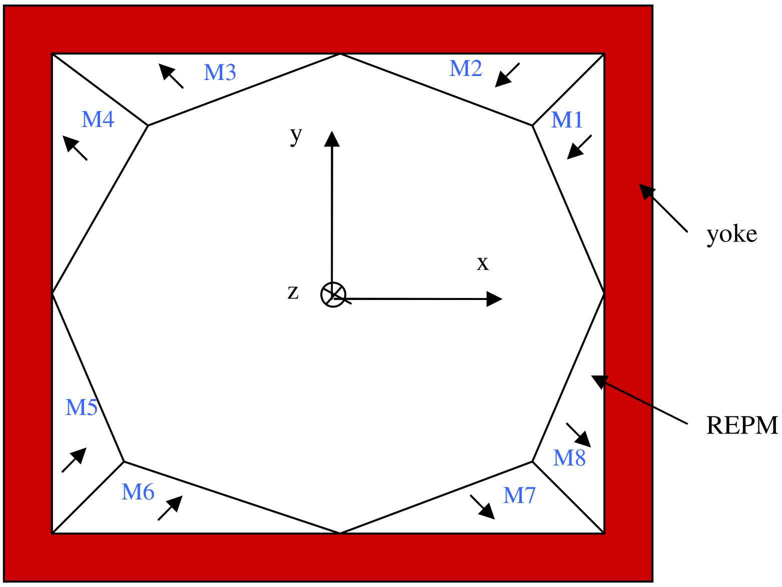

Figure 116: QSM-type quadrupole magnet cross section. The coordinate system used for its description and simulations and REPM block magnetization vectors are shown.

As it is shown in Ref. [34] in order to exclude molecular currents at the surfaces of the REPM blocks certain requirements must be fulfilled, namely

(a) The block magnetization vectors must be normal to the face facets,
(b) If the blocks have the same magnetization, which is our case, the mutual facet must bisect the angle between two neighbouring face facets.

Due to the existing symmetry it is sufficient to consider only one quarter of the magnet cross section. The dimensions of the yoke, REPM blocks and working aperture are determined by the angles β and ψ and other geometrical parameters shown in Fig. 117. In the design of the quadrupole of the UPC 12 MeV RTM a square-shape yoke was chosen. The REPM block magnetization vectors are normal to the face facets. Under these conditions the angle β=45° and $H=ha+Da$ so that requirements (a) and (b) above are fulfilled. This geometry is shown in Fig. 118. The quadrupole working aperture is characterized by the radius $r_0$ which is related to the yoke internal half height by the formula

$$H = \frac{r_0}{\cos\psi}. \tag{126}$$

Using simple geometrical considerations one obtains that

$$ha = r_0 \frac{\sin(\beta)}{\cos(\beta-\psi)}, \qquad Da = hb = ha\tan(\psi) \tag{127}$$

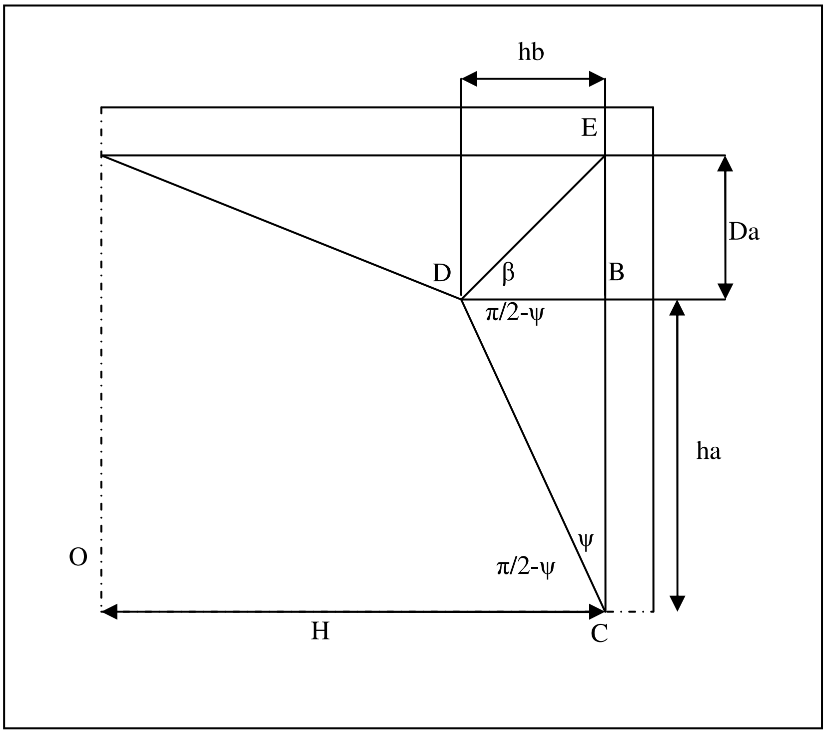

Figure 117: Parameterization of the quadrupole magnet geometry.

From the main relations of the QSM quadrupole magnets it follows that the field gradient $G_{2D}$ inside the working region is expressed through the REPM block residual magnetization $B_r$ and its geometrical parameters as follows [34]:

$$\left|G_{2D}\right| = \frac{B_r}{2r_0}\sin 2\psi. \tag{128}$$

This formula will be used in the next section for estimating $B_r$ in our design.

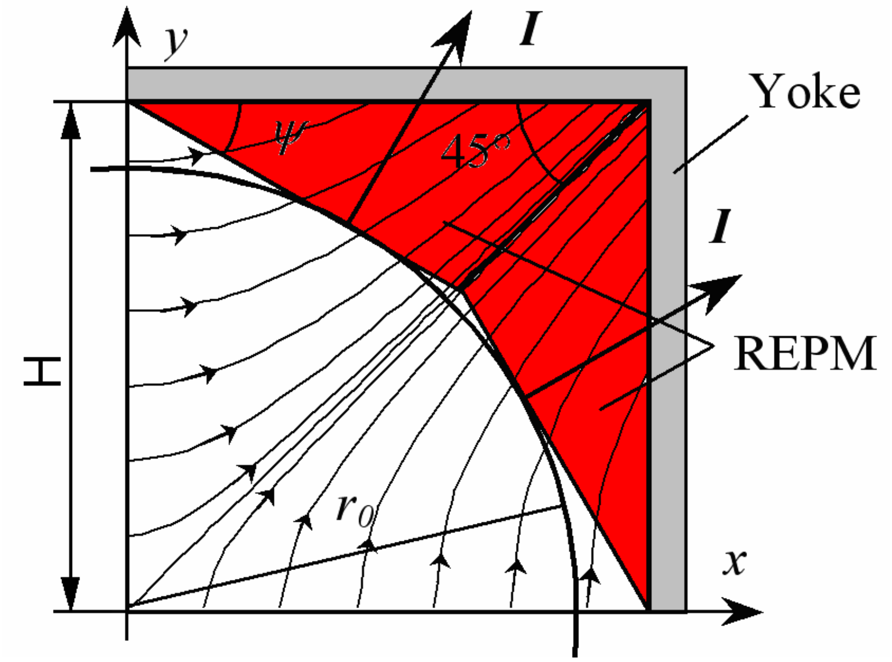

Figure 118: First quadrant of the cross section of the quadrupole magnet with square-shape yoke.

Similar to the design calculations of the RTM end magnets and extraction dipoles described in the previous sections of this chapter we will first perform 2D simulations and fix main geometrical parameters. As a next step 3D simulations using ANSYS code will be carried out which will allow us to take into account the finite size of the quadrupole magnet in the longitudinal direction and adjust the REPM block magnetization in order to fulfill the design specifications.

### 4.3.2 - 2D design simulations of the quadrupole magnet.

On the basis of preliminary design studies the angles determining the REPM geometry and the working aperture radius were chosen to be equal to the values listed in Table 24 [66].

Table 24: Main quadrupole parameters.

| Parameter | Value |
|---|---|
| $r_0$ | 8 mm |
| ψ | 15° |
| β | 45° |

Using relations (115) and (116) and the fact that the REPM block magnetization vectors are perpendicular to their face facets one gets the dimensions and magnetization vector orientation of these blocks given in Tables 25 and 26.

Table 25: Dimensions of the REPM blocks.

| Parameter | Units | Value |
|---|---|---|
| ha | mm | 6.5357 |
| Da | mm | 1.744 |
| hb | mm | 1.744 |
| H | mm | 8.282 |

Table 26: Angles formed by the magnetization vectors of the REPM blocks with the positive direction of the x-axis.

| Angle | Value (º) |
|---|---|
| $\psi_1$ | 195 |
| $\psi_2$ | 255 |
| $\psi_3$ | 105 |
| $\psi_4$ | 165 |
| $\psi_5$ | 15 |
| $\psi_6$ | 75 |
| $\psi_7$ | 285 |
| $\psi_8$ | 345 |

To obtain an estimate of the effective field gradient $G_{2D}$ and then the residual magnetization $B_r$ by means of formula (118) one has to know the value of the integral in the definition of the magnet effective length $L_{eff}$ in Eq. (115a). In Ref.[64] in order to get the field distribution in the z-direction a simplified model of the magnet shown in Fig. 119 was studied. The field was generated by a permanent magnet block of width *w* and height *h*. Simulations performed with the POISSON code for w=3 mm, h= 3 mm and the yoke internal half height H=8.282 mm (see Table 25) gave $L_{eff} = 1.015\,\text{cm}$. Then from Eqs. (115) and (118) we obtain $G_{2D} = 1.97\,\text{T/m}$ and $B_r = 0.063\,\text{T}$. As we will see in the next section the 2D longitudinal model is too rough and the estimate for the residual magnetization obtained from it is too approximate, it will be corrected in the 3D simulations.

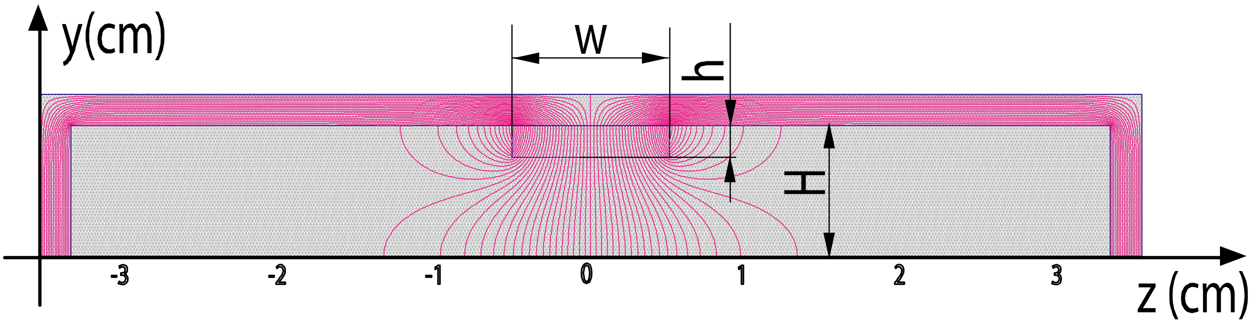

Figure 119: Simple 2D longitudinal model of the quadrupole magnet used for the calculation of the longitudinal field distribution.

In order to check the considerations and estimates given above we performed 2D simulations of the quadrupole magnets using the FEMM code [89]. The geometrical parameters and the magnetizations vectors of the REPM blocks were chosen according to Tables 24-26, their residual magnetization was taken to be $B_r = 0.063$ T. The material of the yoke was the low carbon steel 1010, the relative magnetic permeability of the permanent magnet was $\mu_r$ =1.03. The yoke thickness was taken to be equal to 2.22 mm. This was shown to be enough to have the stray magnetic field below 1G at the position of the neighbor orbit.

In Fig. 120 the map of the magnetic induction $B_{sum}$ and magnetic flux lines obtained in these simulations are shown. The vertical y-component of the magnetic flux density $B_y(x,0,0)$ as a function of $x$ for z=0, y=0 is plotted in Fig.121. As one can see, this function is practically linear in $x$ and the field gradient is equal to $G(x,0,0) = 1.97\ \mathrm{T/m}$ within the interval $-7\ \mathrm{mm} < x < 7\ \mathrm{mm}$ with the precision better than 0.05%.

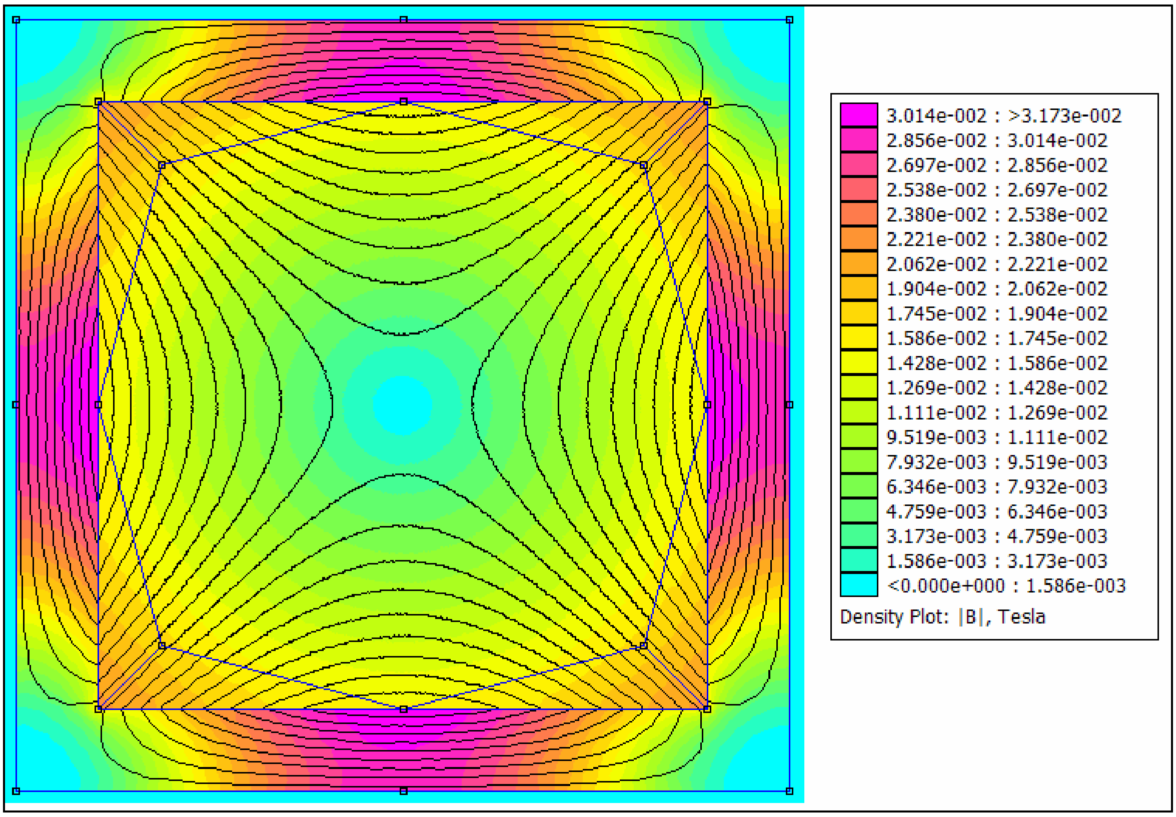

Figure 120: Magnetic flux lines and $B_{sum}$ obtained in the 2D simulations of the quadrupole magnet using the FEMM code.

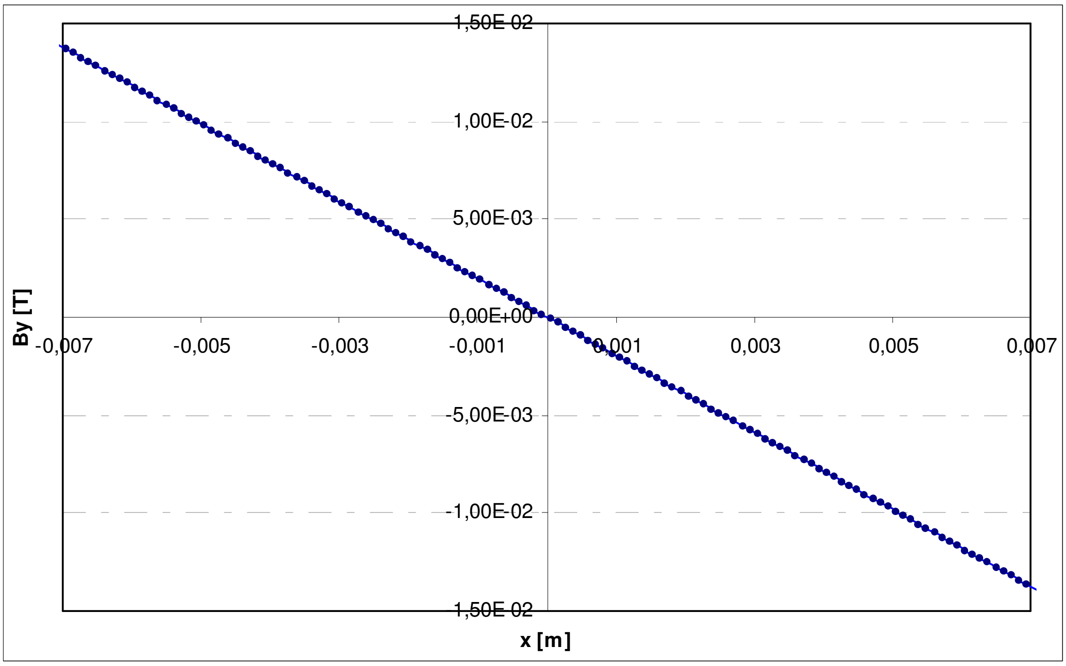

Figure 121: Vertical component of the magnetic flux density $B_y(x,0,0)$ in the symmetry plane $z$=0 and for $y$=0 as a function of the horizontal coordinate $x$.

### 4.3.3 - 3D design simulations of the quadrupole magnet.

As one can expect the magnetic properties of the quadrupole magnet depend on its geometry in the longitudinal direction which is not taken into account in the 2D simulations. To improve the design and adjust the magnet characteristics with the aim to fulfill specifications S-FM-1 – S-FM-5 we performed 3D simulations using the ANSYS code [87].

The 3D geometrical model used in these simulations is shown in Fig. 122. The dimensions and the material of the parts of the magnet are the same as in the 2D simulations. The length of the REPM blocks in the longitudinal direction (analog of the parameter $w$ in the previous section) was taken to be $L_{REPM} = 3$ mm, the length of the yoke $L_{yoke}$ is fixed below.

In order to take into account the magnetization direction of each permanent magnet block it was decided to simulate the complete structure of the quadrupole. We chose different mesh size for different parts of the magnet (see Fig.122) with the idea to have a finer mesh in the region where higher precision of the field values is required. The mesh sizes are summarized in Table 27.

Table 27: Mesh sizes used in the 3D simulations of the quadrupole magnet.

| Volume of the 3D geometry | Element mesh size (mm) |
|---|---|
| Working aperture | 0.5 |
| Yoke | 0.7 |
| REPM block | 0.7 |
| External space | 1.0 |

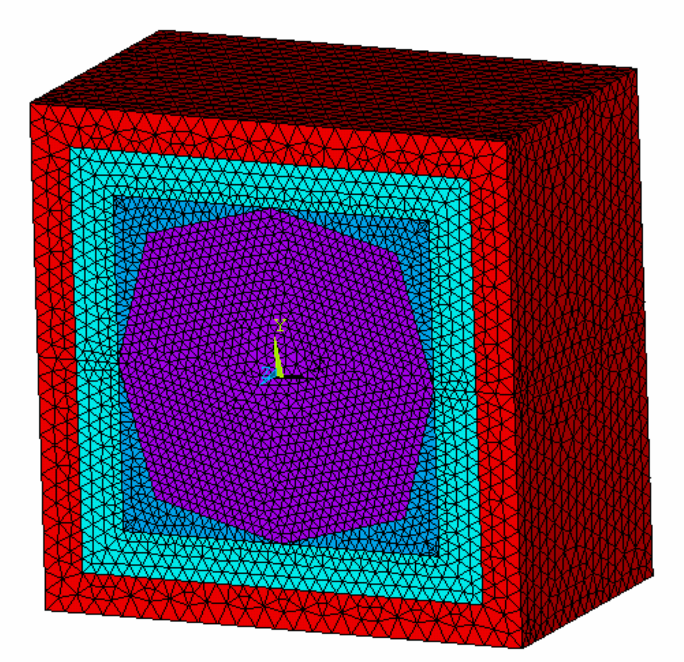

Figure 122: The 3D model of the quadrupole magnet and the mesh used in the simulations with the ANSYS code.

As a first step of the 3D design study we fixed the length of the yoke so that the requirement of low stray field level at the position of the first orbit (specification S-FM-3) is fulfilled. Since $L_{yoke} \geq L_{REPM} = 3$ mm we simulated the field produced by quadrupole magnet with the yoke length varied from $L_{yoke} = 3\,\text{mm}$ up to $L_{yoke} = 20\,\text{mm}$. The results for the two extreme cases, with the minimal and maximal yoke length, obtained in these calculations are shown in Fig. 123. The values of the magnetic flux density at the point in the orbit plane y=0 with coordinates *x*=1.35cm, *z*=1.3 cm are: $B_{sum} = 2.0\times10^{-4}\,\text{T}$ for $L_{yoke} = 3\,\text{mm}$ and $B_{sum} = 1.44\times10^{-6}\,\text{T}$ for $L_{yoke} = 20\,\text{mm}$. For the latter case specification S-FM-3 is fulfilled, so the yoke length was chosen to be $L_{yoke} = 20\,\text{mm}$.

Once the yoke length is fixed we performed simulations of the magnet with the residual magnetization of the REPM blocks equal to $B_r = 0.063\,\text{T}$ as it was given by the 2D estimate. We calculated the field distribution and analyzed the variation of the vertical component $B_y$ of the magnetic flux density in the symmetry plane *z*=0 and of the field integral $I_y$ defined in Eq. (112) across the working aperture. As an illustration in Fig.124 the plot of $B_y(x,0,0)$ as a function of the horizontal coordinate $x$ is given. As one can see the field gradient is clearly nonlinear within the working aperture. In fact, the relative deviation of the magnetic gradient is less than 5% in the range -3.0mm <*x* <3.0mm. More precisely, within this interval the gradient is $G(x,0,0) = -0.67 \pm 0.03\,\text{T/m}$. At the same time the field integral is practically linear within the working aperture and the integrated magnetic gradient is equal to $K = -0.6\times10^{-2}\,\text{T}$.

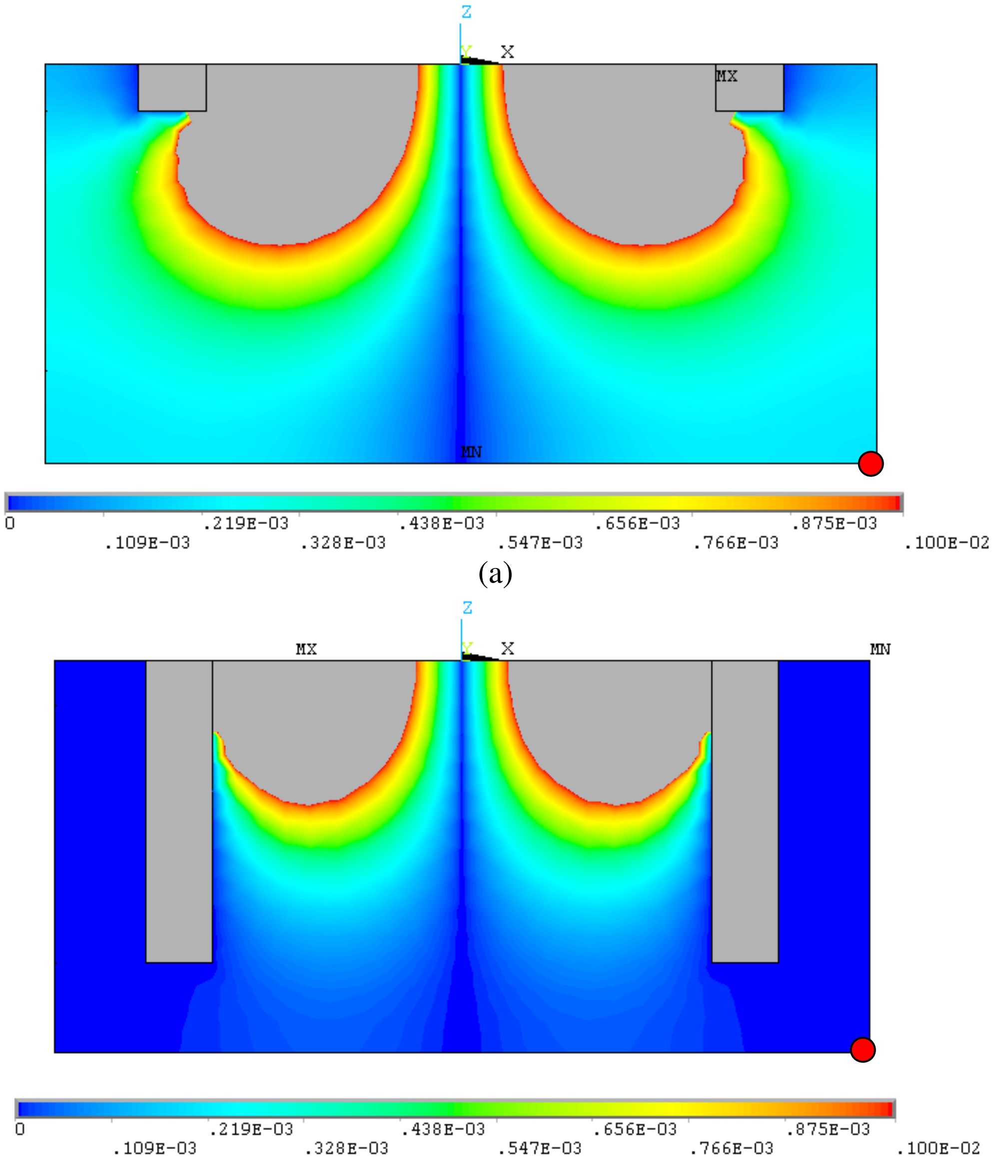

(a)

(b)

Figure 123: The stray magnetic fields distributions $B_{sum}$ in the median plane of the quadrupole for two different lengths of the yoke: (a) $L_{yoke} = 3$ mm and (b) $L_{yoke} = 20$ mm. In the regions colored in grey the values of the magnetic field are outside the scale given below the corresponding map. The coordinates of the red point are $x$=1.35cm, $z$=1.3 cm.

The obtained value is quite different from the integrated field gradient specified by condition S-FM-1. The reason is that the 2D estimate of the residual magnetization of the REPM blocks is very imprecise and cannot be used as an initial approximation. So we performed 3D simulations adjusting $B_r$ until the required value $K = -2.0 \times 10^{-2}$ T is obtained. As a result the value of the residual magnetization was fixed to be equal to $B_r = 0.227$ T.

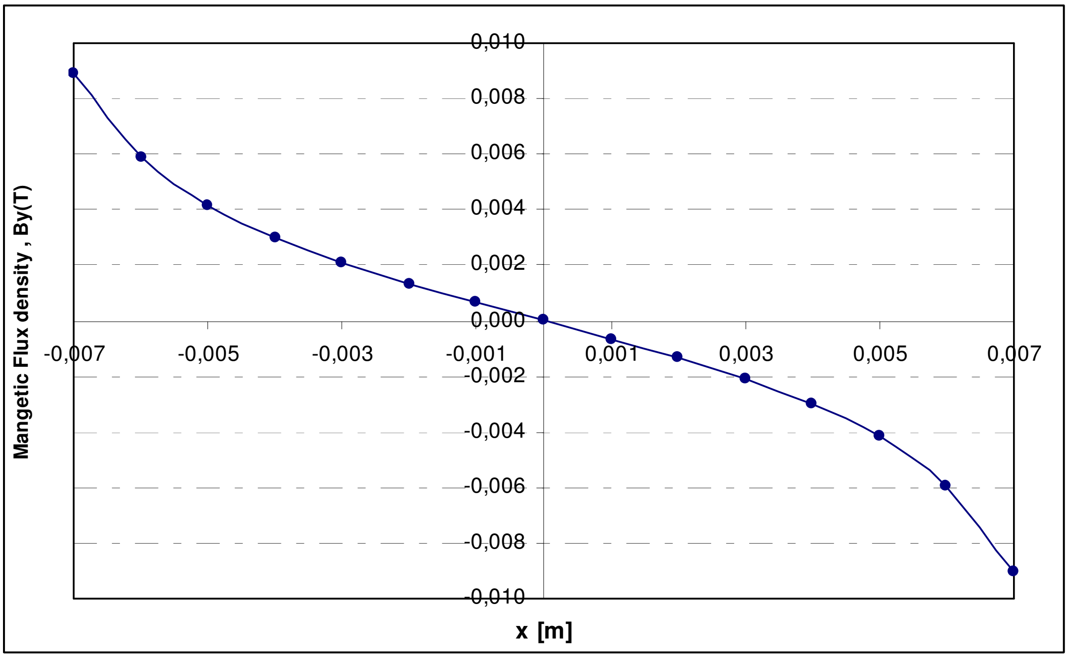

Figure 124: Plot of the vertical component $B_y(x,0,0)$ of the magnetic flux density in the symmetry plane *z*=0 as a function of *x* for $B_r = 0.063$ T.

Results of 3D simulations of the quadrupole magnet for the adjusted value of $B_r$ are shown in Figs. 125-127. The magnetic field distribution in the magnet working aperture is given in Fig.126. In Fig.126 and Fig.127 the plots of the vertical component $B_y$ of the magnetic flux density in the symmetry plane *z*=0 and of its field integral, respectively, are presented. Similar to the case shown in Fig.123 the field $B_y(x,0,0)$ is not linear within the aperture. Of course this is because the REPM block length is smaller than the aperture size. In fact, the field gradient is constant within the 5% accuracy and is equal to $G(x,0,0) = (-0.82 \pm 0.02)$ only in the range -3.0mm <*x* <3.0mm. What is really important is that the field integral $I_y$ is linear with quite good accuracy. We obtained that the within the working aperture integrated magnetic gradient is equal to $K = -(2.005 \pm 0.004)x10^{-2}$ T, so that the main specification S-FM-1 is fulfilled. This result means that short quadrupole magnets with a large aperture can be built.

As the next step we checked that after increasing the residual magnetization $B_r$ of the REPM blocks the level of the stray field at the points of the first orbit is low enough so that specification S-FM-3 is fulfilled. We obtained that the field at the point marked in red in Fig.123 is equal to $B_{sum} = 2.05x10^{-6}$ T.

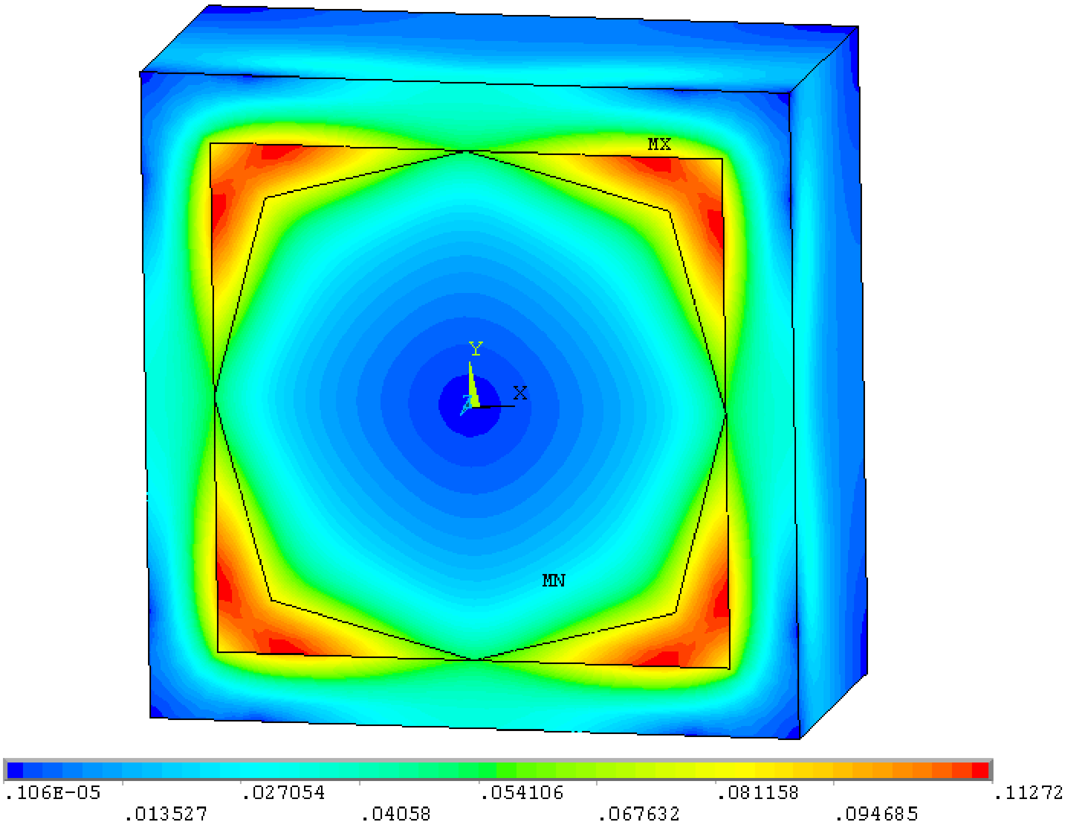

Figure 125: Magnetic field distribution $B_{sum}$ across the quadrupole working aperture for the REPM blocks residual magnetization $B_r = 0.227$ T.

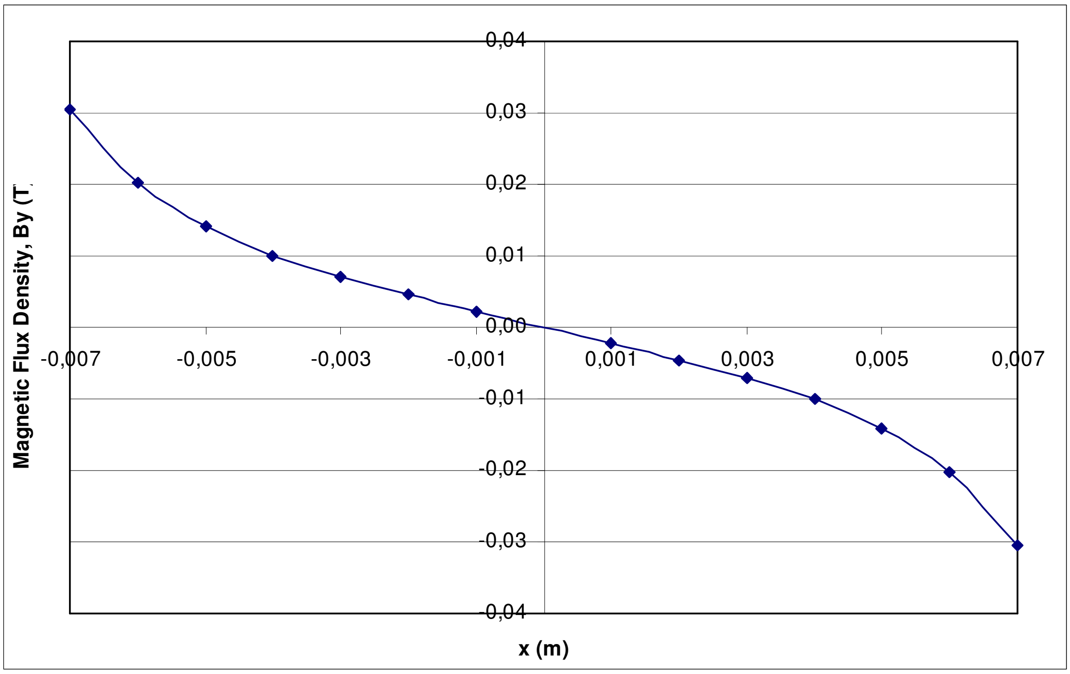

Figure 126: Plot of the vertical component $B_y(x,0,0)$ of the magnetic flux density in the symmetry plane $z$=0 as a function of $x$ for $B_r = 0.227$ T.

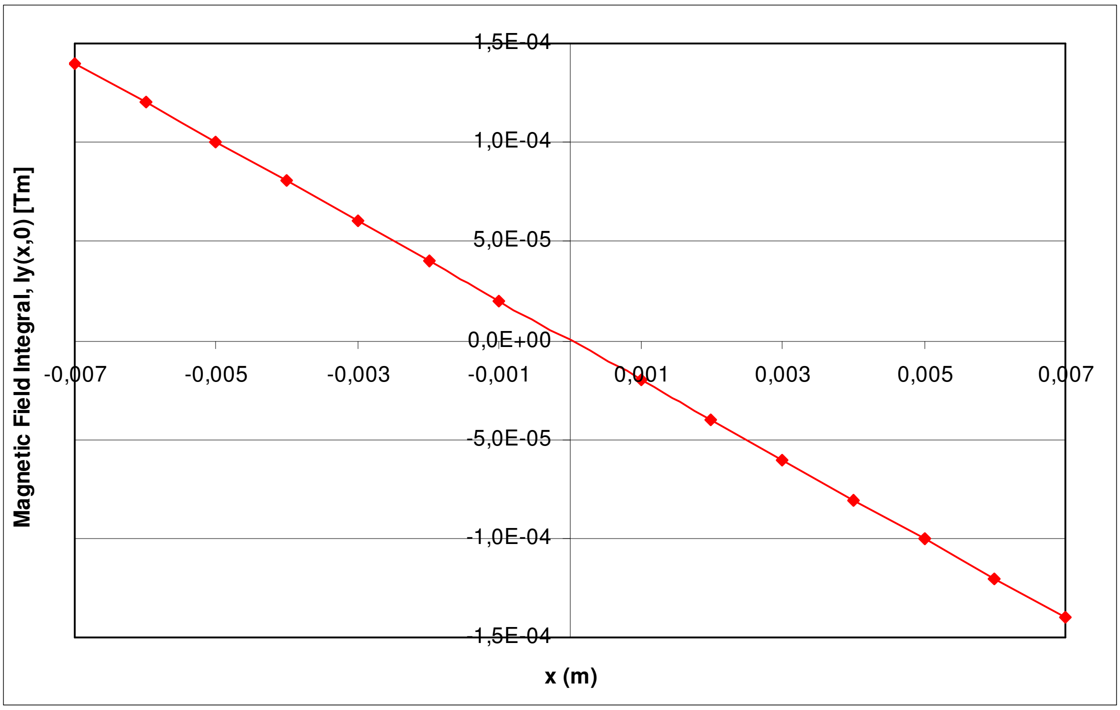

Figure 127: Magnetic field integral $I_y(x)$ as a function of $x$ for $B_r = 0.227$ T.

Finally we studied the field produced by the quadrupole outside the magnet and in particular at the position of the electron gun. The behaviour of the field distribution along the $z$-axis for a few horizontal displacements $x$ is shown in Fig. 128. As one can see, for $z > L_{REPM} / 2 = 1.5\,\text{mm}$ the field decreases quite rapidly. To get an estimate of its value at the electron gun face we considered the scheme given in Fig. 129 that includes the end magnet M2, quadrupole and electron gun. The coordinate of the electron gun $z_{gun}$ is given by the following formula:

$$z_{gun} = L - \frac{1}{2} L_{yoke} - 5.0mm, \qquad (129)$$

where $L$ is the total distance between the electron gun and the end magnet. It takes into account that the distance between the yoke and end magnet faces is 5 mm. In the UPC 12 MeV RTM design $L$=53.07mm, the length of the yoke was chosen to be $L_{yoke} = 20\,\text{mm}$, so that $z_{gun} = 38.97\,\text{mm}$. Using results of the 3D simulations with the ANSYS code we analyzed the magnetic field at the position of the electron gun for $-6\,\text{mm} < x < +6\,\text{mm}$ and checked that specification S-FM-4 is fulfilled. For example for x = - 4.0 mm the vertical component of the magnetic flux density $B_y(-4\,\text{mm}, 0, z_{gun}) = 0.78 \times 10^{-7}\,\text{T}$.

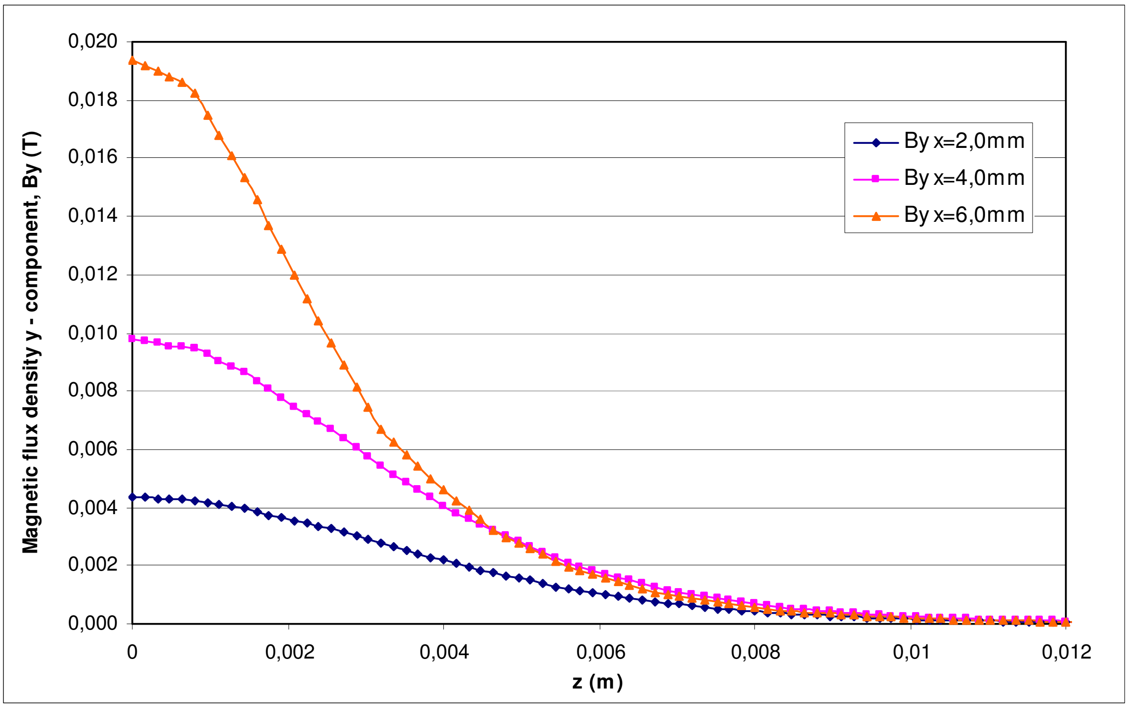

Figure 128: The vertical component $B_y(x,0,z)$ of the magnetic flux density as a function of $z$ for three values of $x$.

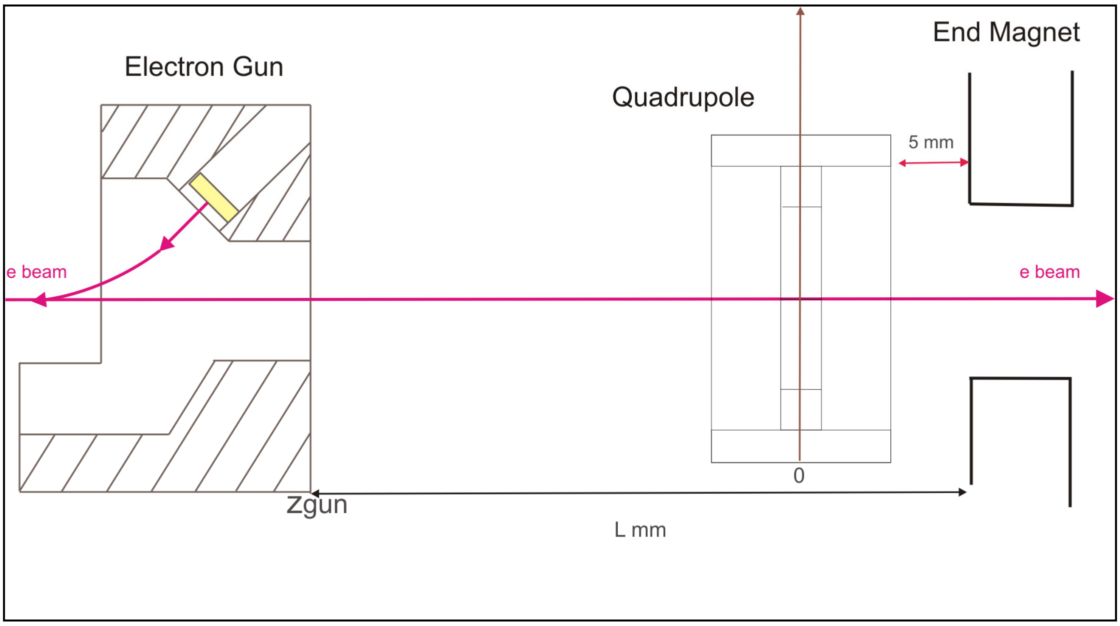

Figure 129: Position of the quadrupole magnet with respect to the electron gun and the end magnet M2.

### 4.3.4. - Concluding remarks on the focusing magnet design.

For the horizontally focusing quadrupole magnet of the UPC 12 MeV RTM the QSM-type design was chosen. Most of the geometrical parameters of the magnet (dimensions, angles of REPM blocks) were fixed on the basis of preliminary design studies and are gathered in Tables 24-26. However, for the length of the yoke and the permanent magnets residual magnetization producing the required integrated magnetic gradient the longitudinal properties of the quadruple are essential, therefore these parameters were fixed from 3D simulations using the ANSYS code. In these simulations we also checked that all the design specifications S-FM-1 – S-FM-5 are fulfilled. We would like just to note that in fact the transverse size of the magnet depends on the yoke thickness and is not fixed in this study, however the proposed design allows to have a quadrupole with external size less than 3 cm, as it is prescribed by S-FM-5.

The results obtained in this section provide all data for the technical design of the quadrupole magnet. Currently this magnet is at the stage of factory manufacturing. After its delivery it will be installed on the supporting platform inside the vacuum chamber of the RTM.

## 4.4. – Hybrid extraction magnet of the SINP 55 MeV RTM.

This section is devoted to the optimization of the extraction dipole of the 55 MeV RTM which was designed and built at the SINP [25]. The description of this machine is given in Sect.1.4, its schematic view is shown in Fig. 131. As it is explained below, it turned out that the original design of the extraction magnet did not satisfy tight requirements on the level of the stray field at the location of the lower orbits. Therefore a task on the improvement of the magnet characteristics was set at the SINP accelerator laboratory, and the UPC group was invited to perform a design upgrade and carry out magnet measurements to validate it.

In this section results of a design optimization of magnetic screens of the extraction magnet and measurements of its characteristics are described. Simulations were performed using the ANSYS codes. Also the results of the simulations and measurements are compared and the degree of agreement between them is discussed. Therefore this study also serves as a benchmarking of the ANSYS code as a tool for calculations of static magnetic field characteristics. Results of this section were published in Ref. [94].

### 4.4.1. – Characteristics of the extraction magnet of the SINP 55 MeV RTM and its initial version.

The extraction system of the 55 MeV RTM is formed by a single dipole magnet which deflects the 55.5 MeV electron beam from the last, 10th RTM orbit and directs it to an experimental area. The extraction magnet position inside the RTM is shown schematically in Fig. 130.

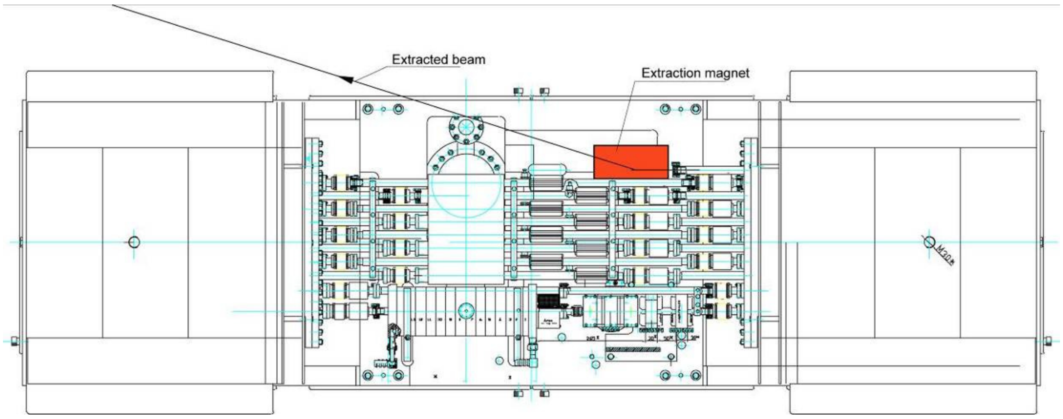

Figure 130: Schematic view of the SINP 55 MeV RTM. The extraction magnet shown is shown as red rectangle.

According to the design of the SINP 55 MeV RTM the extraction magnet must provide the extraction of electrons with the energy $E_{10}$=55.5 MeV and meet the following specifications:

1. - The extraction angle α= 17.5º.
2. - The effective length $L_{eff}$= 175 mm.
3. - The stray magnetic field at the location of the neighboring 9th orbit must be less than $10^{-4}$ T.

Condition α= 17.5º follows from the requirement that the extracted beam does not hit RTM elements along its trajectory. According to Eq. (116) the magnetic field induction in the uniform field region of the dipole magnet is than equal to

$$B_{dip} = \frac{p}{|e|L_{eff}} \sin \alpha = 0.3181\,\mathrm{T}, \tag{130}$$

where $p$ is the extracted particle momentum.

At the initial stage of the development of the extraction magnet different design versions were studied. First the window frame electromagnet with excitation coils was considered, its cross section is shown in Fig. 132. The width of the region spanned by the beam is 27 mm, the distance between the 55.5 MeV and 50.5 MeV orbits is 33.0 mm. However this design has a problem of excessive coil current, namely if the diameter of machined cooling water channels is taken into account, then the current density in the coil would be well above 30 A/mm$^2$ so that with a few turns of the coil the power supply current would be as high as ~1000 A.

Different possibilities to reduce the coil current were analyzed, in particular (1) decrease the bending angle, (2) increase the magnet length, (3) use a pulsed magnet. However, in the first case it would be necessary to drill a hole in the end magnet yoke for beam passage, in the second increase the distance between the end magnets thus increasing the RTM dimensions, and in the third to build a pulsed magnet with a 3000 A current and 30 μs pulses following with the frequency 50 Hz.

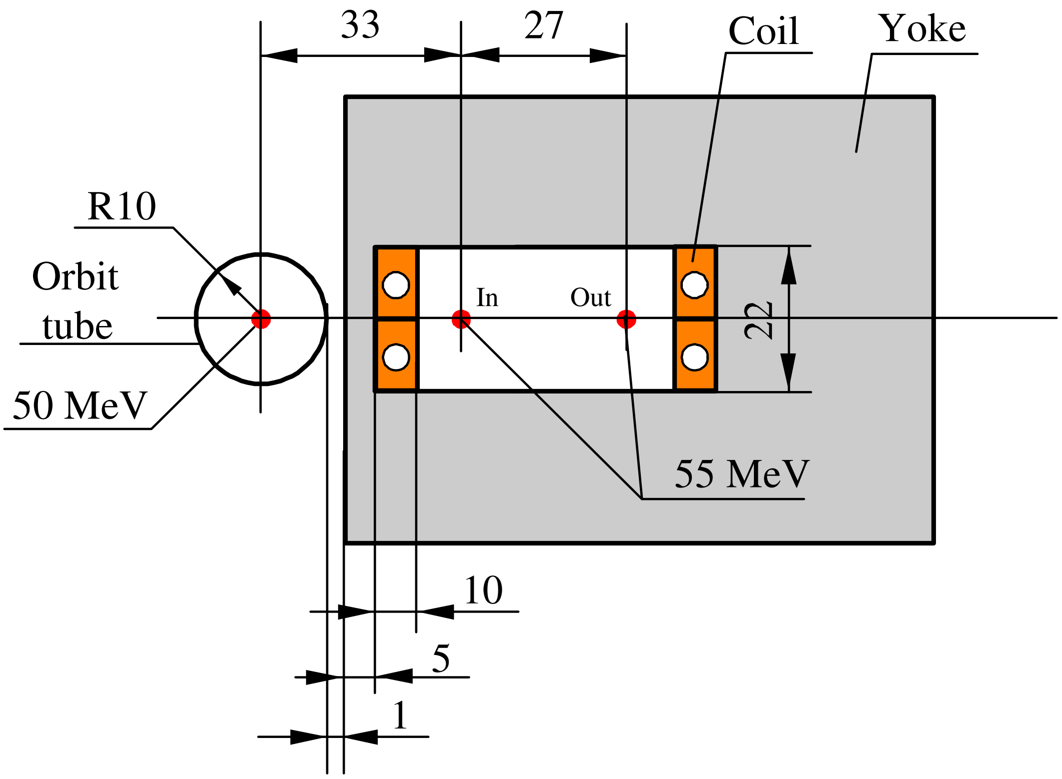

Figure 131: Cross section of the window frame extraction magnet. Dimensions are given in mm.

These three possibilities were rejected as non-optimal. Indeed, solutions (1) and (2) would mean increasing the distance between the end magnets and this was unacceptable because this RTM is supposed to be a compact machine. Possibility (3) was not accepted because a pulsed magnet would be a bulky device producing much electromagnetic noise.

As a solution it was decided to use a hybrid magnet in which the required magnetic field is produced by an REPM material and excitation coils are used only for adjusting the field level. The cross section of this design is shown in Fig. 132.

The hybrid extraction magnet consists of a yoke, poles, REPM (Nd-Fe-B) blocks, excitation coils, non-magnetic insertions and two lateral magnetic screens with an air gap between them. This air gap is necessary for avoiding the saturation in the external magnetic screen. If there would be just one magnetic screen directly attached to the yoke then it would be saturated that is equivalent to the absence of any screen. The residual magnetization of the REPM material necessary to produce the required magnetic field in the 22.0 mm height gap is $B_r = 0.8924$ T. The maximum current in the coils is 2A, the number of turns is 250, the coil area is 510 mm$^2$ and the filling factor is equal to 0.8. The maximum current density in the wire of the diameter 1.0 mm is 2.5 A/mm$^2$. A magnet with such design does not require cooling of the coils.

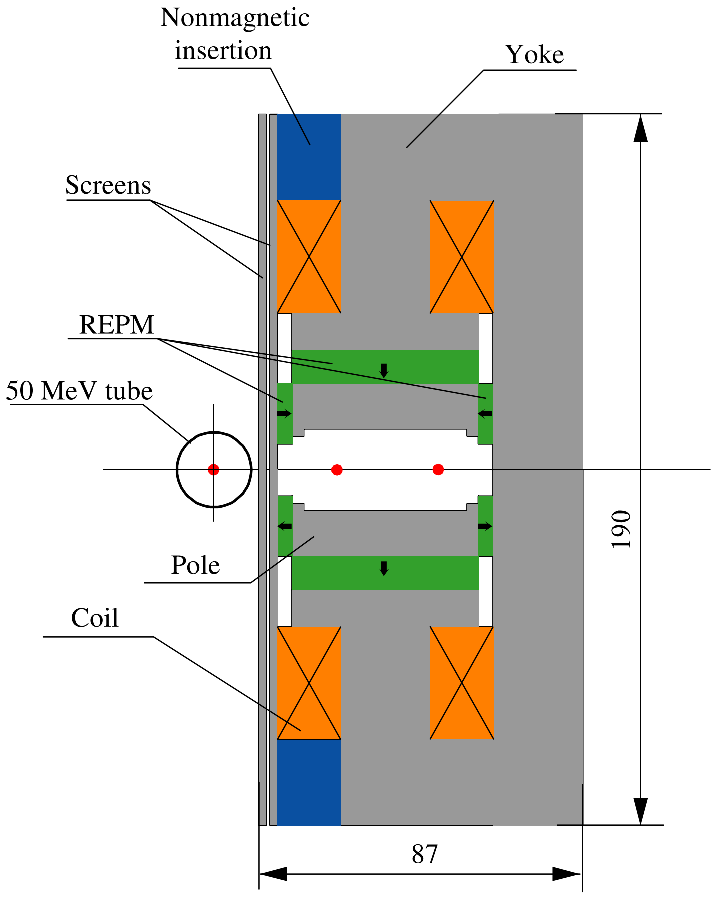

Figure 132: Cross section of the hybrid extraction magnet. Dimensions are in mm.

This first version of the extraction magnet did not include frontal magnetic screens at the entrance and exit. Due to the fringe field its measured effective length appeared to be 192 mm as compared to $L_{eff}$ =175 mm used in preliminary field estimates. In order to provide the beam deflection angle of the 55.5 MeV orbit equal to α=17.5°, as it is required by the specifications, the field level was adjusted to the value $B_{dip}$= 0.285 T. However, during the RTM commissioning it was found that the stray magnetic fields from the extraction magnet in the region of the 9-th and 8-th orbit (50.5 MeV and 45.5 MeV, respectively) were producing a considerable deflection of the beam that could not be compensated by steering coils installed at these orbits.

To solve the stray magnetic field problem additional passive frontal screens, upstream and downstream, of the thickness equal to 2.0 mm were placed at the entrance and exit of the extraction magnet. The material used for these screens was steel 1010. In Fig. 133 two pictures of the magnet showing these screens are given. Due to the screens the effective length of the magnet has decreased to $L_{eff}$=180 mm and the maximum coil current appeared to be insufficient. In order to provide the required magnetic field level $B_{dip}$= 0.325 T the REPM residual magnetization was increased. Since the lateral screen did not cover completely the total side of the extraction magnet, as one can see in Fig.134, adding the frontal screens did not reduce the stray field down to the level required by the specification. In order to diminish the stray field effect on the 50.5 MeV orbit an additional μ – metal magnetic cylindrical cover around the 9-th orbit vacuum tube was installed (see Fig. 134). This second version of the hybrid extraction magnet will be the object of the upgrade studied in the next Section.

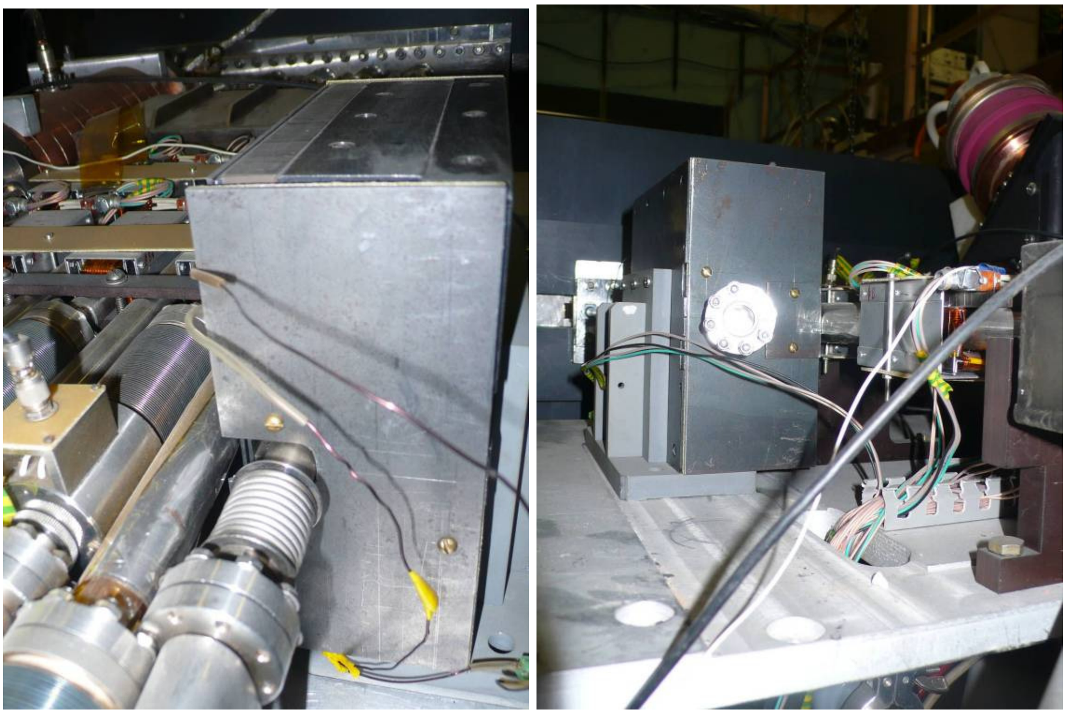

(a) (b)

Figure 133: The extraction magnet with the upstream (a) and downstream (b) screens.

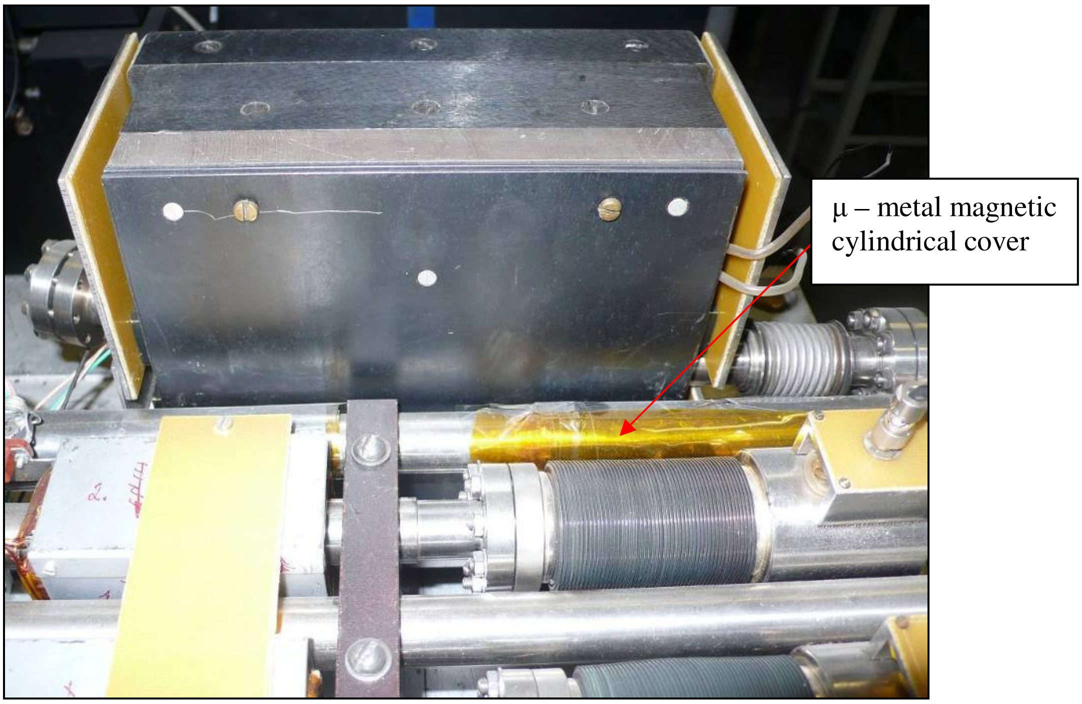

Figure 134: The lateral screen of the second version of the hybrid extraction magnet and cylindrical cover for shielding the 50.5 MeV orbit.

### 4.4.2. – 3D optimization of the magnetic screens of the extraction dipole.

The purpose of the extraction magnet upgrade was the reduction of the stray magnetic field at its entrance and exit so that the specifications are fulfilled. The additional requirement that was imposed at this stage is that the angle of the deflection of the 9-th orbit $\alpha_9$ caused by the stray magnetic field must be less than $\alpha_{9\max} = 0.15$

mrad. Such deviation can be compensated by a steering coil of that orbit. The optimized design was simulated using the ANSYS code. The procedure of 3D simulations included the following steps:

1. Generate the extraction magnet geometry from the technical drawings provided by the SINP group.

2. Perform simulations of the second version of the extraction magnet with the magnetic screens proposed by SINP group, check the previous results obtained during the RTM commissioning.

3. Perform an optimization study of the magnetic screens geometry with the aim to achieve a deflection angle of the 9th orbit less than $\alpha_{9\,\max} = 0.15$ mrad.

4. Verify experimentally the results obtained in the 3D simulations with the ANSYS code.

The last step will also serve as a kind of benchmarking of the use of the ANSYS code for the 3D design of magnetic system, i.e. it will allow us to determine the precision that can be achieved in these calculations.

The coordinate system in the horizontal (beam orbit) plane used in the ANSYS simulations is shown in Fig. 135. It was also used in magnetic field measurements described below. As one can see, the positions of the beam at the entrance and exit of the extraction magnet with respect to the longitudinal *z*-axis are *x*= -13.5 mm and *x*=13.5 mm, respectively.

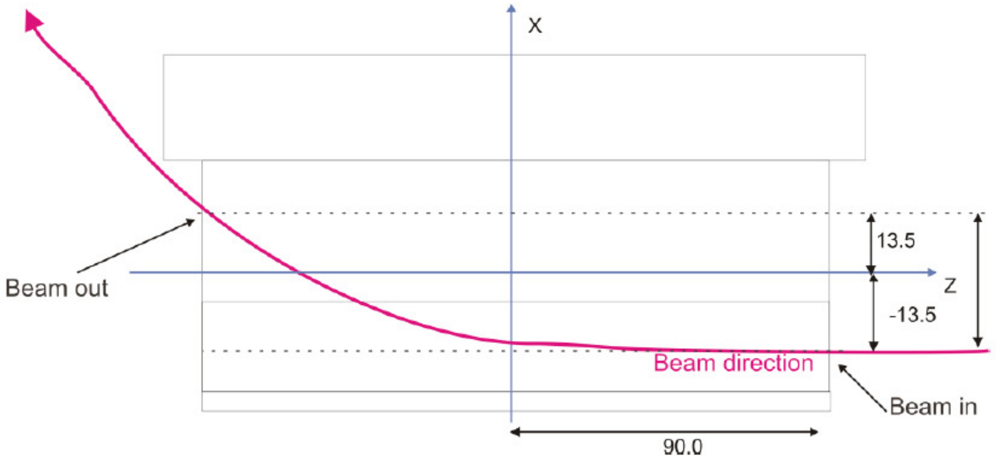

Figure 135: Coordinate system in the horizontal plane used in the ANSYS simulations. The dimensions are in mm.

From the technical drawings of the initial version of the extraction magnet provided by the SINP group the 3D geometry in the ANSYS format was generated (see Fig. 6. In fact, taking into account the symmetries of the magnet it is sufficient to perform simulations for a 1/4 of the full magnet and impose the appropriate boundary conditions at the symmetry planes.

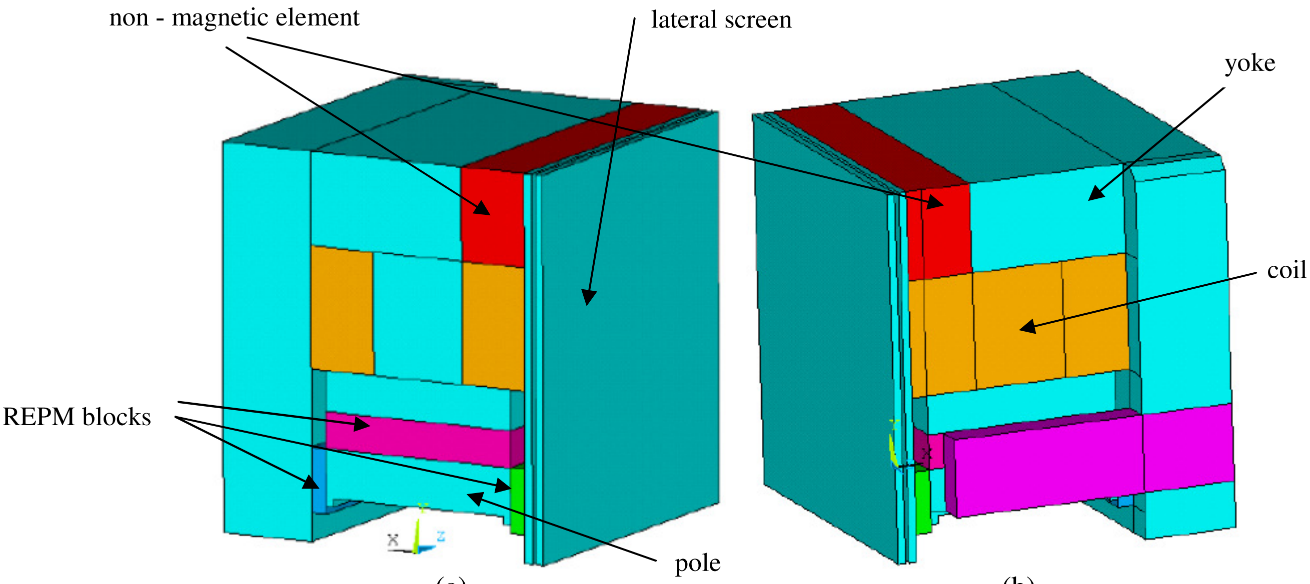

(a) (b)

Figure 136: 3D ANSYS geometry: symmetry plane (a) and entrance plane (b) views.

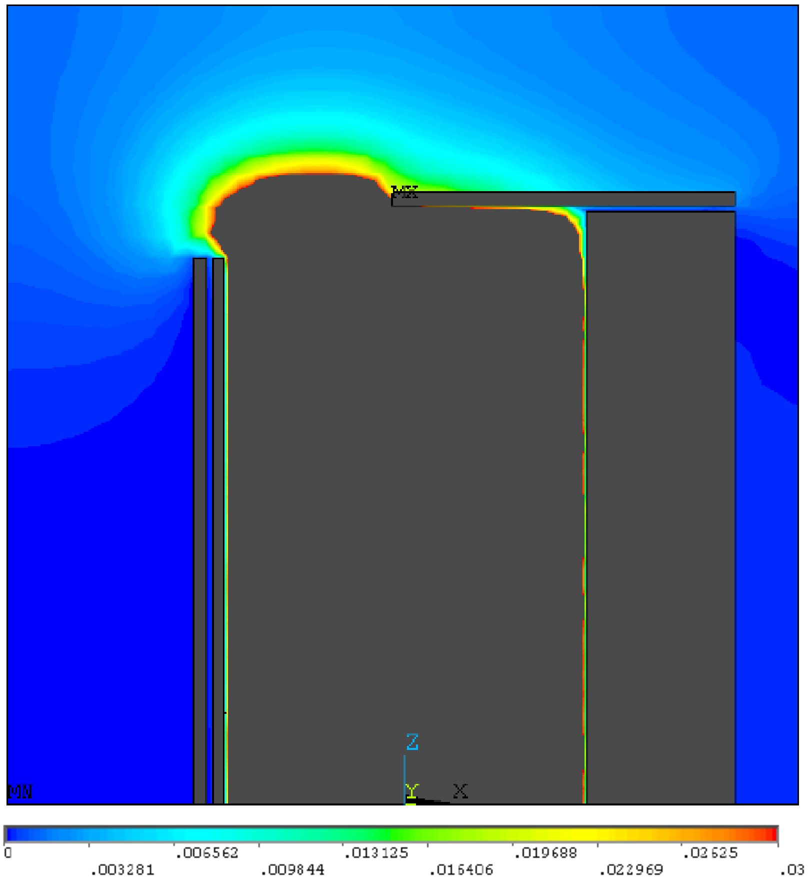

Figure 137: Magnetic flux density distribution $B_{sum}$ in the orbit plane for the initial version of the extraction magnet.

The geometry in Fig.138 was the initial point of the design optimization of the extraction dipole. As the material of the yoke and magnetic screen the steel 1010 was used. We performed the 3D simulations of the field distribution inside and outside the magnet. As an example, in Fig. 137 the magnetic field distribution in the orbit plane at the side of the upstream frontal magnetic screen is shown. We obtained that the angle of the beam deflection of the 9th orbit trajectory caused by the stray fields is

$\alpha_9 = 1.425$ mrad which one order of magnitude above the required value of $\alpha_{9\max} = 0.15$ mrad.

With the aim to fulfil the limit on the deviation angle $\alpha_9$ and comply with the magnet specifications a few modifications of the screens were simulated.

**Modification 1:** The upstream and downstream frontal screens of the initial version of the extraction dipole with the rectangular beam aperture (see Fig. 138a) were replaced by frontal screens with a circular aperture of radius 12.0 mm (Fig. 138b). After this modification the frontal sides of the magnet are closed completely except for openings through which the vacuum tube passes. The magnetic field distribution in the orbit plane at the upstream screen position obtained in the 3D simulations is shown in Fig. 140. The comparison of the distributions in Figs. 137 and 139 shows that the change for the circular apertures reduces the stray magnetic field at the entrance and exit of the extraction magnet. We obtained that its magnetic field integral along the 50.5 MeV trajectory became equal to $I_9 = 1.916\times10^{-4}$ T·m that corresponds to the angle of deviation of this orbit $\alpha_9 = 1.2$ mrad.

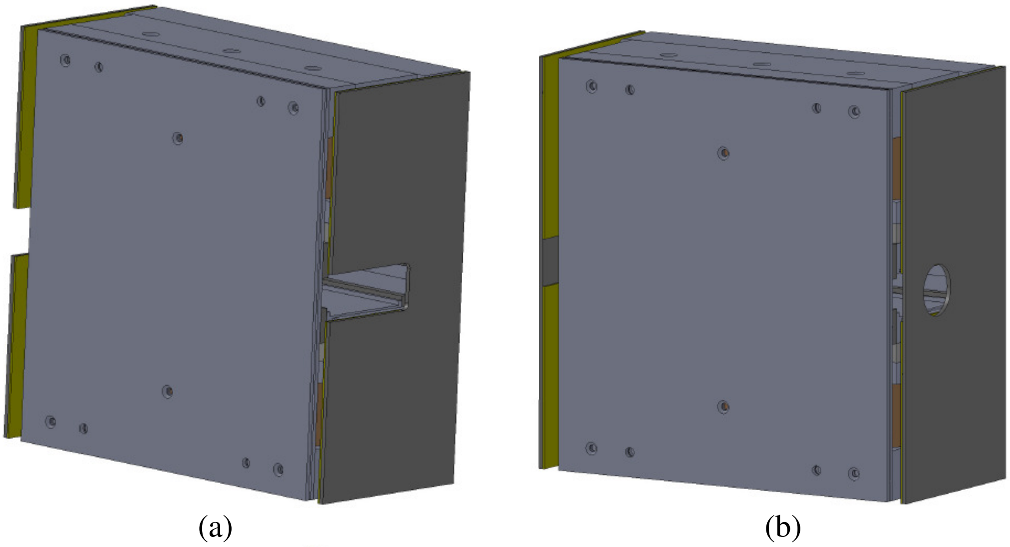
(a) (b)

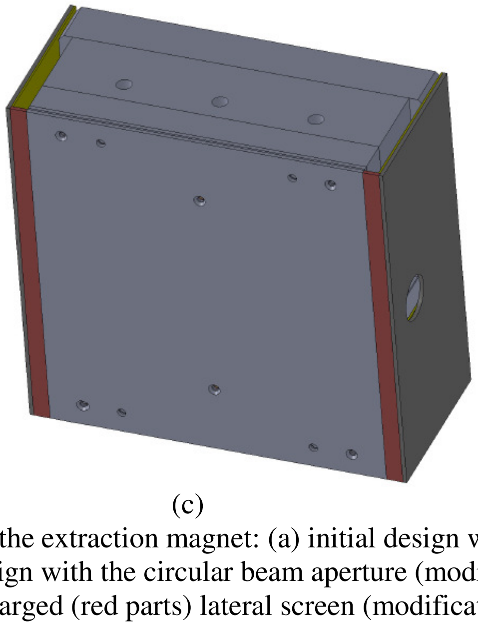
(c)

Figure 138: 3D view of the extraction magnet: (a) initial design with the rectangular beam aperture; (b) modified design with the circular beam aperture (modification 1); (c) design with an enlarged (red parts) lateral screen (modification 2).

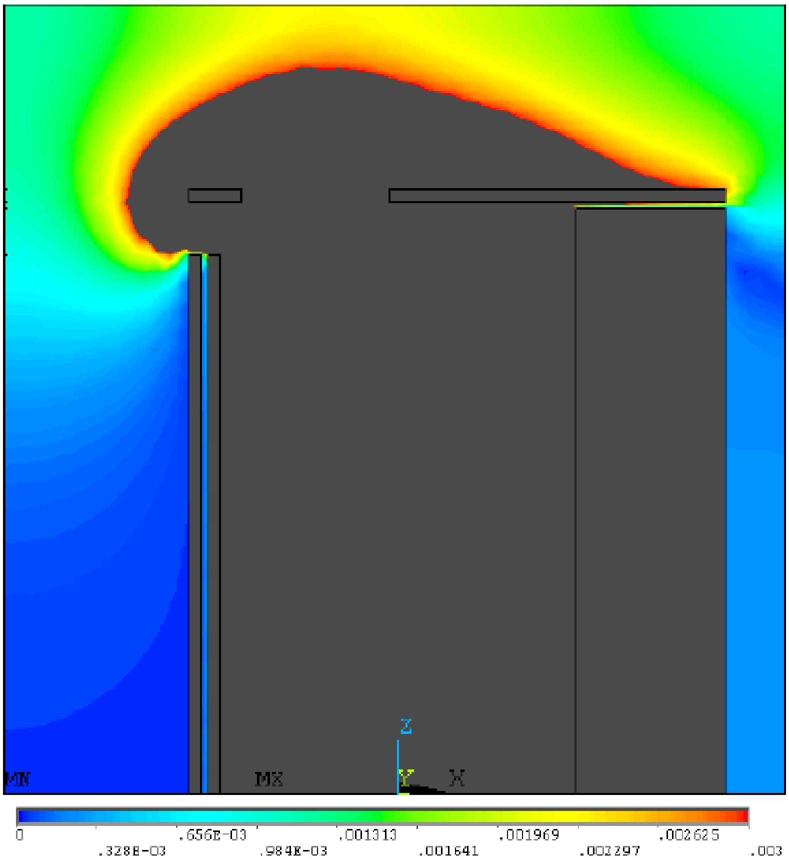

Figure 139: Magnetic flux density distribution $B_{sum}$ in the orbit plane after Modification 1 of the magnet screens. The region with the field values $B_{sum} > 0.003\,\mathrm{T}$ is shown in grey color.

**Modification 2:** The length of the *outer lateral screen* was increased by 7.5 mm at each edge so that the magnet is now completely covered from this side (Fig. 138c). The thickness of this screen cannot be increased because it is limited by the distance between the extraction magnet and the vacuum tube of the 9th orbit. The magnetic field distribution in the orbit plane is shown in Fig. 140. As one can see with the increased lateral screen the stray magnetic field outside the dipole is smaller than in the previous case, namely the value of the integral of the vertical component of the magnetic field induction along the 50.5 MeV orbit becomes equal to $I_9 = 5.922 \times 10^{-5}\,\mathrm{T \cdot m}$ and the corresponding angle of the deviation of this trajectory is $\alpha_9 = 0.36$ mrad. This value still exceeds the upper limit of the bending angle $\alpha_{9\,\mathrm{max}} = 0.15\,\mathrm{mrad}$.

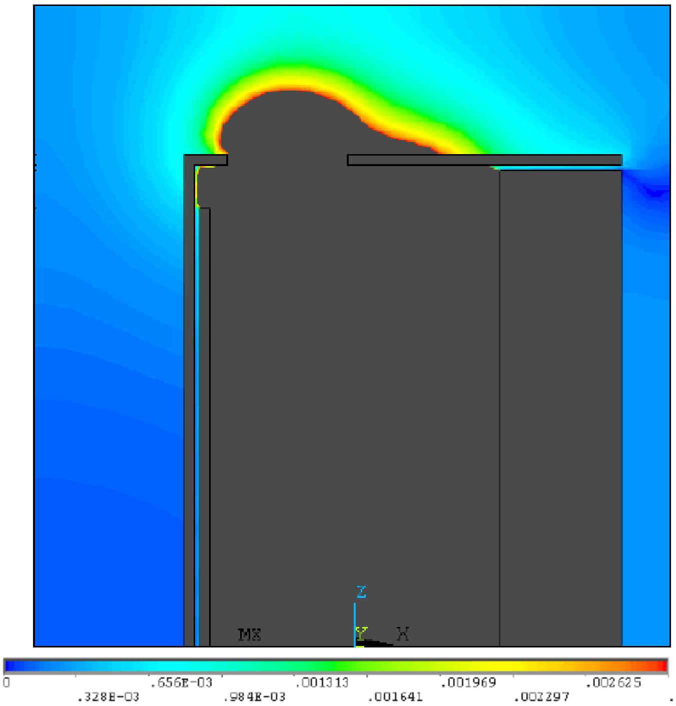

Figure 140: Magnetic flux density distribution $B_{sum}$ in the orbit plane after Modification 2 of the magnet screens. The region with the field values $B_{sum} > 0.003\,\mathrm{T}$ is shown in grey color.

**Modification 3:** The thickness of the *upstream and downstream frontal screens* was increased until the deviation angle $\alpha_9$ becomes smaller than the allowed limit $\alpha_{9\,\max} = 0.15\,\mathrm{mrad}$. For this a set of screens with the thicknesses increasing from 2.0 mm up to 5.0 mm with the step 0.5 mm were considered and the field distribution for each configuration was simulated using the ANSYS code. In this process the geometry of the screens was maintained unchanged and only the thickness of the frontal magnetic screens was successively increased. As a result it was found that for the screen thickness equal to 5 mm the value of the dipole magnetic field integral along the 50.5 MeV orbit becomes equal to $I_9 = 2.232\times10^{-5}\,\mathrm{T\cdot m}$ and the corresponding angle of the deviation of this trajectory is $\alpha_9 = 0.13$ mrad so that the condition is fulfilled. The magnetic field distribution $B_{sum}$ for this case is shown in Fig. 141.

In order to understand the effect of the screens on the longitudinal distribution of the magnetic field in Fig. 142 we plotted the vertical component of the magnetic field density as a function of the longitudinal coordinate $z$ along the 55.5 MeV orbit. As it can be seen, the installation of the frontal screens and their optimization lead to a reduction of the fringe field at the entrance of the extraction magnet.

To summarize, the screen system of the extraction dipole which is proposed after the optimization study consist of

1. A lateral magnetic screen with the thickness 2 mm and length 200mm,
2. Upstream and downstream magnetic screens with dimensions 85 x 190 x 5 mm with a circular aperture of the radius 12 mm.

This proposal is shown schematically in Fig. 143. Once the 3D design simulations were completed the new magnetic screens were machined at the SINP shop and installed in the extraction magnet. In Fig. 144 two pictures of the extraction magnet with new upstream and downstream screens are given.

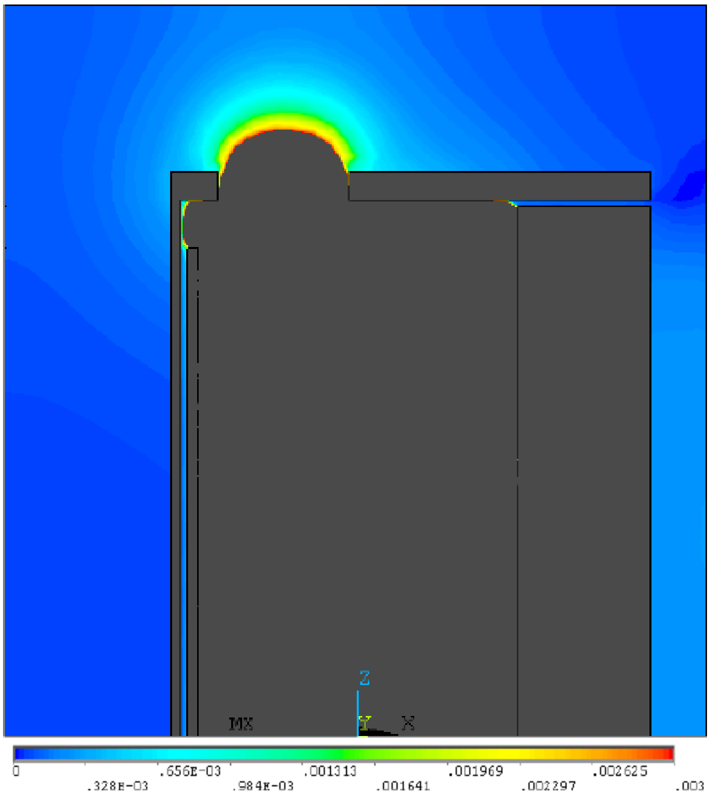

Figure 141: Magnetic flux density distribution $B_{sum}$ in the orbit plane after Modification 3 of the magnet screens. The region with the field values $B_{sum} > 0.003$ T is shown in grey color.

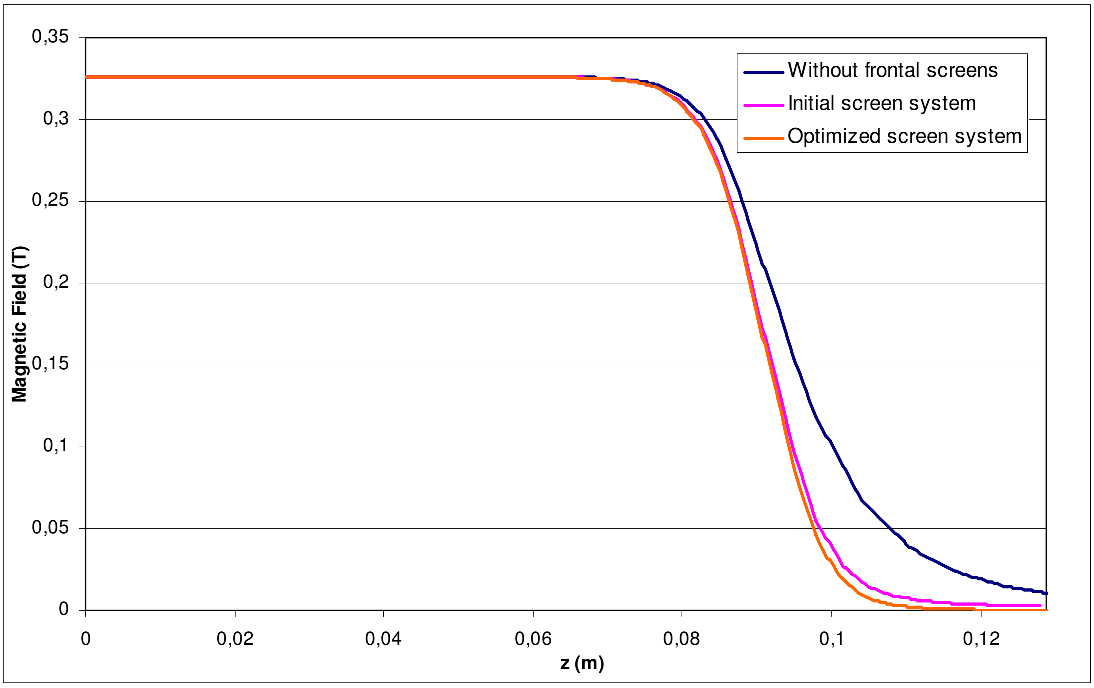

Figure 142: Magnetic field profiles along the longitudinal direction of the 55.5 MeV orbit for the three screen system designs.

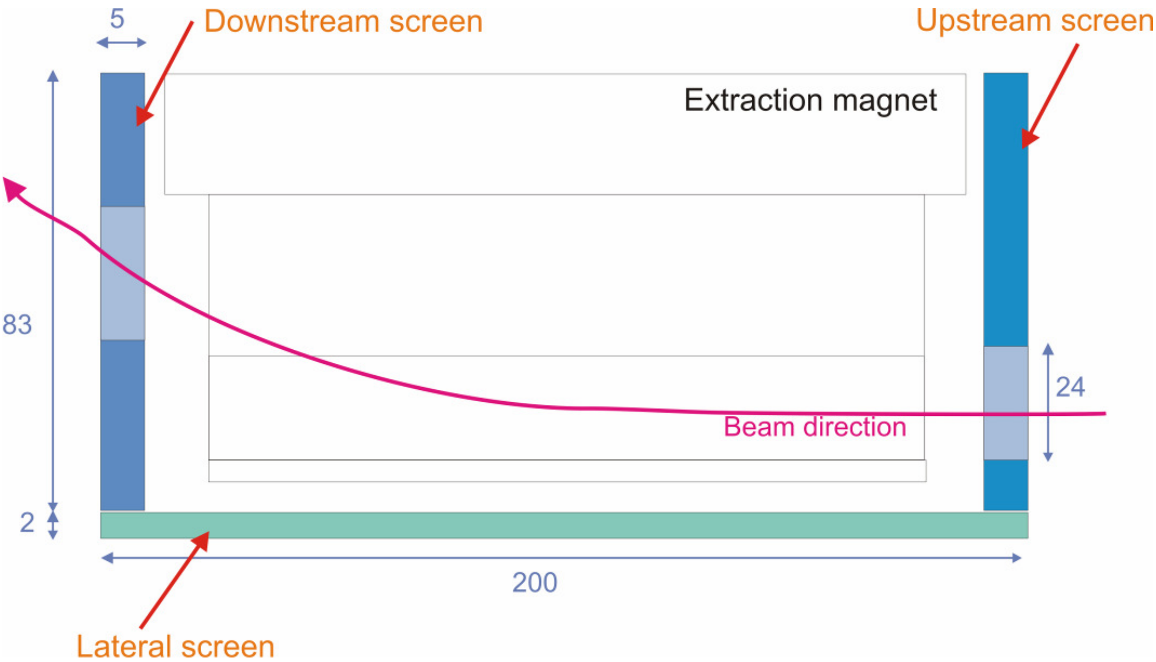

Figure 143: Scheme of the screens of the extraction magnet after its optimization.

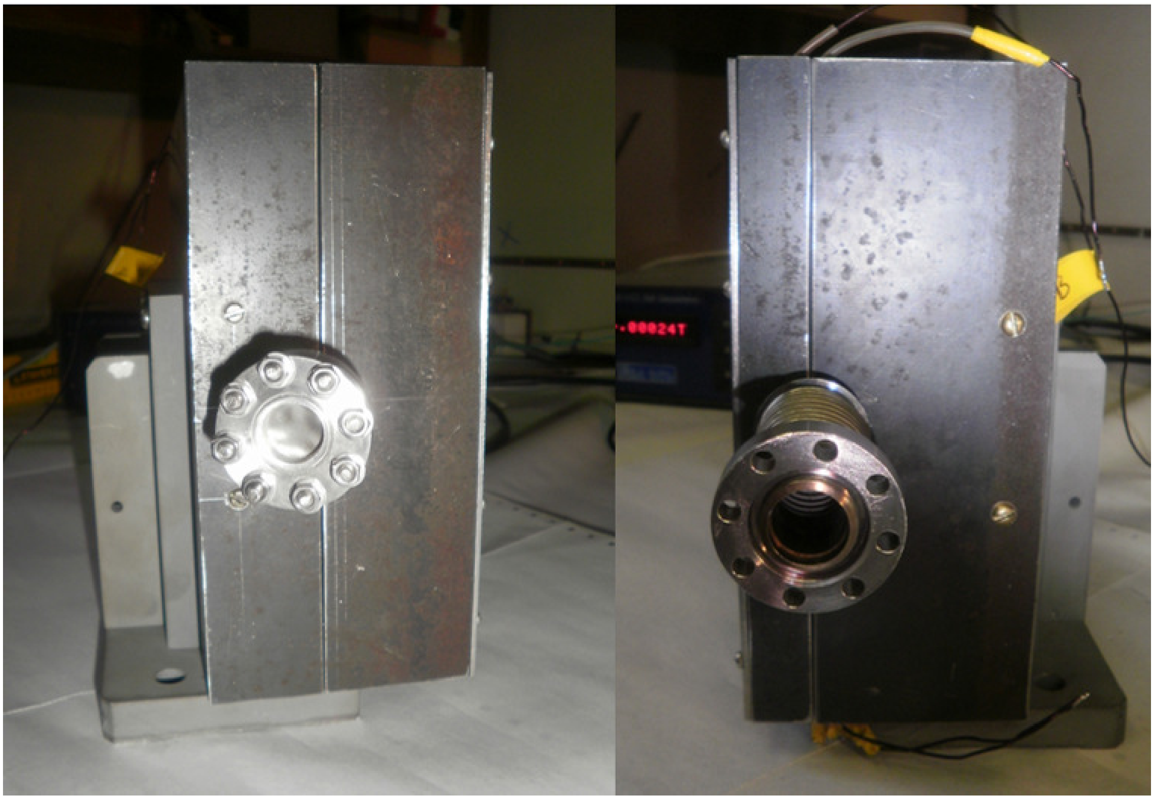

(a) (b)

Figure 144: New extraction magnet with the optimized screens, (a) downstream screen, (b) upstream screen.

### 4.4.3. – Experimental validation of the extraction magnet upgrade.

The optimization of the magnetic screens simulated in the previous section was validated by means of experimental measurements of the extraction magnet characteristics. Results of these measurements were also used for benchmarking the ANSYS code in this type of calculations.

The measurements were performed in the accelerator laboratory of the SINP (Moscow State University). The field distribution for the following three versions of the extraction magnet were measured: (1) without frontal screens, (2) with the initial frontal screens (Fig.133), and (3) with the new version of the frontal and lateral screens simulated in the previous section. For each of these configurations two types of measurements were carried out:

(a) Measurements of the magnetic field distribution in a region outside the extraction magnet in the region of the 50.5 MeV orbit shown in Fig. 145. The aim was to determine the level of the stray fields in that region. Results of this study allow to estimate the effect of the stray fields on the 50.5 MeV beam and evaluate the accuracy of the ANSYS simulations.

(b) Measurements of the magnetic field profile along the 55.5 MeV trajectory. The aim of this study is to determine the influence of the screen system parameters on the fringe field profile and the nominal magnetic field value in the working region.

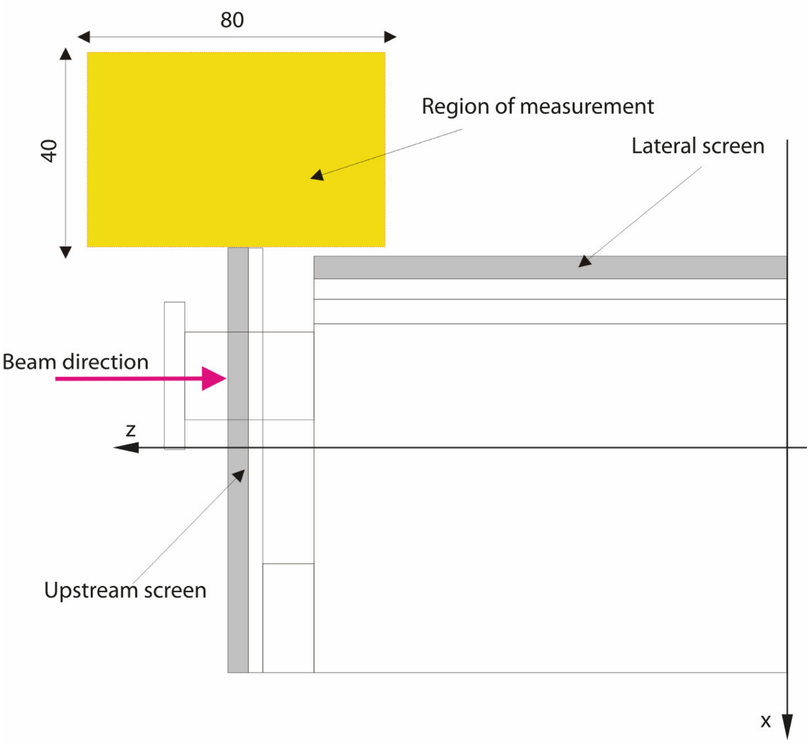

Figure 145: Region of measurements of the stray magnetic field (dimensions are in mm).

In Fig. 146 the stand for magnetic measurements is shown. The extraction magnet is placed on platform (1) which is fixed on table (2). The magnetic field induction is measured with a Caylar GM-H103 Hall Gaussmeter (3) with a probe hold by copper stem (4). The stem is fixed on a supporting platform which can be moved in the *x*-direction along rail (5). This rail in its turn rests on supports movable in the *z*-direction along two other rails, one of them, rail (6), is seen in Fig. 146. The Hall probe position with respect to the extraction magnet in the vertical (*y*) direction is adjusted by moving platform (1) up or down with respect to table (2).

The magnetic field distributions in the region of measurements outside the extraction magnet (see Fig. 145) for the three designs described above are given in Fig. 148.

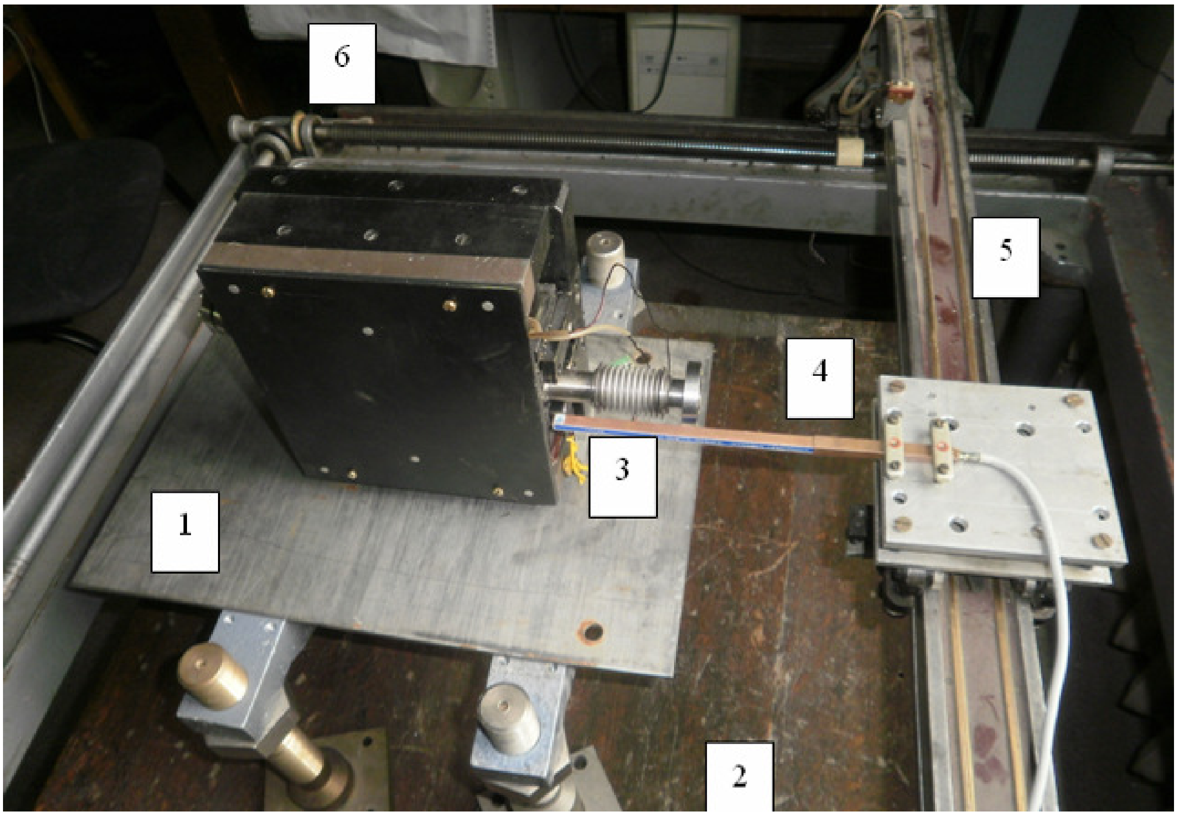

Figure 146: Stand for magnetic measurements.

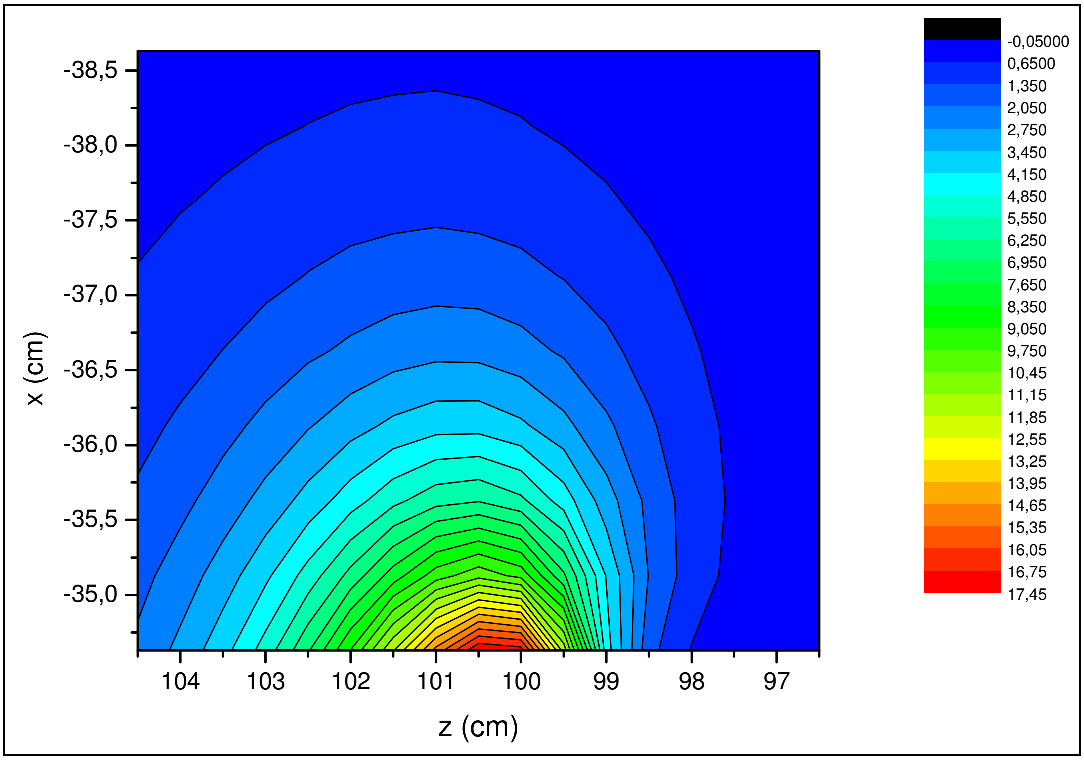

(a)

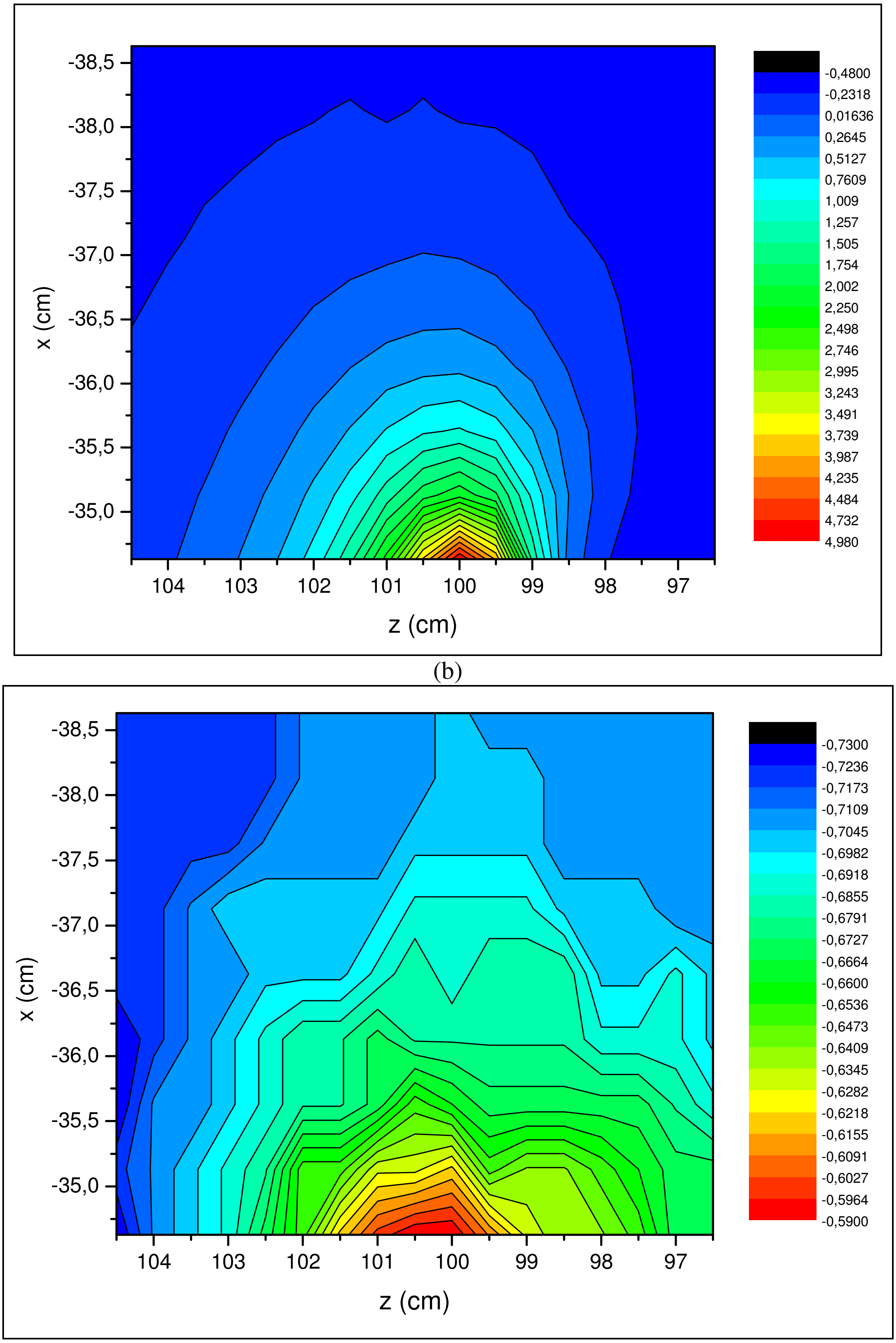

(b)

(c)

Figure 147: Magnetic field maps in the region of measurement: (a) without frontal screens, (b) with the initial frontal screens, (c) with the new version of the frontal and lateral screens simulated in Sect. 4.4.2 (field induction is given in mT).

From the magnetic field maps in Fig. 147 one can see that in the three measured cases the maximum level of the stray field is reached at the end of the lateral screen ($z$=100 mm). Installation of the frontal screens reduced the field level in this region for about four times (Fig. 147b). Increasing the upstream screen thickness together with the closure of the magnet interior by upstream and lateral screens reduced the stray magnetic field to the level of the background magnetic field in the laboratory and sensitivity of magnetometer, namely to less than 1 G (Fig. 147c). Some remnants of the stray field near $z$ = 100 mm in this case are explained by effects of saturation of the lateral screen material.

Using the data obtained in the magnetic measurements in Fig. 148 we plotted the magnetic field profiles along the straight line $x$=-13.5 mm for the initial screen system and the optimized one. Let us remind that at the entrance to the extraction dipole the $x$=-13.5 mm line coincides with the 55.5 MeV beam trajectory (see Fig. 135). As one can see, in the case of the initial screen the measured magnetic field in the centre of the dipole at $z$=0 has the required value $B_{dip} = 0.325\,\text{T}$. In the case of the optimized screens $B_{dip}$ is 0.4% lower. Thus, in order to get the required magnetic field in the working region a field adjustment by means the excitation coils will be necessary.

Finally we compared the results of 3D simulations using the ANSYS code with the results of the experimental measurements. As examples in Figs. 149 and 150 the longitudinal magnetic field distributions obtained in these two approaches for the extraction magnet with the initial frontal screens (Fig. 149) and that with the new version of the frontal and lateral screens simulated in Sect. 4.4.2. (Fig.150) are given. Let us recall that in the 3D simulations the value of the residual magnetization was set to be $B_r$=0.97814 T. As one can see the experimental results practically coincide with the theoretical ones inside the magnet, from $z$=0 up to the end of the magnet pole at $z$=0.09 m. Some difference is seen in the tails of the distributions. Thus, in the case of the extraction magnet with initial frontal screens (Fig. 149) the maximal difference between the curves is about $\Delta B$=0.02 T at $z$=0.1 m. It is due to small differences in the geometry and dimensions between the real and simulated beam holes. For the case of the optimized screen system the experimental data practically coincide with the ANSYS simulations for the whole studied interval in $z$ (Fig. 150).

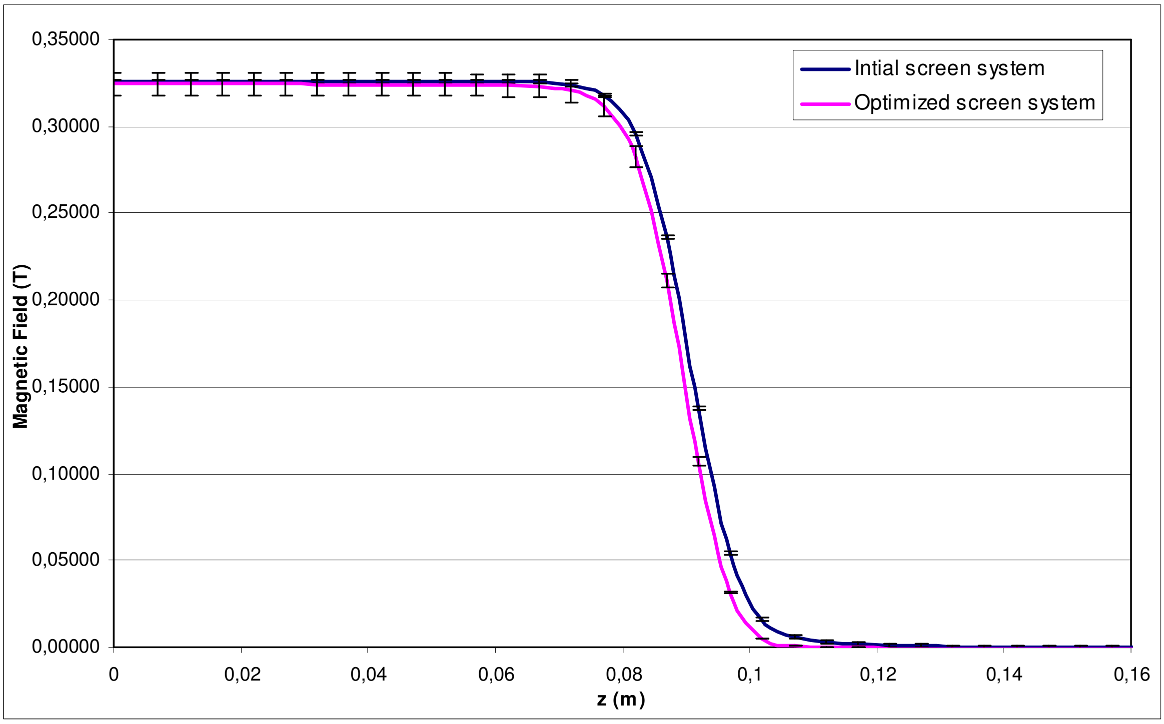

Figure 148: Magnetic field profile along the straight line *x*=-13.5 cm in the range 0<z<0.13 cm for two versions of the extraction magnet: with the initial frontal screens and with the new version of the frontal and lateral screens simulated in Sect. 4.4.2.

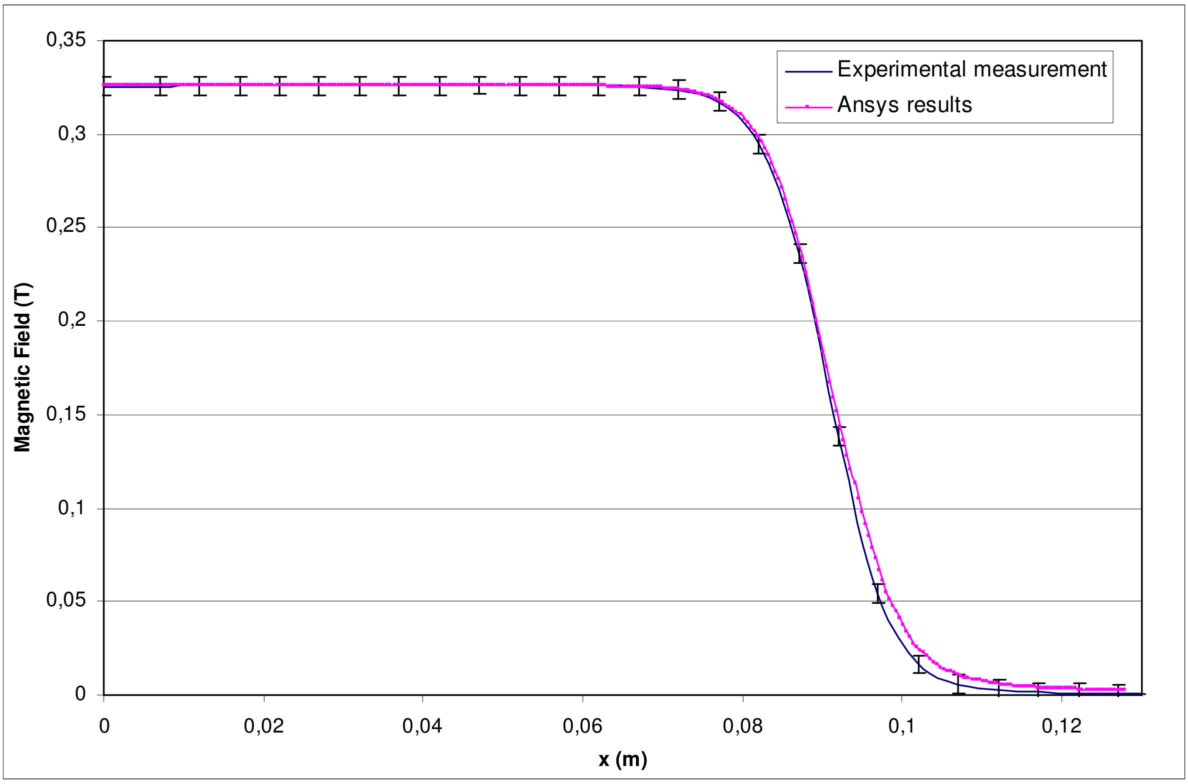

Figure 149: Measured and simulated magnetic field profiles along the straight line *x*=-13.5 mm for the extraction magnet with the initial frontal screens.

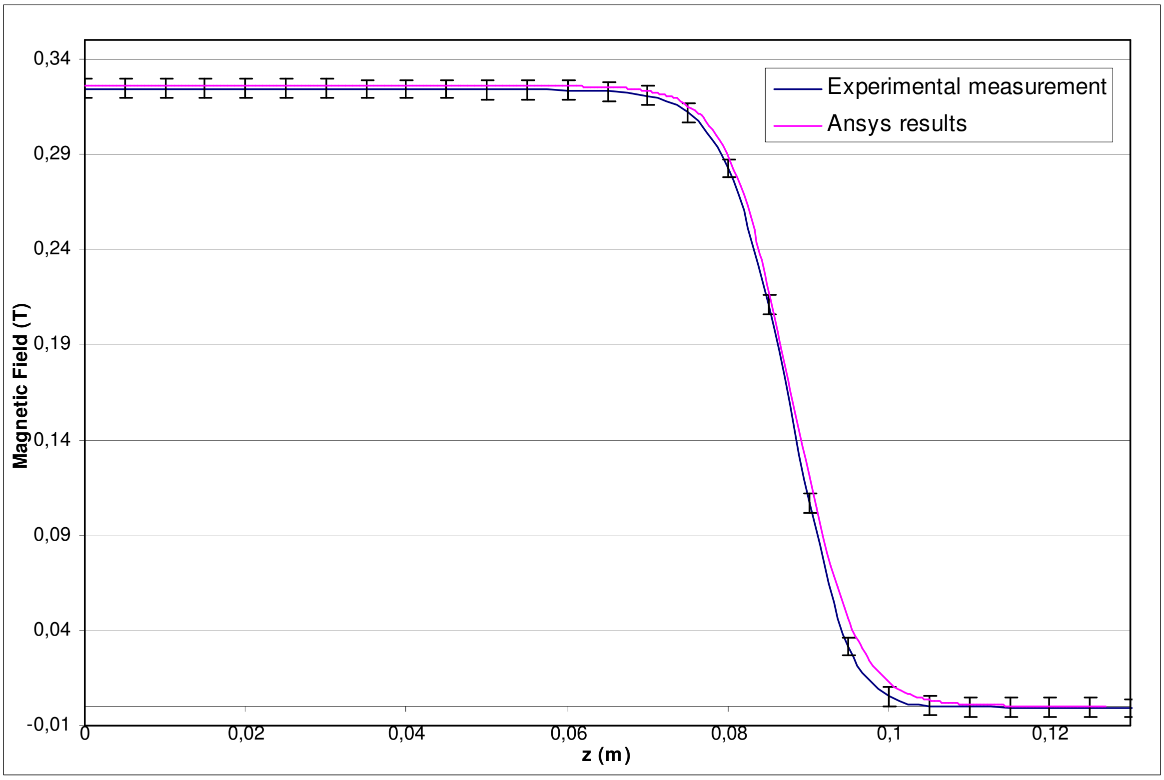

Figure 150: Measured and simulated magnetic field profiles along the straight line $x$=-13.5 mm for the extraction magnet with the new version of the frontal and lateral screens simulated in Sect. 4.4.2.

### 4.4.4. – Concluding remarks on the upgrade of the magnetic screens of the 55 MeV RTM extraction dipole.

The motivation of the study described in this section was the necessity to modify the magnetic screens of the hybrid extraction dipole of the SINP 55 MeV RTM with the aim to reduce the level of the stray magnetic field at the position of the neighboring orbits. To achieve this goal certain changes in the geometry of the screens were proposed, namely the modification of the beam aperture and the thickness of the frontal magnetic screens and increase of the length of the lateral screen. The extraction dipole with these modifications of the magnetic screens was simulated using the ANSYS code. Their final dimensions fixed in this study are the following: lateral magnetic screen with the thickness 2 mm and length 200mm, and upstream and downstream magnetic screens with dimensions 85x190x5 mm with a circular beam aperture of the radius 12 mm. The proposed modifications of the magnetic screens allowed to obtain the system that fulfils the required specifications. In particular, the level of the stray magnetic field at the position of neighboring 50.5 MeV orbit was reduced to the acceptable level so that its deviation angle became less than $\alpha_{9\,\mathrm{max}} = 0.15\,\mathrm{mrad}$.

Following the results of the 3D simulations the new magnetic screens were machined and installed. The experimental measurements, which also form part of the thesis, confirmed the validity of the proposed magnet screens upgrade. Also their comparison with the results of the 3D simulations of the extractions dipole with optimized magnetic screens showed very good agreement between the measurements and theoretical studies. This allows to conclude that the ANSYS code is quite a reliable tool for simulations of magnetic systems with permanent magnets.

We would like to mention that some other systems of the 55 MeV RTM, like the RF system, high voltage supply and gas system, have been upgraded recently [94]. The accelerator is currently used for physical experiments on the $^{18}F$ isotope production and radiation safety.

## Chapter 5

# Beam dynamics effects in RTM magnetic systems.

This chapter is devoted to the study of two effects which take place in the RTM beam dynamics. In Section 5.1 the effect of a phase-slip of a non-relativistic beam is analyzed. It is especially relevant for accelerators with low energy injection. In Section 5.2 the beam focusing by the fringe field of an end magnet with an additional thin dipole, similar to the one considered in Sect. 4.1, is studied. Both effects turn out to be important for the UPC 12 MeV RTM design.

## 5.1. – Beam phase slip in magnetic systems.

Formulas of the longitudinal beam dynamics given in Sect. 2.4 are written for the case of electrons whose velocity is practically equal to the speed of light. However, in many machines the beam after injection is far from being ultra-relativistic and these formulas cannot be applied. As a consequence the RTM synchronicity conditions, Eqs.(2) and (3), are not fulfilled and the phase of the beam at the entrance into the accelerating structure slips. We are going to analyze the phase slippage caused by the motion of a non-relativistic beam in magnetic systems and work out a formalism that gives the injection phase of a synchronous phase trajectory. The results of this study were published in Ref.[95].

### 5.1.1 Longitudinal dynamics of non – relativistic beams.

The main formulas of the longitudinal beam dynamics for the case of ultra-relativistic electrons with $\beta = v/c = 1$ are given in Sect. 2.4. More specifically equations of the energy and phase evolution with turns of the ultra-relativistic synchronous particle in an RTM with end magnets in the hard edge approximation were discussed there (see Eqs. (70), (71)).

Let us consider a simplified model of an electron RTM with a zero length accelerating structure already introduced in Sect. 2.4. In the present section the relativistic factor of the particles $\beta \leq 1$ and arbitrary field profile in the end magnets is considered. Similar to the discussion in Sect. 2.3.3 we suppose that the vertical component of the magnetic field in the median plane $B(Z)$ is described by the X-component of the vector potential $A_x(Z)$, namely $B(Z) = dA_x(Z)/dZ$. Here we use the same coordinate system and the same notations as in Ch. 2. We would like to note that a study of the phase dynamics of a non-relativistic beam with the end-magnets in the hard-edge approximation was done in Refs. [28,95]. In the case studied here the magnetic field profile is arbitrary and may include the fringe field, additional poles, etc.

For a non – relativistic electron the time of the *n*th revolution of a particle with energy $E_n$ is given by

$$T_n = \frac{2l}{\beta(E_n)c} + \frac{2}{\beta(E_n)c} L(E_n) \tag{131}$$

(cf. Eq. (72)), where $l$ is the distance between the end magnets, $\beta(E)$ is the relativistic factor $\beta = v/c$ understood as a function of energy $E$ and $L(E)$ is the length of the electron trajectory in the end magnet. To calculate this latter factor we introduce the maximum penetration $Z_{\max}(E)$ of the particle inside the end magnet which is defined from the condition $|e|A(Z_{\max}) = |p_z(E)|$ , where $p_z(E)$ is the longitudinal particle momentum at the entrance of the magnet. We suppose that the turn point $Z = Z_{\max}(E)$ is located in the region of the homogeneous field $B = B_0$, so that the vector potential $A_x(Z)$ is linear in $Z$ there. Then one can easily find that

$$Z_{\max}(E) = R(E) + \frac{\Delta Z_0}{2} \ , \tag{132a}$$

$$\Delta Z_0 = 2Z_B - 2\frac{A(Z_B)}{B_0} . \tag{132b}$$

Here $Z_B$ is an arbitrary point in the region of the constant magnetic field $B_0$ and

$$R(E) = \frac{E\beta(E)}{ecB_0} = \frac{\lambda\nu}{2\pi}\frac{E}{\Delta E_s}\beta(E) \tag{133}$$

is the radius of the trajectory of an electron of energy $E$ inside this region, where $\lambda$ is the RF field wavelength and $\Delta E_s$ is the energy gain of the corresponding ultra-relativistic synchronous particle. It is easy to check that physical results do not depend on the choice of $Z_B$. Calculating the path length of a charge particle moving in a magnetic field characterized by the potential $A(Z)$ one gets,

$$L(E) = \int_0^{Z_{\max}} \frac{dZ}{\sqrt{1 - \left[\dfrac{A_x(Z)}{B_0 R(E)}\right]^2}} \tag{134}$$

It is obvious that in the non-relativistic case the revolution time $T_n$ given by Eq. (131) cannot satisfy resonance conditions (2), (3) with integer $\mu_n$ and $\nu$ for all *n*. Nevertheless, as we are going to show now, even in this case it is possible to introduce the notion of *synchronous particle*.

For a given ultra-relativistic synchronous trajectory with synchronous phase $\varphi_s$ and energy $E_{n,s}$ described in Sect. 2.4 (recall that there the end magnet does not have fringe field) we define *synchronous particle* as the particle whose phase variables $(\varphi_n (\mathrm{mod}\, 2\pi), E_n)$ tend to $(\varphi_s, E_{n,s})$ as the orbit number $n \to \infty$, i.e.

$$\varphi_n (\mathrm{mod}\, 2\pi) \to \varphi_s \quad \text{as} \quad E_n \to E_{ns}. \tag{135}$$

Therefore the synchronous particle phase trajectory asymptotically approaches that of the corresponding ultra-relativistic synchronous particle. Note that, as it can be seen from Eq. (133), in this limit the effect of the fringe field becomes negligible. The phase $\varphi_n (\mathrm{mod}\, 2\pi)$ of the synchronous particle defined here is not constant but varies from turn to turn approaching the value $\varphi_s$ as $n \to \infty$. This is precisely the *phase slip effect*.

Let us show that a solution for the synchronous particle exists and derive analytic formulas describing the evolution of $\varphi_n$ and $E_n$. In what follows we will use the notations $\varphi_{n,s}$ and $E_{n,s}$ for the phase and energy of the corresponding ultra-relativistic synchronous particle, respectively.

The recurrence relations between $(\varphi_{n+1}, E_{n+1})$ and $(\varphi_n, E_n)$, analogous to (76), (77), are

$$E_{n+1} = E_n + \Delta E_{\max} \cos \varphi_n , \tag{136}$$

$$\varphi_{n+1} = \varphi_n + K(E_{n+1}) , \tag{137}$$

where the term $K(E_{n+1})$ is equal to the phase advance of a particle with energy $E_{n+1}$ in one turn, $K(E_{n+1}) = 2\pi T_{n+1} / T_{RF}$, and is given by the formula

$$K(E) = 4\pi \frac{l}{\lambda} \frac{1}{\beta(E)} + \frac{8\pi}{\lambda \beta(E)} L(E) \tag{138}$$

As the energy grows, the longitudinal phase coordinates get closer to those of the asymptotic synchronous particle, therefore it is reasonable to describe $(\varphi_n, E_n)$ by deviations with respect to the asymptotic synchronous trajectory $(\varphi_{ns}, E_{ns})$. To this end we introduce new dimensionless variables $w_n$ and $\psi_n$ as follows

$$\frac{\Delta E_s}{2\pi \upsilon} w_n = E_n - E_{ns} , \tag{139}$$

$$\psi_n = \varphi_n - \varphi_{ns} \; . \tag{140}$$

For a synchronous particle $w_n$ and $\psi_n$ tend to zero for $n \to \infty$. Combining Eqs. (136), (137) and (139), (140) and using relations (78)-(80) one readily arrives at the following system of difference equations,

$$w_{n+1} = w_n + F(\psi) \tag{141}$$

$$\psi_{n+1} = \psi_n + \Delta K(\varepsilon_{n+1}, w_{n+1}) \tag{142}$$

where,

$$F(\psi) = \Delta E_s \left[ \frac{\cos(\varphi_s + \psi_n)}{\cos(\varphi_s)} - 1 \right] \tag{143}$$

$$\Delta K(\varepsilon_{n+1}, w_{n+1}) = K(E_{n+1,s}) - K_0(E_{n+1,s}) \tag{144}$$

To calculate the deviation of the synchronous trajectory $(\varphi_n, E_n)$ from the asymptotic synchronous one $(\varphi_{ns}, E_{ns})$ known explicitly (see Sect. 2.4) we introduce a dimensionless parameter $\varepsilon_n = \Delta E_s / E_{ns}$ which decreases as *n* grows. We will search for the solution of system (141), (142) as perturbation expansion in powers of $\varepsilon_n$. For this we write

$$\psi_n = \sum_{k=1}^{\infty} a_k \varepsilon_n^k \,, \tag{145}$$

$$w_n = \sum_{k=1}^{\infty} b_k \varepsilon_n^k \,, \tag{146}$$

where $a_k$ and $b_k$ are coefficients independent of $\varepsilon_n$, substitute these series into Eqs. (141) and (142) and calculate the expansions of $F(\psi_n)$ and $\Delta K(\varepsilon_{n+1}, w_{n+1})$ in powers of $\varepsilon_n$. In working out the expressions one should take into account that,

$$\varepsilon_{n+1} = \varepsilon_n - \varepsilon_n^2 + \varepsilon_n^3 - O(\varepsilon_n^4) \tag{147}$$

$$\varepsilon_{n-1} = \varepsilon_n + \varepsilon_n^2 + \varepsilon_n^3 + O(\varepsilon_n^4) \tag{148}$$

Since $\varepsilon_n$ are independent variables by matching the coefficients of equal powers of $\varepsilon_n$ in both sides of Eqs.(141) and (142) one gets a set of recurrence relations from which $a_k$ and $b_k$ up to any given order can be obtained. The solution for $\psi_n$ and $w_n$ with the first three terms in series (145), (146) is the following:

$$\psi_n = -\frac{k_2}{\pi\nu\tan(\varphi_s)}\varepsilon_n^3 + \frac{3k_2}{2\pi\nu\tan(\varphi_s)}\varepsilon_n^5 + \left[\frac{2}{\pi\nu\tan(\varphi_s)}\right]\left[\frac{3}{\pi\nu\tan(\varphi_s)}k_2 - k_2 - k_4\right]\varepsilon_n^7 + O(\varepsilon_n^9) \,, \tag{149}$$

$$w_n = -k_2\varepsilon_n^2 + \left(\frac{3k_2}{\pi\upsilon\tan(\varphi_s)} - k_4\right)\varepsilon_n^4 - \frac{k_2^2}{\pi\nu}\varepsilon_n^6 + O(\varepsilon_n^8), \tag{150}$$

where

$$k_2 = 2\pi\frac{\tilde{l}}{\lambda}\kappa^2 + d_2 \,, \tag{151}$$

$$d_2 = \frac{16\pi^2}{\lambda^3\nu^2}\left[\frac{1}{B_0^2}\int_0^{zB}(A(z))^2 dz - \frac{1}{3B_0^3}(A(z_B))^3\right] , \tag{152}$$

$$k_4 = \frac{3}{2}\pi\kappa^4 \frac{\tilde{l}}{\lambda} + d_4 , \tag{153}$$

$$d_4 = \frac{48\pi^5}{\lambda^5 \nu^4}\left[\frac{1}{B_0^4}\int_0^{zB}(A(z))^4 dz - \frac{1}{5B_0^5}(A(z_B))^5\right]. \tag{154}$$

Here $\kappa = mc^2/\Delta E_s$ and $\tilde{l}$ is a parameter that takes into account the separation between the end magnets and the magnetic profile of the end magnet and is given by

$$\tilde{l} = l + \Delta Z_0 \tag{155}$$

where $l$ is the straight section length and $\Delta Z_0$ is given by Eq. (122b).

Inserting solution (149) and (150) in equations (139) and (140) we obtain the formulas relating the synchronous trajectory $(\varphi_n, E_n)$ to the ultra-relativistic synchronous trajectory $(\varphi_{ns}, E_{ns})$:

$$\varphi_n = \varphi_{ns} - \frac{k_2}{\pi\nu\tan(\varphi_s)}\varepsilon_n^3 + \frac{3k_2}{2\pi\nu\tan(\varphi_s)}\varepsilon_n^5 + \left[\frac{2}{\pi\nu\tan(\varphi_s)}\right]\left[\frac{3}{\pi\nu\tan(\varphi_s)}k_2 - k_2 - k_4\right]\varepsilon_n^7 + O\left(\varepsilon_n^9\right) \tag{156}$$

$$E_n = E_{ns} + \frac{\Delta E_s}{2\pi\nu}\left[-k_2\varepsilon_n^2 + \left(\frac{3k_2}{\pi\upsilon\tan(\varphi_s)} - k_4\right)\varepsilon_n^4 - \frac{k_2^2}{\pi\nu}\varepsilon_n^6 + O\left(\varepsilon_n^8\right)\right] \tag{157}$$

Solutions (156) and (157) determine the synchronous trajectory corresponding to the asymptotic synchronous phase $\varphi_s$ . The phase shift of the non-relativistic synchronous particle follows the well determined pattern described by Eq. (156). We would like to note that a general phase trajectory $(\tilde{\varphi}_n, \tilde{E}_n)$ of an arbitrary particle in addition to terms (156), (157) includes synchrotron oscillations (see Ref.[30]), namely

$$\tilde{\varphi}_n = \varphi_n + C\sin(Qn + \chi_0),$$
$$\tilde{E}_n = E_n + \frac{\Delta E_s}{2\pi\nu}C\sqrt{2\pi\nu\tan\varphi_s}\cos(Qn + \chi_0 - Q/2),$$

where $C$ and $\chi_0$ are constants determined by the initial conditions.

### 5.1.2. – Fixing the synchronous particle injection phase and RTM parameters: analytical approach.

As we will show for each value of $\varphi_s$ and sequence $E_{ns}$ given by (79) there exist only one synchronous phase trajectory that asymptotically approaches $(\varphi_s(\text{mod}\,2\pi), E_{ns})$ when $n \to \infty$. This trajectory is fully defined by two parameters, for example by the initial phase $\varphi_0$ and the initial particle energy $E_0$. In other words, only for certain values of $\varphi_0$ and $E_0$ the phase trajectory is described by formulas (157) and

(158) without synchrotron oscillations. As we will see below in practice it is more natural to fix the initial phase $\varphi_0$ and the ratio $\tilde{l}/\lambda$ for a given $E_0$.

In this section we will derive analytical approximate equation which determines such parameters. Using Eqs. (139) and (140) we write the phase and energy of a synchronous particle at the end of the first orbit as follows:

$$E_1 = E_{1s} + \frac{\Delta Es}{2\pi\nu} w_1\left(\frac{\tilde{l}}{\lambda}\right), \tag{158}$$

$$\varphi_1 = \varphi_s + \psi_1\left(\frac{\tilde{l}}{\lambda}\right). \tag{159}$$

Here $E_{1s} = E_{0s} + \Delta E_s$, where $E_{0s}$ is given by Eq. (75) but with $l$ substituted by $\tilde{l}$, so that

$$E_1 = \frac{\Delta E_s}{\nu}\left[\mu - 2\frac{\tilde{l}}{\lambda}\right] + \frac{\Delta E_s}{2\pi\nu} w_1\left(\frac{\tilde{l}}{\lambda}\right) \tag{160}$$

In these equations and in what follows we indicate the dependence of the functions $w_1$ and $\psi_1$ on $\tilde{l}/\lambda$ explicitly. Note that in Eq. (159) we write $\varphi_s$ instead of $\varphi_{1s}$. Since the difference between them is a multiple of $2\pi$ and the energy gain depends on $\cos(\varphi)$ such substitution does affect the results. For $w_1(\tilde{l}/\lambda)$ and $\psi_1(\tilde{l}/\lambda)$ we will consider only the first three terms of the series (141) and (142), i.e. as in Eqs. (149), (150).

On the other hand, as it follows from Eqs. (136), (137), for a given injection energy $E_0$ one gets

$$E_1 = E_0 + \Delta E_s \frac{\cos(\varphi_0)}{\cos(\varphi_s)}, \tag{161}$$

$$\varphi_1 = \varphi_0 + K\left(E_1, \frac{\tilde{l}}{\lambda}\right), \tag{162}$$

where $E_0$ is the injection energy. Substituting Eq. (162) for $\varphi_1$ into Eq. (159) we obtain a relation that determines the particle injection phase $\varphi_0$:

$$\varphi_0 = \varphi_s + \psi_1\left(\frac{\tilde{l}}{\lambda}\right) - K\left(E_1, \frac{\tilde{l}}{\lambda}\right). \tag{163}$$

Equating Eqs. (160) and (161) and using relation (163) for $\varphi_0$ we obtain the following equation

$$\frac{\Delta E_s}{\nu}\left[\mu - 2\frac{\tilde{l}}{\lambda}\right] + \frac{\Delta E_s}{2\pi\nu} w_1\left(\frac{\tilde{l}}{\lambda}\right) = E_0 + \Delta E_s \frac{1}{\cos(\varphi_s)} \cos\left(\varphi_s + \psi_1\left(\frac{\tilde{l}}{\lambda}\right) - K\left(E_1, \frac{\tilde{l}}{\lambda}\right)\right). \quad (164)$$

Here the energy at the first orbit $E_1$ is considered as a function of $\tilde{l}/\lambda$ given by relation (160). Eq. (164) can be regarded as an equation that determines the injection energy of the reference particle for given $\tilde{l}/\lambda$. However, usually in RTMs the injection energy is fixed by the electron gun or injection line and it cannot be easily changed, whereas the distance $l$ between the end magnets can be adjusted without much difficulties. Therefore we will consider Eq. (163) as equation on $\tilde{l}/\lambda$ for a given $E_0$.

This equation is easily solved by standard numerical methods. Substituting the solution for $\tilde{l}/\lambda$ into Eq. (153) we obtain the value of the particle injection phase $\varphi_0$.

Now let us apply this approach to the calculation of the injection phase and the distance between the end magnets for an RTM whose end magnets are 2-pole magnetic systems of the type studied in Sect. 4.1. We will consider the following two illustrating examples:

**Example 1**: Low energy injection case with $E_0 = 4.536$ MeV. It corresponds to the energy of the electrons after the beam reflection in the M1 end magnet of the UPC 12 MeV RTM studied in Sect. 4.1.

**Example 2**: High energy injection case with $E_0 = 12.536$ MeV.

For both examples we will consider an RTM with the following parameters: harmonic number increment in one turn $\nu = 1$, RF wavelength $\lambda = 5.0\,cm$, maximal beam energy gain in the accelerating structure $\Delta E_{\max} = 2.08 MeV$ and the phase of the asymptotic synchronous particle $\varphi_s = 16°$. We assume that the profile of the vertical component of the magnetic field in the median plane of the end magnets is given by the function

$$B(z) = \frac{B_0}{1 + \exp\left(-\frac{z - z_2}{h_0}\right)} - \frac{B_1}{ch^2\left(\frac{z - z_1}{2h_1}\right)}. \quad (165)$$

The X-component of the corresponding magnetic vector potential is then equal to

$$A_X(z) = B_0 h_0\left(1 + \exp\left(\frac{z - z_2}{h_0}\right)\right) - 2B_1 h_1\left[\tanh\left(\frac{z - z_1}{2h_1}\right) + 1\right]. \quad (166)$$

Parameters characterizing these functions are the following: $B_0$ is the magnetic field value in the uniform magnetic field region of the main pole, $B_1$ is the maximum magnetic field value of the inverse pole, $z_1$ is the position of the inverse pole center, $z_2$ is the position of the main pole face, $h_1$ is the half thickness of the magnetic field distribution of the inverse pole and $h_0$ is the extension of the fringe field of the main pole. For the purpose of illustration the following values of these parameters were chosen: $B_0 = 0.83T$ , $B_1 = 0.3B_0$ , $h_0 = h_1 = 0.1cm$ , $z_1 = 0.75cm$ and $z_2 = 2.0cm$ . The plot of the magnetic field profile is shown in Fig. 151.

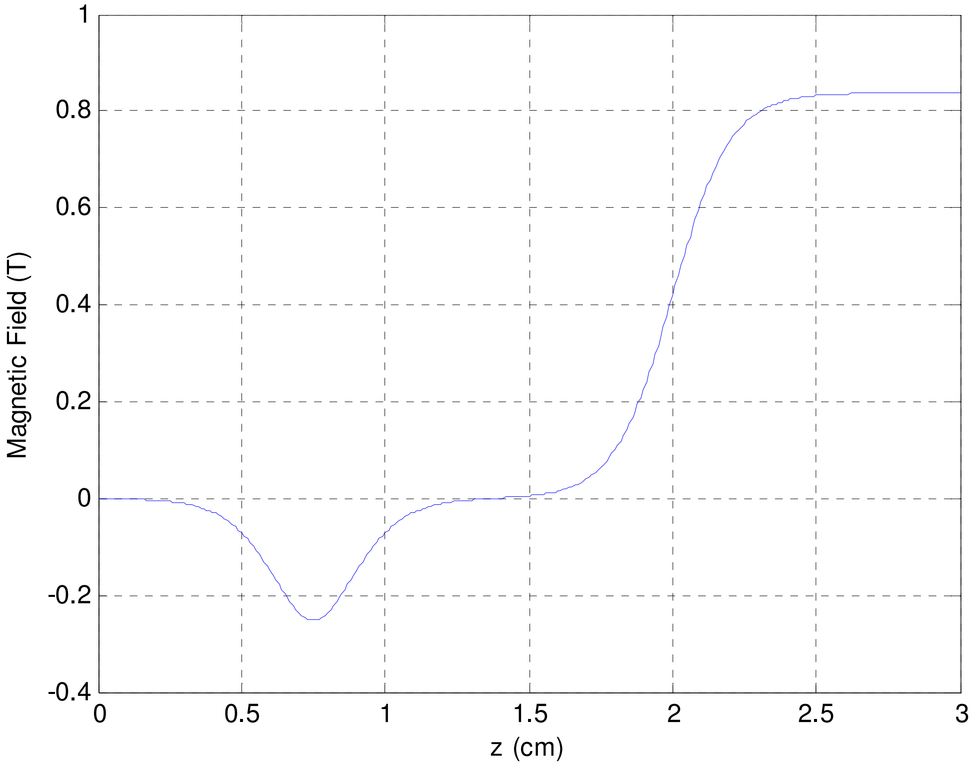

Figure 151: Plot of the vertical component of the magnetic field in the median plane in the 2-pole end magnets for the RTM considered in Example 1 and Example 2.

For the two examples described above we calculate the effective distance between the end magnets $\tilde{l}$ and injection phase $\varphi_0$ for which the trajectory is synchronous, i.e. without synchrotron oscillations.

**Example 1:** We choose μ=13. The solution of Eq. (164) is $\left(\tilde{l}/\lambda\right)_{th} = 4.29732$ . Substituting it into Eq. (152) one obtains the particle injection phase, $\varphi_{0,th} = 11.887^\circ$. Once the distance between the end magnets and the injection phase are determined the next step is to study the particle phase evolution as a function of the orbit number. This is done using recurrence relations (126), (127).

The evolution of the particle phase as a function of the turn number is shown in Fig. 153. As one can see the trajectory with $\varphi_{0,th} = 11.887^\circ$ in fact makes synchrotron oscillations around the synchronous phase trajectory. In the high energy region they are of constant amplitude $\Delta\varphi = 2.17^\circ$ . This is of course due to the approximate character of the method. Indeed, remember that the functions $w_1$ and $\psi_1$ in Eqs. (158), (159) are approximated by only three first terms in the series (145), (146). The value of the expansion parameter is $\varepsilon_1 = 0.3024$ .

**Example 2:** In this case we have chosen μ=17. The solution of Eq. (164) is $\left(\tilde{l}/\lambda\right)_{th} = 4.31452$ and the injection phase, $\varphi_{0,th} = 15.6166^{\circ}$. The change of the particle phase with turns is shown in Fig. 154, this plot is obtained by using Eqs. (136), (137). Some synchrotron oscillations exist in this case too, their amplitude is smaller than in the previous example and is about $\Delta\varphi = 0.24^{\circ}$. The value of the expansion parameter is $\varepsilon_1 = 0.1375$.

From the above examples it can be seen that, as one expects, the precision of the method is better for higher injection energy $E_0$, i.e. when the injected electrons are more relativistic. We would like to note that the accuracy of the formalism for fixing the injection phase $\varphi_0$ and the distance between the end magnet $l$ for a given injction energy $E_0$ described here can be increased by using more precise expressions for the functions $w_1$ and $\psi_1$, i.e. by including more terms in Eqs. (135), (136). In the next section we will consider the same examples adjusting $\tilde{l}/\lambda$ and $\varphi_0$ numerically.

### 5.1.3. – Fixing the synchronous particle injection phase and RTM parameters: numerical calculation.

One can tune the injection phase $\varphi_0$ of the synchronous trajectory and adjust $\tilde{l}/\lambda$ to the corresponding value numerically directly from the recursive relations (126), (127). The procedure consists in varying the parameter $\tilde{l}/\lambda$ and the initial phase $\varphi_0$ for a given injection energy $E_0$ and calculating the phase trajectory $(\varphi_n, E_n)$ for a sufficiently large number of turns for each pair of values $(\tilde{l}/\lambda, \varphi_0)$. The procedure is stopped when the trajectory without synchrotron oscillations is obtained for which the particle phase tends toward a synchronous phase $\varphi_s$ at high energies.

The calculations were performed using a program written in MATLAB. The parameters $\varphi_0$ and $\tilde{l}/\lambda$ were scanned over the two-dimensional region

$$\varphi_{0,\min} \le \varphi_0 \le \varphi_{0,\max}, \qquad 3.0 \le \tilde{l}/\lambda \le 5.0$$

with the steps $\delta\varphi_0 = 10^{-4}$, $\delta(\tilde{l}/\lambda) = 10^{-6}$, respectively. Here $\varphi_{0,\min}$ and $\varphi_{0,\max}$ are vaues which are chosen depending on the particular case on the basis of some preliminary estimates, typically $\varphi_{0,\max} - \varphi_{0,\min} \approx 2^{\circ}$. For each point $(\tilde{l}/\lambda, \varphi_0)$ the phase trajectory was calculated till $n = n_{\max} = 100$ orbits provided no instability appears for $n < n_{\max}$.

The same examples as in the previous section were studied.

**Example 1:** $E_0 = 4.536$ MeV (see Fig. 153). The numerical approach gives $\left(\tilde{l}/\lambda\right)_{num} = 4.29898$, $\varphi_{0,num} = 12.5883^{\circ}$. When compared with the analytical results obtained in the previous section we get that $|\Delta\varphi_0| \equiv |\varphi_{0,num} - \varphi_{0,th}| = 1.08^{\circ}$ and the relative error is $|\Delta\varphi_0|/\varphi_{0,num} \approx 0.06$. For $\tilde{l}/\lambda$ the comparison gives $|\Delta(\tilde{l}/\lambda)| \equiv |(\tilde{l}/\lambda)_{num} - (\tilde{l}/\lambda)_{th}| = 1.7\times10^{-3}$ and the corresponding relative error is about $0.4$. The low accuracy is due to a relatively large value of the expansion parameter.

**Example 2:** $E_0 = 12.536$ MeV (Fig. 154). The results are: $(\tilde{l}/\lambda)_{num} = 4.31467$, $\varphi_{0,num} = 15.73629^\circ$. The comparison with the results obtained within the analytical approach gives $|\Delta\varphi_0| = 0.11^\mathrm{o}$ and the relative error is $|\Delta\varphi_0|/\varphi_{0,num} \approx 0.007$, $|\Delta(\tilde{l}/\lambda)| \equiv |(\tilde{l}/\lambda)_{num} - (\tilde{l}/\lambda)_{th}| = 1.45\times10^{-4}$ and the corresponding relative error is about $3.3\times10^{-3}$. The better accuracy of the analytic procedure in this case is due to the smaller value of the expansion parameter $\varepsilon_1$.

From the plots shown in Fig. 152 and Fig. 153 one can see that the curves obtained within the numerical approach do not have synchrotron oscillations, i.e. they are true synchronous trajectories approaching monotonously the asymptotic synchronous trajectory $\varphi_{s,n} = \phi_s = 16^\circ$. The trajectories obtained within the analytical method experience certain synchrotron oscillations, this is due to the errors of this approach.

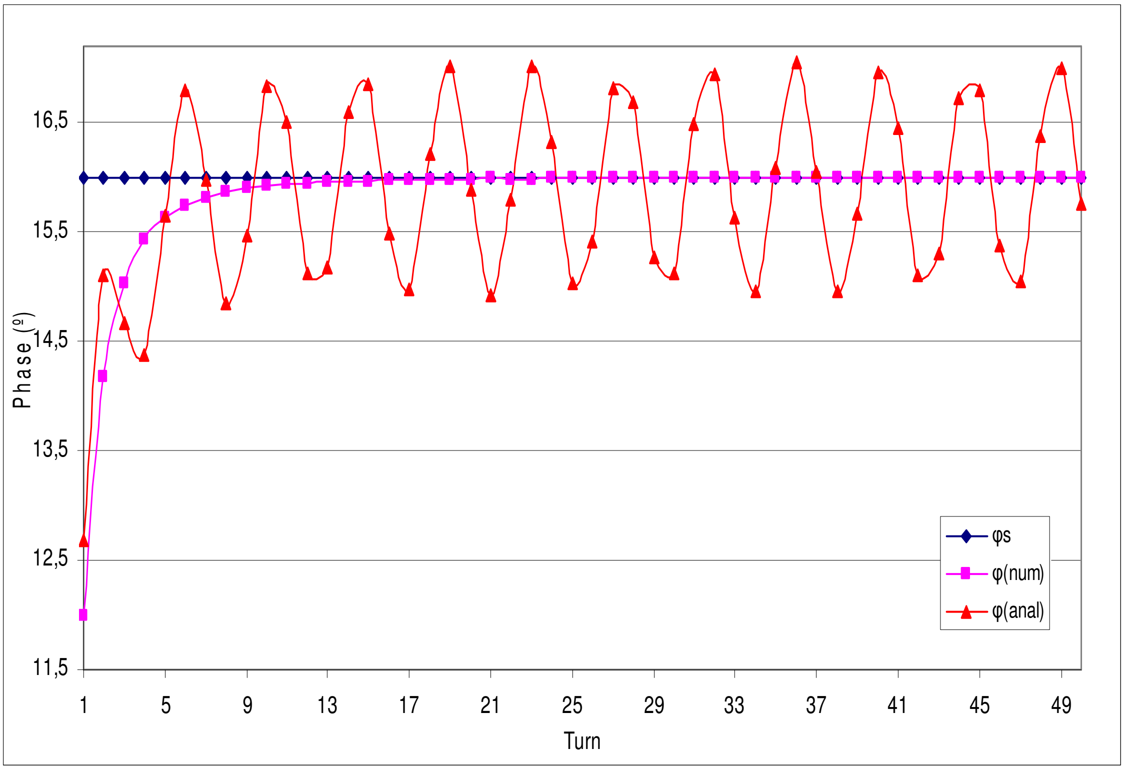

Figure 152: Behaviour of the particle phase with turns in Example 1 with $E_0 = 4.536$ MeV. The results obtained by solving Eq.(164) and by numerical tuning are given, also the asymptotic value $\varphi_s = 16^\mathrm{o}$ is shown.

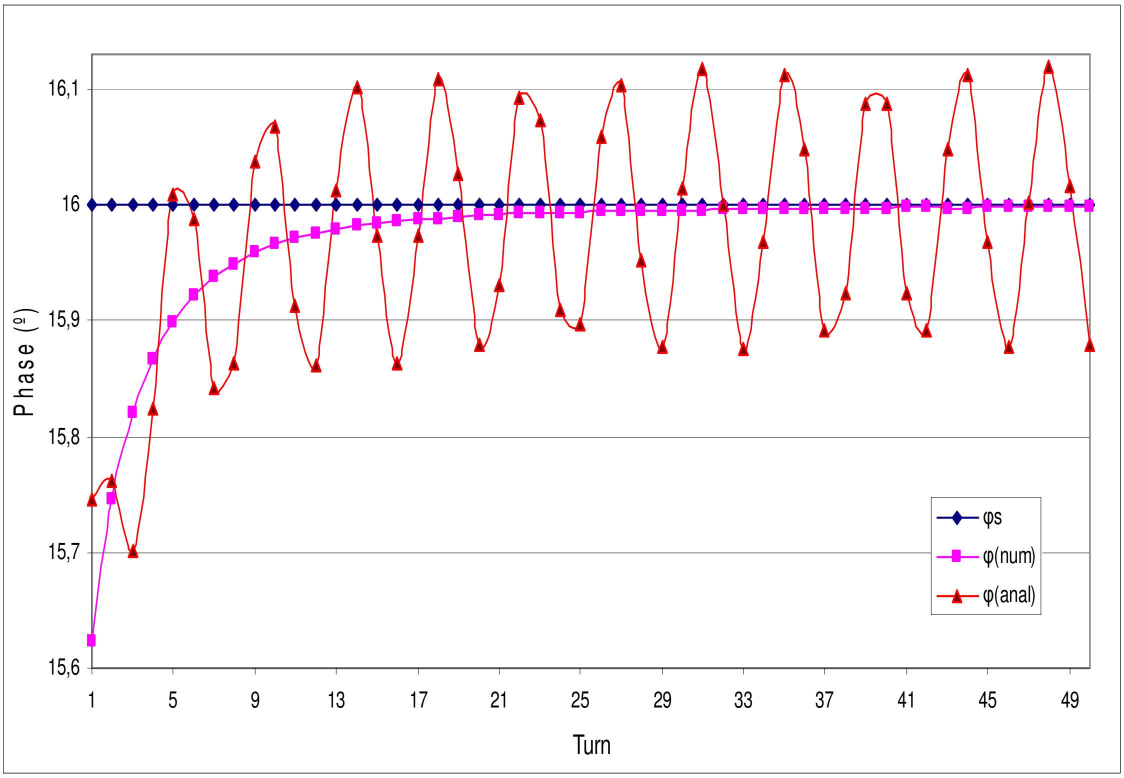

Figure 153: Behaviour of the particle phase with turns in Example 2 with $E_0 = 12.536$ MeV. The results obtained by solving Eq.(164) and by numerical tuning are given, also the asymptotic value $\varphi_s = 16^{\circ}$ is shown.

As a part of the design studies of the UPC 12 MeV RTM we calculated the initial phase $\varphi_0$ of the synchronous trajectory taking as $E_0$ the energies of the accelerator at different orbits. The calculations were done using both the analytical method and the numerical approach. The results of calculations are given in Table 28. As one can see, with the increase of the initial energy the values of $(\tilde{l}/\lambda)_{th}$ and $\varphi_{0,th}$ approach the ones obtained within the numerical approach. This is because the value of $E_{0s}$ of the corresponding asymptotic synchronous trajectory is always close to the initial energy $E_0$ and therefore the parameter $\varepsilon_1 = \Delta E_s / E_{1s}$ decreases with the increase of $E_0$.

Table 28: Results of calculation of the initial phase $\varphi_0$ and parameter $\tilde{l}/\lambda$ for the energies of the orbits of the UPC 12 MeV RTM.

| | φ(º) | | | $\tilde{l}/\lambda$ | | |
|---|---|---|---|---|---|---|
| | $\varphi_{o,num}$ | $\varphi_{o,th}$ | $\varphi_{o,num} - \varphi_{0,th}$ | $(\tilde{l}/\lambda)_{num}$ | $(\tilde{l}/\lambda)_{th}$ | $(\tilde{l}/\lambda)_{num} - (\tilde{l}/\lambda)_{th}$ |
| **4.536 MeV** | 12.5883 | 11.887 | 0.7013 | 4.29898 | 4.29732 | 0.00166 |
| **6.536 MeV** | 14.3712 | 14.1039 | 0.3193 | 4.30671 | 4.30618 | 0.00053 |
| **8.536 MeV** | 15.1478 | 14.9871 | 0.1678 | 4.31086 | 4.31061 | 0.00025 |
| **10.536 MeV** | 15.5308 | 15.4006 | 0.1228 | 4.31322 | 4.31305 | 0.00016 |
| **12.536 MeV** | 15.7363 | 15.6166 | 0.1098 | 4.31467 | 4.31452 | 0.00014 |

We would like to note that in the numerical approach the nonlinear dynamics described by Eqs. (126), (127) is treated in its full version without any approximation, and the accuracy of the method is limited only by the precision of the numerical computations. However, this numerical approach does not allow us to control the dependence of the tuned injection phase $\varphi_0$ of the synchronous trajectory and the adjusted value of $\tilde{l}/\lambda$ on other parameters of the accelerator, as it can be done using Eqs.(163) and (164). This explains the importance of the analytical formalism described in the previous section for the RTM design.

## 5.2. - Focusing properties of the end magnets.

As it was already discussed in the previous chapters the influence of the fringe field of the RTM end magnets on the beam dynamics is important and must be taken into account in the design of accelerators. The main effect is the vertical defocusing that may affect the beam stability. It is especially considerable for the low energy orbits. In this section we analyze the focusing both by the end magnet fringe field and by the magnetic field of narrow dipoles. Using these results we will study analytically some properties of the 2-pole magnetic systems consisting of the main 180º bending dipole and an additional dipole with an inverse field that were considered in the framework of the numerical approach in Sect. 4.1.

To study these effects analytically we will use a linear approximation for the varying part of the magnetic field profile, both for the fringe field and inverse pole field. The results of this section were published in Ref.[51].

### 5.2.1. – Focusing by the dipole fringe field.

Let us study first a dipole magnet using the same reference system as in Ch. 2 with the Z-axis being the longitudinal axis. We suppose that its size in the X-direction is large enough so that the field can be considered constant along the X-axis. The dipole magnetic field in the median plane varies in the interval $0 < Z < l$ and is constant for $Z > l$. As it has been said above we use a linear approximation of the field, i.e. its vertical component in the median plane is given by

$$B(z) = \begin{cases} 0 & Z < 0 \\ B_0 \dfrac{Z}{l} & 0 < Z < l \\ B_0 & Z > l \end{cases} \qquad (167)$$

where $B_0$ is the magnetic field value in the uniform magnetic field region. The magnetic field profile of the dipole is shown in Fig.154.

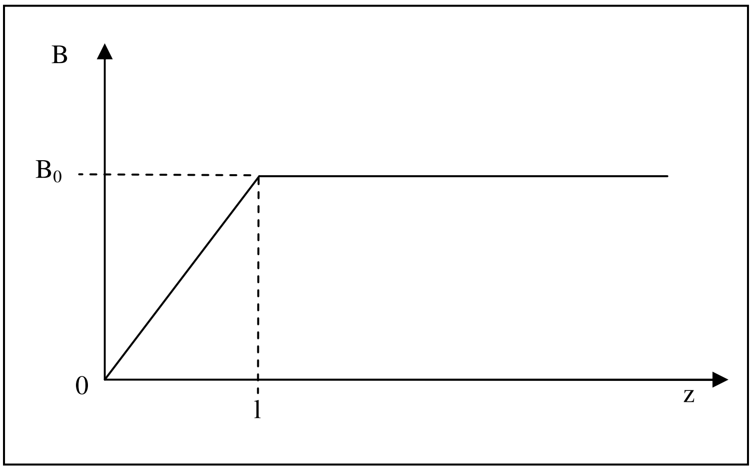

Figure 154: Magnetic field profile of the dipole magnet.

To calculate the vertical focusing power of this magnet we use Eq.(63). The result is

$$\frac{1}{f_{fringe}} = -\frac{l}{6R_0^{\,2}} \tag{168}$$

Here $R_0$ is the radius of the circular trajectory followed by the particle in the uniform magnetic field region. As one can see the dipole fringe field produces a vertical defocusing of the beam and its focal power is proportional to the fringe field width $l$.

Now let us consider electron trajectories in an RTM dipole end magnet with the fringe field introduced above. Particles cross the fringe field at the entrance and exit of the magnet, as it is shown in Fig. 156. We suppose that the width of the fringe field is short, namely $l << R_0$, so that it can be represented by a thin defocusing lens so that to calculate the beam transport through the end magnet we can use the matrix formalism described in Sect. 2.3.1. For the vertical particle motion the magnet corresponds to the doublet of defocusing quadrupoles and the drift space of length $l_0$ equal to the path length of the particle in the uniform magnetic field region,

$$l_0 = R_0\theta_0 \tag{169}$$

where $R_0$ is the parameter introduced in Eq.(167) and $\theta_0$ is the angle of beam bending (see Fig. 156). Since the bending in the horizontal plane produced by the fringe field is small then the electron trajectories are normal to the magnet face at the entrance and therefore $\theta_0 = 180^\circ$. Using the standard formula we obtain that the focusing power of this magnetic system is equal to

$$P_{MP} \equiv \frac{1}{F_{MP}} = \frac{2}{f_{fringe}} - \frac{l_0}{f_{fringe}^2} \tag{170}$$

where $f_{fringe}$ is the focal length of the fringe field given by Eq.(168) and the subindex MP stands for the main pole. For the case $\theta_0 = 180^\circ$ we obtain

$$P_{MP} = -\frac{l}{3R_0^2}\left(1+\frac{\pi}{12}\frac{l}{R_0}\right). \tag{170a}$$

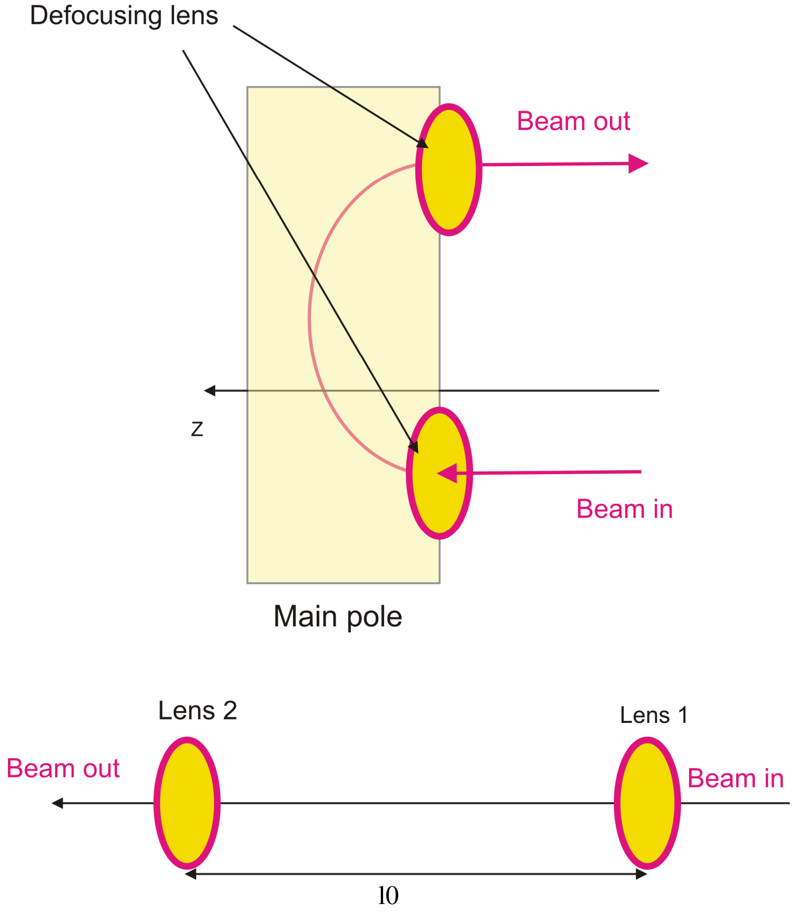

Figure 155: Scheme of the beam motion in the end magnet with the fringe field and its representation within the matrix formalism.

Since the radius of the electron trajectory grows with energy the defocusing by the end magnet fringe field gets weaker as the energy grows. The plot of $P_{MP}$ as a function of energy for the case $B_0 = 0.8T$ , $l = 6.0mm$ is shown in Fig.156.

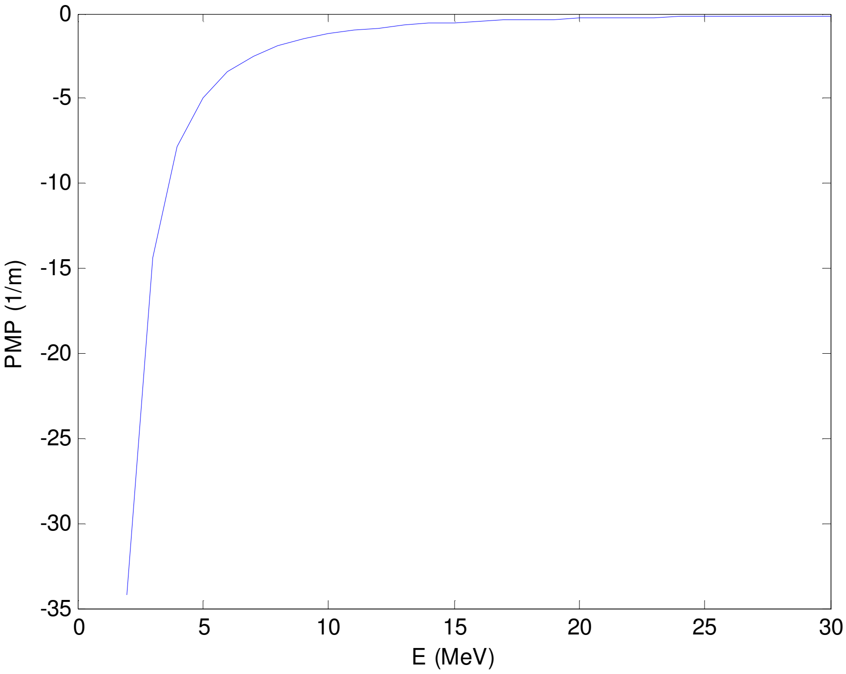

Figure 156: Vertical focusing power of the end magnet as a function of the particle energy.

From the obtained result one can see that the end magnet fringe field produces beam defocusing and leads to a beam instability. The effect is particularly strong for low energies and therefore in RTMs with low energy injection. A solution of this problem proposed by H. Babic and M. Sedlacek in Ref.[26] consists in placing an additional narrow dipole pole with the polarity of the field inverse to that of the main dipole. Such 2-pole end magnet will be studied in the next section.

### 5.2.2. – Focusing properties of a 2-pole end magnet.

In this section we consider the vertical beam focusing produced by the magnetic field of an end magnet consisting of the main 180º bending magnet and a thin dipole of inverse field polarity. Such magnetic system, chosen for the first version of the design of the end magnets of the UPC 12 MeV RTM, was studied numerically in Sect. 4.1. For the sake of brevity such dipole assemblies were called 2-pole magnets.

In the present section we will carry out an analytical study of such 2-pole magnet using a linear model. The magnetic field of the inverse pole is localized in the interval $0 < Z < 2Z_1$ with the minimum magnetic field value $(-B_1) < 0$. The fringe magnetic field of the main pole has the width $d$ and extends from $Z = l - d$ to $Z = l$. The uniform magnetic field of the main dipole is equal to $B_0 > 0$ for $Z > l$. The vertical component of the magnetic field of this system in the median plane is shown in Fig. 157 and is described by the following relations:

$$B(z)=\begin{cases} -B_1\dfrac{Z}{Z_1} & 0<Z<Z_1 \\ B_1\dfrac{Z}{Z_1}-2Z_1 & Z_1<Z<2Z_1 \\ B_0\dfrac{Z}{d}-B_0\dfrac{(l-d)}{d} & l-d<Z<l \\ B_0 & Z>l \end{cases} \tag{171}$$

Here, as before, $R_0$ is the radius of the circular trajectory followed by the particle in the uniform magnetic field region of the main pole. Using Eq. (70) we obtain that the focusing power of the thin dipole is equal to

$$\frac{1}{f_1}=\frac{2}{3R_0^2}\left(\frac{B_1}{B_0}\right)^2 Z_1. \tag{171a}$$

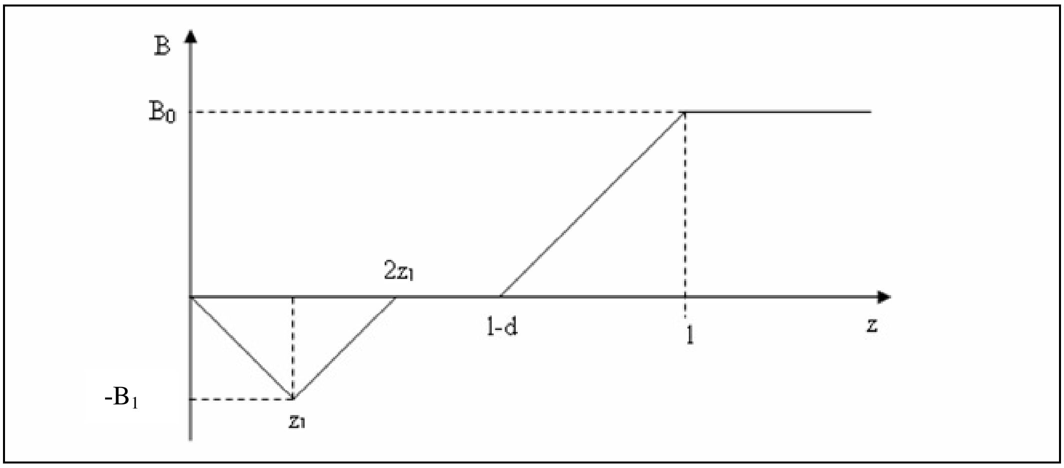

Figure 157: Plot of the vertical component of the magnetic field in the median plane of the 2-pole magnetic system within the linear model.

We suppose that the width of the inverse pole $2Z_1$ and that of the main pole fringe field $d$ are small in comparison with $R_0$ so that the focusing properties of the magnet can be described within the matrix formalism representing the system as the transport line with four lenses and three drift spaces as shown in Fig.158. The main pole fringe field is modeled by 2 defocusing quadrupoles, as in the previous section, placed at $Z=l$, whereas the inverse pole is modeled by two focusing quadrupoles placed at the entrance and exit of the magnetic system at $Z=Z_1<<l$. Then the 2-pole magnetic system can be considered as a transport line consisting of two quadrupole doublets separated by a drift space of length $l_0=R_0\theta_0$ as in Eq. (159). Each doublet is formed by one focusing lens and one defocusing lens with the drift space of length $l$ between them (see Fig.158). The trajectory length in the uniform magnetic field is determined by the arc angle $\theta_0=\pi-2|\alpha|$, where $\alpha$ is the trajectory bending angle in the inverse pole given by (see Eq.(48))

$$\sin\alpha=\frac{d}{R_1}, \tag{172}$$

where $R_1$ is the beam orbit radius in the inverse pole.

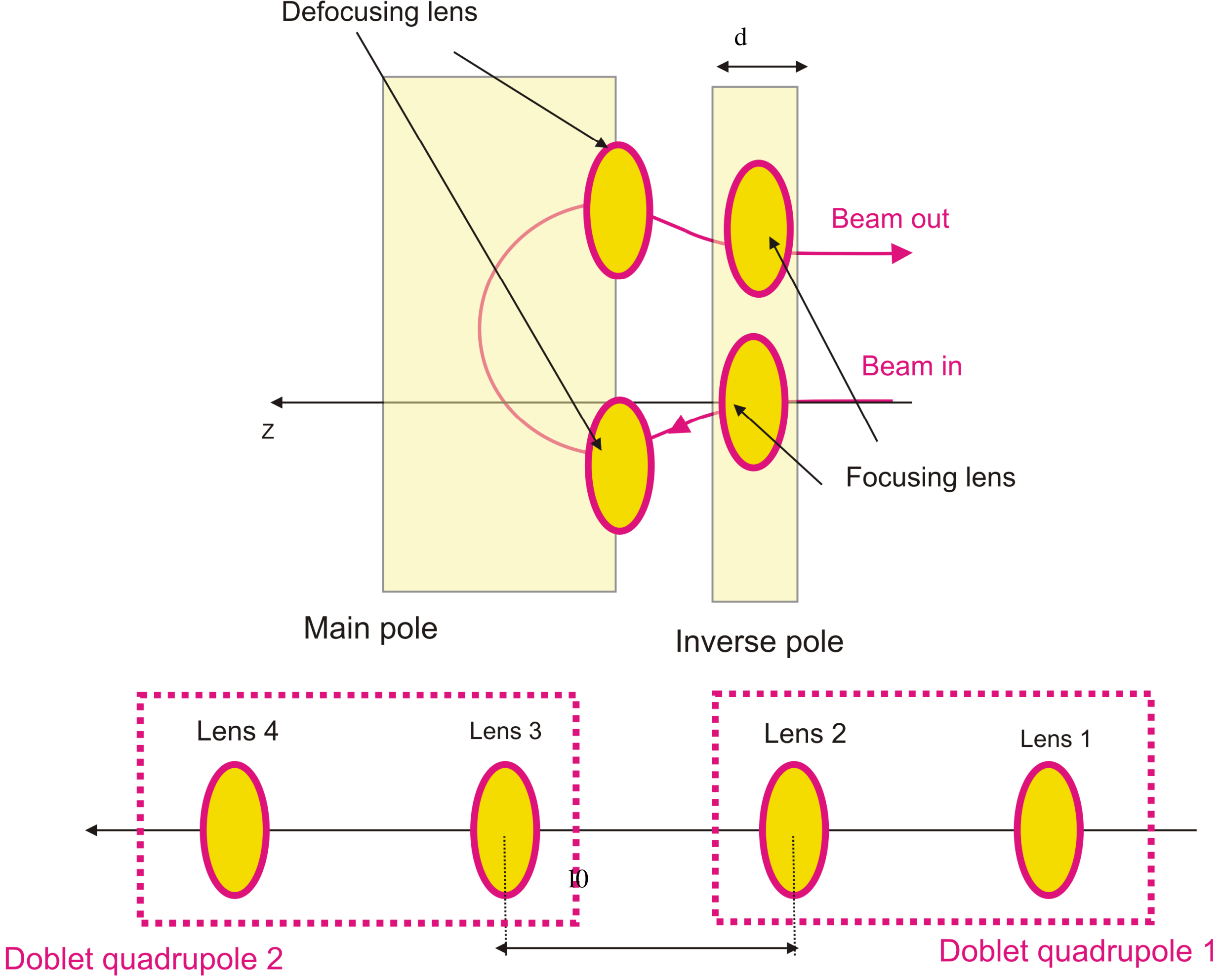

Figure 158: Scheme of the beam motion in the 2-pole end magnet and its representation within the matrix formalism as a beam transport line.

By straightforward calculations we obtain the following expression for the vertical focusing power of this magnetic system:

$$P = \frac{1}{F} = 2\left(\frac{1}{f_1} + \frac{1}{\tilde{f}_2}\right) + l_0\left(\frac{1}{f_1} + \frac{1}{\tilde{f}_2}\right)^2 + 2ll_0\left(\frac{1}{f_1^{\,2}\tilde{f}_2} + \frac{1}{f_1\tilde{f}_2^{\,2}}\right) + \frac{ll_0}{f_1\tilde{f}_2^{\,2}} + \frac{2l_0}{f_1\tilde{f}_2} + \frac{l^2}{f_1\tilde{f}_2^{\,2}} \qquad (173)$$

where $1/f_1$ is the focusing power of the the inverse pole given by Eq. (171a) and $1/\tilde{f}_2$ is the focusing power of the fringe field of the main pole equal to

$$\frac{1}{\tilde{f}_2} = \frac{1}{R_0^{\,2}}\left(-\left(\frac{B_1}{B_0}\right)Z_1 - \frac{d}{6}\right). \qquad (174)$$

This formula is obtained using Eq.(70). Note that in the formula for $1/\tilde{f}_2$ we took into account that the angles of the beam entrance into the defocusing quadrupoles describing the fringe field and that of the exit from it are non-zero.

In order to simplify the notations we introduce the following dimensionless variables: $\mu = Z_1/l$ , $k = B_1/B_0$ , $\delta = d/l$ and $r = R_0/l$ . Then $1/f_1$ and $1/\tilde{f}_2$ can be written as

$$\frac{l}{f_1} = \frac{2}{3r^2}k^2\mu, \qquad \frac{l}{\tilde{f}_2} = \frac{1}{r^2}\left(-k\mu - \frac{\delta}{6}\right) \tag{175}$$

Following the procedure of the 2-pole magnet design described in Sect. 4.1 we impose the condition of the first orbit beam reflection. For this we calculate the beam displacement Δ after passing through the magnet under consideration using Eq. (56). The result is

$$\Delta = -2R_0 + \frac{1}{R_0}\left[k^2{Z_1}^2 + \frac{d^2}{4} - kZ_1 d\right] + \frac{1}{R_0}\left[-2k{Z_1}^2 - \frac{d^2}{3} + 2kZ_1 l\right] \tag{176}$$

The condition of the orbit closure is $\Delta = 0$. Then the ratio $k = B_1/B_0$ becomes equal to

$$k_0(\mu) = \frac{-\left[\left(1-\frac{\delta}{2}\right)-\mu\right]+\sqrt{\left[\left(1-\frac{\delta}{2}\right)-\mu\right]^2+\left[2r_0+\frac{\delta^2}{12}\right]}}{\mu} \tag{177}$$

Finally we substitute expression (177) into Eqs. (173) and (175) and obtain a formula for the vertical focusing power of the 2-pole end magnet. Plots of $l/F$ as a function of $\mu$ for different values of the distance $l$ and certain choice of other parameters are shown in Fig.159. As one can see this function has a minimum for $\mu << 1$. As it was explained in Sect. 4.1 the beam motion is stable if the absolute value of the focusing power $P = 1/F$ is small enough. If the focal length is less than the distance between the end magnets beam instabilities may appear that lead to current losses and excessive stray radiation.

Here we will look for the case when $l/F = 0$. A simple analysis shows that this takes place if $r < r_{\max} = 0.11$. For a fixed initial energy $E_0$ this means that the distance between the main and inverse poles must be larger than certain minimal value, namely $l > l_{\min} = 9.09R_0$. This gives a limit on the minimal size of a 2-pole end magnet which reflects the beam with energy $E_0$ and has a long enough focal length for trajectories of this energy.

As an illustration of application of the result let us consider the initial design of the end magnets of the UPC 12 MeV RTM. The value of the uniform magnetic field in the main pole is $B_0 = 0.8T$, the beam energy $E_0 = 2.531$ MeV. Then $R_0 = 1.03$ cm, the minimal distance between the poles is $l_{\min} = 9.09R_0 = 9.4$ cm, $Z_1 = 5.7mm$ and $d = 6.0mm$ , and the ratio of the magnet field values obtained with Eq.(177) is $k = B_1/B_0 = 0.1592$.

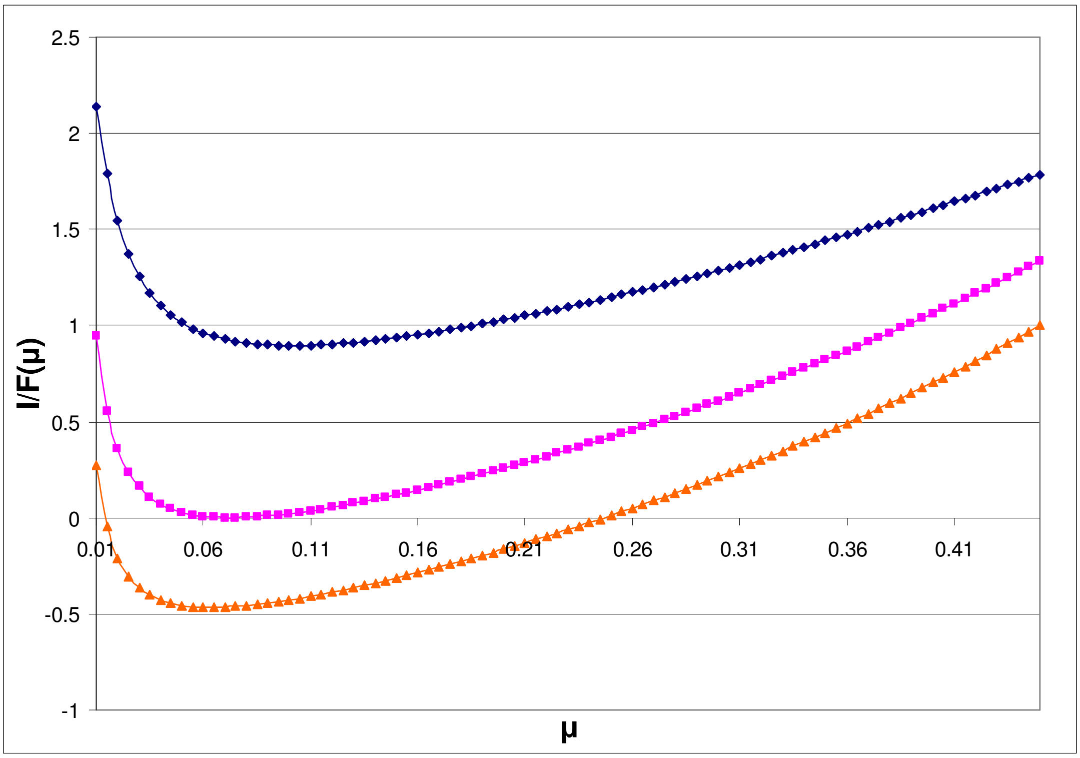

Figure 159: Plots of the function $l/F(\mu)$ for $k = k_0(\mu)$ given by Eq. (167) and $l = 6$cm, 8.67cm and 10cm (from top to bottom).

One concludes that a 2-pole end magnet which provides the closure of the first orbit (with $E_0 = 2.531\,\text{MeV}$ in our example) and has the focusing power equal to zero must have the distance between the dipoles larger than a certain limit in the Z-direction. This does not allow to get a sufficiently compact magnetic system. A similar result was obtained in Sect. 4.1 by means of 2D simulations using the POISSON and RTMTRACE codes. To get a compact end magnet with required properties, i.e. low enough vertical focusing power and orbit closure for the beam energy of 2.531 MeV, in Sect. 4.1 it was proposed to use a 4-pole system consisting of the main 180º bending dipole, inverse field dipole and two additional dipoles.

# Chapter 6

# conclusions

The objectives of this PhD thesis were listed in Sect. 1.5. The obtained results are the following:

- Design studies, analysis of magnetic properties and calculation of parameters of the magnetic systems of the 12 MeV RTM of the UPC project were carried out. These systems are the 4-pole end magnet, focusing quadrupole magnet and extraction dipoles. As a source of the magnetic field in these magnets the REPM material is used. The numerical calculations were erformed using the ANSYS, POISSON and FEMM codes.

- A procedure of the design of complex magnetic systems with permanent magneets was proposed. It was applied to the design studies mentioned above.

- A tuning system for the adjustment of the magnetic field in the end magnets of the UPC 12 MeV RTM was proposed and its design simulations were carried out.

- Design studies, numerical simulations with the ANSYS code and optimization of parameters of the magnetic screens of the extraction magnet of the 55 MeV RTM of the SINP (Moscow State University) were carried out. Also measurements of its characteristics and the experimental validation of the proposed optimization were performed. The obtained experimental results also allowed us to check the accuracy of the ANSYS code for this class of design simulations.

- An analytic method of calculation of the phase motion of electrons with arbitrary velocity (also non-relativistic velocities) in arbitrary magnetic systems was developed. It allows to calculate the phase slip effect which is important in RTM with low energy injection.

- The method of calculation of the particle phase motion of the previous point was applied to the computation of the optimal injection phase and the distance between the end magnets in the case of RTM with 2-pole end magnets. This optimal injection phase corresponds to the synchronous trajectory. Also the accuracy of this analytical approach was estimated by comparing the results to the ones obtained numerically.

- An analytical study of properties of 2-pole end magnets with fringe fields and inverse pole was carried out. For the case of designs with the reflection of the lowest orbit and low focusing power an estimate on the minimal size of the magnetic system was obtained. The results are in agreement with the ones obtained in the numerical calculations.

## Future works.

Once the engineering design of the magnetic systems of UPC 12 MeV RTM is finished and they are manufactured the next step will be to verify experimentally the results obtained in the design simulations and carry out necessary adjustments and field corrections.

## Publications.

The results of the thesis are published in the following papers:

[1] Miquel Ferrer, Yuri Koubychine, Antón Poseryaev, Juan Pablo Rigla, “Equipo para radioterapia intraoperatoria basado en un microtrón de pista de 12 MeV”, XVI Nacional Congress of Medical Physics (Granada, 22-25 Mayo 2007), “Física Médica”, vol. 8, núm 1 (2007), pp 86-87.

[2] Y.A.Kubyshin, J.P.Rigla, A.V. Poseryaev, V.I.Shedunov, “Analytic description of the phase slip effect in race track microtrons”, PAC07 (Particle Accelerator Conference), Albuquerque, USA, June 25 – 29, (2007), pp.3369-3371.

[3] M. Ferrer, Yu. A. Kubyshin, J. P. Rigla, A. V. Poseryaev, V. I. Shvedunov, “Compact Design of Race-track Microtron Magnets”, EPAC08 (European Particle Accelerator Conference), Genova, Italia, June 23 – 27, (2008), pp.2380-2382.

[4] Yu. A. Kubyshin, J. Berenguer, A.Crisol, X.González, G. Montoro, J.P. Rigla, F. Roure, D. Carrillo, L. Garcia-Tabares, F. Toral, J. Lucas, A.V. Aloev, V.I. Shvedunov, “Current Status of the 12 MeV UPC Race-track Microtron”, PAC09 (Particle accelerator conference), Vancouver, Canada, May 4 – 8, (2009), pp. 2775-2777.

[5] Yu. A. Kubyshin, J. P. Rigla, I.Yu. Vladimirov, N.I. Pakhomov,, V. I. Shvedunov, SINP, V.V. Zakharov, I.V. Chernov, “Performance of the Magnetic System of a 12 MeV UPC Race-Track Microtron”, RUPAC2012 (Russian Particle Accelerator Conference), Saint – Petersburg, Russia, September 24 – 28, (2012), pp.472 - 474.

[6] A.N. Ermakov, V.A. Khankin, Yu.A. Kubyshin, N.I Pakhomov, J.P. Rigla, V.I. Shvedunov, “Design and magnetic measurements of the extraction magnet for 55 MeV Race – Track Microtron”, MSU-SINP Preprint No 2011-2/866, 21 p., 2011.

# Annex 1

# Codes used in the simulations

Below short decryptions of the software packages used in this thesis are given.

## Poisson – Superfish program.

The Poisson - Superfish was developed in the 90's by Los Alamos Accelerator Code Group (LAACG), founded in 1986 by the Department of Energy of the United States [86]. It is a package of 30 programs written in the Fortran code which can be used under Windows and Unix operation system. It allows to calculate electrostatic and magnetostatic fields, as well as electromagnetic fields, both in 2D Cartesian coordinates and cylindrical coordinates with axial symmetry. This program solves the generalized Poisson equation by the relaxation method. It also contains a number of programs that allow to plot the calculated fields and other auxiliary quantities.

## ANSYS Multiphysics 10.0.

The ANSYS program is a finite element numerical code that includes a large number of options [87]. It allows to do structural and thermal calculations and perform fluid dynamics or electromagnetic analysis. The finite element method is based on discretization, i.e. transformation of a body of continuous nature into an approximate discrete model. The volume to be studied is divided into a finite number of parts, called elements, whose characteristics are specified by a finite number of parameters associated with certain characteristic points called nodes. These nodes are the points of attachment of each element to adjacent ones. The unknowns of the problem are no longer continuous functions and but the values of these functions at the nodes. The complete system is formed by the assembly of the elements and its solution is found using methods of discrete problems. The behavior inside each element is defined by the behavior of the known values at the nodes through appropriate interpolation functions or shape functions.

## MATLAB Code.

MATLAB (MATrix Laboratory) is a powerful tool for scientific and technical computing. The program performs numerical calculations with vectors and matrices. One of its most attractive capabilities is that it performs a wide variety of graphics in two and three dimensions. MATLAB has its own programming language. For certain operations, when one can run native code functions with appropriate sizes to take advantage of vectorization capabilities, the code is very fast. In other applications it is much slower than the equivalent code development in C/C+ + or Fortran. However, it is always a good tool for developing high-level technical applications. It is easy to use and increases significantly the programmer productivity in comparison with other programming environments.

# Bibliography

[1] Roy E. Rand, “Recirculating electron accelerators”, Harwood Academic Publish-Ers (1984).

[2] L.Merminga, R.D.Douglas and G.A.Krafft, “High – current Energy Recovering Electron Linacs”, Annu. Rev. Nucl. Part. Sci. Vol. 543, pp.387 - 429 (2003).

[3] J.W.Veksler, “A new method of acceleration relativistic paticles”, Jour.Phys. USSR, Vol.9 pp.153 (1945).

[4] P.Redhead,”Microtrons in Canada”, Physics in Canada, Vol.59 (2003).

[5] M.E.Rowem, “Tantalus I: A dedicated storage ring synchrotron radiation source”, Part. Accel., Vol.4, pp. 211-227 (1973).

[6] M.E.Moroz, “A cyclotron with sectional magnets”, Sov. Phys. Doklay, Vol.1, pp.236 (1956).

[7] A.Roberts, “The microtron as a high-energy, high current particle accelerator”, Ann. of Phys., Vol.4, pp.115 (1958).

[8] K.Buerkmann, T.Birke and J.Boninkof, “Commisssioning of the 100 MeV race – track microtron of the metrology light source”, in Proc. of the 22nd PAC07, Alburquerque, pp..944-996, (2007).

[9] Sergei P. Kapitza, Genrich D. Bogomolov, Lev.A. Wainshtein, Vitalii V. Zavialov, “The microtron and the free electron laser”, Nucl. Instrum. Methods Phys. Res. A, Vol.259, Issue 1, pp 285-287 (1987).

[10] Masterson M.E., “Beam characteristics of a new generation 50 MeV race – track microtron”, Med. Phys., Vol.22, pp. 781-795 (1995).

[11] Tsipenyuk, “The Microtron: Development & Applications”, Hardcover (2001).

[12] P.W.Trower, I.A.Karev, N.V.Melekhin, V.I.Shvedunov and N.P.Sobenin, “A mobile light source for carbon/nitrogen cameras”, Nucl. Instrum. Methods Phys. Res. B, Vol.99, Issues 1-4, pp. 736-738 ( 1995).

[13] A.Jankoviak, “The Mainz microtron MAMI: Past and Future”, 20 years of physics at Mainz Microtron MAMI (2005).

[14] Nagamine K., Miyadera H., Jason A., Seki R., “Compact muon source with electron accelerator for a mobile μSR facility”, Physica B: Condensed Matter, Vol.404, Issue 5, pp.1020–1023 (2009).

[15] K.Kawase, M.Kando, T.Hayakawa, “Development of a sub-MeV X-ray source via Compton backscattering”, Nucl. Instrum. Methods Phys. Res., A, Vol.637, Issue 1,pp.141-144 (2011).

[16] Skobletsyn Institute of Nuclear Physics – Lomonosov Moscow State University, website, http://www.sinp.msu.ru/.

[17] V.I.Shvedunov, A.N.Ermakov, I.V.Gribov and E.A.Knapp, “A 70 MeV race – track microtron”, Nucl. Instrum. Methods Phys. Res., A, Vol.550, Issues 1-2, pp.39-53 (2005).

[18] S.S.Belyshev, A.N.Ermakov, A. A. Kuznetsov, I. V. Makarenko and V. V. Khankin, “The RTM-70 accelerator as a pulsed source of neutrons and photons”, Moscow University Physics Bulletin, Vol.62, pp.360-362 (2007).

[19] V.I.Shvedunov, R.A.Barday, D.A.Frolov and V.P.Gorbachev, “A race track microtron with high brightness beams”, Nucl. Instrum. Methods Phys. Res., A, Vol.531, Issue 3, pp.346-366 (2004).

[20] H.Herminghaus, A.Feder, K-H. Kaiser, W.Manz and H.Schmitt,“The Design of a Cascaded 800 MeV Normal Conducting C.W. Race Track Microtron”**,** Nucl. Instrum. Methods, Vol.138, pp.1970-1976, (1976).

[21] H.Herminghaus, K-H.Kaiser and U.Ludwig-Mertin, “The Design of Double-Sided-Microtrons”, in Proc. of the LINAC81, pp.260-262, (1981).

[22] Jankowiak A., Aulenbacher K., “Commissioning and Operation of the 1.5 GeV Harmonic Double Sided Microtron at Mainz University”, in Proc. of the 11th EPAC 2008, Genoa, Italy, pp.51-56, (2008).

[23] C.W.Leemann, D.R.Douglas and G.A.Krafft, “The continuous electron beam accelerator facility: CEBAF at the Jefferson Laboratory”, Annu. Rev. Nucl. Part. Sci., Vol.51, pp.413-450, (2011).

[24] H.Wiedemann, “Particle Accelerator Physics”, Springer no 9783540490432, (2007).

[25] H.Babić and M.Sedlaček, “A method for stabilizing particle orbits in the race-track microtron”, Nucl. Instrum. Meth., Vol.56, pp.170-172, (1967).

[26] S.Rosander, M.Sedlaček, O.Wernholm and H.Babic., “The 50 MeV racetrack microtron at the royal institute of technology Stockholm”, Nucl. Instrum. Meth. Vol.204, Issue 1, pp.1-20, (1982).

[27] I.A.Karev, P.L.Kapitza, V.I.Shvedunov and N.P.Sobenin, “A permanent race – track microtron end magnet”, in Proc. of the 16th PAC95, Dallas, Texas, pp.1375-1377 (1995).

[28] Y.A.Kubyshin, P.A.Poseryaev and V.I.Shvedunov, “Longitudinal beam dynamics with phase slip in race-track microtrons”, Nucl. Instrum. Methods Phys. Res,.A, Vol.596, Issue 2, pp.147-156, (2008).

[29]Kraus H.R., “The overview and history of permanent magnet devices in accelerator technology”, IEEE transactions on magnetics, Vol.30, no 4, (1994).

[30] K. Halbach, “Design of permanent multipole magnets with oriented rare earth cobalt material”, Nucl. Instrum. Meth. Vol.169, Issue 1, pp.1-10, (1980).

[31] K. Halbach,”Physical and optical properties of rare earth cobalt magnets”, Nucl. Instrum. Meth. Vol.187, Issue 1, pp.109-117, (1981).

[32] K. Halbach, “Conceptual design of a permanent quadrupole magnet with adjustable strength”, Nucl. Instrum. Meth. Vol.206, Issue 3, pp.353-354 (1983).

[33] A.Young, “A compact permanent magnet cyclotrino for accelerator mass spectrometry”, Halbach Symposium on Magnet Technology Vol. 1, Berkeley, CA (US), (1995).

[34] V.S.Skachkov,“Quasi-sheet multipole permanent magnets”, Nucl. Instrum. Methods Phys. Res. A, Vol.500, no 1-3,pp.43-54, (2003).

[35] V.S.Skachkov and G.A.Novikov, “Large quasi-sheet dipole magnets”, Nucl. Instrum. Methods Phys. Res. A, Vol.526, Issue 3, pp.199-205, (2004).

[36] R.H.Kraus, “Overview and history of permanent magnet devices in accelerator technology”, in IEEE Transactions on Magnetics (ISSN 0018-9464), Vol.30, no 4 part 2, pp. 1547-1554, (1993).

[37] F.Putris, “Permanent magnet-based dipole for a small storage ring”, in Proc. of the 14th PAC94, San Francisco, CA, pp.2351-2353, (1994).

[38] G. Tosin, J. F. Citadini, P. P. Sanchez, R. Basilio, M. Rocha, E. W. Siqueira, M. Potye and Liu Lin, “Design of magnet prototypes for the new Brazilian synchrotron light source – SIRIUS”, in Proc. of the IPAC´10, Kyoto, Japan, pp.3084-3086, (2010).

[39] J.A.Clarke, “The Science and Technology of Undulators and Wigglers”, Oxford Series on Synchrotron Radiation, (2004).

[40] C.Benabderrahmane, P.Berteaud, M.Valléau, C.Kitegi, K.Tavakoli, N.Béchu, A.Mary, J.M.Filhol and M.E.Coupriel, “$Nd_2Fe_{14}B$ and $Pr_2Fe_{14}B$ magnets characterisation and modelling for cryogenic permanent magnet undulator applications Nucl. Instrum. Methods Phys. Res. A 669, Issue ,pp.1-6 (2012).

[41] B.Ishkhanov, I.N.Pakhomov, N.V.Shvedunov, V.I. Shvedunov and P.Gorbachev, “Conceptual design of the miniature electron accelerator dedicated to IORT”, in Proc. of the RUPAC2004, pp.474-476, (2004).

[42] Miquel Ferrer, Yuri Koubychine, Antón Poseryaev, Juan Pablo Rigla, “Equipo para radioterapia intraoperatoria basado en un microtrón de pista de 12 MeV”, XVI Nacional Congress of Medical Physics (Granada, 22-25 Mayo 2007), “Física Médica”, vol. 8, núm 1 (2007), pp 86-87.

[43] A.V.Poseryaev, V.IShvedunov, M.F.Ballester and Y.A.Kubyshin.,"Design a 12 MeV RTM for multiple applications", in Proc. of the 10th EPAC´06, Edinburgh, Scotland, pp.2340-2342 (2006).

[44] L.L.Gunderson, F.A.Calvo, G.C.Willett and B.L.Harrison, "Intraoperative Irradiation: Techniques and Results", Second Edition, Ed. Humana Press, (2011).

[45] Mobetron website, http://md51.com/

[46] G.Tosi and M.Ciocca,"IORT with mobile linacs: the Italian experience", Oncología (Barc.) v.27 n.6 Madrid 2004.

[47] David Carrillo Barrera et al, "C-Band linac for a racetrack microtron", Thesis of Universidad Complutense de Madrid, (2010).

[48] Yu. A. Kubyshin, J. Berenguer, A.Crisol, X.González, G. Montoro, J.P. Rigla, F. Roure, D. Carrillo, L. Garcia-Tabares, F. Toral, J. Lucas, A.V. Aloev, V.I. Shvedunov, "Current status of the 12 MeV UPC Race-Track Microtron", in Proc. of the 23rd PAC09, Vancouver, Canada, pp.2775-2777, (2009).

[49] Y.A.Kubyshin et al, "RF and Accelerating Structure of 12 MeV UPC Race-track Microtron" Proc. of 2nd IPAC11, San Sebastian, pp.169-171 (2011).

[50] A.V. Aloev, D. Carrillo, Yu.A. Kubyshin, N.I. Pakhomov and V.I. Shvedunov, "Electron gun with off-axis beam injection for a race-track microtron", Nucl. Instrum. Methods Phys. Res. A, Vol.624, no 1, pp.39-46,(2010).

[51] M. Ferrer, Y.A.Kubyshin, J.P.Rigla, A.V.Poseryaev and V.I.Shvedunov, "Compact Design of Race-track Microtron Magnets", in Proc. of the 11th EPAC08, Genoa, Italy, pp.2380-2382, (2008).

[52] C. De la Fuente, M.A.Duch, Y.A.Kubyshin.and V.I.Shvedunov, "Monte Carlo Simulation of the Total Dose Distribution around the 12 MeV UPC Race-track Microtron and Radiation Shielding Calculations", in Proc. of the 2nd IPAC2011, San Sebatian, pp.2370-2372, (2011).

[53] A.I. Karev, A.N. Lebedev, V.G. Raevsky, A.N. Kamanin, N.I. Pahomov and V.I. Shvedunov, "55 MeV Race – track microtron of Lebedev Institute", Proceedings of XXI RuPAC 2008, Zvenigorod, Moscow region, pp.124-126 (2008).

[54] V.V. Khankin, N.I.Pakhomov, V.I.Shvedunov, A.I.Karev and V.G.Raevsky, "Operational experience with 55 MeV pulsed RTM", ", in Proc. of the 23th RUPAC2012, Saint – Petersburg, Russia, pp.538 - 540, (2012).

[55] E.A Knapp, A.W Saunders, V.I Shvedunov, N.P Sobenin and W.P Trower, "A mobile racetrack microtron", Nucl. Instrum. Methods Phys. Res. B, Vol.139, Issue 1-4, pp.517-521, (1998).

[56] G.A Novikov, O.V Chubarov, K Halbach, A.I Karev, V.I Shvedunov and W.P Trower, “Novel race track microtron end magnets”, Nucl. Instrum. Methods Phys. Res. B, Vol.139, Issues 1-4, pp.527 - 530, (1998).

[57] J.Rosander, M.Sedlacek and O.Wernholm, “Method and apparatus for compensation of effects of misalignment between deflecting magnetic fields and a linear accelerator in a race track microtron”, Patent US4123720, October 31, 1978.

[58] N.A.Ermakov et al., “An Injection and Acceleration System of a Pulsed Race-Track Microtron”, Instruments and Experimental Techniques, Vol.45, no 4, pp.482-489, (2002).

[59] A.S.Alimov et al., “Generating high-brightness electron beams”, In Proc. of the 18th PAC99, New York, USA, pp.2301-2303, (1999).

[60] M. Borland, "A High-Brightness thermionic microwave electron gun", PhD Thesis, Stanford linear accelerator center - Stanford University, Stanford, (1991).

[61] H.A.Enge, “Achromatic Magnetic Mirror for Ion Beams”, The Review of Scientific Instruments, Vol.34, Issue 4, (1963).

[62] G.A.Novikov., “A permanent magnet electron beam phase-shifter”, Nucl. Instrum. Methods Phys. Res. A, Vol.524, Issues 1–3, pp.60-67, (2004).

[63] J. Roßbach and P. Schmüser, Proceedings of 1992 CERN Accelerator School, CERN 94-01, (1994), pp. 17-88.

[64] Jean-François, “Longitudinal profile and effective length dipole magnet”, In Proc. of the 15th PAC93, Washington D.C, pp.2901-2904, (1993).

[65] P.A.Banford, “The transport of charged particle beams”, London, F. and F.F. Spon Limte, (1966).

[66] V.Shevdunov and Y.Kubyshin, “Intraopeartive radiation therapy dedicated race – track microtron design, Final report”, Technical report T-08-01, Barcelona, (2008).

[67] R.L. Ayres et al., "The NIST-NRL Free Electron laser facility", Nucl. Instrum. Methods Phys. Res. A, Vol.296, pp.25 - 32, (1990).

[68] P.H. Debenham, "The injection chicane of the NBS Los ALamos Racetrack MicrotroN", Proc. of the 12th IEEE Particle Accelerator COnference, Washington D.C., pp.1452 - 1454, (1987).

[69] P.Axel, S.L.Cardman and O.A.Hanson, A.O., “Status of MUSL-2, the Second Microtron Using a Superconducting Linac”, IEEE Transactions on Nuclear Science, Vol.NS-24, nº 3, (1977).

[70] Y.A.Kubyshin, A.P. Poseryaev and V.I.Shvedunov, "Longitudinal beam dynamics with phase slip race - track microtron", Nucl. Instrum. Methods Phys. Res. A, Vol.539, Issues 1-2, pp.147-156, (2008).

[71] A.M.Gloston and H.Heffner, “Focusing of an electron beam by periodic fields”, J. Appl. Phys. 25, 436 (1954).

[72] E. P. Furlani , "Magnetic Materials," Engineering Materials and Processes Desk Reference. Ed. M. Ashby et al., Butterworth-Heinemann, (2008).

[73] P. Campbell, “Permanent Magnet Materials and their Application”, Cambridge Ubiversity Press, Cambridge - United Kingdom (2008).

[74] CAS - CERN Accelerator School on Superconductivity and Cryogenics for Accelerators and Detectors**,** 8 - 17 May 2002, Erice, Italy.

[75] Henry B. Luna, Xavier K. Maruyama, Nicholas J. Colella, John S. Hobbs, Robert S. Hornady, Bernhard Kulke, James V. Palomar, “Bremsstrahlung radiation effects in rare earth permanent magnets”, Nucl. Inst. and Methods in Phys. A, Vol.285, Issues 1–2, pp.349-354, (1989).

[76] The art and science of magnet design: Selected notes of Klaus Halbach, Symposium on Magnet Technology honor Klaus Halbach, vol.1, Berkley - USA, (1995).

[77] G.A Novikov, O.V Chubarov, K Halbach, A.I Karev, V.I Shvedunov and W.P Trower, “Novel race track microtron end magnets”, Nucl. Instrum. Methods Phys. Res. B, Vol.139, Issues 1-4, pp.527 - 530, (1998).

[78] V.S.Skachkov, A.V.Selin, I.M.Kapchinskiy and N.V.Lazarev, “Circular permanent magnet quadrupoles for higher frequency and higher shunt – impedance linacs”, Proceedings of Third EPAC 92, Berlin, pp. 1400 – 1403, (1992).

[79] V.S.Skachkov, N.A.Ermakov and V.I.Shvedunov, “A fixed gradient permanent alpha - magnet”, in Proc. of the 7th EPAC 2000, Vienna, Austria, pp. 2125-2127, (2000).

[80] V.S. Skachkov, "A variable gradient rare earth permanent alpha - magnet", in Proc. of the 7th EPAC00, New York, USA, pp.2301-2303, (1999).

[81] Skachkov S.V., Ermakov N.A., Shvedunov I.V., “Quasi-sheet quadrupole triplets”, Nucl. Instrum. Methods Phys. Res., A, Vol.524, Issues 1–3, pp.39-45, (2004).

[82] V.Massana, “Caracterizació d´un imant de curvatura combinar mitjanzant sondes d´efecte Hall”, Master project, Autonoma Univesity of Barcelona, Barcelona, (2005).

[83] G.Le Bec and J.Chavanne, “Permanent magnet steerers for canted undulators at the ESRF”, Nucl. Instrum. Methods Phys. Res., A Vol.664, Issue 1, pp.214-222, (2012).

[84] D.R.Schlueter et al, “Passive temperature compensation in hybrid magnets with application to the FERMILAB stacker and recycler ring dipole design, LBL – 37341, June 1995.

[85] V.I.Shvedunov et al., RTMTRACE, VINiTI, N183-B89, (1989).

[86] POISSON Code, http://laacg1.lanl.gov/laacg/services/download_sf.phtml.

[87] ANSYS Multiphysics program, http://www.ansys.com/.

[88] Yu. A. Kubyshin, J. P. Rigla, I.Yu. Vladimirov, N.I. Pakhomov, V. I. Shvedunov, V.V. Zakharov, I.V. Chernov, “Performance of the Magnetic System of a 12 MeV UPC Race-Track Microtron”, in Proc. of the 23th RUPAC2012, Saint – Petersburg, Russia, pp.472 - 474, (2012).

[89] FEMM Code, http://www.femm.info/wiki/HomePage.

[90] A. Novikov, “Magnetic systems of accelerators with recirculation”. Ph.D. thesis, Moscow State University, 2001 (in Russian).

[91] J.K.Lim et al, “Adjustable, short focal length permanent-magnet quadrupole based electron beam final focus system”, Phys. Rev. ST Accel. Beams 8, 072401 (2005), July 15, 2005.

[92] M.A.Asner, P.Bossard and F. Röhner, “A new "split-pole" quadrupole lens”, CERN-64-05.

[93] Skachkov S.V., Ermakov N.A., Shvedunov I.V., “Quasi-sheet quadrupole triplets”, Nucl. Instrum. Methods Phys. Res., A, Vol.524, Issues 1–3, pp.39-45, (2004).

[94] A.N. Ermakov, V.A. Khankin, Yu.A. Kubyshin, N.I Pakhomov, J.P. Rigla, V.I. Shvedunov, "Design and Magnetic Measurements of the Extraction Magnet for 55 MeV Race Track Microtron". MSU-SINP Preprint No 2011-2/866, (2011) 21 p.

[95] Yu.A. Kubyshin, J.P. Rigla, A.V. Poseryaev, V.I. Shvedunov, "Analytic Description of the Phase Slip Effect in Race-Track Microtrons", in Proc. of the 22nd PAC2007, Alburquerque, New Mexico, pp.3369-3371, (2007).

RTMTrace.

The main part of the RTMTrace program code was written in 1984 at the Skobeltsyn Institute of Nuclear Physics of the Moscow State University by M.A.Sotnikov and V.I.Shedunov and later modified with the participation of A.V.Tiunov and I.V.Surma [85]. This code is used for calculation of beam trajectories and their characteristics in RTMs and their main systems such as bending and focusing magnets, chopper, buncher, capture sections, accelerating structures, beam transport lines, etc.

The code essentially solves the Maxwell equations and calculates the particle motion in given electric and magnetic fields. It was originally developed for the use on computers with limited capabilities, so the authors dedicated much effort to the development of fast algorithms for the integration of the equations of particle motion. The program includes options for calculation of the electron trajectories using approximate and simplified algorithms, in particular for relativistic energies. For some elements there are several ways to perform the calculations, for example there are 4 of them for the accelerating structures and 4 for the 180 ° bending magnets.

FEMM (Finite Element Method Magnetics)

Similar to the ANSYS the FEMM code [90] is based on the finite element method and is used for solving both electrostatic and magnetoestatic problems. The difference with the ANSYS code is that the FEMM performs calculation in 2D only.